

Development of an intense attosecond source based on relativistic plasma mirrors at high repetition rate

Jaismeen Kaur

▶ **To cite this version:**

Jaismeen Kaur. Development of an intense attosecond source based on relativistic plasma mirrors at high repetition rate. Physics [physics]. Institut Polytechnique de Paris, 2024. English. ⟨NNT : 2024IPPAE007⟩. ⟨tel-04719180v2⟩

HAL Id: tel-04719180

https://theses.hal.science/tel-04719180v2

Submitted on 8 Apr 2026

HAL is a multi-disciplinary open access archive for the deposit and dissemination of scientific research documents, whether they are published or not. The documents may come from teaching and research institutions in France or abroad, or from public or private research centers.

L'archive ouverte pluridisciplinaire **HAL**, est destinée au dépôt et à la diffusion de documents scientifiques de niveau recherche, publiés ou non, émanant des établissements d'enseignement et de recherche français ou étrangers, des laboratoires publics ou privés.



HAL Authorization

INSTITUT POLYTECHNIQUE DE PARIS

NNT : 2024IPPAE007

Thèse de doctorat

ENSTA

IP PARIS

Development of an intense attosecond source based on relativistic plasma mirrors at high repetition rate

Thèse de doctorat de l'Institut Polytechnique de Paris
préparée à l'École nationale supérieure de techniques avancées

École doctorale n°626 École doctorale de l'Institut Polytechnique de Paris (EDIPP)
Spécialité de doctorat: Optique, Laser et Plasma

Thèse présentée et soutenue à Palaiseau, le 21 Juin 2024, par

JAISMEEN KAUR

Composition du Jury :

Sophie Kazamias Professeure, Université Paris-Saclay (Laboratoire Irène Joliot-Curie)	Présidente
Matt Zepf Professor, Friedrich-Schiller-Universität Jena	Rapporteur
Eric Cormier Professor, Université de Bordeaux (Laboratoire à Photonique Numerique et Nanosciences)	Rapporteur
Jean-François Hergott Directeur de recherche, CEA Paris-Saclay (Laboratoire Interactions, Dynamiques et Lasers)	Examinateur
Stefan Haessler Chargé de recherche, CNRS (Laboratoire d'Optique Appliquée)	Directeur de thèse
Rodrigo Lopez-Martens Ingénieur de recherche, Ecole polytechnique (Laboratoire d'Optique Appliquée)	Co-directeur de thèse
Louis Daniault Ingénieur de recherche, Ecole polytechnique (Laboratoire d'Optique Appliquée)	Invité

Acknowledgments

Knowing where to start is often the hardest part. I always knew that doing a PhD is not a solo endeavor, but over the last five years, I discovered that it truly takes a village.

First and foremost, I want to acknowledge the people I spent most of my time with during this enriching journey: the PCO family. Rod and Stefan, thank you for integrating me into the team, for your unwavering support and confidence throughout my time at LOA. Rod, thank you for giving me a space to learn, for making it acceptable to make mistakes, and for encouraging to learn from them (I certainly broke my fair share of things :D). Thank you for creating a place where people can truly enjoy working, with the freedom to explore all sorts of crazy ideas (not always for the best :P). I cherished this the most during my time in the PCO team. I can't thank you for enough for sending me to several conferences around the world (Argentina, South Korea, US, China, Italy, and where not...its a very long list :D), giving me an opportunity to network on a platform that is unimaginable for a PhD student. I don't believe I could have done this anywhere else. Stefan, you are the epitome of kindness and patience, the go-to person for deep, nagging physics questions or when we couldn't make head or tail of our experiments (more often than not :D). Thank you for your constant guidance and support throughout this roller coaster of a ride. This manuscript would not have been possible without you.

Louis – the king of post-compression and all things lasers – thank you for introducing me to the world of multipass cells. What started off as a fun experiment turned into something so interesting and ultimately became a very important part of this manuscript. Your encouragement, support, and stimulating discussions over coffee and beers have been invaluable. Marie, I am deeply indebted to you. Thank you for teaching me everything that prepared me for this thesis, all the intricacies and inner workings of Salle Noire, and always with so much patience and kindness. Apart from the technical know-how and the secrets of Salle Noire, what I learned the most from you was to never give up! Truly, whenever (more like every day...) we would be stuck with something or the other in the lab, you always came up with innovative ideas, never stopped trying or gave up, no matter how hard it was, even if it meant doing the same thing over and over. I really enjoyed working with you, you are the best !! Towards the end, our minds were synchronized to the point that before I could even finish my sentence, you already knew what I was thinking. Thank you for understanding my *bla bla bla*. I would also like to thank Zhao for his infinite wisdom and patience. He is truly the laser whisperer. Without his superior laser expertise, I would never have been able to build a whole new amplifier from scratch and, not to mention, keep the Salle Noire laser running and alive. It was an honor to learn from him and work with him.

A special thanks is owed to the *Salle Noire* laser. I have always said that this laser is like a living, breathing being – temperamental, needing attention, and most importantly, a modicum of respect. Thanks to the *Salle Noire* laser, without whom this thesis could not have even begun and much less take the form that it has today!

Thank you, Antoine, for the invigorating and riveting "fresh-air" and coffee conversations, and for all the fun times at conferences and summer schools. Thank you, André, for all the help with the wavefront measurements. I am grateful to Fred for helping me, even after leaving the group, to debug and understand the target and its very mysterious controller. Thank you to the APPLI group members: Aline, Igor, Jérôme, Slava, Pierre, Joséphine, Neïl, Isa, Lucas and Julius. Thank you for always keeping the spirits high and creating a fun atmosphere in the lab. Thanks for your good humor and fun evenings at the bar and restaurants. Thank you, Igor, for always being there to help with simulations. A special mention for some other members of LOA too: the secretaries – Patricia, Sandrine, Catherine, and Magali – for all their help, always so efficient and prompt; Mouhcine, Pascal, Loïc, Sébastian, Bernard, and not to forget Charlie (the dream team) for running the trains on time despite the shortage of hands; Jean-Philippe, Max, Lena, Rostyslav, Pierrick, Mateusz, Guillaume, Silin, Marie, Amélie and Laurent for their help with the experiments, equipment, and offering good advice and conversation whenever needed. These are the little things that makes LOA such a special place!

Thank you to all those who contributed to this thesis through collaborations: Dan Levy, Victor Malka, Alessandro Flacco, Li Lu, Mingyuan Shi, Chaoneng Wu, David Gauthier, Nok Rungsawang, Xu Liu, Philippe Zeitoun, Jean-François Hergott, Marc Hanna, Federico Furch, Tobias Witting, and Tamas Nagy. I had the chance to meet some brilliant scientists and humble and kind people through scientific collaborations. Thanks to Subhendu Kahaly, Sudipta Mondal, Kwinten Nelissen, Indranuj Dey, Shirozhan Mojtaba, for welcoming us at ELI. Many thanks to Team Ardop: Matthieu Veihnhard, Everzeg Le Bouffant, and Mathias Le Pennec, for all the trips to Szeged and, importantly, for funding my thesis. I would also like to thank Arjun and Naveed for helping us retain some semblance of sanity during the chaotic times in Szeged.

I also want to thank the reviewers, Matt Zepf and Eric Cormier, for taking the time to read my manuscript. Their constructive feedback helped to further improve the scientific quality of my work. Thanks to Jean-François Hergott and Sophie Kazamias for agreeing to be a part of the jury. It was a pleasure to discuss my work with you.

On a more personal note, I cannot write acknowledgments without mentioning my family – my brother, Harry for the pep talks and always putting things into perspective and most importantly and my mother, who is the sole reason I could reach where I am today. Thanks to my friends, Rahul, Shreya, Aditya, Naveen, Saba and Rishabh, who were always there despite the distance. Thanks to Alok, Sujit, Pooja and Roman, who made Palaiseau not only bearable but more fun than I could imagine. I truly thank Alok for his "silly" questions (which were more thought-provoking than silly :D). Thanks to the Erasmus fam: Naveen, Sid, Shishir, Jordi, Leo, David, Shubo, Gayathri, Ali, and many more. You were a home away from home! Thank you all for being there! Last and perhaps the most special, thanks to Amar for always standing by my side come what may. I can't wait to see what the future holds for us!

Endings are always tough, but there can't be new beginnings without endings. Here's to the end of one chapter and the start of another.

Cheers !

Résumé

Les impulsions laser ultracourtes, à l'échelle de la femtoseconde ($0,000000000000001 = 10^{-15}$ s), ont conduit à l'invention du domaine de la « femtochimie », qui nous permet d'observer des phénomènes ultrarapides au sein des atomes et des molécules en temps réel à l'échelle microscopique. Depuis lors, les chercheurs s'efforcent d'améliorer la résolution temporelle et d'entrer dans le domaine de l'attoseconde (10^{-18} s), c'est-à-dire un milliardième de milliardième de seconde), afin d'observer et de contrôler le mouvement des électrons à leur échelle de temps naturelle. Les progrès de la technologie laser, en particulier la technique d'amplification à dérive de fréquence des impulsions, nous ont permis d'atteindre des puissances crête élevées (jusqu'à plusieurs Peta-Watts, 1 PW$= 10^{15}$ W) et de déclencher des phénomènes non-linéaires pour générer des événements encore plus brefs. Aujourd'hui, nous pouvons générer des flashs lumineux à l'échelle de temps de l'attoseconde dans la gamme de l'ultraviolet extrême (UVX), mais l'efficacité de génération reste faible. C'est pourquoi le développement de sources intenses à l'échelle de l'attoseconde est un domaine de recherche très actif à l'échelle mondiale. Depuis près d'un demi-siècle, de nombreux efforts de recherche se sont concentrés sur de nouvelles alternatives basées sur l'interaction laser-plasma. Les motivations qui sous-tendent ces travaux de recherche sont nombreuses. D'une part, les accélérateurs laser-plasma ont été reconnus comme très prometteurs en raison de leur capacité à accélérer les électrons à des vitesses proches de la vitesse de la lumière sur des distances extrêmement courtes, contrairement aux accélérateurs conventionnels qui s'étendent sur plusieurs kilomètres. D'autre part, lorsqu'un plasma dense interagit de manière non-linéaire avec une impulsion laser intense ($> 10^{16}$ W/cm^2), la surface du plasma elle-même agit comme un miroir oscillant à une vitesse relativiste, ce qui entraîne l'émission de faisceaux de particules hautement énergétiques (ions et électrons) et la génération d'un rayonnement cohérent UVX énergétique, correspondant à des impulsions attosecondes dans le domaine temporel. Les propriétés spatio-temporelles et l'efficacité de conversion des impulsions attosecondes ainsi produites sont extrêmement prometteuses. Contrairement à la méthode traditionnelle de génération d'impulsions attosecondes par ionisation et recombinaison d'électrons dans des jets de gaz, il n'y a pratiquement aucune limite à l'intensité de l'impulsion laser génératrice, ce qui permet en principe de produire des impulsions attosecondes beaucoup plus lumineuses. Ainsi, l'interaction laser-plasma dans le régime relativiste permet la production de nouveaux outils qui serviront à la communauté scientifique au sens large pour sonder la matière sur des échelles de temps sans précédent. De nombreuses autres applications sont également envisagées, telles que l'utilisation de ces miroirs plasma comme intermédiaires pour atteindre des intensités laser extrêmes, ce qui permettrait de sonder les fluctuations quantiques du vide à l'aide de lasers pétawatt. Le travail

expérimental présenté dans ce manuscrit a été réalisé dans le groupe *Physique du Cycle Optique*, dirigé par Rodrigo Lopez-Martens, au *Laboratoire d'Optique Appliquée*, sur l'installation laser *Salle Noire*. Cette installation délivre des impulsions laser quasi mono-cycle d'une énergie de plusieurs millijoules à un taux de répétition au kHz. L'objectif de ce travail de thèse est double. La première partie se concentre sur l'amélioration des performances de la source laser *Salle Noire* en augmentant l'énergie d'impulsion disponible et en améliorant la stabilité de la forme d'onde, ce qui rend la source laser plus fiable et plus stable avec des performances quotidiennes plus reproductibles. En outre, nous explorons un nouveau schéma de post-compression : les cellules multi-passages (MPC), à des niveaux d'énergie de l'ordre du millijoule. À l'avenir, ce schéma de post-compression, lorsqu'il sera rendu compatible avec de plus fortes énergies et intégré dans la chaîne laser *Salle Noire*, améliorera encore l'intensité de l'impulsion focalisée pour les expériences. La deuxième partie de ce travail se concentre sur l'utilisation de ce système laser pour piloter les miroirs plasma dans le régime relativiste à la surface de cibles initialement solides, afin de générer des faisceaux de particules hautement énergétiques (ions et électrons) et des rayonnements harmoniques dans la région UVX, correspondant à des impulsions attosecondes dans le domaine temporel. Nous avons produit des faisceaux d'électrons relativistes par injection localisée d'électrons dans le champ laser réfléchi de manière non-linéaire par le miroir plasma. En outre, nous avons généré des faisceaux de protons presque collimatés de classe MeV dans le cadre d'une expérience pompe-sonde contrôlée. En contrôlant et stabilisant phase enveloppe-porteuse des impulsions laser incidentes, nous avons pu limiter dans temps le processus d'interaction sur la surface de la cible et produire des impulsions attosecondes isolées (brillantes). Ce manuscrit est structuré comme suit :

- **Le chapitre 1** pose les bases théoriques de la génération, la compréhension et la manipulation des impulsions laser femtosecondes.
- **Le chapitre 2** décrit brièvement l'architecture du laser *Salle Noire* telle que héritée de mes prédécesseurs en 2019, et détaille les améliorations du laser que j'ai mises en œuvre au cours de ma thèse. La mise à niveau la plus critique étant la construction et l'intégration d'un amplificateur multi-passages avec refroidissement cryogénique pour augmenter l'énergie d'impulsion disponible et améliorer la stabilité de la phase enveloppe-porteuse, rendant la source laser plus stable et plus fiable et offrant des performances reproductibles au jour le jour.
- **Le chapitre 3** détaille les études expérimentales de la post-compression laser dans les MPC remplies de gaz. En outre, je décris l'intégration de deux techniques non-linéaires d'ordre 3 pour l'amélioration du contraste temporel des impulsions laser dans les architectures MPC : la rotation non linéaire d'ellipse et la génération d'onde à polarisation croisée. À l'avenir, ce schéma de post-compression, lorsqu'il sera intégré à la chaîne laser *Salle Noire*, permettra d'améliorer encore les propriétés de l'impulsion laser sur cible.
- **Le chapitre 4** présente les principes fondamentaux des interactions laser-plasma. Je décrirai plus en détail les miroirs plasma et la variété des émissions issues des miroirs plasma relativistes pilotés par laser, en discutant des mécanismes physiques et des propriétés fondamentales de trois émissions de miroirs plasma : les harmoniques d'ordre élevé, les électrons et les protons.

- **Le chapitre 5** fournit une description détaillée de la ligne de faisceaux de miroirs plasma kHz conçue de manière unique dans le groupe PCO. Je détaillerai les outils expérimentaux utilisés pour caractériser les émissions du miroir plasma à travers une large gamme de paramètres, y compris quelques nouveaux diagnostics que j'ai mis en œuvre pendant mon travail de thèse.
- J'ai divisé en deux chapitres les résultats expérimentaux obtenus au cours de ma thèse sur cette installation à miroir plasma. **Le chapitre 6** est consacré à la détection simultanée des trois émissions : harmoniques, électrons et protons, et à l'étude des corrélations entre elles, conséquence directe de leur détection simultanée. En outre, j'aborderai en détail l'accélération des protons à partir des miroirs plasma.
- **Le chapitre 7** est consacré aux résultats expérimentaux obtenus en mettant en œuvre le contrôle de la phase enveloppe-porteuse des impulsions laser incidentes pour piloter l'interaction avec les miroirs plasma, générant ainsi des impulsions attosecondes isolées. Ce chapitre comprend également une étude paramétrique systématique et complète visant à caractériser et à optimiser les propriétés spatiales et spectrales des impulsions UVX attosecondes émises, servant ainsi de base pour leur refocalisation en vue de nouvelles applications.

Contents

Acknowledgments 1

Résumé 5

List of acronyms 13

Introduction 17

1 Fundamentals of femtosecond lasers: Mathematical formalism 23
- 1.1 Electromagnetic waves in optics . . . 25
- 1.2 Nonlinear optics . . . 27
  - 1.2.1 Second-order nonlinearities . . . 27
  - 1.2.2 Third-order nonlinearities . . . 28
- 1.3 Light amplification in Ti:Sa crystals . . . 30
- 1.4 Commonly used laser parameters . . . 32

2 TW-peak power waveform controlled near-single-cycle laser 35
- 2.1 *Salle Noire*: Global architecture . . . 40
  - 2.1.1 Oscillator . . . 40
  - 2.1.2 First CPA . . . 40
  - 2.1.3 Nonlinear contrast filtering . . . 41
  - 2.1.4 Second CPA . . . 45
  - 2.1.5 Post-compression to near-single-cycle regime . . . 46
- 2.2 CEP detection and stabilization . . . 50
  - 2.2.1 CEP stabilization of the oscillator . . . 53
  - 2.2.2 CEP stabilization at the end of the laser chain . . . 54
- 2.3 Laser upgrades . . . 56
  - 2.3.1 HCF extension arm . . . 57
  - 2.3.2 Cryogenically-cooled multi-pass Ti:Sa amplifier . . . 57

3 Nonlinear optics in multipass cells 67
- 3.1 Multipass cells: Fundamentals . . . 70
- 3.2 Nonlinear mode-matching . . . 71
- 3.3 State-of-the-art . . . 73
- 3.4 Post-compression in multipass cells . . . 76

3.4.1 Identification of different propagation regimes . . . 77
3.4.2 Results in optimal conditions . . . 80
3.4.3 Summary . . . 82
3.5 Contrast enhancement in multipass cells . . . 83
3.5.1 Nonlinear ellipse rotation . . . 83
3.5.2 Cross-polarized wave generation . . . 88
3.5.3 Summary . . . 94
3.6 Conclusion . . . 95

4 Laser-Plasma interactions: Physical mechanisms **99**
4.1 Generation of plasmas: Ionization mechanisms . . . 101
4.2 Plasmas: key parameters . . . 104
4.3 Pre-plasma expansion . . . 105
4.4 Ponderomotive force . . . 106
4.5 Laser absorption in plasmas . . . 107
4.6 What is a plasma mirror? . . . 109
4.7 High-harmonic response of plasma mirrors . . . 110
4.7.1 Sub-relativistic regime . . . 110
4.7.2 Relativistic regime . . . 112
4.8 Electron acceleration mechanisms . . . 114
4.8.1 Vacuum laser acceleration . . . 115
4.8.2 Laser wakefield acceleration . . . 117
4.9 Ion acceleration mechanisms . . . 118

5 kHz Relativistic Plasma Mirror Beamline **121**
5.1 Relativistic plasma mirror beamline: Overview . . . 123
5.2 kHz Solid target . . . 125
5.3 Shooting sequence . . . 127
5.4 XUV detection . . . 129
5.4.1 XUV Spectrometer . . . 129
5.4.2 Spatial-intensity profile detection . . . 130
5.4.3 Wavefront characterization . . . 132
5.5 Electron detection . . . 133
5.5.1 Spatial charge distribution . . . 133
5.5.2 Magnetic electron spectrometer . . . 135
5.6 Ion detection . . . 136
5.6.1 Thomson Parabola Spectrometer . . . 136
5.6.2 Time of flight detector . . . 138
5.7 Plasma density gradient calibration . . . 141

6 Light and particle radiation from plasma mirrors: Experimental results **145**
6.1 Correlations between secondary emissions . . . 147

6.1.1 Anti-correlation between CWE-harmonics and electron emissions 147
6.1.2 Direct correlation between RHHG and electron emissions 149
6.2 LWFA of electrons 152
6.3 Low-divergence energetic proton beams 154
6.3.1 Experimental results 154
6.3.2 Analytical model 158
6.3.3 2D PIC simulations 159

7 Waveform-controlled relativistic plasma mirror emissions 163
7.1 State-of-the-art 165
7.2 CEP effects on RHHG and relativistic electrons 167
7.2.1 Varying plasma gradient scale length 167
7.2.2 At the optimal gradient scale length 167
7.2.3 From spectral measurements to temporal insights 170
7.2.4 Correlated behavior of relativistic electrons 172
7.3 Wide-range electron angular-charge detection 174
7.4 XUV wavefront 175
7.4.1 Silicon plate calibration 176
7.4.2 Wavefront sensor calibration 177
7.4.3 At the optimal gradient scale length 178
7.4.4 CEP effects 179

Conclusion and outlook 181

Perspectives 185

A Power scaling of HCF-based laser-post compression 189

B RHHG-beamline at ELI-ALPS: Conception and implementation 193
B.1 RHHG beamline: General description 194
B.2 VC1: Laser contrast enhancement 196
B.3 VC2: Beam shaping and diagnostics 200
B.4 VC3: RHHG 204
B.5 First results and next challenges 207

List of publications and conference Contributions 209

List of Publications 211

Bibliography 239

List of acronyms

AOI	Angle of incidence
AOM	Acousto-Optic Modulator
AOPDF	Acousto-Optic Programmable Dispersion Filter
APT	Attosecond Pulse Train
AR	Anti-Reflective
ARIES	Attosecond time-Resolved Interferometric Electric field Sampling
ASE	Amplified Spontaneous Emission
A.U.	Arbitrary Units
BBO	Beta Barium Borate
BGP	Baeva-Gordienko-Pukhov theory
BSI	Barrier Suppression Ionization
CCD	Charge Coupled Device
CEP	Carrier-to-Envelope Phase
CPA	Chirped Pulse Amplification
CRM	Curved Relativistic plasma Mirror
CSA	Collisionless Shock-wave Acceleration
CSE	Coherent Synchrotron Emission
CW	Continuous Wave
CWE	Coherent Wave Emission
DFG	Difference Frequency Generation
D-Scan	Dispersion Scan
DM	Deformable Mirror
ELI-ALPS	Extreme Light Infrastructure-Attosecond Light Pulse Source
FDI	Frequency Domain Interferometry
FFT	Fast-Fourier Transform

FTL	Fourier-Transform-Limited
FWHM	Full-Width at Half-Maximum
GDD	Group Delay Dispersion
HC	High-Contrast
HCF	Hollow Core Fiber
HeNe	Helium-Neon laser
HHG	High-Harmonic Generation
HR	Highly-Reflective
HWP	Half-Wave Plate
IAP	Isolated Attosecond Pulse
ICF	Inertial Fusion Confinement
IF	Interferometric Filter
IPN	Integrated Phase Noise
IR	Infra-Red
kW	kilo-Watt
LC	Low-Contrast
LIDT	Laser-Induced Damage Threshold
LOA	Laboratoire d'Optique Appliquée
LR	Low Reflectivity
LWFA	Laser WakeField Acceleration
LWS	Light-Wave Synthesizer
MCP	Micro-Channel Plate
MPC	Multi-Pass Cell
MPI	Multi-Photon Ionization
MTA	Medium shielded Target Area
NA	Numerical Aperture
NIF	National Ignition Facility
NLO	Nonlinear Optics
OAP	Off-Axis Parabola
OPCPA	Optical Parametric Chirped Pulse Amplifier
OSU	Ohio State University
pB	Proton-Boron
PBS	Polarizing Beam Splitter

PCO	Physique du Cycle Optique
PIC	Particle-In-Cell
PM	Plasma Mirror
PPLN	Periodically-Poled Lithium Niobate
PSD	Position Sensitive Device
PSF	Point-Spread Function
PW	Peta-Watt
QWP	Quarter-Wave Plate
RABBIT	Reconstruction of Attosecond Beating By Interference of Two-photon transitions
RES	Relativistic Electron Spring
RHHG	Relativistic High-Harmonic Generation
ROC	Radius of Curvature
ROM	Relativistic Oscillating Mirror
RMS	Root Mean Square
RPA	Radiation Pressure Acceleration
RPACE	Radiation Pressure Assisted Coulomb Explosion
SDI	Spatial Domain Interferometry
SEA	SYLOS Alignment laser
SFG	Sum Frequency Generation
SHG	Second Harmonic Generation
SPM	Self-Phase Modulation
SRSI	Self-Referenced Spectral Interferometry
SS	Self-steepening
SW	Shutter Wheel
SYLOS	Single-Cycle Laser Systems
SZTU	Shenzhen Technology University
TGC	Transmission Grating Compressor
THG	Third Harmonic Generation
Ti:Sa	Titanium:Sapphire
TIPTOE	Tunneling Ionization with a Perturbation for the Time domain Observation of an Electric field
TNSA	Target Normal Sheath Acceleration

TOF	Time Of Flight
TOUCAN	Temporal dispersion based One-shot Ultrafast Carrier envelope phase ANalysis
TPS	Thomson Parabola Spectrometer
TW	Tera-Watt
VC	Vacuum chamber
VLA	Vacuum Laser Acceleration
XPM	Cross-Phase Modulation
XPW	Cross-Polarized Wave generation
XUV	Extreme Ultra-Violet
Yb	Ytterbium

Introduction

The pursuit of visualizing events on short time scales represents a compelling journey that transcends both time and scale, pushing the boundaries of human understanding and technological capabilities. What began as a mere endeavor to settle a debate initiated by Leland Stanford, a prominent businessman and racecourse owner in California (USA), as to whether all four of a horse's hooves leave the ground simultaneously during a gallop, culminated in Eadweard Muybridge's groundbreaking achievement: "The Horse in Motion" (figure 1), earning him the recognition as "the photographer who stopped time". Captured in 1878, this series of photographs not only revolutionized our perception and comprehension of motion but also sparked a profound curiosity to explore and comprehend movements unfolding on time scales beyond the limits of human perception.

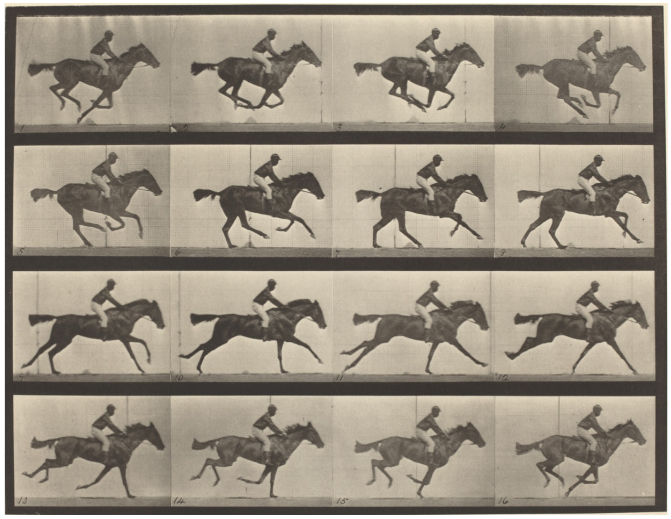

Figure 1: Eadweard Muybridge's "The Horse in Motion" 1878. All four of the horse's hooves are in air in frames 2 and 3. Courtesy of National Gallery of Art, Washington, United States.

The journey from capturing motion on a millisecond ($1\ \mathrm{ms} = 0.001\ \mathrm{s}$) to a femtosecond ($1\ \mathrm{fs} = 0.000000000000001 = 10^{-15}\ \mathrm{s}$) time scale (figure 2) represents an extraordinary feat of relentless technological advancement spanning over nearly a century. This remarkable leap was made possible thanks to the groundbreaking invention of lasers in 1960 by Theodore Maiman [1]. Over the subsequent two decades, continued technological innovations led to the demonstration of picosecond ($1\ \mathrm{ps} = 10^{-12}$ s) pulses and the eventual realization of femtosecond-scale imaging capabilities.

The significance of this field and the driving force behind the continued research are underscored by the prestigious accolades it has garnered. Notably, the Nobel Prize in Chemistry was awarded to

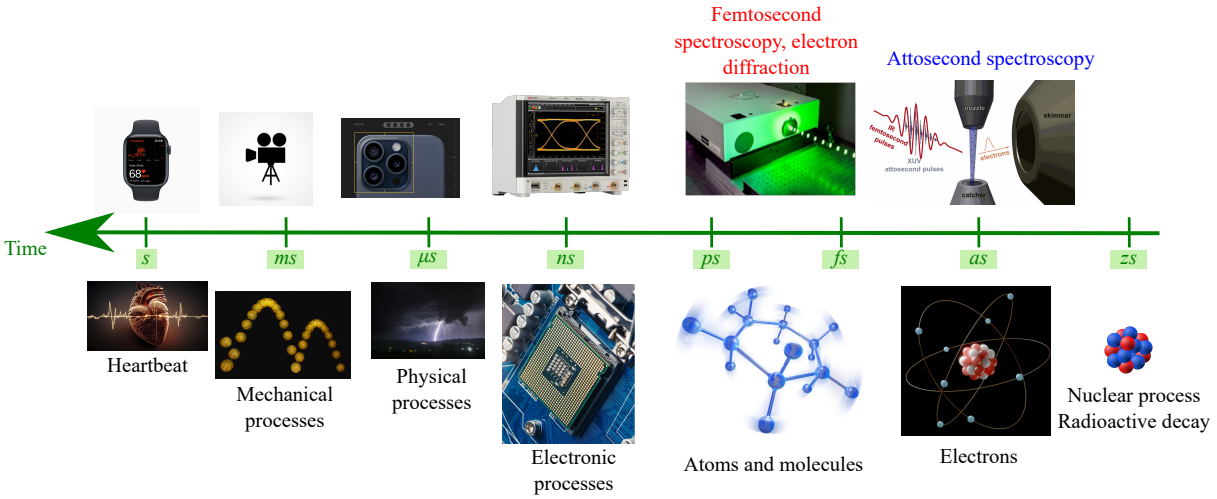

Figure 2: Events across varying time scales and the corresponding appropriate tools for their visualization.

Ahmed Zewail in 1999 for the pioneering use of femtosecond lasers to study the transition states in chemical reactions, giving birth to the field of "femtochemistry". In 2018, the Nobel Prize in Physics was awarded to Gérard Mourou and Donna Strickland for devising the chirped pulse amplification (CPA) scheme [2] (figure 3), which has revolutionized femtosecond pulse generation and enabled a myriad of applications across medicine, scientific research, and beyond. The CPA technique lies at the heart of most high-power laser facilities in the world, enabling the physicists to build Peta-Watt (PW)-class lasers that are orders of magnitude more powerful than previously achievable.

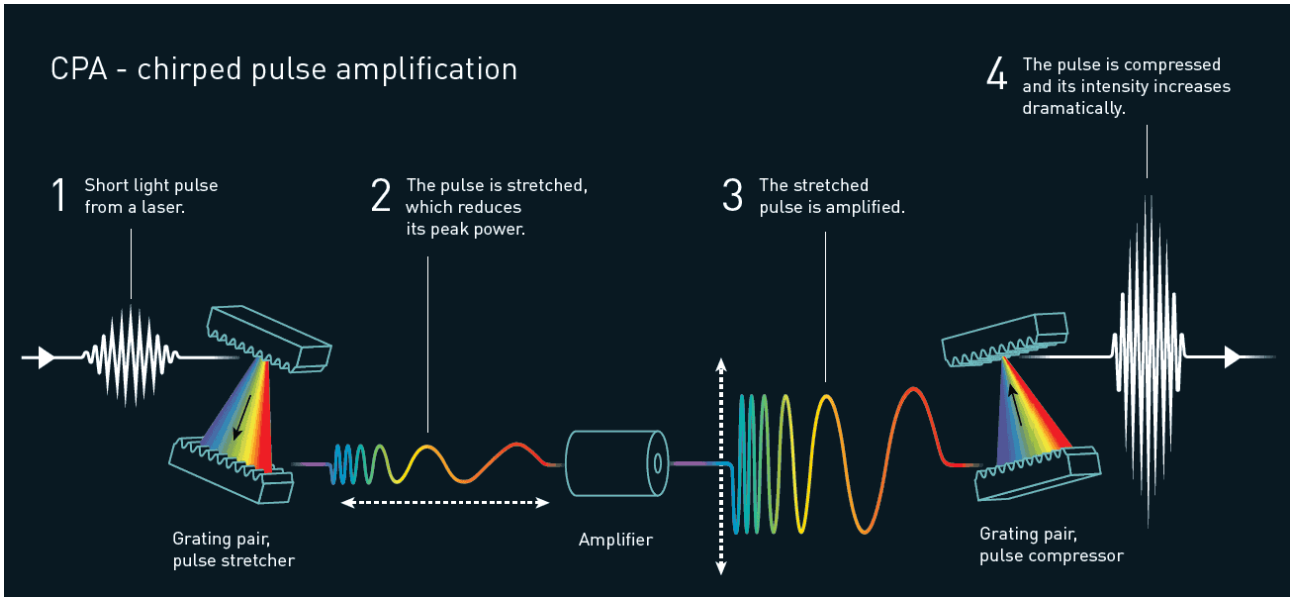

Figure 3: Principle of the chirped pulse amplification process. Courtesy of the Nobel Foundation.

After scaling the femtosecond summit, attention naturally turns towards the attosecond ($1\,\mathrm{as} = 10^{-18}\,\mathrm{s}$, i.e. a billionth of a billionth of a second) time scales. An attosecond is so short

that there are as many in one second as there have been seconds since the birth of the universe. Electron dynamics within atoms and molecules unfold at an attosecond time scale. Most recently, the Nobel Prize in Physics in 2023 was awarded to Anne L'Huillier, Pierre Agostini, and Ferenc Krausz for their groundbreaking work in generating attosecond pulses of light – the shortest known events to mankind, to date.

The genesis of attosecond pulses traces back to 1977 when Burnett *et al.* [3] focused a $10.64\,\mu\mathrm{m}$ CO_2 laser pulse onto a solid target and generated higher-order harmonics extending up to the eleventh harmonic, around $0.95\,\mu\mathrm{m}$. Despite their groundbreaking observation, the underlying process eluded full explanation within the existing theoretical framework at the time. Nearly a decade later, McPherson *et al.* [4] made a similar observation, but this time from the interaction of laser pulses with a gaseous medium. In 1988, L'Huillier and her team [5] observed analogous behavior in a rare gas, measuring the odd harmonics with a relatively constant intensity from the 5th to the 33rd harmonic, and approaching a cut-off thereafter. This observation marked the first instance of a clear intensity profile of the generated harmonics, identifying three distinct features: the initial intensity fall-off, the plateau, and the cut-off (figure 4). A plateau-like intensity profile of high-harmonic generation (HHG) offered promising potential, suggesting the bandwidth necessary for producing extremely short pulses, "possibly" extending into the attosecond regime. However, harnessing HHG for practical applications necessitated a deeper understanding of the underlying physical mechanism.

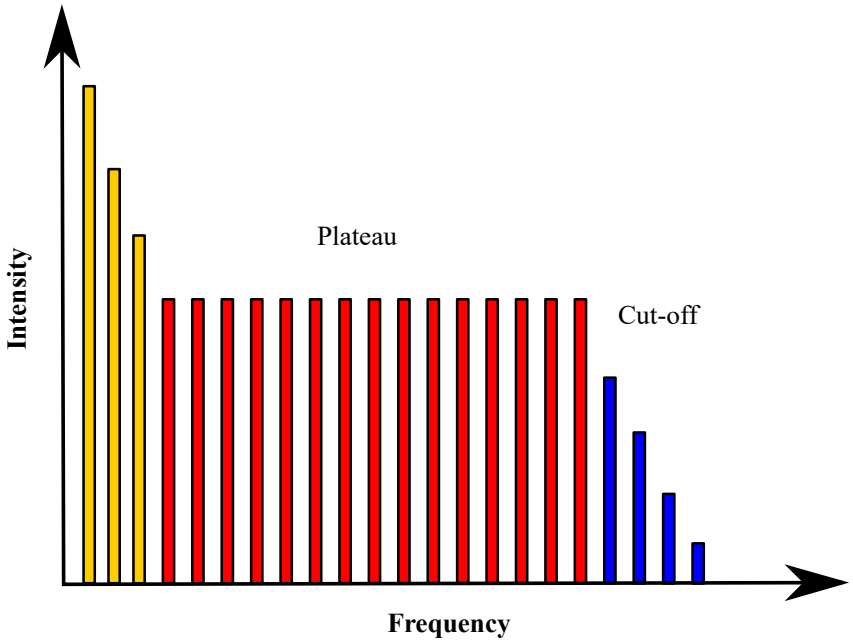

Figure 4: A generic HHG spectrum from the interaction of a laser with a gaseous medium. Adapted from [6].

In 1991, L'Huillier *et al.* [7] presented numerical insights into the HHG process, predicting the spectral shape and initiating discussions on macroscopic phase matching. Shortly thereafter, Corkum [8], and Schafer *et al.* [9] introduced the widely acclaimed, semi-classical, "three-step model": strong-field ionization of an atomic or molecular gas launches free electrons that are accelerated in the laser

field and upon re-collision with the parent ion emit a high-energy photon, as illustrated in figure 5. While the roadmap to attosecond pulse generation was largely laid out, the next crucial step involved developing metrology tools to accurately measure and characterize these pulses in time. In 1994, at LOA, Pierre Agostini and his team laid the foundation for what is now the most commonly used technique to characterize attosecond pulses: RABBIT - Reconstruction of Attosecond Beating By Interference of Two-photon transitions [10]. The path to isolated attosecond pulses was explored by Ferenc Krausz and his team, who used a few-cycle driving laser source to generate isolated 650 as pulses [11]. Further insights into the major achievements, milestones, and current technological capabilities of the field can be found in [12–14].

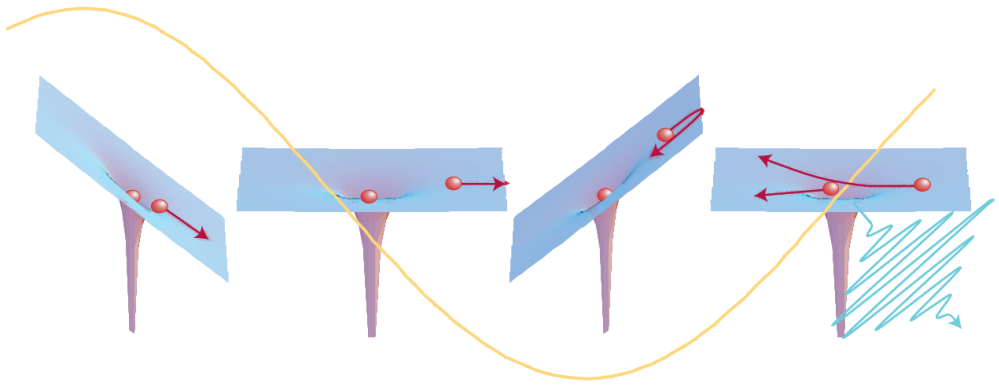

Figure 5: Representation of a semi-classical three-step model describing the gas-HHG. Reprinted from [13].

The work on the development of attosecond sources continues to this day. The physical mechanism to generate attosecond pulses via gas-HHG works only when the medium is not fully ionized, thus placing an upper limit on the intensity of the driving laser pulses and by extension on the driver infra red (IR)-to-extreme ultraviolet (XUV) conversion efficiency, which prompted physicists to explore other novel approaches to accessing the attosecond realm. HHG in solid- [15] and liquid-phase [16, 17] have quite recently been explored.

As the laser technology advanced, enabling access to intensity ranges spanning from Tera-Watt (TW) to PW, physicists naturally revisited the seminal observations of HHG from initially-solid targets or near-solid density plasmas [3]. In 2009, Nomura *et al.* [18] presented the initial evidence of production of attosecond light pulses from plasmas, marking a significant milestone in the field. This was closely followed by a study from Teubner and Gibbon [19] in the same year, which provided significant experimental and theoretical insights, representing a pivotal step in understanding HHG from plasmas . The physical mechanism and emission properties of HHG from plasmas significantly differs from those observed with gases. When the laser-pulse is reflected nonlinearly off an overdense plasmas, under certain conditions, the laser field induces relativistic oscillations of the plasma reflective layer. This oscillatory motion triggers a periodic frequency up-shift of the reflected laser wave, effectively compressing the electric field temporally. These newly generated frequencies occur periodically, every optical cycle, and interference effects result in the observation of both odd and even harmonic orders of the incident laser [20].

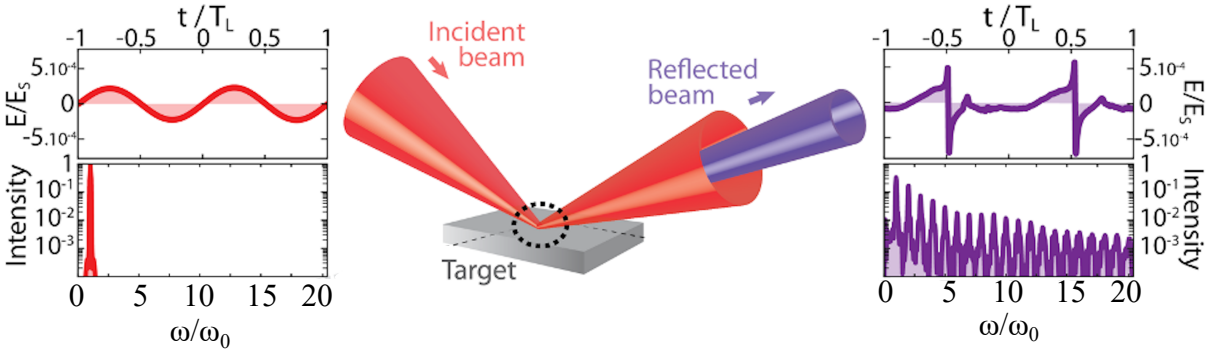

Figure 6: Principle of HHG from plasmas. Reprinted from [21].

Despite the experimental challenges and stringent requirements imposed on the driver laser pulses, research activity on HHG in plasmas has witnessed a surge on the international stage in the recent years, driven by progress in laser technology and simulation tools, primarily because this approach promises to significantly boost the available pulse energy and brightness [20, 22]. Since the goal is to trigger nonlinear interaction of an overdense plasma with the laser pulses, there is inherently no limitation on the intensity of the driving pulse, consequently, promising significantly higher conversion efficiencies compared to those observed with gases. Additionally, along with a promising source of attosecond pulses, overdense plasmas also offer very high accelerating field strengths, ideal to accelerate charged particles, such as sub-femtosecond bunches of electrons [23] and protons [24, 25] suitable for applications.

This manuscripts presents a detailed parametric study of secondary emissions from dense plasmas: energetic particle beams (ions and electrons) and HHG in the XUV region , identifying optimal conditions for the generation of each of these signals. Moreover, by using a waveform-controlled near-single-cycle driving laser pulse, we can gate the interaction with the plasma and produce (bright) isolated attosecond pulses. Through a comprehensive parameter study, we could characterize and optimize the spatio-spectral properties of the emitted XUV attosecond pulses, building the framework for their refocusing for future experiments.

Manuscript outline

- **Chapter 1** provides the theoretical foundation for the generation, understanding and manipulation of femtosecond laser pulses
- **Chapter 2** briefly describes the architecture of the *Salle Noire* laser as I inherited from my predecessors in 2019, and details the laser upgrades I implemented during the course of my thesis. The most critical upgrade being the construction and integration of a cryogenically-cooled multi-pass Titanium:Sapphire amplifier to augment the available pulse energy and enhance the waveform stability, making the laser source more stable and reliable, exhibiting reproducible day-to-day performance.
- **Chapter 3** details the experimental investigations of laser post-compression in gas-filled multi-pass cells (MPC). Additionally, I will describe the integration of two third-order nonlinear tech-

niques for laser contrast enhancement within MPC architectures. In the future, MPC-based post-compression scheme when power-scaled and integrated into the *Salle Noire* laser chain will further enhance the laser capabilities.

- **Chapter 4** introduces the fundamentals of laser-plasma interactions. I will describe the so-called plasma mirrors (PM) and the intriguing emissions from laser-driven relativistic PMs in more detail, discussing the physical mechanisms and fundamental properties of three PM emissions: HHG, electrons and protons.

- **Chapter 5** provides a detailed description of the uniquely designed kHz PM beamline in the PCO group. I will detail the experimental tools used to characterize the PM emissions across a wide range of parameters, including some new diagnostics that I implemented during my thesis.

- I have divided the experimental results obtained with the PM beamline during my thesis into two chapters. **Chapter 6** is dedicated to the simultaneous detection of all three emissions: harmonics, electrons, and protons, and to studying direct correlations between them, finding optimized generation conditions for each of the emissions. Additionally, I will discuss proton acceleration from PMs in detail in this chapter.

- **Chapter 7** is dedicated to the experimental results obtained by implementing waveform control of the driving laser pulses to time-gate the interaction with the PMs, consequently generating isolated attosecond pulses. This chapter also includes a systematic, comprehensive parametric study to fully characterize and optimize the spatial-spectral properties of the emitted XUV attosecond pulses, laying the groundwork for their refocusing, for applications.

Chapter 1

Fundamentals of femtosecond lasers: Mathematical formalism

"*Laser is a solution seeking a problem.*"
-Theodore Maiman

Outline

1.1 Electromagnetic waves in optics **25**
1.2 Nonlinear optics **27**
1.2.1 Second-order nonlinearities 27
1.2.2 Third-order nonlinearities 28
1.3 Light amplification in Ti:Sa crystals **30**
1.4 Commonly used laser parameters **32**

1.1 Electromagnetic waves in optics

Maxwell's equations establish the theoretical framework for understanding the behavior of electromagnetic fields, and are fundamental to understanding the interaction of light with matter. First introduced in the 19th century by a Scottish physicist, James Clerk Maxwell [26], they are most often used in their differential form, as follows:

$$\begin{aligned} \textbf{Gauss law} \qquad & \vec{\nabla}.\vec{E} = \frac{\rho}{\varepsilon_0} \\ \textbf{Gauss law for magnetism} \qquad & \vec{\nabla}.\vec{B} = 0 \\ \textbf{Maxwell-Faraday equation} \qquad & \vec{\nabla}\times\vec{E} = -\frac{\partial\vec{B}}{\partial t} \\ \textbf{Maxwell-Ampère circuital law} \qquad & \vec{\nabla}\times\vec{B} = \mu_0\vec{J} + \mu_0\varepsilon_0\frac{\partial\vec{E}}{\partial t} \end{aligned} \tag{1.1}$$

Here, ρ and $\vec{J}$ are the charge and current densities, respectively, and ε_0 and μ_0 are the vacuum permittivity and permeability, respectively. The electric field, $\vec{E}$ and magnetic field, $\vec{B}$ can be determined by the Lorentz force imposed on a test charge q moving with a velocity $\vec{v}$, given by

$$\vec{F} = q\vec{E} + q(\vec{v}\times\vec{B}) \tag{1.2}$$

The electric and magnetic fields can either be generated by the present charge density, ρ and current density, $\vec{J}$, or they can also be self-sustained by time-varying field strengths, $\frac{\partial\vec{E}}{\partial t}$ or $\frac{\partial\vec{B}}{\partial t}$. If we try to solve the coupled differential equations in the absence of any free carriers and currents, i.e. $\rho = 0$ and $\vec{J} = 0$

$$\begin{aligned} \vec{\nabla}\times\vec{\nabla}\times\vec{E} &= -\vec{\nabla}\times\frac{\partial\vec{B}}{\partial t} \\ \vec{\nabla}(\vec{\nabla}.\vec{E}) - \nabla^2\vec{E} &= -\mu_0\varepsilon_0\frac{\partial^2\vec{E}}{\partial t^2} \\ \nabla^2\vec{E} - \frac{1}{c^2}\frac{\partial^2\vec{E}}{\partial t^2} &= 0 \end{aligned} \tag{1.3}$$

This is the so-called wave-equation, where $c = 1/\sqrt{\mu_0 \varepsilon_0}$ is the propagation speed. The presence of an electric field $\vec{E}$ within an optical medium leads to a displacement of positive and negative charges, thereby inducing an electric polarization, $\vec{P} = \varepsilon_0 \chi \vec{E}$, where χ is the susceptibility tensor. To look at the Maxwell's equations from a macroscopic point-of-view, we separate the bound and free charge distributions.

$$\rho = \rho_b + \rho_f \quad \text{and} \quad \vec{J} = \vec{J}_b + \vec{J}_f \tag{1.4}$$

$$\begin{aligned} \vec{\nabla}.\vec{E} &= \frac{\rho_f + \rho_b}{\varepsilon_0} \\ &= \frac{\rho_f - \vec{\nabla}.\vec{P}}{\varepsilon_0} \end{aligned} \tag{1.5}$$

Let's define an auxiliary field, $\vec{D} = \varepsilon_0 \vec{E} + \vec{P}$. Finally, the Maxwell's equations in a dielectric medium are given as

$$\begin{aligned} \vec{\nabla}.\vec{D} &= \rho_f \\ \vec{\nabla}.\vec{B} &= 0 \\ \vec{\nabla} \times \vec{E} &= -\frac{\partial \vec{B}}{\partial t} \\ \vec{\nabla} \times \vec{B} &= \mu_0 \vec{J}_f + \frac{\partial \vec{D}}{\partial t} \end{aligned} \tag{1.6}$$

In the absence of free charges, the wave equation is given as

$$\nabla^2 \vec{E} - \frac{1}{c^2} \frac{\partial^2 \vec{E}}{\partial t^2} = \mu_0 \frac{\partial^2 \vec{P}}{\partial t^2} \tag{1.7}$$

Optical media are often classified by the nature of relationship between $\vec{E}$ and $\vec{P}$. If we develop the polarization in a power series expansion of the electric field, we can distinguish between the linear and nonlinear material responses.

$$\begin{aligned} \vec{P} &= \vec{P_L} + \vec{P_{NL}} \\ \vec{P} &= (\varepsilon_0 \chi^{(1)} \vec{E}) + (\varepsilon_0 \chi^{(2)} \vec{E}^2 + \varepsilon_0 \chi^{(3)} \vec{E}^3 + ...) \end{aligned} \tag{1.8}$$

Here, $\chi^{(m)}$ is the mth-order susceptibility tensor of rank $m+1$. In linear optics, it is a sufficiently good approximation that $\vec{P}$ depends linearly on $\vec{E}$, with $n^2 = 1 + \chi^{(1)}$, where n is the refractive index. However, in case of high field strengths, the relationship between $\vec{E}$ and $\vec{P}$ is nonlinear. Assuming, the nonlinear contribution is much smaller than the linear one, the nonlinear wave equation is given as

$$\nabla^2\vec{E} - \frac{n^2}{c^2}\frac{\partial^2\vec{E}}{\partial t^2} = \mu_0\frac{\partial^2\vec{P_{NL}}}{\partial t^2} \tag{1.9}$$

1.2 Nonlinear optics

The term "*nonlinear optics*" (NLO) was first coined in 1941 by Erwin Schrödinger [27]. This branch of optics encompasses the study of behavior of light in nonlinear media, in which the electric polarization $\vec{P}$ responds nonlinearly to the electric field $\vec{E}$. Typically, this requires high field strengths, of the order of 10^8 V/m, that can be induced by laser field. The laser electric field can be expressed as a combination of monochromatic progressive plane waves

$$\vec{E}(\vec{r},t) = \frac{1}{2}\left(\Sigma_m\vec{E}(\omega_m)e^{i(\omega_m t - \vec{k}_m.\vec{r})} + c.c.\right) \tag{1.10}$$

Assuming a memory-less instantaneous response of the material to the electric field, the nonlinear polarization can be decomposed as,

$$\vec{P}_{NL}(\vec{r},t) = \frac{1}{2}\left(\Sigma_l\vec{P}_{NL}(\omega_m)e^{i(\omega_m t - \vec{k}_m.\vec{r})} + c.c.\right) \tag{1.11}$$

For example, if the electric field consists of two oscillating components at ω_1 and ω_2, the corresponding nonlinear polarization acts as a source of new frequency components at $\omega \in (2\omega_1, 2\omega_2, \omega_1 + \omega_2, \omega_1 - \omega_2, 0)$. This section gives a brief overview of the nonlinear processes of interest that occur as a consequence of equations 1.8 and 1.9.

1.2.1 Second-order nonlinearities

The second order nonlinear terms can be described by the polarization vector as

$$\vec{P}(\vec{r},t,\omega_3 = \omega_1 + \omega_2) = \varepsilon_0\chi^{(2)}(\omega_3;\omega_1,\omega_2)\vec{E}(\omega_1)\vec{E}(\omega_2) \tag{1.12}$$

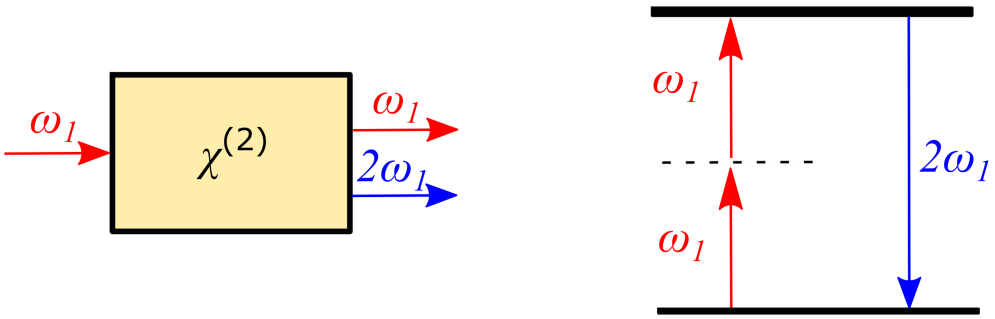

Figure 1.1: Interaction scheme (left) and energy-level diagram (right) describing the SHG process. Adapted from [28].

- **Second harmonic generation (SHG)**: The second harmonic of a monochromatic wave at frequency ω_1 oscillates at $\omega = 2\omega_1$. In this case, the nonlinear polarization is given as

$$P_{SHG}(\vec{r},t,2\omega_1) = \frac{1}{2}\varepsilon_0\chi^{(2)}E^2(\vec{r},t,\omega_1) \tag{1.13}$$

  Figure 1.1 shows the interaction scheme and the energy-level diagram of the SHG process. Simply put, two photons interact to generate a single photon with twice the energy. Under the optimized phase matching conditions, nearly all the power in the incident beam at ω_1 can be efficiently transferred to SHG at $2\omega_1$. Most commonly used pump lasers in Ti:Sa laser systems, for example Nd:YAG emit at $1064\,\mathrm{nm}$ and are frequency-doubled by the SHG process to $532\,\mathrm{nm}$, matched to the peak of the absorption spectra of Ti:Sa (figure 1.4).

- **Sum frequency generation (SFG):** In this case, $\omega_1 \neq \omega_2$, and the newly generated wave is given by $\omega_3 = \omega_1 + \omega_2$.

- **Difference frequency generation (DFG):** Likewise, we have $\omega_3 = \omega_1 - \omega_2$, where $\omega_1 > \omega_2$. The DFG process has several applications, however, in the scope of this thesis, we will be using DFG for measuring the carrier-to-envelope phase (CEP) of the laser electric field, discussed in detail in section 2.2.

1.2.2 Third-order nonlinearities

The third-order nonlinear processes involve interactions between four waves: three input waves at ω_1, ω_2, and ω_3 and a fourth wave generated at ω_4. Several wave-mixing processes are possible, a few of them are listed below:

- **Third harmonic generation (THG):** $\omega_1 = \omega_2 = \omega_3$ and $\omega_4 = 3\omega_1$.

- **Self phase modulation (SPM):** An intrinsically phase-matched process in which the incident wave modulates its own phase. The nonlinear polarization in this case is given as

$$\begin{aligned} P_{SPM}(r,t,\omega_1) &= \frac{3}{4}\varepsilon_0\chi^{(3)}|E(r,t,\omega_1)|^2E(r,t,\omega_1) \\ P_{tot}(r,t,\omega_1) &= \varepsilon_0\chi^{(1)}E(r,t,\omega_1) + \frac{3}{4}\varepsilon_0\chi^{(3)}|E(r,t,\omega_1)|^2E(r,t,\omega_1) \end{aligned} \tag{1.14}$$

  The effective susceptibility can be given as

$$\chi_{eff} = \chi^{(1)} + \frac{3}{4}\chi^{(3)}|E(r,t,\omega_1)|^2 \tag{1.15}$$

  The effective refractive index of the medium, $n^2 = 1 + \chi_{eff}$ can be decomposed into a linear index n_0 and a nonlinear index n_2, such that $n = n_0 + n_2 I$, where $I = 2n_0\varepsilon_0 c|E|^2$ is the incident laser intensity. The nonlinear index is given as [28]

$$n_2 = \frac{3}{4n_0^2\varepsilon_0 c}\chi^{(3)} \tag{1.16}$$

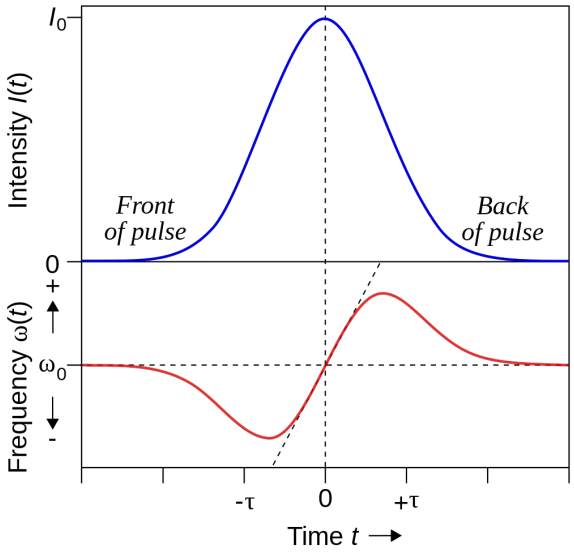

Figure 1.2: Instantaneous frequency shift of an intense laser pulse due to SPM. Figure created by Emmanuel Boutet, licensed under CC-BY-SA-2.5.

In case of a femtosecond laser pulse with a time-varying intensity profile $I(t)$, a time-varying nonlinear phase is acquired during propagation in the medium, $\phi_{NL} = -n_2 I(t)\omega_1 L/c$. As a result, the spectrum of the emitted wave is modified and typically accompanied by the generation of new frequency components.

For a more intuitive insight into this process, let's consider an instantaneous frequency, $\omega(t) = \omega_0 + \delta\omega$, where, $\delta\omega(t) = d\phi_{NL}(t)/dt$ is the time-dependent variation of the instantaneous frequency, depicted in figure 1.2. The maximum value of this frequency shift, given as $\delta\omega_{max} = \Delta\phi_{NL}^{max}/\tau_0$, where τ_0 is the laser pulse duration, is obtained during the steepest slope of the intensity profile. SPM is considered to be significant whenever $\delta\omega > \Delta\omega$, where $\Delta\omega$ is the spectral width of the incident laser pulse.

- **Cross phase modulation (XPM):** It is another intrinsically phase-matched third-order nonlinear process in which a strong wave at ω_1 imposes a phase modulation onto a second wave at ω_2. The nonlinear polarization can be given as

$$P_{XPM}(r,t,\omega_2) = \frac{6}{4}\varepsilon_0\chi^{(3)}|E(r,t,\omega_1)|^2 E(r,t,\omega_2) \tag{1.17}$$

Similar to SPM, when a femtosecond laser pulse undergoes XPM, the induced nonlinear phase is time-dependent and leads to spectral broadening. In case of linear and circularly polarized input waves, a scalar understanding of the phenomenon assuming co-polarized waves is often sufficient. However, in case of elliptically polarized laser pulses, one has to take into account a vector approach [29], revealing a phenomenon called nonlinear ellipse rotation (NER). Elliptically polarized laser pulses launched into a nonlinear medium undergo XPM-induced rotation of the polarization ellipse as they propagate through the medium. Simultaneously, there is also an energy transfer between the two waves at ω_1 and ω_2, while the total energy remains conserved.

Exploiting the fact that the rotation of the polarization ellipse exhibits a cubic intensity dependence [28], NER is well established in the ultrafast community as a polarization-discrimination based temporal intensity contrast enhancement technique [30–34]. This technique will be used later in this manuscript, in chapter 3 for simultaneous contrast enhancement and spectral broadening of ultrashort laser pulses.

- **Cross-polarized wave generation (XPW):** Yet another intrinsically phase-matched, but degenerate third-order nonlinear process in which a linearly polarized input wave generates a new wave at an orthogonal polarization, $\omega_{\perp} = \omega_{\parallel} + \omega_{\parallel} - \omega_{\parallel}$. This process is governed by the anisotropy of the real part of $\chi^{(3)}$ tensor, exhibited by materials such as, BaF_2 and CaF_2 [35–37]. This technique was first developed at LOA and has evolved to be a well-established and perhaps the most widely used technique for temporal contrast enhancement in high-energy Ti:Sa laser systems [38] and will be discussed on multiple accounts in this manuscript, in chapters 2 and 3.

1.3 Light amplification in Ti:Sa crystals

"Laser" is an acronym that stands for "Light Amplification by Stimulated Emission of Radiation". Theoretical groundwork was laid by Albert Einstein in 1916 when he introduced the concept of population inversion and stimulated emission [39]. However, it was not until the late 1950s that physicists found an application of stimulated emission [40] and soon after, the first ever working laser was built in 1960 by an American physicist Theodore Maiman, at Hughues Research Laboratory in California [1], demonstrating the operation of an optically pumped Ruby laser emitting at 694.3 nm. At first, the relevance of this accomplishment was unclear, and Maiman's remark, "*a laser is a solution seeking a problem*" could not have been more accurate. Despite the clear potential to focus light to unprecedented levels of precision and intensity, many in the scientific community and beyond were uncertain about the practical use of lasers, as their invention was driven purely by scientific curiosity. Over time, opinions dramatically shifted as lasers found their way into numerous applications, revolutionizing various fields, from welding to laser cutting industry, vision correction in the field of medicine, etc.

In the following decades, as the demand for more powerful, tunable, and versatile lasers intensified, several materials were explored as potential gain media. In 1982, Titanium-doped Sapphire was identified as a particularly promising gain medium, marking a significant advancement in laser technology [41]. Since its discovery, Ti:Sa has emerged as the cornerstone or the ultrafast laser technology, reigning the industry for nearly half a century.

Titanium-doped Sapphire or Ti:Sa is a synthetic crystal in which Titanium ions (Ti^{3+}) are embedded octahedrally ($3d1$ configuration) in a Sapphire lattice (Al_2O_3). The laser emission is based on a 4-level energy scheme as shown in figure 1.3. The system is first excited from its stable ground state E_1 to E_4 by absorbing a photon with energy $\omega_{\text{pump}} \propto E_4 - E_1$, with a central wavelength $\lambda_{\text{pump}} \approx 450 - 570$ nm. The absorption and emission spectra of Ti:Sa are shown in figure 1.4. The higher energy state E_4 has a short life time of ≈ 3.2 ps and quickly depopulates to E_3 through a non-radiative transition.

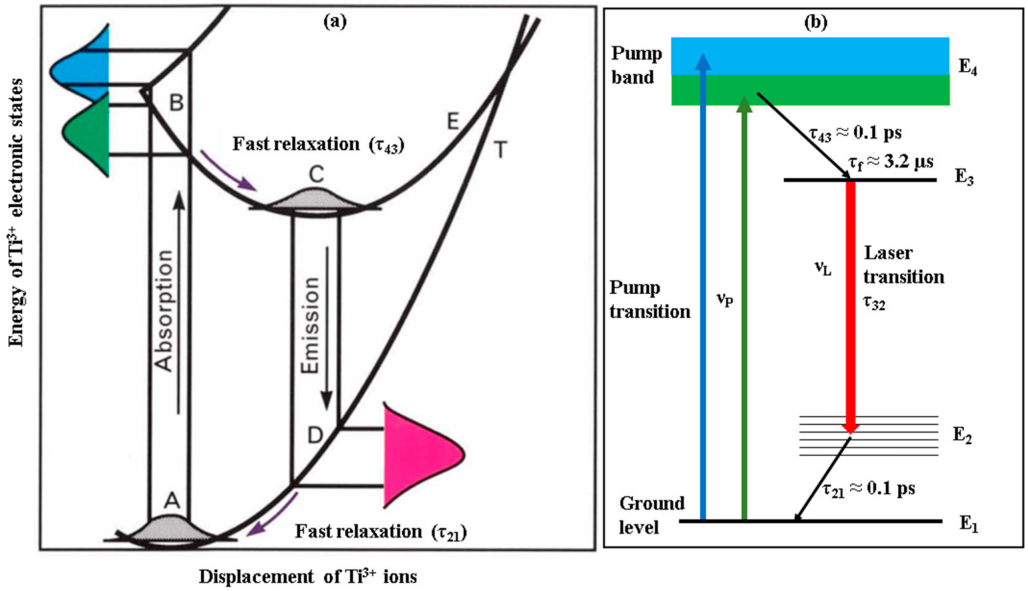

Figure 1.3: Configurational diagram of Ti^{3+}-doped Sapphire. Displacement band-structure of the upper and lower energy levels (a) and a simplified energy level diagram (b). Reprinted from [42].

This makes it difficult to efficiently use flash lamps to pump Ti:Sa crystals. Typically, frequency-doubled Nd:YAG, Nd:YVO_4 and Nd:YLF lasers emitting between $527 - 532$ nm are used to achieve population inversion. Radiative decay is triggered from E_3 to E_2 with photon energy $\omega_0 = E_3 - E_2$. Typically, emission is most efficient around 800 nm, however, the emission bandwidth spans from $600 - 1050$ nm. Large gain bandwidths supporting pulses as short as 8 fs [43], wavelength tunablity, readily available diode-pumps, high thermal conductivity and high saturation fluence are some of the key advantages of Ti:Sa lasers which led to their high demand and subsequent industrialization.

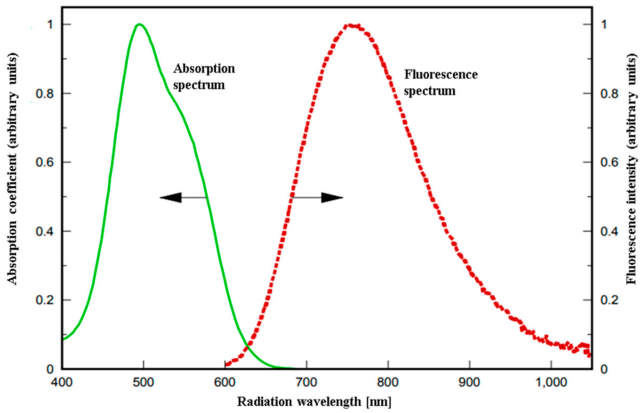

Figure 1.4: Absorption and emission spectra of Ti^{3+}- doped Sapphire. Reprinted from [42].

However, there are several challenges associated with Ti:Sa systems as well, with the most notable being high quantum defect i.e. the energy mismatch between the pump and emitted photons resulting in the generation of significant thermal load that has to be actively dissipated. There are several advantages of cooling the Ti:Sa crystals [44]:

- **Thermal conductivity** increases significantly when the crystal is cooled below 150 K [45, 46]. A $T = 300\,\mathrm{K}$ (room temperature), the thermal conductivity, $K_1 = 42$ W/m/K is boosted to $K_1 = 1000$ W/m/K when the crystal is cryogenically cooled down to $T = 77$ K.

- The **refractive index gradient**, $(\partial n/\partial T)_{T=T_0}$ also shows strong variations with crystal temperature. At $T = 300\,\mathrm{K}$, $\partial n/\partial T = 5.05 \times 10^{-6}\ \mathrm{K}^{-1}$, whereas at $T = 77\,\mathrm{K}$, $\partial n/\partial T = 0.34 \times 10^{-6}\ \mathrm{K}^{-1}$ [47].

- Perhaps one of the most crucial benefits of cooling down Ti:Sa crystal is the **mitigation of transient thermal lensing** arising due to a refractive index gradient inside the medium. The equivalent focal length of the thermal lens is given by [48]

$$f_{\mathrm{eq}}^{\mathrm{thermal}} = \frac{2\pi r_p^2 K_1}{P_{th}(\partial n/\partial T)_{T=T_0}} \tag{1.18}$$

  where P_{th} is the pump-power that is lost to heat. At $T = 300$ K, when $\approx 40W$ is deposited in beam of radius, $r_p = 0.68$ mm on the crystal, $f_{eq}^{thermal} \approx 2.5$ mm, whereas at $T = 77$ K, it is significantly increased to $f_{eq}^{thermal} = 900$ mm, thereby reducing the aberrations and greatly improving the spatio-temporal beam quality.

- When the crystal is cooled down to $T = 77$ K, in principle, the **quantum efficiency** approaches unity $(\eta = 1)$ which means that no pump photon will contribute to non-radiative transitions, which in turn leads to better energy extraction out of the amplifier for the same input pump energy [49–52].

1.4 Commonly used laser parameters

Consider a monochromatic, linearly polarized light wave, with the electric field component in the direction of polarization given by

$$E(t) = \frac{1}{2}E_0 e^{-i\omega t} + \mathrm{c.c.} \tag{1.19}$$

The magnitude of the **Poynting vector** of this wave, $\vec{S}(t) = 1/\mu_0 \vec{E}(t) \times \vec{B}(t)$gives the intensity of this wave

$$I(t) = \overline{|S(t)|} = \frac{1}{2}\sqrt{\frac{\mu_0}{\varepsilon_0}}E_0^2 \tag{1.20}$$

For a Gaussian pulse profile and assuming there are no spatio-temporal couplings present,

- **Peak intensity**

$$\begin{aligned} I_{\mathrm{peak}} &= \frac{W}{(\text{Effective spatial area}) \times (\text{Effective temporal area})} \\ &= 2 \times 0.94 \times \frac{W}{\tau_{\mathrm{FWHM}} \pi \omega_r^2} \end{aligned} \tag{1.21}$$

  Here, W is the measured pulse energy, τ_{FWHM} is the pulse duration at full-width at half-maximum (FWHM) and ω_r^2 is the beam radius at $1/e^2$ width.

- **Peak fluence** or energy per unit area of the beam at the peak of the Gaussian spatial profile is given as

$$F_{\text{peak}} = \frac{2W}{\pi\omega_r^2} \tag{1.22}$$

- **Peak-power**

$$\begin{aligned} P_{\text{peak}} &= 0.94\frac{W}{\tau_{\text{FWHM}}} \\ &= \frac{\pi\omega_r^2}{2} I_{\text{peak}} \end{aligned} \tag{1.23}$$

- **Normalized laser amplitude** or vector potential

$$a_0 = \frac{eE_0}{m_e\omega c} \tag{1.24}$$

  A more commonly used definition in terms of laser intensity is given as,

$$a_0 = \sqrt{\frac{I\ [\text{W/cm}^2]\ \lambda^2\ [\mu\text{m}^2]}{I_0}} \tag{1.25}$$

  where, $I_0 = 1.37 \times 10^{18}$.

For the *Salle Noire* laser system [53], typical on-target parameters are listed below:

- Repetition rate, $f_{\text{rep}} = 1\,\text{kHz}$
- Tunable pulse duration $\tau_{\text{FWHM}} = 30 - 3.5\,\text{fs}$
- Central wavelength, $\lambda_0 = 780 - 800\,\text{nm}$, depending on output the pulse duration
- Pulse energy, $W = 2.5\,\text{mJ}$ on-target
- Peak power, $P_{\text{peak}} \sim 1\,\text{TW}$ (in case of $\tau_{\text{FWHM}} = 3.5\,\text{fs}$)
- Average power, $P_{\text{av}} \approx 2.5\,\text{W}$
- Beam size in-focus, on-target, $\omega_r \approx 1.8\,\mu\text{m}$
- Peak intensity

$$\begin{aligned} I_{\text{peak}} &= 2 \times 0.94 \times \frac{2.5 \times 10^{-3}\,[\text{J}]}{3.5\,[\text{fs}]\,\pi(1.8 \times 10^{-4})^2\,[\text{cm}^2]} \\ &= 1.3 \times 10^{19}\,\text{W/cm}^2 \end{aligned} \tag{1.26}$$

- Normalized vector potential,

$$\begin{aligned} a_0 &= \sqrt{\frac{I_{\text{peak}}(0.8)^2}{1.37 \times 10^{18}}} \\ &\approx 2.5 \end{aligned} \tag{1.27}$$

Chapter 2

TW-peak power waveform controlled near-single-cycle laser

“*May the laser be with you !*”

Outline

2.1 *Salle Noire*: Global architecture **40**
2.1.1 Oscillator 40
2.1.2 First CPA 40
2.1.3 Nonlinear contrast filtering 41
2.1.4 Second CPA 45
2.1.5 Post-compression to near-single-cycle regime 46
2.2 CEP detection and stabilization **50**
2.2.1 CEP stabilization of the oscillator 53
2.2.2 CEP stabilization at the end of the laser chain 54
2.3 Laser upgrades **56**
2.3.1 HCF extension arm 57
2.3.2 Cryogenically-cooled multi-pass Ti:Sa amplifier 57

Since their inception in 1982 [41], Ti:Sa-based laser systems have established themselves as the cornerstone of ultrafast laser technology. At *Laboratoire d'Optique Appliquée* (LOA), the development of a Ti:Sa-based laser system, named *Salle Noire*, started in 2005 in the Physique du Cycle Optique (PCO) group, led by Rodrigo Lopez-Martens. The primary objective was to reach relativistic intensities on-target ($\geq 10^{18}$ W/cm^2 at $\lambda = 800$ nm) using a λ^3 - approach, a concept first introduced by Gérard Mourou [54]. The central idea was to temporally compress the laser pulses to a single light-wave oscillation of the electric field and spatially focus them down to a diffraction-limited $\sim \lambda$ spot size, where λ is the pulse central wavelength. The laser intensity on-target is given as

$$I \propto \frac{W}{\tau A} \approx \frac{W}{(\frac{\lambda}{c}).\lambda^2} = \frac{Wc}{\lambda^3} \tag{2.1}$$

Here, W is the pulse energy, A is the beam surface area in-focus on-target, and τ is the laser pulse duration at FWHM. The conventional approach to reaching the relativistic intensity regime is to use 100 TW-class [55] or even PW-class laser systems [56]. However, these laser systems suffer from low repetition rates (0.1 - 10 Hz), rendering the generated light and particle radiation unsuitable for numerous practical and societal applications such as XUV imaging [57], nuclear physics [58], biomedical applications [59], and ultrafast electron diffraction [60]. In the λ^3 - regime, due to the extremely tight focusing and short pulse durations, relativistic intensities can be achieved with moderate laser pulse energies, in the mJ-range. Thus, the λ^3 - approach allows us to work at higher repetition rates ($\sim$ kHz range), thereby improving the average brightness and flux of the secondary emissions of interest. A high repetition rate also makes it feasible to collect large data sets to perform statistical studies while scanning a high-dimensional parameter space in a reasonable time, also opening the possibility of closed-loop automated optimizations [61]. Furthermore, relatively modest peak-power ($\sim$ 1 TW) allows for easy and efficient management of thermal effects, necessary for a continuous operation at kHz repetition rate. Simultaneously, moderate mJ-level pulse energies can be safely

transported with reasonably sized optics ($\sim$ 2 - 3 inches), thereby allowing to maintain an overall practical footprint of the system.

Following the λ^3 - approach, the *Salle Noire* laser system (figure 2.1) has been meticulously developed in-house, with the fundamental goal being compression of mJ-level laser pulses down to the single-cycle regime with waveform control, while ensuring high spatio-temporal beam quality such that the laser pulses can be focused down to a diffraction limited spot size on-target to access the relativistic intensity regime. Furthermore, to ensure clean and controlled interaction conditions on-target, the laser system features a nonlinear contrast filter to remove all the unwanted components before the main pulse peak. After nearly two decades of continuous evolution, *Salle Noire* can now routinely deliver on-target 1 TW peak power, ~ 2.5 - $3\,\mathrm{mJ}$ energy pulses with tunable duration from 30 fs to sub-4 fs while maintaining a high temporal intensity contrast ratio ($> 10^{10}$) and waveform control at 1 kHz repetition rate [53].

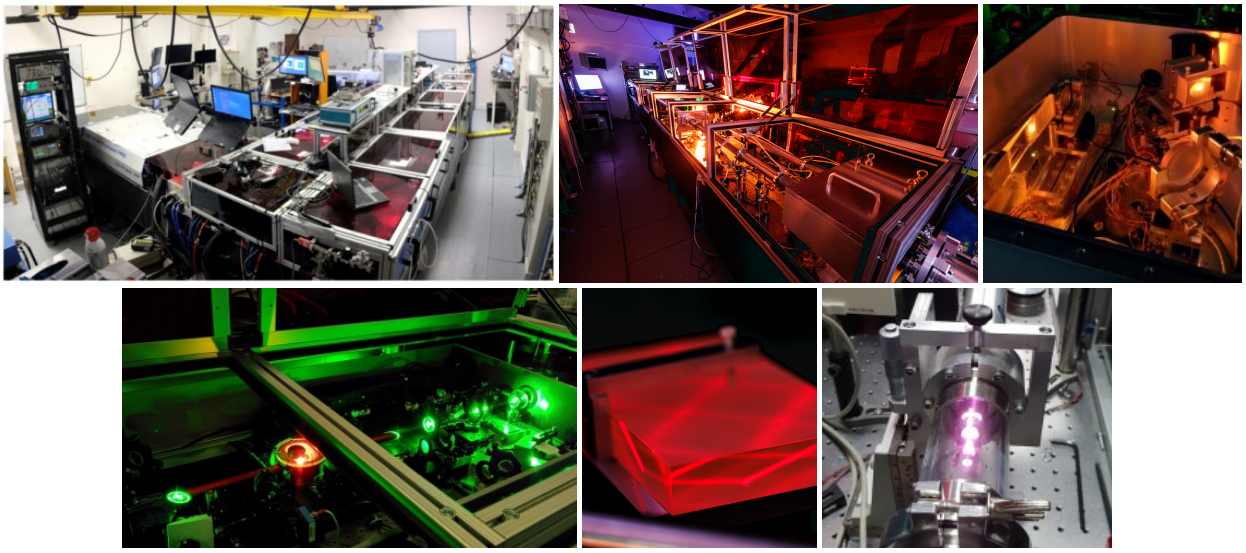

Figure 2.1: The *Salle Noire* laser system.

This chapters starts with an overview of the *Salle Noire* laser architecture, which I inherited from my predecessors in 2019. Next, I will detail the CEP measurement techniques used and the tools implemented to control the CEP at full repetition rate of the laser system, which is a crucial step towards on-demand generation of isolated attosecond pulses from relativistic PMs [62–64]. Having acquired the proficiency and autonomy not only in the day-to-day operation of the laser system but also intricately understanding each and every component within the system, I undertook the implementation of two major upgrades on the laser system to augment the available laser energy while simultaneously improving the stability of the source properties and the overall day-to-day reliability of the system. These upgrades are summarized towards the end of this chapter.

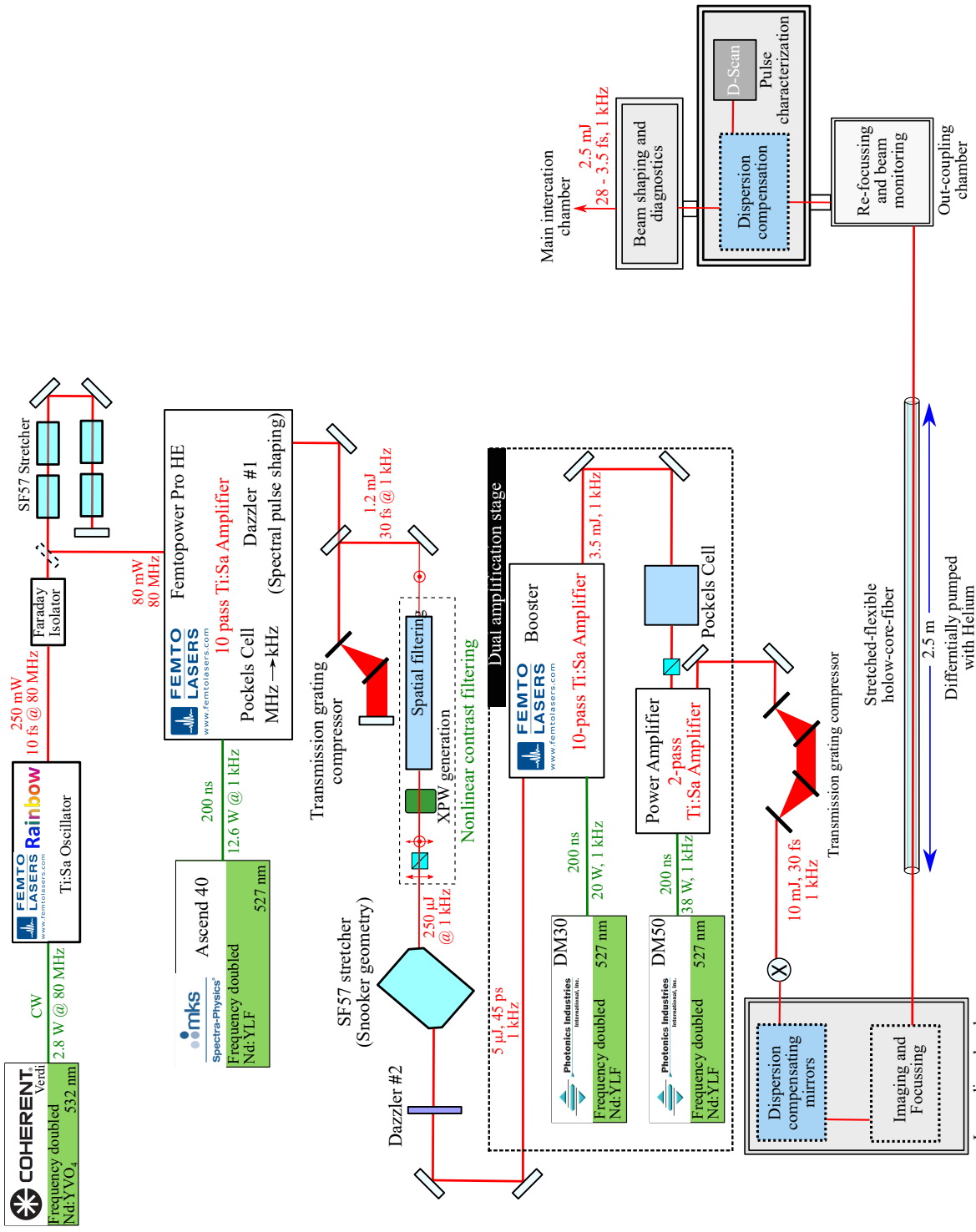

Figure 2.2: Global architecture of the *Salle Noire* laser. CW: Continuous wave, XPW: cross-polarized wave generation.

2.1 *Salle Noire*: Global architecture

A schematic layout highlighting the main building blocks of *Salle Noire* is illustrated in figure 2.2. It is a dual-CPA system delivering up to 10 mJ - 30 fs laser pulses, centered around $\lambda = 800\,\mathrm{nm}$ at 1 kHz repetition rate. The laser system features an XPW nonlinear filter (see 1.2.2) to enhance the temporal intensity contrast ratio to $> 10^{10}$ at $t < -10\,\mathrm{ps}$ before the main pulse peak [65]. The laser pulses are then post-compressed in a 2.5 m long, stretched flexible hollow core fiber (HCF) differentially filled with Helium gas. By varying the gas pressure in the fiber, the laser pulse duration can be tuned from 30 fs to 3.5 fs while maintaining approximately the same pulse energy at the output [53]. Additionally, whilst ensuring the same beam fluence, the laser pulses can also be stretched from 30 fs to up to 1.5 ps by adding group delay dispersion (GDD) using an acoustic-optic programmable dispersion filter (AOPDF, *Dazzler, Fastlite*) [66] integrated upstream in the laser chain. In this section, I will present a brief overview of the key components, while extensive details about the laser system can be found in [53, 67].

2.1.1 Oscillator

The first block in the laser chain is a commercial Ti:Sa oscillator (*Rainbow, Femtolasers GmbH*) operating at 80 MHz repetition rate. A schematic representation of the optical layout of the oscillator is illustrated in figure 2.3. It is pumped by a 3 W continuous-wave (CW) frequency-doubled Nd:YVO4 laser (*Verdi, Coherent*) at 532 nm, corresponding to the maximum absorption wavelength of a Ti:Sa crystal. The oscillator is mode-locked via Kerr lensing by quickly moving a mirror in the cavity (MLM in figure 2.3). The output coupler, OC, is wedged to prevent unwanted reflections, followed by a compensating plate, CP, to eliminate angular dispersion. The oscillator cavity also consists of broadband dispersion-compensating mirrors and a pair of thin fused silica wedges to partially compensate for the GDD picked up in the cavity. Finally, at the output, we obtain, $\sim$ nJ-energy 10 fs pulses with an average power of ~ 250 mW. The oscillator also features a fast CEP stabilization loop, detailed later in this chapter, in section 2.2.

2.1.2 First CPA

After the oscillator, the beam goes through a Faraday rotator to prevent potentially catastrophic, unwanted reflections back-propagating to the oscillator. A schematic layout of the first CPA is highlighted in figure 2.2. The laser pulses are stretched to $\sim 20\,\mathrm{ps}$ in a bulk glass stretcher (SF57) and then amplified to 1.8 mJ in a commercial 10-pass Ti:Sa amplifier (*Femtopower, Femtolasers GmbH*). The Ti:Sa crystal is $3\ \mathrm{mm} \times 6\ \mathrm{mm}$ in size with $8\,\mathrm{mm}$ of propagation length, cooled down to 180 K to mitigate thermal lensing, in a small vacuum chamber maintained at 0.1 mbar. The chamber windows are made of 0.5 mm thick fused silica installed at the Brewster angle to ensure clean polarization and prevent unwanted reflections. The crystal is pumped with $\approx 13\,\mathrm{W}$ at 527 nm by a low-noise frequency-doubled Nd:YLF laser (*Ascend 40, Spectra Physics*) at 1 kHz repetition rate. The MHz pulse train from the oscillator is amplified in the first four passes with an overall gain of $\sim 10^4$. After the fourth pass, the pulses are sent to a Dazzler (Daz#1) consisting of a birefringent uniaxial crystal with a piezo-electric

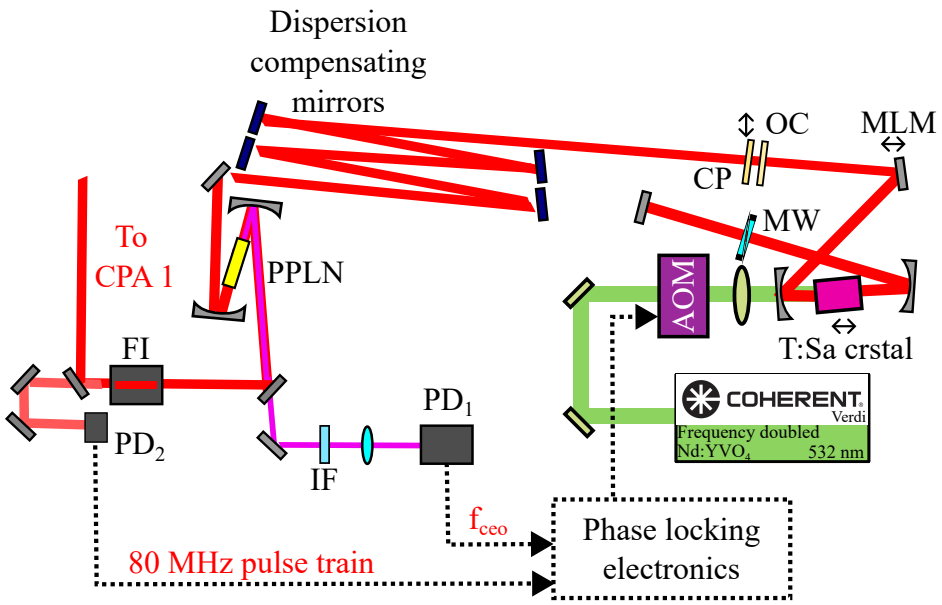

Figure 2.3: Schematic representation of the oscillator cavity and its CEP stabilization setup. AOM: acousto-optic modulator, MW: motorized wedges, MLM: mode-locking mirror, OC: output coupler, CP: compensating plate, PPLN: periodically-poled Lithium Niobate, IF: Interference filter, FI: Faraday isolator, PD: Photodiode

transducer and an RF-frequency generator [66]. A carefully shaped acoustic wave is launched into the crystal to manipulate the pulse spectral phase and amplitude. Thanks to the precise engineering of the pulse spectral shape using the Dazzler, Daz#1, we can mitigate gain narrowing and gain shifting in the next passes in the amplifier. After the Dazzler, the pulses go through a Pockel's cell (PC1) to reduce the repetition rate down to 1 kHz. The Pockel's cell also consists of a birefringent material, in our case, KD*P, which acts like a half wave plate when high voltage is applied to the material. A pair of crossed polarizers are used before and after the PC1 to filter out the rotated pulses. The kHz pulse train is then further amplified to 1.8 mJ in the next six passes in the amplifier.

The beam is then collimated and expanded to ≈ 15 mm in diameter and sent to a double-pass transmission grating compressor (TGC) for pulse compression. The laser pulses at the output are characterized using self-referenced spectral interferometry (SRSI or *Wizzler, Fastlite*) [68]. The Wizzler sends a feedback to the Dazzler in the amplifier, fine tuning the pulse spectral phase, such that we can obtain nearly Fourier-Transform limited (FTL) 28 fs - 1.2 mJ pulses at 1 kHz repetition rate. Figure 2.4 shows the spectrum and pulse intensity profile measured using a Wizzler device at the output of the first CPA.

2.1.3 Nonlinear contrast filtering

The temporal intensity contrast ratio of the laser is defined as the ratio of maximum intensity of the laser pulse peak to the intensity at a time t ranging from a few picoseconds to nanoseconds before the main pulse peak. It is a crucial parameter in laser-plasma interactions on the surface of a solid or liquid target since it determines the actual interaction conditions of the laser peak intensity with

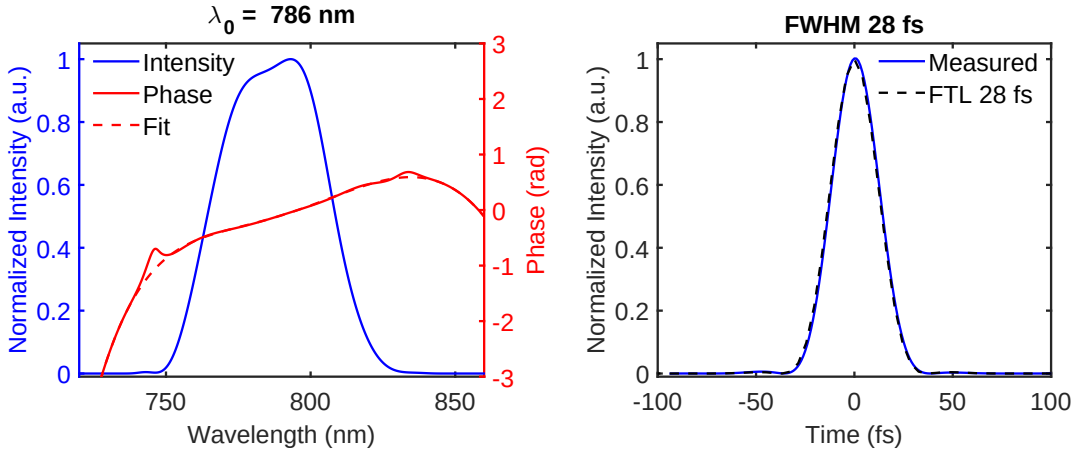

Figure 2.4: Pulse spectral (left) and temporal (right) intensity profiles measured at the output of first CPA using a Wizzler device.

the PM [69]. Typical pulse structure out of CPA is illustrated in figure 2.5. The main pulse peak is accompanied by: (1) a long incoherent pedestal due to amplified spontaneous emission (ASE), typically on a nanosecond time scale, corresponding to the pump pulse duration, (2) a coherent pedestal due to imperfect temporal compression (residual spectral phase) and modulations in the spectral intensity profile, (3) post-pulses due to back-reflections in transmissive optical elements (windows, lenses, etc), and (4) pre-pulses generated by post-pulses during nonlinear interaction in a CPA [70]. The typical contrast of a multi-pass Ti:Sa CPA is around $10^6 - 10^7$ on a nanosecond time scale. To ensure clean laser-plasma interaction conditions, the ASE pedestal and the pre-pulses arriving on-target before the main pulse peak should be well below the ionization threshold of the target (typically, $\sim 10^{10}$ W/cm^2). When working in the relativistic intensity regime ($> 10^{18}$ W/cm^2), laser-plasma experiments often demand a contrast of $\sim 10^9 - 10^{10}$.

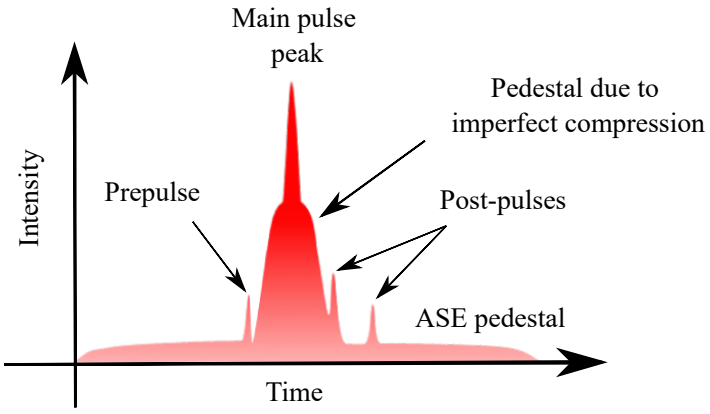

Figure 2.5: Typical contrast of a CPA system.

Various techniques have been used to enhance the temporal intensity contrast ratio, such as saturable absorbers [71, 72], electro-optic switches, optical parametric amplifiers [73–75], SHG [76], spectrally filtered SPM [77], PMs [78, 79] and NER [30–34, 80]. In *Salle Noire*, to enhance the

temporal intensity contrast, we use an in-house developed third-order nonlinear technique: XPW generation [38] (see 1.2.2). In principle, using XPW, the contrast can be enhanced from C_i to C_i^3, where C_i is the contrast of the input pulse. In practice, the contrast enhancement is limited by the extinction ratio of the output analyzer used to filter out the XPW. This is a standard problem encountered in all polarization discrimination based contrast enhancement techniques. The choice of the polarizing optics varies according to the targeted application. Thin film polarizers typically offer an extinction ratio $\sim 10^2 - 10^3$ with low-dispersion but often generate a train of post-pulses. In our case, we can afford to accommodate a high-dispersion Glan polarizer offering a higher extinction ratio of $\sim 10^4$. However, nowadays high-quality low-dispersion nano-particle based polarizers are commercially available offering extinction ratios as high as $\sim 10^5$.

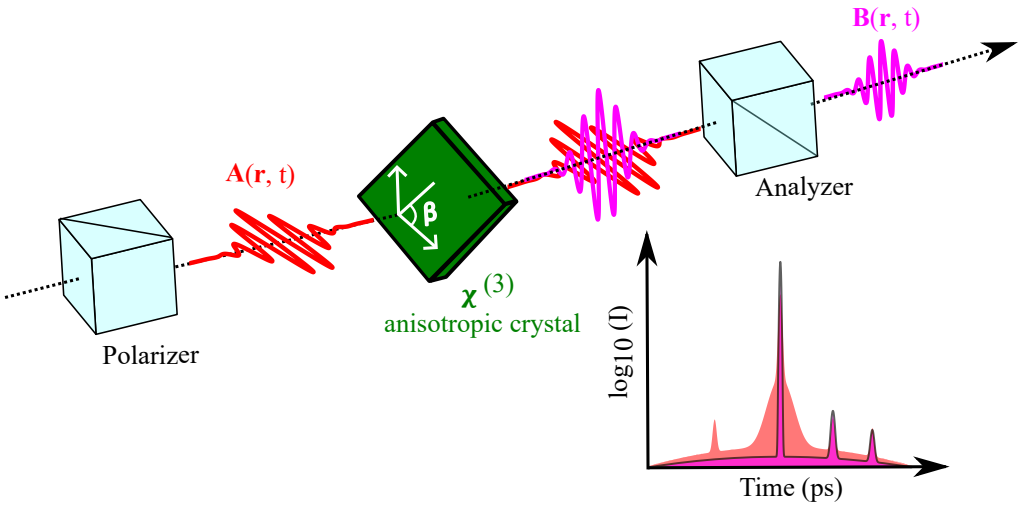

Figure 2.6: Principle of temporal contrast enhancement via the XPW technique.

The conventional XPW implementation is quite straightforward: a linearly polarized pulse is focused on a $\chi^{(3)}$ anisotropic crystal (in our case, BaF_2) placed between two crossed polarizers (figure 2.6). The XPW conversion efficiency depends on: (1) the intensity of the pulse incident on the crystal, (2) thickness of the crystal, (3) input spatio-temporal pulse quality and its spectral phase. The incident intensity on the XPW crystal is limited by the threshold of white light generation in the crystal ($\sim 10^{12}\,\mathrm{W/cm^2}$ in BaF_2). Using thicker crystals to achieve higher conversion efficiency leads to unwanted nonlinear third-order processes that tend to compete with the XPW generation. Additionally, it also makes the XPW beam properties sensitive to spatio-temporal couplings. The input intensity is also limited by damage due to self-focusing inside the crystal, which also reduces its life time. Taking into account all the above factors, the *Salle Noire* experimental setup was designed to maximize the conversion efficiency while maintaining good spatio-temporal beam properties.

Experimental setup: The optical layout of the *Salle Noire* XPW setup is shown in figure 2.7. After the first CPA, 1.2 mJ, near-FTL 28 fs, s-polarized pulses are focused by a concave mirror, ROC = -1500 mm, to a $\sim 160\,\mu\mathrm{m}$ spot at the entrance of a $250\,\mu\mathrm{m}$ inner diameter, 50 cm long fused silica capillary,

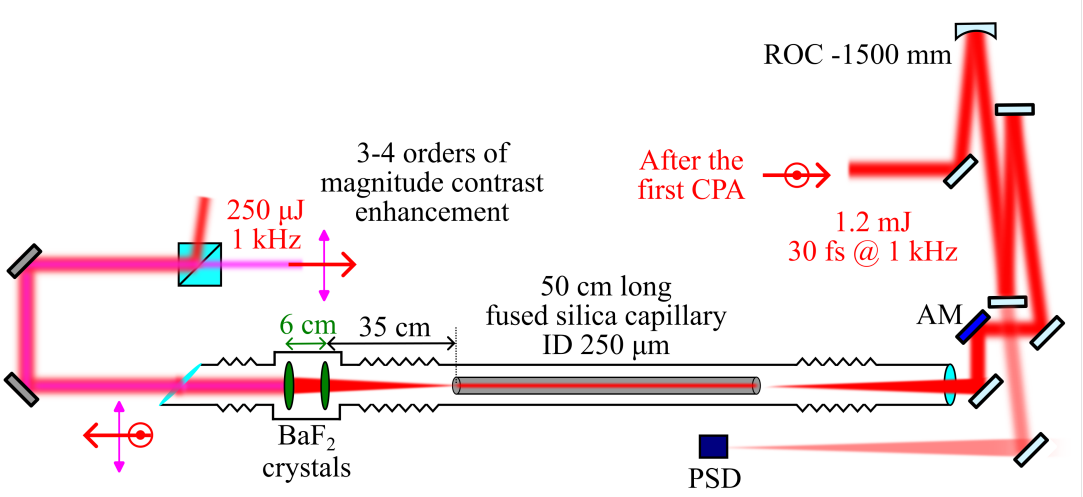

Figure 2.7: Experimental implementation of XPW in *Salle Noire*. ROC: radius of curvature, AM: active mirror, PSD: position sensitive device, and ID: inner diameter.

placed under vacuum. Spatial filtering via the fused silica capillary helps to improve the spatial beam quality and consequently the XPW conversion efficiency. Dispersion due to propagation in air and the entrance window of the setup is compensated by the Dazzler, Daz#1. I installed a piezo-electric based fast beam-stabilization of the input beam, in the far-field, to effectively reduce the beam pointing fluctuations at the input of the capillary, which are otherwise translated into energy fluctuations by the filtering setup. As a result, this enhancement ensures both short-term and long-term operational stability.

About 28 cm after the capillary, two holographic-cut uncoated BaF_2 crystals, $10\ \text{mm} \times 10\ \text{mm}$ in size and $1.5\,\text{mm}$ in thickness are used to generate high contrast XPW pulses at $p-$polarization. By changing the distance of the BaF_2 crystals from the capillary exit, one can adjust the beam-size on the crystals and thereby the conversion to XPW. A two-crystal configuration where the two crystals are separated by twice the thickness of the first crystal was found to overcome the saturation of XPW conversion and yield higher efficiencies [81]. A 0.5 mm thick elliptical fused silica window is placed at the Brewster angle at the output to preferentially select the XPW (p-polarized) beam and avoid any back-reflections. Finally, the high-contrast XPW pulses are selected using a Glan polarizer.

Output characteristics: With 1.2 mJ - 28 fs pulses entering the XPW setup, we can obtain overall $650\ \mu\text{J}$ and $\approx 230\ \mu\text{J}$ XPW pulses (measured after the Glan polarizer), corresponding to 35% internal (w.r.t. total throughput) and 17% global (w.r.t. input) efficiency. Figure 2.8 (left panel) shows a contrast enhancement between the input and the XPW pulses of nearly three orders of magnitude, measured using a commercial high dynamic range third-order auto-correlator with a 4 ns scanning window (*TUNDRA, Ultrafast Innovations*). Typically recorded input and XPW spectra are shown in figure 2.8 (right panel). The XPW spectrum is broadened by at least a factor of $\sqrt{3}$ as compared to the input spectrum. Even larger broadening is observed here due to the SPM experienced by the XPW in the BaF_2 crystals.

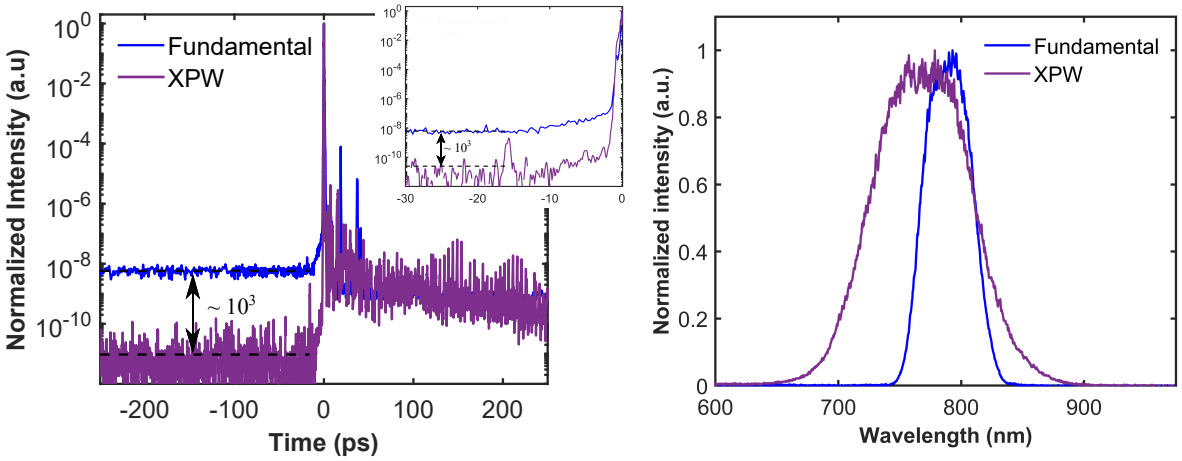

Figure 2.8: Temporal contrast enhancement between the input and XPW pulses (left) and typically recorded input and XPW spectra (right).

2.1.4 Second CPA

After nonlinear temporal filtering via XPW, a second CPA is used to boost the available laser energy. A block diagram of the second CPA is highlighted in figure 2.2. It consists of a bulk stretcher, a two-stage amplifier, and finally, a TGC and a set of dispersion-compensating mirrors to temporally compress the laser pulses.

Stretcher: The laser pulses are stretched to ≈ 40 ps in a bulk SF57 stretcher implemented in a snooker geometry with a total of six internal reflections. A picture of the stretcher is displayed in figure 2.1(bottom-center).

Dazzler II: After the stretcher block, the beam is collimated to 1 mm diameter (at $1/e^2$ width) using an afocal telescope and sent to another Dazzler (Daz#2, single-pass) [66] for pulse spectral shaping. The Dazzler changes the polarization to s-pol which is then flipped again to p-pol using a cross-periscope and sent to the first Booster amplifier of this CPA stage. Due to the limited transmission of the stretcher and the set diffraction efficiency of the Dazzler, we are left with around 5 μJ to seed the first booster amplifier of this CPA stage. Daz#2 helps to spectrally shape the seed spectrum to mitigate gain narrowing and gain shifting in the amplifiers as well as provide precise control over the pulse spectral phase.

Booster amplifier: It is a commercial 6-pass Ti:Sa amplifier from *Femtolasers GmbH*. The Ti:Sa crystal and the housing chamber is identical to the one used in Femtopower. It is pumped with 20 W at 527 nm using a frequency doubled Nd:YLF laser (*DM30, Photonics Industries*) at 1 kHz repetition rate. Finally, at the output of the booster amplifier we obtain 3.4 mJ energy pulses at 1 kHz repetition rate. A picture of the Booster amplifier is depicted in figure 2.1(bottom-left).

Pockel's cell (PC2): At the output of the Booster amplifier, we use another Pockel's cell placed between two crossed polarizers to rotate the polarization of the pulses from p-pol to s-pol for a short window of time. This helps to prevent unwanted reflections from the subsequent stages back-propagating into the Booster amplifier.

Power amplifier: To further boost the laser energy, a two-pass Ti:Sa amplifier in a "bow-tie" configuration was designed in-house. A $6\,\mathrm{mm} \times 6\,\mathrm{mm}$ Ti:Sa crystal with the same gain length of $8\,\mathrm{mm}$ is pumped with 38 W at 527 nm using another frequency doubled Nd:YLF pump laser (*DM50, Photonics Industries*). The pump is focused to a 1 mm (at $1/e^2$ width) spot size on the crystal. The crystal chamber is equipped with 1.5 mm thick elliptical fused silica windows, bigger in size as compared to the Booster amplifier, also installed at a Brewster angle. After PC2, the transmitted 2.8 mJ pulses are amplified to 10 mJ available at the output of the power-amplifier.

Compressor: The output beam is first collimated to approximately 15 mm (at $1/e^2$ width) and then sent to a TGC, designed in an unfolded configuration, i.e. consisting of four gratings. To avoid nonlinear effects in the last grating, the compression is finished off with a set of dispersion-compensating mirrors. In principle, these mirrors can be right after the compressor, but for the next block of the laser chain (section 2.1.5), these mirrors were installed in a vacuum chamber. To fine-tune the compression, a Wizzler measurement is made after the compressor and a feedback is sent to the Dazzler, Daz#2 to correct for the residual pulse spectral phase. Figure 2.9 shows the output spectrum and the pulse intensity profile measured with a Wizzler. Finally, after the compressor, we obtain 8.5 mJ, nearly-FTL 26 fs pulses.

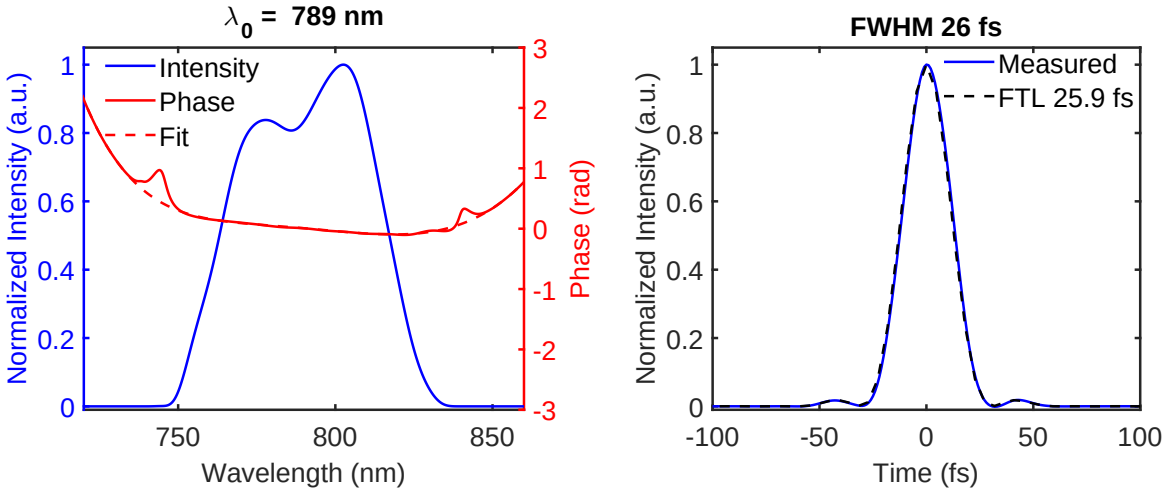

Figure 2.9: Pulse spectral (left) and temporal (right) intensity profiles measured at the output of second CPA using a Wizzler device.

2.1.5 Post-compression to near-single-cycle regime

The laser pulses at the output of the second CPA are nearly-FTL 26 fs in duration, corresponding to ≈ 10 optical cycles at $\lambda = 790\,\mathrm{nm}$. In order to reach the near-single-cycle regime (< 2 optical cycles), we need to spectrally broaden the laser pulses via nonlinear interaction between the intense laser pulses and the propagating medium. In the course of such interactions, the pulses undergo nonlinear time-dependent spectral phase distortions leading to emergence of new spectral components (see 1.2.2). In an ideal case, the laser pulse energy is only redistributed without any losses to the new spectral components. Although the spectrum broadens, but the pulse envelope remains nearly the

same during the interaction [28]. As a result, a pulse with a sufficiently simple phase-modulation corresponding to approximately a linear chirp is obtained such that it can be compressed to much shorter durations by simply using dispersion-compensating mirrors [82]. However, it is crucial that the spectral phase is well defined and smooth over the entire bandwidth in order to obtain high-fidelity temporally compressed pulses. Thus, in most cases, "post-compression" schemes encompass two distinct steps, spectral broadening followed by dispersion-compensation.

There are several techniques to post-compress high energy laser pulses to a few optical cycles. An exhaustive review of these techniques can be found in [83, 84]. In *Salle Noire*, we rely on SPM-induced spectral broadening in stretched-flexible HCFs, differentially filled with Helium [85, 86]. Patented by Tamas Nagy and Peter Simon [86], this technique is a widely used technique in the mJ-energy range. HCF-based post-compression setups are now even commercially available through Ultrafast Innovations GmbH and Few Cycle Inc. This setup was designed and implemented in *Salle Noire* by one of the previous PhD students in the group, Frederik Böhle in collaboration with the inventor of the technique himself, Tamas Nagy (MBI Berlin). I will briefly describe the *Salle Noire* post-compression setup in this section, while a more detailed description can be found in [53, 67, 87].

Power scaling

Scaling this post-compression scheme for high input peak powers necessitates meticulous consideration of the fiber geometry and the nonlinear medium to prevent excessive ionization and self-focusing, which can quickly prove to be detrimental for the pulse coherence and compressibility [88]. Thus, in order to achieve controlled spectral broadening with minimal losses while maintaining the temporal pulse quality, Vozzi et al. [88] proposed to strictly respect two limiting criteria:

1. To avoid self-focusing and eventually a complete pulse-collapse, the peak power of the input pulse should remain well below the critical power

$$P < P_{cr} = \frac{\lambda^2}{2\pi n_2} \tag{2.2}$$

2. Peak intensity has to be lower than the photo-ionization threshold

$$\frac{P}{A_{eff}} < I_{th} \tag{2.3}$$

This also imposes a limit on the effective beam area in the fiber, $A_{eff} \propto D^2$, implying higher input energies require fibers with larger inner core diameter. Vozzi et al. [88] propose to make sure that the ionization induced plasma phase-shift should stay at least three orders of magnitude below the SPM-induced phase-shift. Using the Ammosov–Delone–Krainov (ADK) theory to calculate the free electron density, they derive a simple condition on the fiber core diameter

$$D > 2A\frac{W^{0.51}}{\tau^{0.45}} \tag{2.4}$$

Here, A is a constant determined by the choice of nonlinear medium that can be minimized by selecting a gas with high ionization threshold, for example Helium.

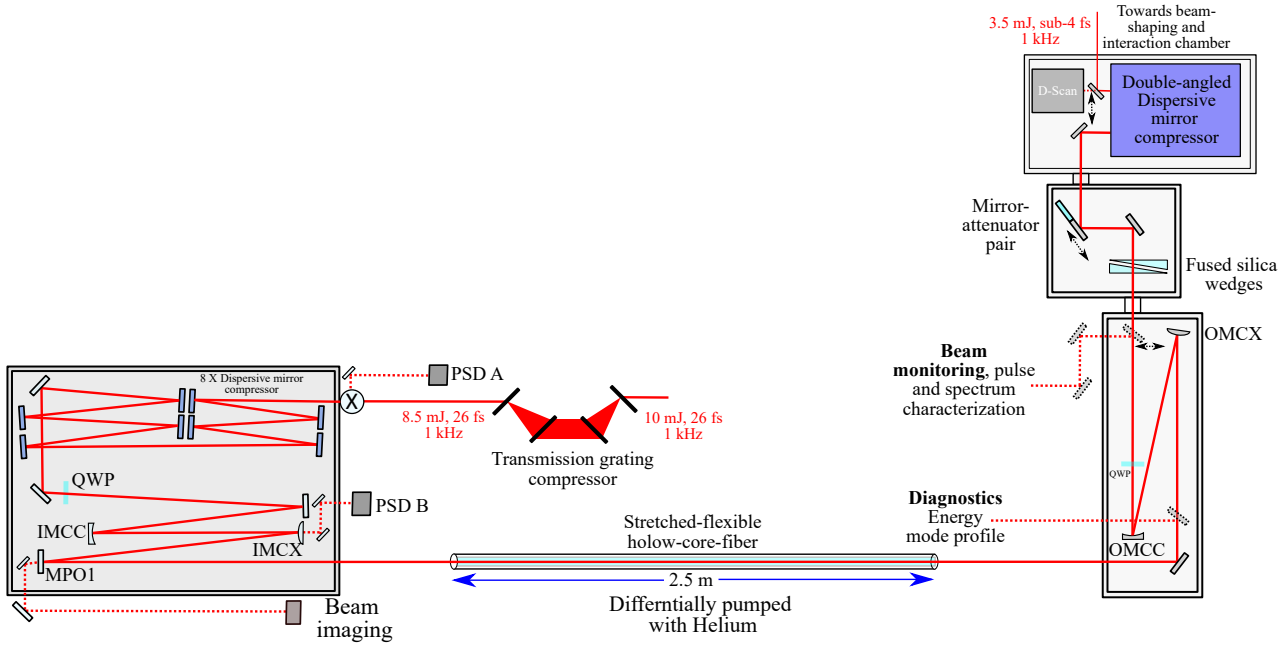

Figure 2.10: Layout of the *Salle Noire* HCF-based compression setup. PSD: position sensitive device, QWP: Quarter-wave plate, MCC: Concave mirror, and MCX: convex mirror. Figure inspired from [53].

Experimental implementation

The optical layout of the HCF-based post-compression setup is schematically shown in figure 2.10. After the TGC, the pulses are injected into a vacuum chamber. A set of dispersion compensating mirrors (~ -2000 fs^2 in total, HD58, Ultrafast Innovations) compensate for the residual GDD in the pulse spectral phase. A zero-order QWP changes the polarization to circular in order to reduce the peak laser electric field amplitude by a factor of $\sqrt{2}$ and the ionization in the fiber by at least one order of magnitude [89, 90]. The nonlinear refractive index, n_2, also reduces by a factor of $2/3$, leading to a more defined mode beating and therefore, more stable spectral broadening [91]. The HCF is differentially pumped with Helium (Grade 6 purity rating), i.e. the fiber entrance is continuously pumped and maintained at $\sim 10^{-1}$ mbar, while the output chamber is filled with Helium. The fiber itself is 2.5 m long with an inner core diameter of $530\,\mu$m. Conductance of gas through the fiber varies by $\approx D^4$ and $1/L$, where L is the length of the fiber. A pressure gradient through the fiber helps to avoid excessive ionization and self-focusing induced distortions in the beam profile [92]. However, this also reduces the effective nonlinear propagation by $\approx 33\%$. The decrease in the accumulated B-integral has to be compensated by increasing the gas-pressure at the output of the fiber [93].

To optimize the coupling into the fiber, the beam size at the entrance of the fiber is matched to the fundamental mode EH_{11}. The relative energy coupled into different modes of the fiber as a function of the Gaussian beam size is shown in figure 2.11. For a Gaussian beam, coupling to EH_{11} is optimized at 98% for a beam size of $2\omega_0 = 0.64D = 340\ \mu$m. A smart and fast beam stabilization system (TEM Messtechnik Aligna) is used to compensate for beam pointing instabilities to prevent damaging the fiber entrance as well as to ensure long-term stable operation. Additionally, for robust protection against slight misalignments, a conical glass taper is co-axially aligned with the fiber entrance. A leak from the mirror MPO1 is used to image and continuously monitor the focal spot at the entrance of the

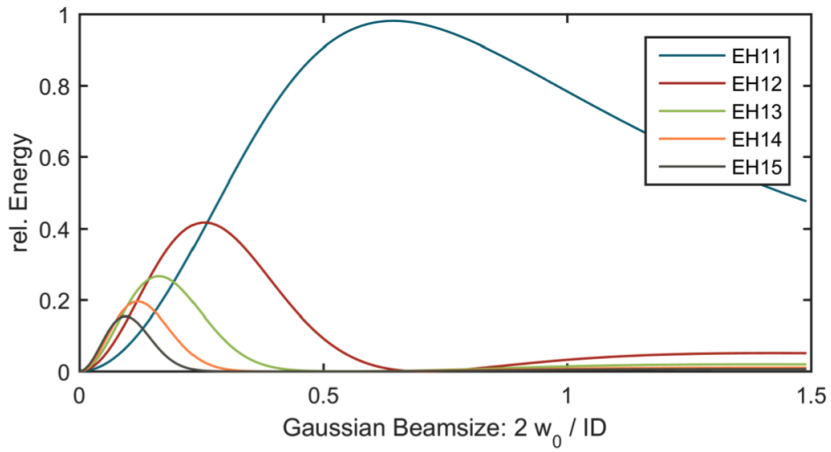

Figure 2.11: Relative energy coupling between different hybrid modes of a HCF and a Gaussian beam mode size of ω_0. Reprinted from [87].

fiber, outside the vacuum chamber.

After the fiber, the beam is allowed to diverge for $\approx 1.6\,\mathrm{m}$ and the first mirror is placed at 45°, directing the beam towards an up-sizing and collimating telescope. An insertable mirror sends the beam towards the fiber entrance, straight along its length, to image, optimize the beam profile while tweaking the fiber entrance, as well as to measure the transmitted energy. After the telescope, a broadband air-spaced QWP (B.Halle) compensates for the retardation introduced by the first QWP and rotates the beam back to p-polarization. Another insertable mirror directs the beams towards diagnostics for beam position, angular references and pulse characterization using a Wizzler device. However, the Wizzler has a narrow-band characterization range and can only be used to characterize pulses without any induced spectral broadening, i.e. without any gas in the fiber. A Wizzler measurement in this case helps to ensure that FTL high-fidelity pulses are focused at the entrance of the fiber. Once the second insertable mirror is removed, the beam is directed to another vacuum chamber through an AR-coated transparent window. The linear and quadratic pulse chirp is compensated by a set of thin fused silica wedges and 6 pairs of double-angled broadband dispersion compensating mirrors ($\sim -240\ \mathrm{fs}^2$ in total, PC70, Ultrafast Innovations). To characterize the few-cycle pulses, we use a vacuum integrated SHG-based dispersion-scan or D-Scan (Sphere Photonics) device [94].

Output characteristics

At the output, we obtain nearly 5 mJ energy pulses (measured before the compressor), corresponding to a transmission of $\approx 60\%$ of the fiber itself. A notable advantage of this technique is the ability to tune the output pulse duration by simply varying the gas pressure in the fiber. As the gas pressure is increased, the acquired B-integral increases, leading to spectrum broadening, subsequently reducing the pulse duration at the output, while maintaining nearly the same output energy (figure 2.12). With increasing gas pressure, we can see a clear blue shift of the output spectrum owing to the self-steeping in the fiber. Figure 2.13 shows D-Scan measurements for three different gas pressures, 400 mbar, 650 mbar and 1000 mbar, resulting in high-fidelity 6.9 fs, 4.9 fs and 3.8 fs output pulses, respectively. Thus, this post-compression setup allows us to routinely generate 3.5 mJ energy (mea-

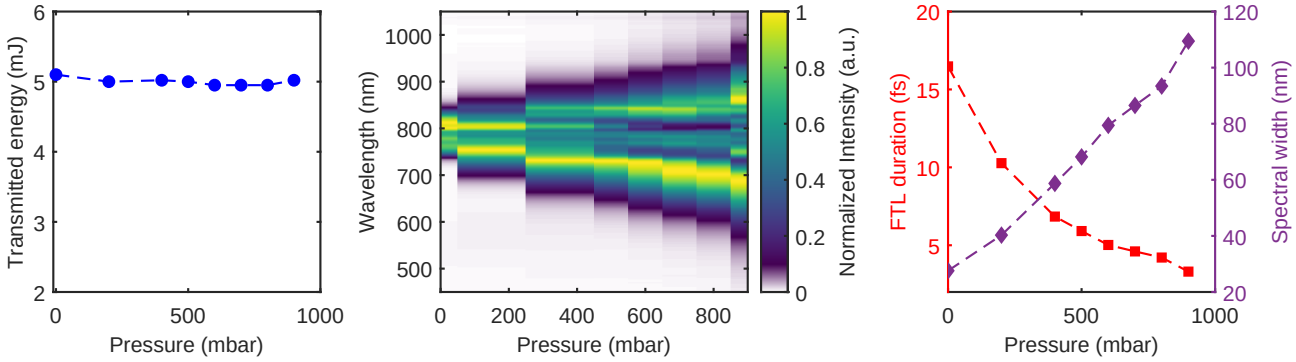

Figure 2.12: Evolution of the transmitted energy through the fiber with the gas pressure (left). Variation of the output spectrum (center) and the corresponding FTL-duration and RMS spectral width (right) with gas pressure.

sured after the compressor), high-fidelity, tunable pulses from 26 fs to 3.8 fs (≈ 1.5 optical cycles at $\lambda = 780\,$nm) at 1 kHz repetition rate, with an overall efficiency of $\approx 42\%$.

2.2 CEP detection and stabilization

This section details the techniques used for CEP detection and stabilization at two distinct stages in the *Salle Noire* laser chain. Firstly, a fast loop operating on the MHz scale stabilizes the pulse train out of the oscillator. Secondly, a slower loop operating at the kHz scale compensates for the phase noise that is accumulated during propagation through the laser chain.

The output of our mode-locked oscillator is a frequency comb spaced by the free cavity spectral range of $c/2L$, also representing the repetition rate f_{rep}. Here, c is the speed of light and L is the oscillator cavity length. In the time domain, this corresponds to,

$$\tau \sim \frac{1}{m f_{rep}} \tag{2.5}$$

where m is the number of phase-locked oscillating modes, separated by the cavity round-trip time, $t_{rt} = 1/f_{rep}$. Representation of a mode-locked pulse train structure in the frequency and time domain is shown in figure 2.14. The frequency of the nth mode is given by,

$$f_n = n f_{rep} + f_{ceo} \tag{2.6}$$

This offset frequency of the comb f_{ceo} is linked to the pulse-to-pulse change of CEP by [95],

$$f_{ceo} = \Delta\phi_{cep} \frac{f_{rep}}{2\pi} \tag{2.7}$$

$\Delta\phi_{cep}$ varies or slips whenever there is a mismatch between the group (v_g) and the phase velocity (v_ϕ). The group velocity or the speed at which the pulse envelope propagates is given as:

$$\frac{1}{v_g} = \frac{dk(\omega)}{d\omega} = \frac{n(\omega)}{c} + \frac{\omega}{c}\frac{dn(\omega)}{d\omega} \tag{2.8}$$

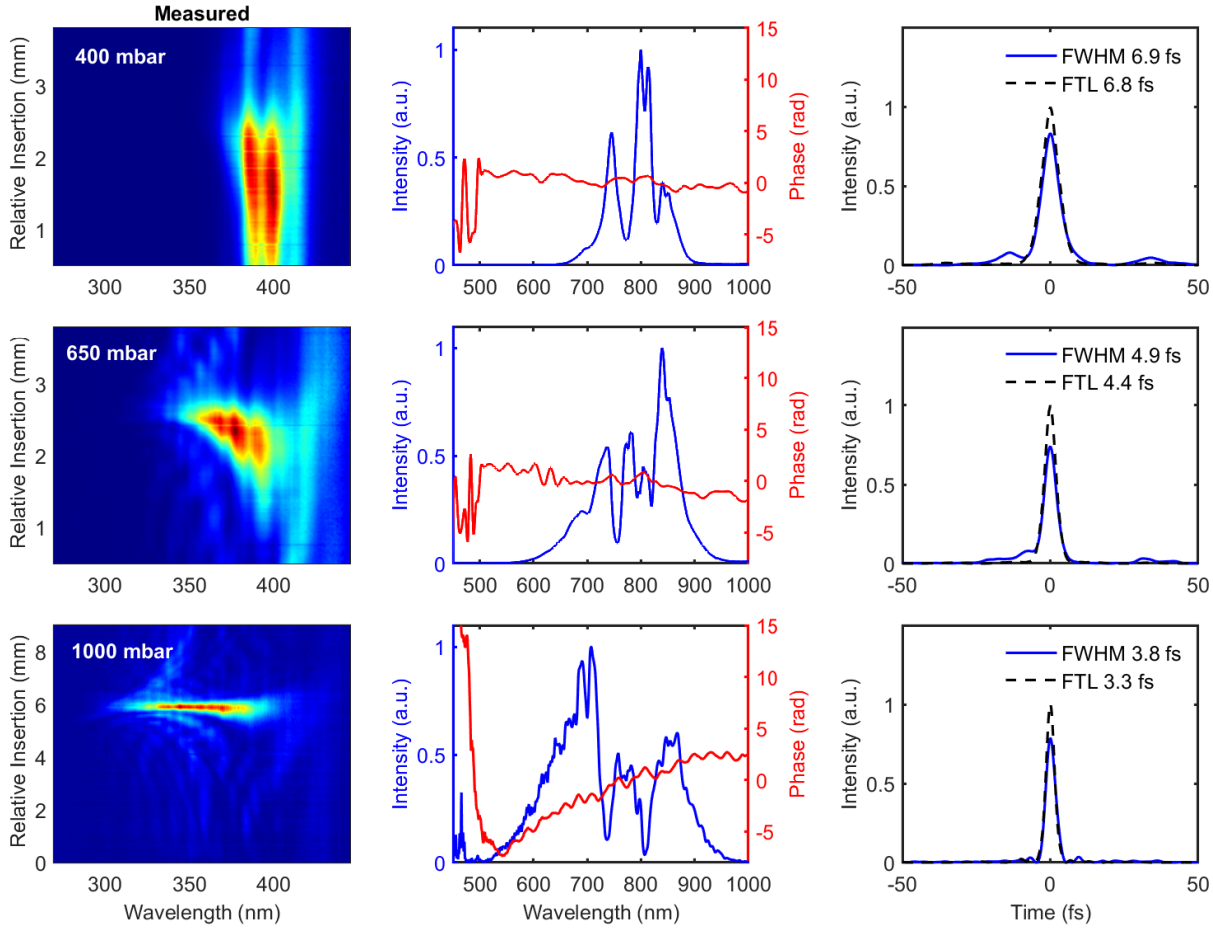

Figure 2.13: Measured D-scan traces (left), retrieved pulse spectral intensity and phase (middle) and pulse temporal intensity profile (right) for increasing Helium pressures in the fiber, 400 mbar, 650 mbar, and 1000 mbar.

The phase velocity or the speed at which the carrier wave (or electric field) propagates is given as:

$$\frac{1}{v_\phi(\omega)} = \frac{k(\omega)}{\omega} = \frac{n(\omega)}{c} \tag{2.9}$$

This means that the $\Delta\phi_{cep}$ changes whenever $\frac{dn(\omega)}{d\omega} \neq 0$. Changes in the refractive index can be introduced by mechanical vibrations and path length, fluctuations in beam pointing, ambient conditions (such as temperature, pressure, humidity, etc) and intensity fluctuations (due to nonlinear effects, $n = n_0 + n_2 I$) [97, 98]. In the oscillator cavity, propagation through air, the Ti:Sa crystal and the wedges induce dispersion due to which every round trip there is a mismatch between the group and the phase velocities. Thus, there is already CEP noise at the output of the oscillator, which is further accumulated as the pulses propagate through the laser chain, essentially due to dispersion and intensity fluctuations.

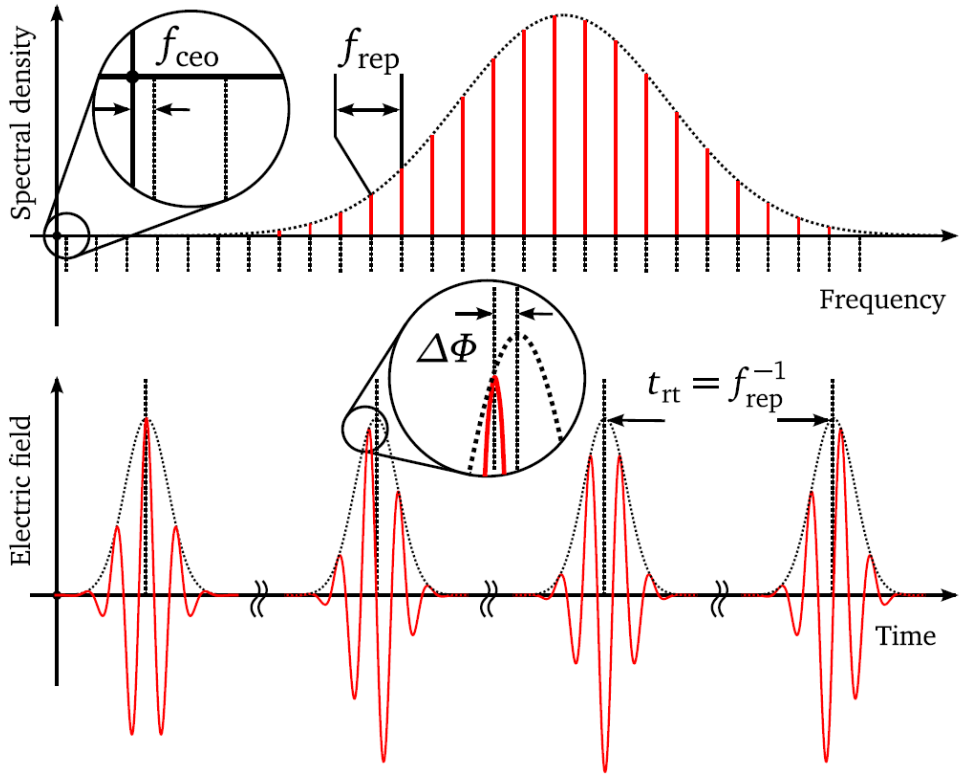

Figure 2.14: Representation of a mode-locked oscillator pulse train output in frequency (top) and time (bottom) domain. Reprinted from [96].

As a consequence of the difference between the group- and phase-velocity, the CEP of the laser pulses traveling through any kind of dispersive components, for example, stretcher and compressor, is subject to a drift, that is often non-negligible [98–100]. CEP-drifts in the stretcher and compressor are especially sensitive to mechanical perturbations, beam-pointing drifts, and air-flows introducing a change in the effective path length. Li et al. [99] found that a $1\,\mu m$ change of the distance between grating separation causes a CEP drift of 3.7 ± 1.2 rad. Thus, it is important to ensure stability of the optical mounts used for gratings, otherwise their vibration and thermal drift can lead to significant phase error.

The CEP noise also depends on the thermal load during amplification and has been studied experimentally in multi-pass Ti:Sa amplifiers by Borzsonyi et al. [101]. A CEP drift of 11 mrad$/°C/mm$ was observed over 30 minutes when the Ti:Sa crystal cooling was turned off. Thus, the CEP noise can also be accumulated due to thermal instabilities in the amplifier.

There are several ways to measure the CEP of an optical pulse, to name a few, attosecond time-resolved interferometric electric field sampling (ARIES) [102], single-shot above-threshold ionization phase-meter [103], tunneling ionization with a perturbation for the time-domain observation of an electric field (TIPTOE) [104, 105], temporal dispersion based one-shot ultrafast carrier envelope phase analysis (TOUCAN) [106], and finally, the most widely used techniques, f-to-$2f$ and 0-to-f interferometry [107–109].

The *Salle Noire* laser system relies on the two most widely used CEP measurement techniques,

0-to-f and f-to-2f interferometry. The former is used to measure the CEP of the front end (oscillator) while the latter is used to measure the CEP at the end of the chain. Implementation of both the techniques in *Salle Noire* and their respective stabilization feedback mechanisms are detailed below.

2.2.1 CEP stabilization of the oscillator

To measure the $\Delta\phi_{cep}$ or f_{ceo} at the output of the oscillator, we use 0-to-f interferometry technique [107–109] which relies on difference frequency generation (DFG), combining the generation of an octave-spanning spectrum with frequency conversion in a single crystal. Figure 2.15 illustrates the principle of measuring f_{ceo} using 0-to-f interferometry. The input comb f_n is broadened to f_m ($m > n$) and the DFG generates,

$$\begin{aligned} f_m - f_n &= m f_{rep} + f_{ceo} - (n f_{rep} + f_{ceo}) \\ &= (m-n) f_{rep} \end{aligned} \tag{2.10}$$

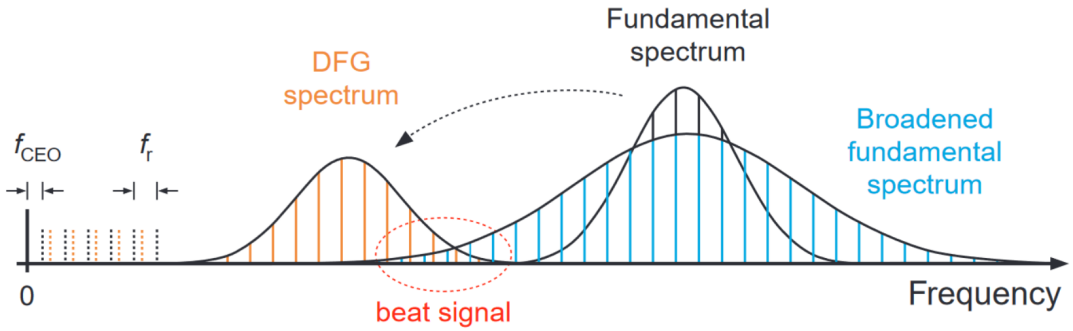

Figure 2.15: Principle of f_{ceo} detection using 0-to-f interferometry. Reprinted from [109].

The DFG component, $f_m - f_n$ is created with $f_{ceo} = 0$ while the fundamental comb f_n still has the same offset frequency, f_{ceo}. At the overlap of the fundamental and newly generated DFG comb, a beat signal between $f_m - f_n$ and $f_{m-n} = (m-n) f_{rep} + f_{ceo}$ is generated at f_{ceo}. This technique is nearly immune to external noise and drifts and offers CEP-stable operation from over several hours to even days [109].

In *Salle Noire*, the commercial oscillator operates at a 80 MHz repetition rate which is reduced down to 1 kHz in the following first CPA (see section 2.1.1 and 2.1.2). Therefore, it is sufficient to stabilize the CEP over every fourth pulse of the oscillator, i.e. at 20 MHz. A schematic representation of the oscillator cavity and the CEP detection setup is illustrated in figure 2.3. A pair of intra-cavity dispersion compensating mirrors compensate partially for the GDD introduced in the cavity. At the output, the beam is focused into a Periodically Poled Lithium Niobate (PPLN) crystal for spectral broadening and intra-pulse DFG. A spherical mirror after the PPLN collimates the beam and a leak from the following dichroic mirror is sent to a low-noise photodiode coupled to a spectrum analyzer after spectral filtering through an interferometric filter (IF), to detect the beat signal at f_{ceo}. A pair

of thin motorized wedges in the oscillator cavity allow to finely adjust the beat signal to 20 MHz. The detected signal is then sent to the phase-locking electronics (XPS800 from Menlo Systems) which computes an error signal at $f_{rep}/4 = 20\,\mathrm{MHz}$. A correction signal is sent to an acousto-optic modulator (AOM) that modulates the pump intensity, inducing changes in the nonlinear index of the Ti:Sa crystal, thereby changing the f_{ceo} through nonlinear phase-shifts [95, 110], reducing the CEP-noise to $< 150\,\mathrm{mrad}$ RMS.

2.2.2 CEP stabilization at the end of the laser chain

As the laser pulses propagate through the chain, significant CEP drifts are accumulated, especially in the stretcher and compressor where the spectrum is spatially dispersed [99, 111] as well as during amplification [101]. These *Salle Noire* laser system was designed to minimize this source of noise by using bulk stretchers with low-stretching factors and ultra-stable gratings compressor mounts to reduce mechanical vibrations [112].

To measure the CEP at the end of the laser chain we use f-to-$2f$ interferometry technique. The principle is quite similar 0-to-f interferometry but instead of DFG, it is based on SHG. In this technique, typically, first a crystal, for example, Sapphire, is used to generate an octave spanning spectrum which is then sent to an SHG crystal, for example, Beta Barium Borate (BBO). The spectral beat signal at f_{ceo} between the SHG comb $2f_n$ and the fundamental comb component f_{2n} is given as

$$\begin{aligned} f_n &= n f_{rep} + f_{ceo} \\ 2f_n &= 2n f_{rep} + 2f_{ceo} \\ f_{2n} &= 2n f_{rep} + f_{ceo} \\ 2f_n - f_{2n} &= f_{ceo} \end{aligned} \tag{2.11}$$

Figure 2.16 shows a layout of the f-to-$2f$ interferometer installed at the end of the laser chain to measure the accumulated CEP noise. Since the laser spectrum is itself nearly octave spanning, we don't need a broadening crystal. The beam is directly focused into a 0.5 mm thick BBO crystal for SHG. We have two spectrometers to analyze the resulting spectrogram. First, we have a USB 2.0 spectrometer (APS800, Thorlabs) which has a broadband spectral range, 390 nm to 630 nm. In the region where f_n and $2f_n$ overlap, we can see fringes due to internal dispersion within the spectrometer itself. By selecting this narrow spectral window and applying a fast Fourier transform (FFT), we can retrieve $\Delta\phi_{cep}$ relative to an arbitrary CEP value. The modulus of the FFT peaks at a position corresponding approximately to the group delay between the f and the $2f$ components, while the phase of the FFT around this peak corresponds to the position of the fringes or $\Delta\phi_{cep}$. An error signal can be computed and sent back to the AOM in the oscillator. This spectrometer is capable of fast detection at 1 kHz, however, the correction feedback loop is limited to 100 Hz.

In order to stabilize the CEP at the full repetition rate of the laser i.e. 1 kHz, we use a fast spectrometer (Fringeezz, Fastlite) with a narrow spectral window of 30 nm centered around 480 nm. Once we have strong fringes in the spectral overlap region, we use a flip mirror in the beam path to send

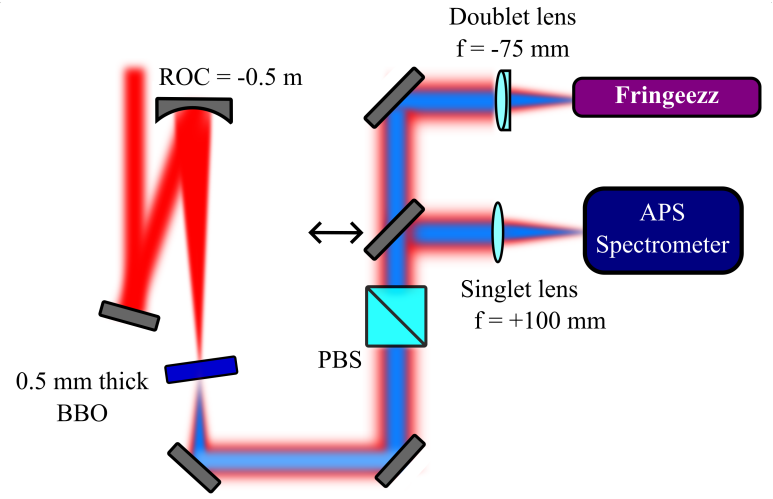

Figure 2.16: Schematic layout of the f-to-$2f$ interferometer used to measure and stabilize the CEP at the end of the *Salle Noire* laser chain. Focal lengths are specified in millimeters. BBO: Beta Barium Borate, and PBS: Polarizing beam-splitter.

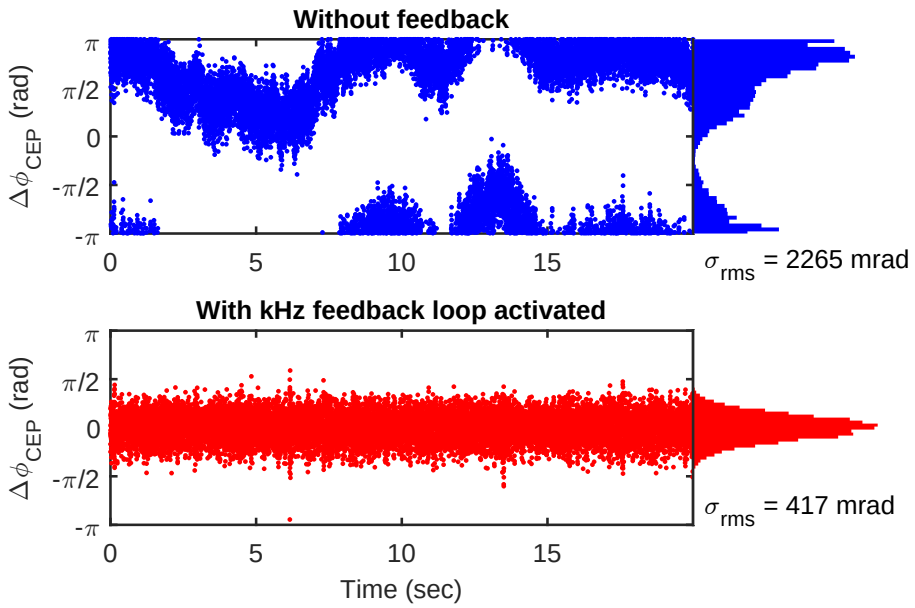

Figure 2.17: Shot-to-shot CEP stability at the end of the laser chain without (top) as well as with (bottom) kHz correction loop activated, measured using the f-$2f$ interferometer and Fringeezz spectrometer from Fastlite.

the signal to the Fringeezz spectrometer. Fringeezz is a fast spectrometer with on-board computation unit capable of acquisition as well as feedback at up to 100 kHz [113]. It uses two spectral fringes (one period) to compute $\Delta\phi_{cep}$ relative to an arbitrary CEP value. The computed error signal is feedback to the Dazzler, Daz#1, integrated in the first CPA. Figure 2.17 shows shot-to-shot CEP fluctuations measured using the Fringeezz at the end of the laser chain, both without and with the correction loop activated. In the current laser configuration, we can routinely achieve a CEP stability of $\sim 400\,\mathrm{mrad}$ RMS which can be maintained for extended periods ($\sim$ hours) as illustrated by our recent observations of CEP effects in relativistic laser-wakefield electron acceleration experiments [114].

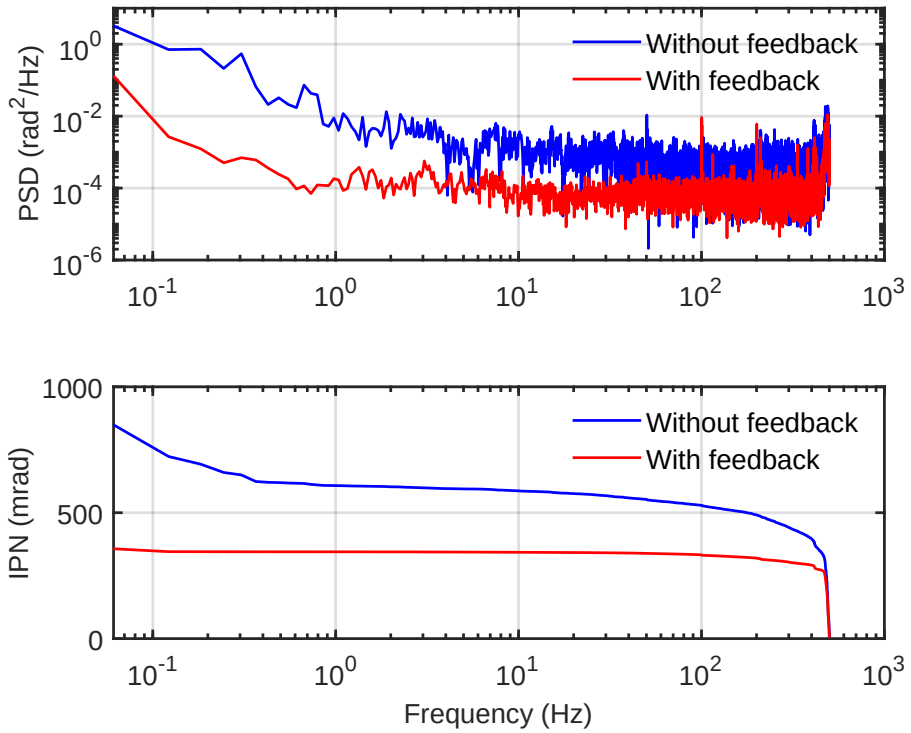

Figure 2.18: Noise analysis of the shot-to-shot CEP measurement both without and with kHz feedback loop activated at the end of the laser chain. PSD: power spectral density, and IPN: integrated phase noise.

A noise analysis of the shot-to-shot CEP stability measured at the end of the laser chain is shown in figure 2.18, both without and with kHz feedback loop activated. The kHz feedback loop clearly helps in reducing the integrated frequency noise (IPN) by at least a factor of 2. The main frequency components are at 50 Hz, 100 Hz and 300 Hz. The component at 50 Hz corresponds to the electrical grid frequency in Europe. If full-wave rectifiers are used, this can also induce noise at twice the frequency, i.e. 100 Hz. Most of the fast overall noise level above 100 Hz can be reduced, however, fast noise above 100 Hz is hard to suppress in case of a kHz laser. Below 50 Hz, most of the noise should be dissipated by the optical tables. Additionally, we have noticed that air flows in the lab also disturb the CEP stability. Perhaps a vacuum integrated CEP detection setup will help further improve the stability. Another key source of CEP instability comes from the power amplifier of the second CPA which is currently running in a weakly saturated regime. Saturating the amplifier as well as reducing the remaining thermal load on the Ti:Sa crystal should further help reduce the accumulated CEP noise.

2.3 Laser upgrades

During my thesis, I implemented two major upgrades on the laser system: Firstly, together with the former PhD student in the group, Marie Ouillé (LOA), I installed an extension arm after the HCF post-compressor to decrease the fluence on the first mirror after the fiber and subsequently reconfigured the beam collimation and transport after. Secondly, to help mitigate the CEP noise of the laser sys-

tem, with help of Zhao Cheng (LOA), I constructed a cryogenically cooled multi-pass Ti:Sa amplifier which replaced the booster and power amplifiers of the second CPA stage. I will provide detailed descriptions of both upgrades in this section.

2.3.1 HCF extension arm

One of the major issues that we faced with the HCF-based post-compression setup described above (see 2.1.5) was slow damage of the first mirror after the HCF-exit, over a period of few days. We reckon this was because of the relatively high fluence on the mirror. We were using enhanced-silver coated on a UVFS substrate (from EKSMA) with a laser-induced damage threshold (LIDT) of $0.21\,\mathrm{J/cm^2}$ specified at $\lambda = 800\,\mathrm{nm}$ for 50 fs pulses at 1 kHz repetition rate. Working in the near-single cycle regime necessitates using silver-coated mirrors, despite their limitations. These mirrors typically have a reflectivity of $\approx 98.5\%$ and a lower LIDT compared to dielectric coated mirrors. However, no dielectric coated mirrors are currently available that can support broad bandwidths of the near-single cycle pulses.

For a transmitted energy of $\approx 6\,\mathrm{mJ}$, the peak fluence on this mirror is estimated to be,

$$\begin{aligned} F_{peak} &= \frac{2E}{\pi\omega_M^2} \approx \frac{2.(6\times10^{-3})}{\pi(2.1\times10^{-1})^2} \\ &= 0.09\ \mathrm{J/cm^2} \end{aligned} \tag{2.12}$$

where, $\omega_M = 0.21\,\mathrm{cm}$ is the measured beam radius on the mirror. Although we were operating at nearly 50% of the specified LIDT of the mirror, it is generally recommended to maintain the peak fluence below 30% of the specified LIDT, to maintain the integrity of the coating and ensure longevity. In our case, since the beam out of the HCF is diverging, the easiest solution to reduce the peak fluence was to increase the distance between the HCF and the first mirror, which meant adding an extension arm.

A schematic layout of the installed extension arm is shown in figure 2.19. By extending the distance between the HCF and the first mirror from 1.6 m to 3.5 m in total, we could effectively increase the beam size to $\omega_M = 4.5\,\mathrm{mm}$ and reduce the peak fluence by a factor of ≈ 4.5, to $F_{\mathrm{peak}} = 0.02\,\mathrm{J/cm^2}$ at $\approx 10\%$ of the specified LIDT. This allows to have some breathing room for future upgrade of the *Salle Noire* laser to augment the available pulse energy. In order to minimize beam pointing fluctuations due to ambient vibrations, the extension chamber was installed on a separate optical table and the breadboard is decoupled from the chamber using metallic chassis bolted into the floor. In order to keep the same beam parameters for experiments, we reconfigured the HCF exit chamber. A concave mirror with an ROC = 3.5 m (OMCC1) was used in the extension chamber to re-collimate the beam, followed by an afocal telescope (OMCX and OMCC2) to expand the beam by a factor of 1.5 to finally have a 20 mm beam (at $1/e^2$ width)at the output of the HCF exit chamber.

2.3.2 Cryogenically-cooled multi-pass Ti:Sa amplifier

Given that the second CPA stage of the *Salle Noire* system was operating in a weakly saturated regime, it resulted in energy and phase instabilities at the end of the laser chain. In order to overcome

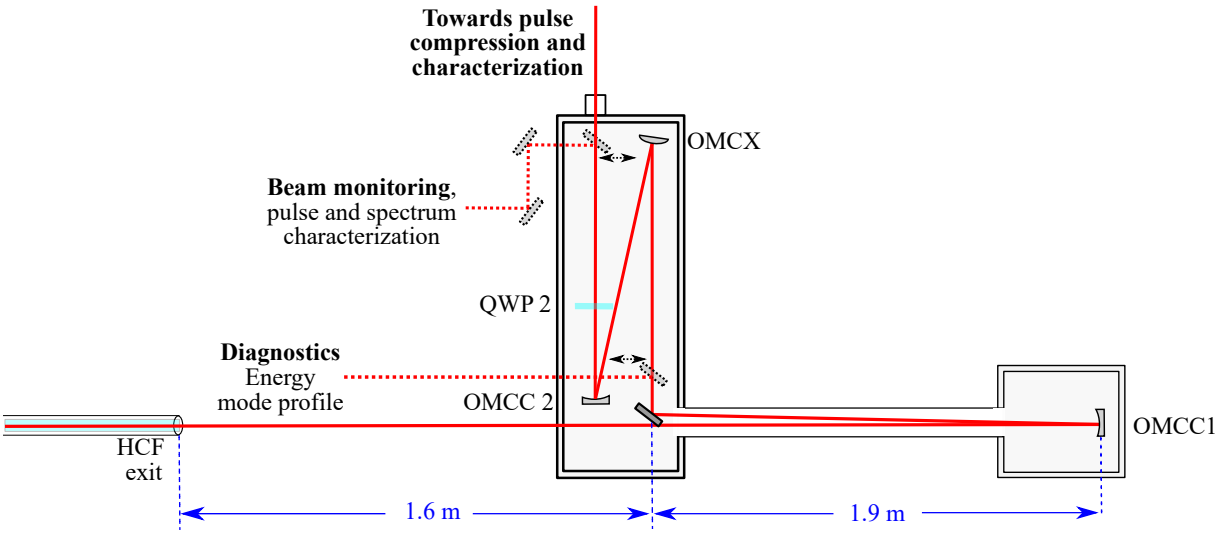

Figure 2.19: HCF post-compression setup after adding an extension arm for additional 1.9 m beam propagation after the fiber exit. QWP: Quarter-wave plate, OMCC: output plano-concave mirror, and OMCX: output plano-convex mirror.

these limitations, we opted to replace the two amplifiers of the second CPA with a single cryogenically-cooled amplification stage. With help from Zhao Cheng (LOA), first, I developed a new multi-pass amplifier with cryogenic cooling on a test bench designed to emulate the *Salle Noire* system. After achieving the desired performance metrics, this amplifier was seamlessly retrofitted into the *Salle Noire* laser.

Cryogenic cooling systems have significantly enhanced the performance of solid-state lasers since the inception of laser technology. Notably, in 1960, the second laser system ever developed, a Uranium-doped CaF_2 laser was cooled down to cryogenic temperatures using liquid Helium [115]. An early cryogenic laser patent was issued to Bowness [116] for a liquid-Nitrogen cooled Ruby laser. In a pioneering effort, Moulton first demonstrated the benefits of cryogenically-cooling Ti:Sa using liquid-Nitrogen in 1986 [51]. This breakthrough was soon followed by the demonstration of extracting 350 W of power from a liquid-nitrogen-cooled Ti:Sa crystal – over 200 times higher than the obtainable output at room temperature at the time [117]. Despite the early adoption of cryogenic technology, their widespread integration in the laser industry was limited by operational challenges and associated high costs. Over time, advancements in laser technology further reduced the reliance on cryogenic cooling. However, clearly, the benefits of cryogenic cooling outweighed the challenges, particularly for systems requiring high peak and average power outputs [118–123].

The key benefits of implementing cryogenic cooling in Ti:Sa-based laser systems have been discussed in 1.3. In a nutshell, by simply reducing the crystal temperature, we can extract more energy while improving the energy stability and reducing the phase noise. However, as the temperature decreases, the width of the fluorescence line shape and the central emission wavelength change which in turn affects gain narrowing as well as lead to gain shifting [44]. Thus, one needs to carefully take into account the change of gain cross-section with temperature when designing a cryo-cooled amplifier.

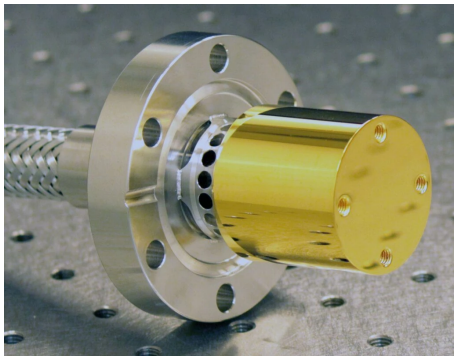

Figure 2.20: A compact high-performance Gold cryo-head from CryoSpectra.

To achieve cryogenic cooling, we use an ultra-low vibration, no-maintenance, Stirling-type cryo-cooler (K130100W, CryoSpectra) capable of extracting 100 W, reaching temperatures as low as 120 K. A picture of the cryo-head is shown in figure 2.20. It is a high performance Gold cryo-head mounted on a CF40 flange which is then attached on-top of the crystal-chamber. The crystal itself is mounted in a block of Copper dissipator attached to the cryo-head for fast heat dissipation. In order to avoid freezing the water vapour, consequently degrading the laser performance and adversely affecting the performance and longevity of the cooling system, the crystal chamber is maintained at high vacuum ($\sim 10^{-6}$ mbar) using a turbo-molecular pump (T85 Station, Edwards). A small vibration-free ion-getter pump (Agilent Technologies) is also connected to the chamber which can be used to reach ultra-high vacuum ($\sim 10^{-8}$ mbar) if necessary. A series of images showcasing the amplifier in operation are depicted in figure 2.21.

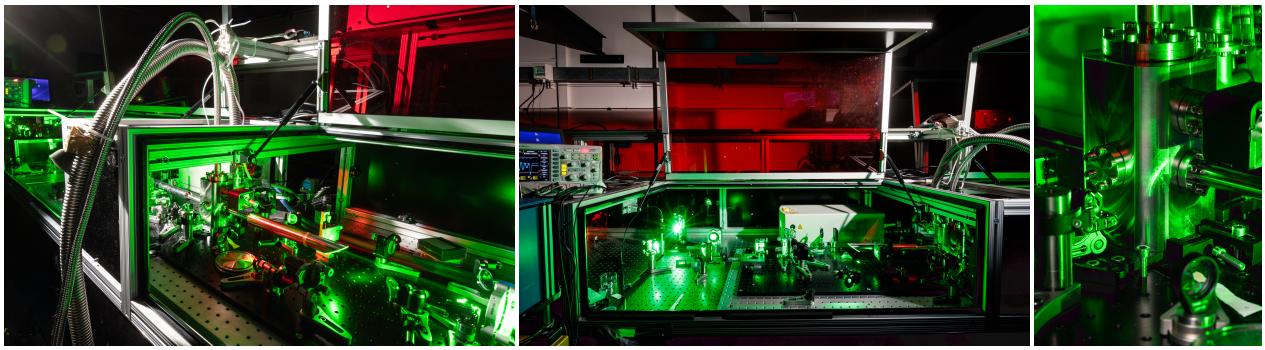

Figure 2.21: Pictures capturing the cryogenically-cooled multi-pass Ti:Sa amplifier in operation. Courtesy of Jérémy Barande.

Optical design

The optical layout of the 6-pass cryogenically cooled Ti:Sa amplifier is shown in figure 2.22. The Ti:Sa crystal is $6\,\mathrm{mm} \times 6\,\mathrm{mm}$ in size with 8 mm of gain length, Brewster-cut (uncoated) with an absorption coefficient of $\alpha = 1.90 \pm 0.35\ \mathrm{cm}^{-1}$ at $\lambda_{\mathrm{pump}} = 527\,\mathrm{nm}$. The crystal chamber consists of two 30 cm long tubes on either side, with 1.5 mm thick elliptical fused silica laser windows at the Brewster angle. This helps to maintain a clean laser polarization during the amplification process as well as to avoid the generation of post-pulses which can generate prepulses during the amplification

process [70]. An s-polarization of the seed and the pump pulses is chosen for designing this amplifier to capitalize on the largest bandwidth supported by the dielectric mirrors, thereby maximizing the extracted spectral bandwidth. The crystal is pumped at 527 nm by two frequency-doubled Nd:YLF laser systems (Ascend 40 and Ascend 60, Spectra-Physics) at 1 kHz repetition rate with a total pump power of approximately 50 W, injected off-axis from both sides with a small angle between them. The pump laser energy transmitted by the crystal is focused back using 2" diameter enhanced silver-coated concave mirrors with a 2 m ROC. We used enhanced silver-coated mirrors because they were readily available off the shelf in the lab and will be replaced by highly reflective dielectric mirrors in the future to enhance the available pump energy. The amplifier consists of two 2" diameter, 1.5 m ROC dielectric-coated mirrors (M1 and M2) separated by the sum of their focal lengths, i.e. 1.5 m. The mirror coating is designed to be highly reflective at 800 nm and highly transmissive for 527 nm at a 0° angle of incidence.

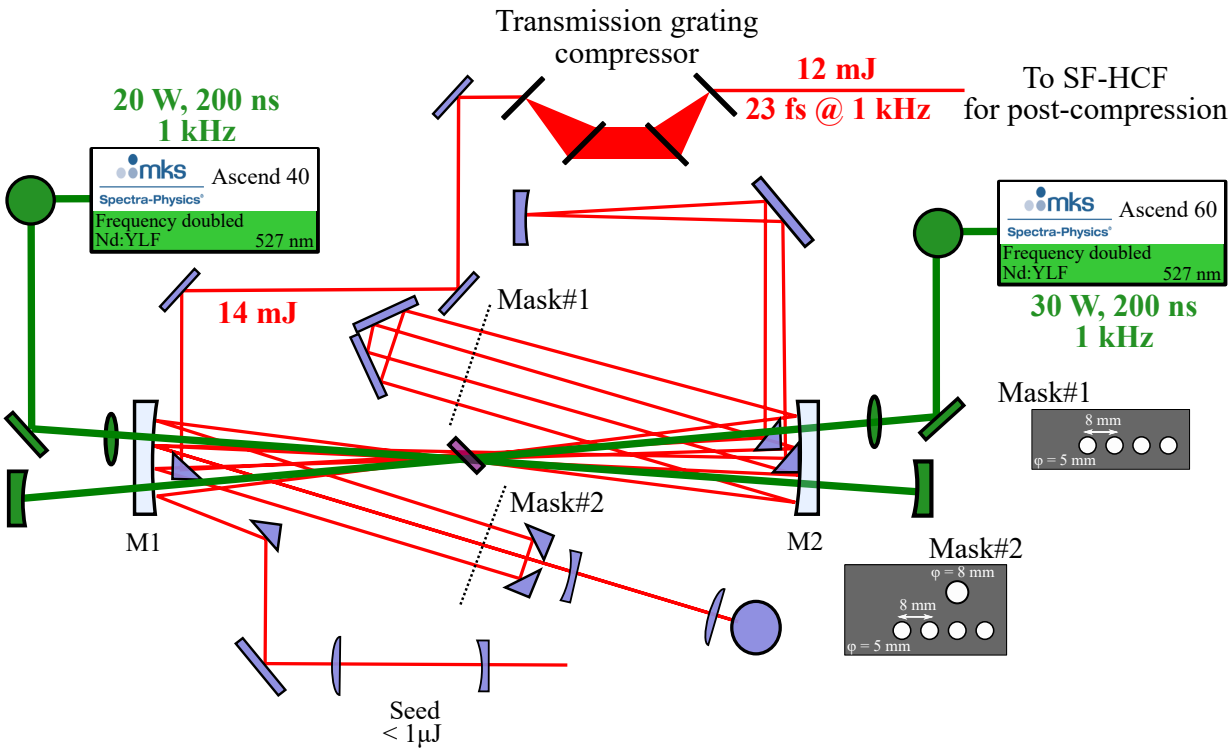

Figure 2.22: Optical layout of the cryogenically cooled 10-pass Ti:Sa amplifier. For the sake of clarity, the crystal chamber is not displayed here.

The seed beam is injected off-axis and is alternately focused onto the crystal by the mirrors M1 and M2, with beam size for each pass meticulously engineered to ensure that the fluence remains below a conservative threshold of $1\,\mathrm{J/cm^2}$, despite the specified LIDT of $10\,\mathrm{J/cm^2}$ for Ti:Sa crystals. As depicted in figure 2.22, the two "masks" integrated into the amplifier design not only establish the reference positions for aligning each pass through the crystal but also limit the ASE, thereby preventing degradation of the temporal intensity contrast. Figure 2.23 shows the measured beam profiles of the input beam on the crystal and in-focus, typically positioned $12-15\,\mathrm{cm}$ before the crystal. This setup, where a diverging beam approaches the crystal, helps to slightly counterbalance self-

focusing effects in the crystal. Additionally, the focus position relative to the crystal or the chamber windows is carefully chosen to keep the fluence on the windows well below their LIDT for each pass. These small tricks help to ensure longevity of the optical components, allowing the system to operate for extended periods without any intervention. Furthermore, the entire amplifier is assembled on a water-cooled breadboard to prevent thermal drifts throughout the day.

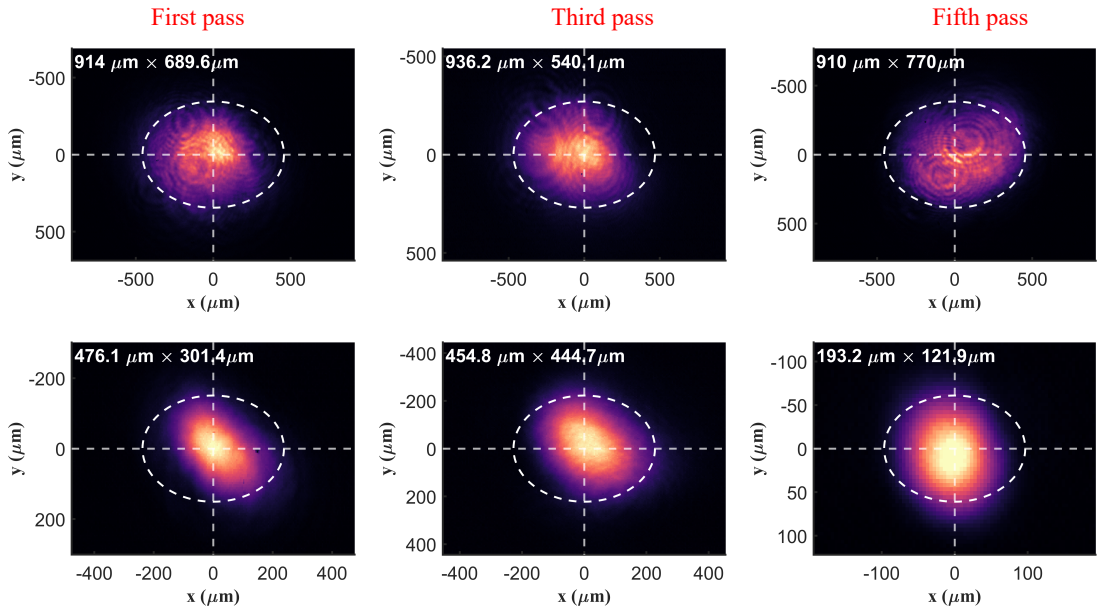

Figure 2.23: Measured input beam profiles at the crystal position (top panel) and in-focus (bottom panel), typically $12-15\,\mathrm{cm}$ before the crystal, for the first, third and fifth pass through the amplifier.

The input seed energy can be tuned from $<1\,\mu\mathrm{J}$ to up to $18\,\mu\mathrm{J}$ by changing the diffraction efficiency of the Dazzler Daz#2, within the laser chain. Figure 2.24 shows the variation of the extracted energy at output with the increasing seed energy after the first, second, fourth, fifth and sixth pass through the amplifier, while maintaining a constant pump power of 25 W. It is evident that for the reduced pump power of 25 W, the output gain begins to saturate from seed energies above $5\,\mu\mathrm{J}$, indicating that the amplifier is operating in a saturated regime, which is beneficial as it minimizes phase and energy instabilities. As the pump energy is increased to 50 W, the seed energy is proportionally decreased to maintain consistent gain values per pass, ensuring continued operation within the saturation regime.

Output performances

In the amplifier configuration integrated into the *Salle Noire* chain, the seed energy is approximately $1\,\mu\mathrm{J}$. The seed spectrum is shaped using the Dazzler, Daz#2, to counteract gain narrowing in the amplifier. Finally, at the output, we obtain a maximum of 14 mJ energy pulses at 1 kHz repetition rate, achieving a total gain of 14×10^3. The laser pulse duration is measured to be 24 fs after the TGC, using a Wizzler device [124] as shown in figure 2.25. Table 2.1 summarizes the output parameters of the second CPA following the upgrade.

After a thorough characterization of the upgraded second CPA stage, the output pulses were coupled into the next stage in the *Salle Noire* chain for post-compression to the single-cycle regime.

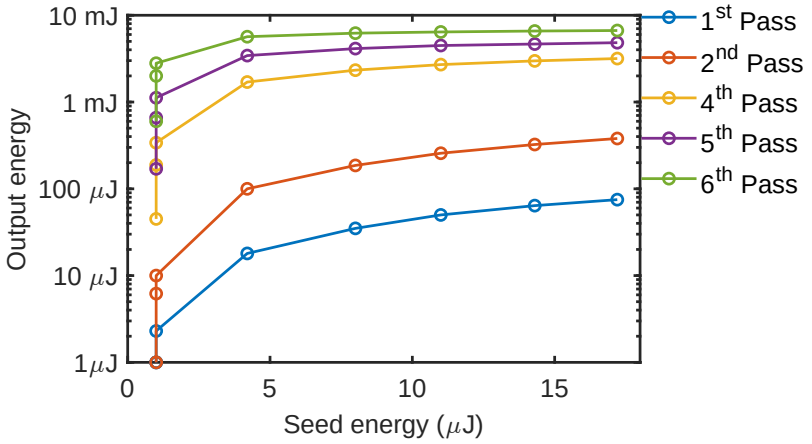

Figure 2.24: Variation of the extracted pulse energy as a function of the increasing seed energy through multiple passes in the amplifier, for a constant pump power of 25 W.

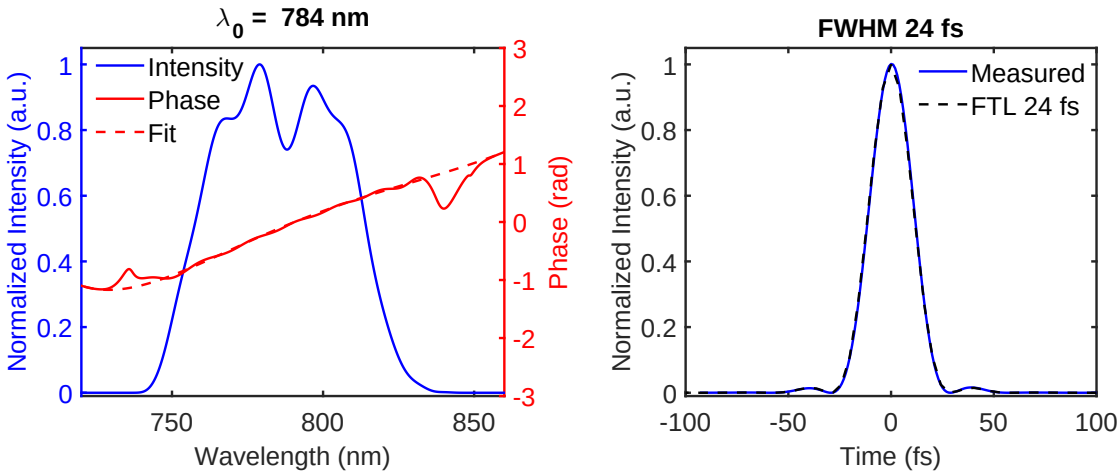

Figure 2.25: Pulse spectral intensity and phase (right) and temporal intensity profile (left), measured with a Wizzler device after the upgraded second CPA stage.

However, the current post-compression setup cannot handle a 1.5-fold increase in peak-power. Consequently, it will need to be replaced with a suitably longer HCF featuring a larger core diameter. To maintain compatibility with the existing post-compression setup in the interim, while the next upgrade is being planned, the output of the amplifier was reduced to 9 mJ by decreasing the pump energy and proportionately increasing the seed energy, such that the amplifier continues to run in a saturated regime, ensured by maintaining consistent gain values per pass. After the TGC, 7.65 mJ energy pulses are available to seed the post-compression stage, thereby matching the input peak power to the post-compression setup prior to the upgrade.

The laser pulses are characterized spectrally and temporally using the D-scan [94] device at the end of the chain. As shown in figure 2.26, an octave-spanning bandwidth could be generated and compressed down to sub-4 fs pulses. A CEP measurement made at the end of the chain with the sub-4 fs pulses, using an f-2f interferometer and a Fringeezz spectrometer from Fastlite is shown in figure 2.27. As expected, with the upgraded amplifier, we see a clear improvement in the CEP stability. Contrasting the noise analysis of the CEP measurement before the upgrade (figure 2.18), in

Total input pump power	50 W @ 527 nm
Extracted output energy (after the amplifier)	14 mJ
Available pulse energy (after the TGC)	12 mJ
Currently used pulse energy	7.65 mJ
Energy stability	$<$0.2% RMS
Central Wavelength	785 nm
Spectral width	70 nm FWHM
Output pulse duration (measured after TGC)	24 fs
Polarization	s-pol
Repetition rate	1 kHz
Temporal intensity contrast ratio	$> 10^{10}$
Pulse-to-pulse CEP noise	$\sim$ 200 mrad RMS

Table 2.1: Output characteristics of the upgraded second CPA-stage.

figure 2.27(c), we see a further decrease in the IPN of the low frequency components. Now, we can routinely reduce the CEP noise to $\approx 200\,\mathrm{mrad}$ RMS.

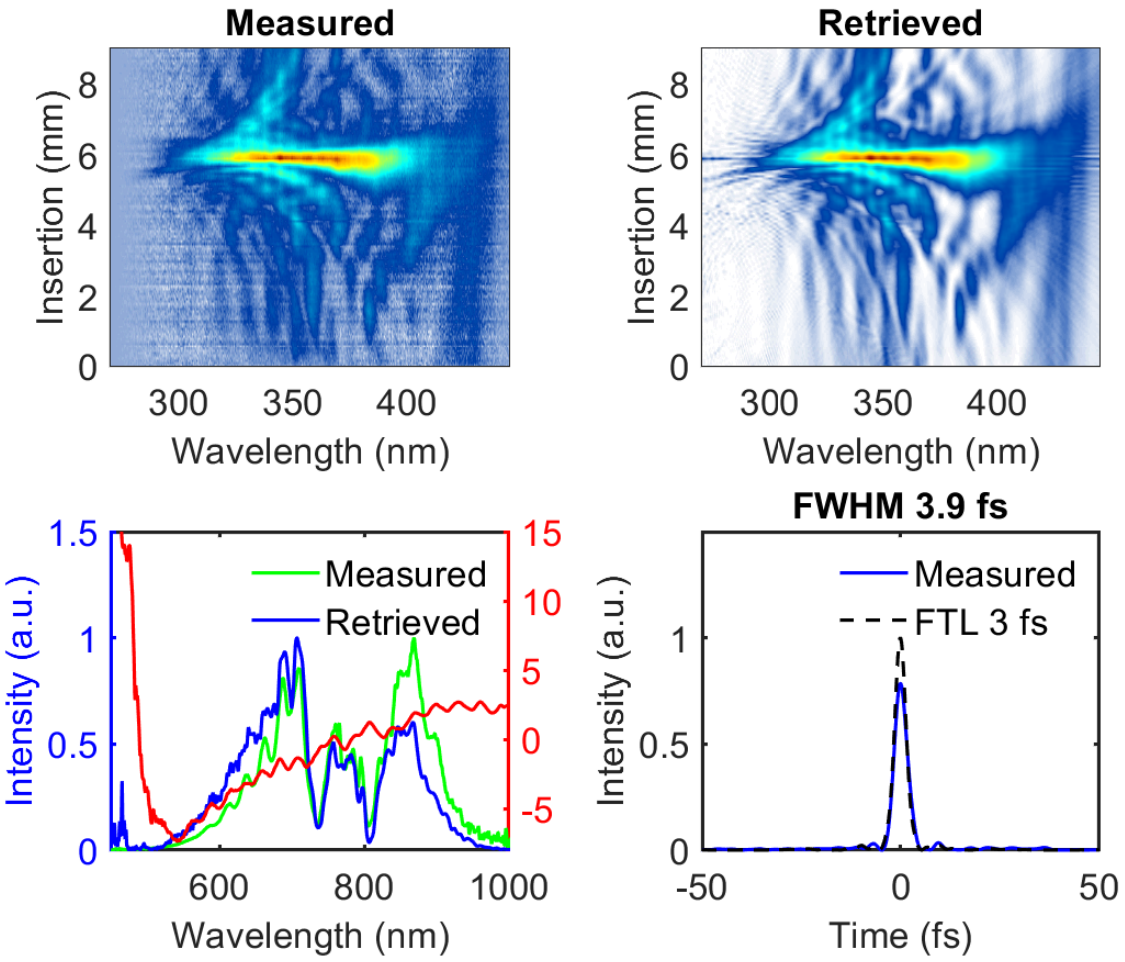

Figure 2.26: Top: Measured (left) and retrieved (right) SHG D-Scan traces. Bottom: Measured and retrieved spectral intensity and phase (left) and, FTL and measured temporal intensity pulse profile (right).

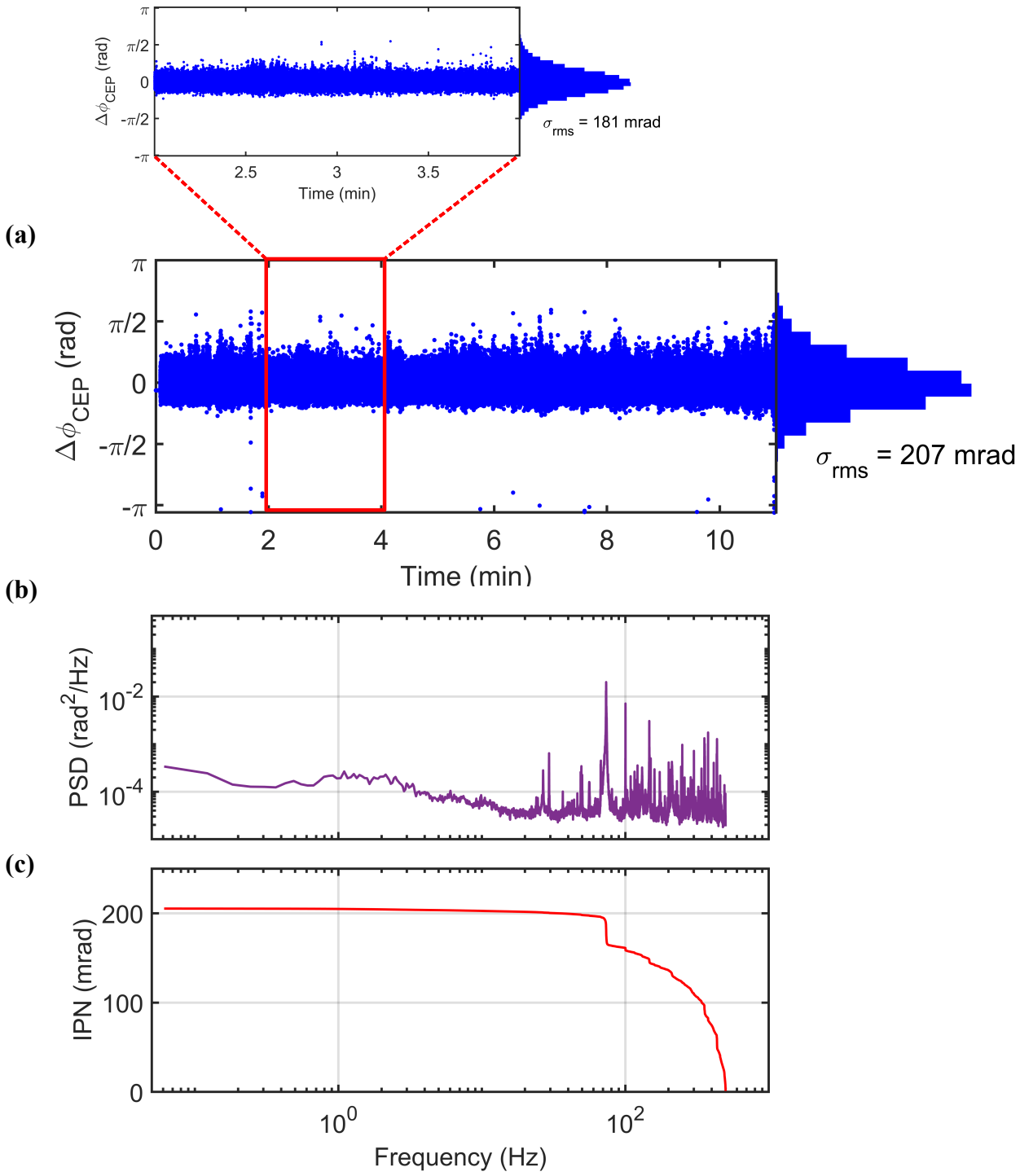

Figure 2.27: Shot-to-shot relative CEP noise measured at the end of the laser chain using f-2f interferometer and the Fringeezz spectrometer from Fastlite with an inlay zoomed-in over a two minute time scale (a), power spectral density (b), and integrated phase noise (c). PSD: power spectral density, and IPN: integrated phase noise.

Chapter 3

Nonlinear optics in multipass cells

"*Do or do not, there is no try*"
- Yoda

Outline

3.1 Multipass cells: Fundamentals **70**
3.2 Nonlinear mode-matching **71**
3.3 State-of-the-art **73**
3.4 Post-compression in multipass cells **76**
3.4.1 Identification of different propagation regimes 77
3.4.2 Results in optimal conditions 80
3.4.3 Summary 82
3.5 Contrast enhancement in multipass cells **83**
3.5.1 Nonlinear ellipse rotation 83
3.5.2 Cross-polarized wave generation 88
3.5.3 Summary 94
3.6 Conclusion **95**

The concept of off-axis propagation with multiple passes in a two spherical mirror arrangement was first introduced by D. Herriott, H. Kogelnik, and R. Kompfner in 1964 [125]. The so-called "Herriott cells" were traditionally used to implement long propagation lengths for molecular absorption spectroscopy [126], Raman spectroscopy [127, 128], laser resonators, and optical delay lines [129]. Herriott-type multipass cells (MPC) are now commercially available for weak-trace-gas absorption spectroscopy applications such as environmental monitoring, bio-sensing, combustion processes, and fundamental studies in atomic and molecular physics.

SPM assisted laser post-compression using a Herriott-type MPC was demonstrated for the first time by Schulte *el al.* in 2016 [130]. The principle of laser post-compression in MPCs is illustrated in figure 3.1. The central idea was similar to post-compression in HCFs [131], inducing spectral broadening via SPM with extended propagation in a nonlinear medium, followed by compensation of the SPM-induced chirp to temporally shorten the pulses. However, in this case, to induce SPM, free-space propagation was used and the nonlinearities were distributed over a large propagation distance by inserting a nonlinear medium in a recirculating cell. Schulte *el al.* [130] used bulk-plates to induce SPM in an MPC, where $\sim 400\,\mathrm{W}$ - 850 fs input pulses were spectrally broadened and shortened in time by a factor of 5 with over 90% efficiency. In the very first experimental demonstration, in terms of average power handling, MPCs exceeded at the time best performance of the solid-core fibers [132] and hollow-core Kagome photonic crystal fibers [133]. Schulte *et al.* [130] demonstrated similar average power handling as compared to gas-filled capillaries [131] but with a much higher efficiency. Since then, MPCs have attracted significant attention within the scientific community as well as in the industrial sector as highly efficient [130, 134–137] and cost-effective tools to boost laser peak power with high compression factors [138], easy energy [139, 140] and power scalability [140, 141], and excellent output spatio-spectral beam quality [142]. These results are exceptionally promising and have established MPCs at the forefront of laser post-compression.

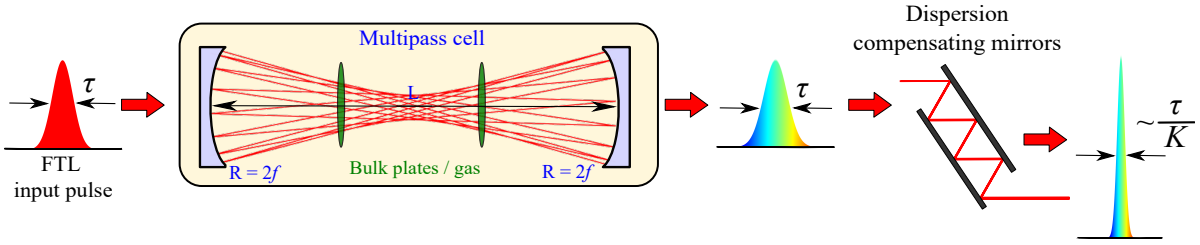

Figure 3.1: Principle of laser post-compression in a Herriott-type MPC. τ is the laser pulse durations and K is the compression factor.

3.1 Multipass cells: Fundamentals

Typically, a Herriott-type MPC consists of two identical co-axially positioned concave mirrors with a radius of curvature (ROC), R, facing each other and separated by a distance $L \leq 2R$. A Herriott-type MPC can be analyzed as a periodic imaging system consisting of a series of equidistant thin lenses with a focal length $f = R/2$, as shown in figure 3.2. When the input beam is injected off-axis in the MPC, it is reflected back and forth in the cell, trapped in the vicinity of the optical axis of the stable periodic optical system. In such a configuration, consecutive traversing beams form an ellipse, or for particular launching angles and cell geometries, a circular pattern with evenly spaced spots on the cell-mirrors [129], as shown in figure 3.2. The periodicity of the optical system results in a sinusoidal advance of the transverse coordinates of the spots on the cell mirrors after each round trip. The angular advance of the spots on the mirrors is given as

$$\theta = \frac{2\pi n}{N}, \text{ where } n = 1, 2...N-1 \tag{3.1}$$

where, N is the number of passes in the cell after which the beam returns back to its original position.

The stability condition can be determine by drawing an equivalence to a two-mirror optical resonator for a Gaussian beam, whose evolution in free space can be described by the complex beam parameter

$$\frac{1}{q} = \frac{1}{R} + i\frac{\lambda}{\pi\omega^2} \tag{3.2}$$

This equation can also be simplified to

$$q(z) = z + iz_R \tag{3.3}$$

where, the Rayleigh range, $z_R = \pi\omega_0^2/\lambda$, z is the propagation direction and λ is the central wavelength. The overall transformation of the Gaussian beam can be calculated using the ABCD matrix approach. To match the input beam to the stationary or the Eigen mode of the cell, the beam should maintain the same size and curvature after every round trip in the cell. When translated to the self-consistency requirement of the complex beam parameter

$$q' = \frac{Aq + B}{Cq + D} = q \tag{3.4}$$

For the given MPC geometry determined by R and L, there exists a beam waist located at the center of the cell for which the beam size and radius of curvature evolution is periodic over a round trip in the cell. The beam radius at the waist is given by:

$$\omega_0 = \sqrt{\frac{\lambda L}{2\pi}\sqrt{\frac{2R}{L}-1}} \tag{3.5}$$

The beam expands upon propagation to a radius at the cell mirror:

$$\omega_m = \omega_0\sqrt{\frac{2R}{2R-L}} \tag{3.6}$$

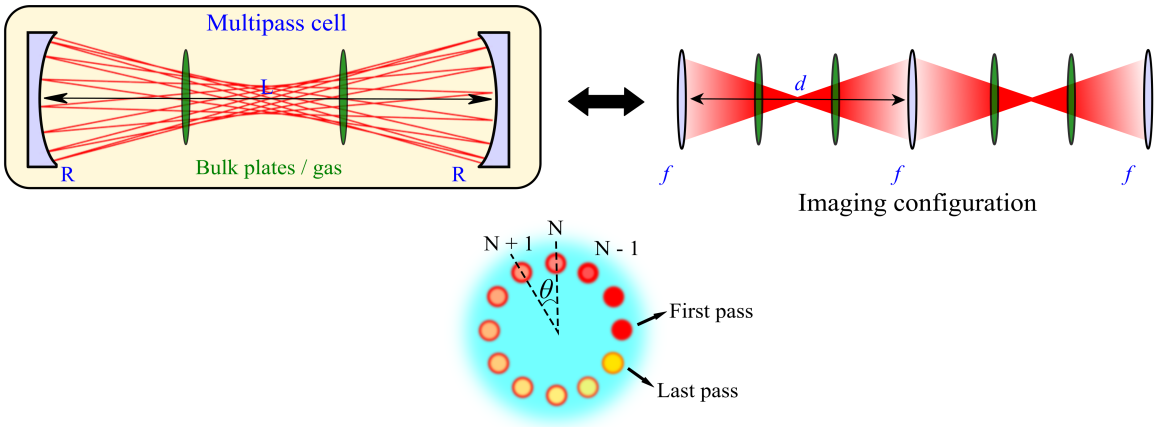

Figure 3.2: MPC geometry

The beam is aligned on a path for which the spot pattern does not overlap, such that it is possible to inject and extract the beam with small mirrors that do not intersect the beam path inside the cell or through holes in the cell mirrors. When the input beam is matched to the conditions in equations 3.5 and 3.6, it ensures that nonlinearities are accumulated homogeneously and the beam caustics remains stable for every round trip in the cavity, i.e. the beam size on the mirrors and the position of the beam waist remains approximately constant. However, this is a linear approximation. In real experimental implementations, there are often deviations from the Eigen-mode due to self-focusing or refraction effects in the cavity. When an MPC is not ideally mode-matched, the beam parameters on the cell mirrors oscillate upon propagation with a period of oscillation that depends on the accumulated Gouy phase per pass and the amplitude of these oscillations depends on the degree of mismatch between the input beam parameters and the Eigen-mode of the cavity. [143].

3.2 Nonlinear mode-matching

When starting from a linearly matched input beam, often, mode-matching has to be fine-tuned experimentally to compensate for other nonlinear effects that accompany SPM. Most of the post-

compression studies using MPCs are increasingly leaning towards operation in a highly nonlinear regime as it allows to minimize the number of round trips in the cell, thereby relaxing the constraints on mirror coating performance, in terms of reflectivity as well as dispersion. In case of such highly nonlinearly driven MPCs, when starting from a linearly-matched case, as the beam propagates in the MPC, due to Kerr lensing there are significant oscillations in the beam size that can quickly prove to be detrimental for the cell mirrors [144]. Thus, nonlinear mode-matching taking into account Kerr-lensing and self-focusing effects is quickly becoming the standard for operating the MPCs, helping to make the design more accurate by ensuring a constant beam size on the cell mirrors and at the beam waist for a fixed nonlinearity level [145]. In this section, I will briefly describe an analytical model introduced in [145] for mode-matching in MPCs taking into account the nonlinear propagation. Detailed information about nonlinear mode-matching for gas-based MPCs and the impact of Kerr-lensing as opposed to the linearly matched case can be found in [145] and [144].

We consider the nearly concentric MPC geometry discussed in the previous section. To obtain the waist of the Eigen-mode in the nonlinear regime, the ROC of the nonlinear beam is fixed to be equal to the mirror radius of curvature at the mirror location, yielding,

$$\omega_0 = \sqrt{\frac{\lambda L}{2\pi}\sqrt{\left(1-\frac{P}{P_{cr}}\right)\left(\frac{2R}{L}-1\right)}} \tag{3.7}$$

Here, critical power for self-focusing, $P_{cr} = 3.77\lambda^2/8\pi n_0 n_2$ [146]. Let's define,

$$\sigma = 1 - \frac{P}{P_{cr}} \tag{3.8}$$

In order to determine the optimal beam waist size and the location in the absence of any nonlinear medium, one must start from the center of the MPC with the optimal nonlinear beam size and back propagate through the optical system, all the way to the entrance window using the modified q parameter in the nonlinear regime [147], q_{NL}, given as,

$$\frac{1}{q_{NL}} = \frac{n_0}{R} + i\sqrt{\sigma}\frac{\lambda}{\pi\omega^2} \tag{3.9}$$

From the entrance window, the beam can then be linearly propagated ($\sigma = 1$) towards the MPC center to reveal the target beam waist and position to be used during the mode-matching procedure. However, this approach is limited if the pulse properties change during propagation, for example, due to dispersion in the cell, which impacts the pulse peak power.

Nonlinear mode matching in MPCs presents a complex but critical challenge. Accurate modeling and/or simulation of the nonlinear interactions and meticulous adjustment of the system parameters is crucial for a precise optical design, which is essential to optimize the performance of such systems.

3.3 State-of-the-art

MPCs have rapidly gained popularity for nonlinear post-compression where extended nonlinear propagation can be folded over a relatively small footprint and large B-integrals can be accumulated in small increments for every pass with minimal spatio-temporal couplings. Several experimental validations have been conducted across a broad range of input parameters, including input pulse energies ranging from $\sim \mu$J [148] to 200 mJ [140], input pulse duration from 10 ps [149] to < 50 fs [150, 151], and average power handling in the Watt to kilo-Watt (kW) range [140]. MPCs also provide a large number of degrees of freedom in terms of choice of the nonlinear medium as they are compatible with bulk material [130], gases [135, 136, 152], and even hybrid geometries [153].

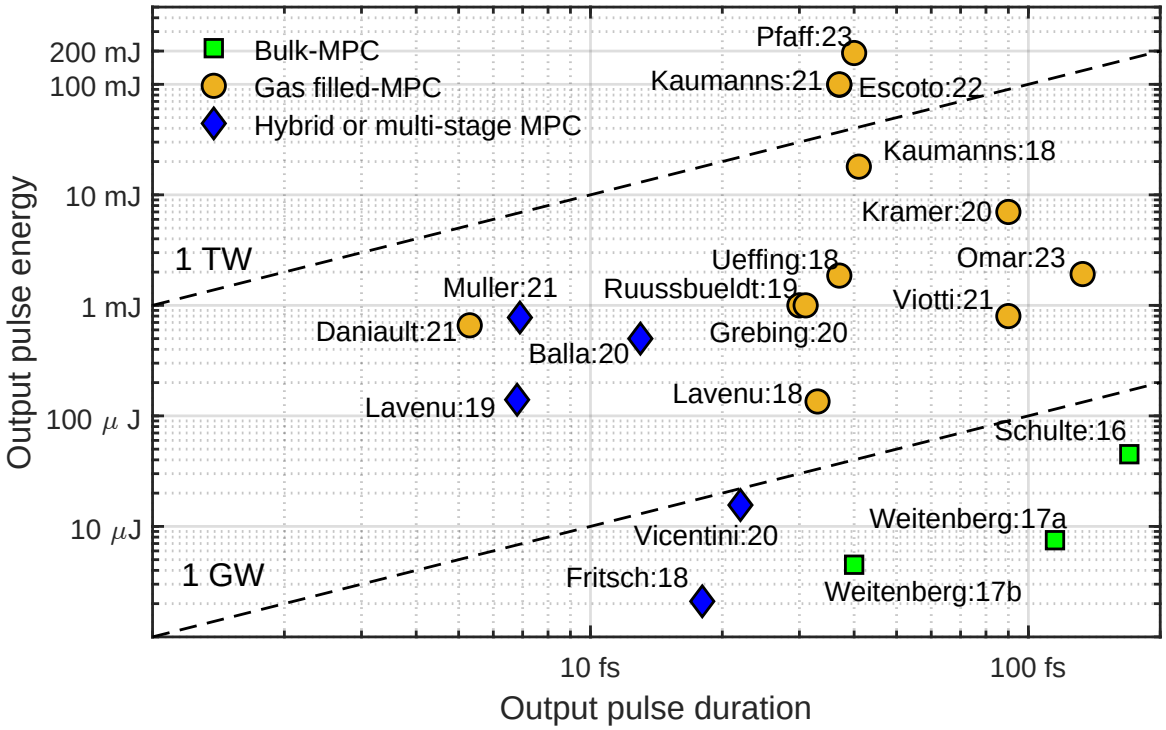

Figure 3.3: A pulse energy-duration diagram highlighting experimental achievements with MPCs. Schulte:16 [130], Weitenberg:17a [134], Weitenberg:17b [148], Ueffing:18 [152], Lavenu:18 [135], Fritsch:18 [154], Kaumanns:18 [136], Lavenu:19 [155], Russbueldt:19 [156], Vicentini [157], Balla:20 [138], Kramer:20 [158], Grebing:20 [141], Viotti:21 [159], Kaumanns:21 [139], Müller:21 [137], Omar:23 [160], Pfaff:23 [140], Daniault:21 [151], and Escoto:22 [142].

An overview, albeit not exhaustive, of experimental post-compression achievements in MPCs up to the present date is depicted in figure 3.3. In the $1-100\,\mu$J range, MPCs are an attractive alternative to gas-filled HCFs as they offer higher throughput, higher tolerance for beam pointing instabilities, simpler design and implementation. The very first implementation of post-compression in MPCs in 2016 [130] used a novel bulk dielectric approach, with concave-convex cavity mirrors oriented such that the fused silica substrates of the cavity mirrors themselves served as the nonlinear medium to induce SPM at each reflection. Schulte *et al.* [130] could compress 400 W - 870 fs pulses to 170 fs with an outstanding efficiency of over 90%. Since then, adhering to the same principle, post-compression experiments in MPC at a low-energy level ($\sim \mu$J) but at high repetition rates (> 1 kHz or

$\sim$MHz) have been performed several times, using one or multiple plates [134, 148, 154]. This work was further expanded with cascading or a series (two or three) of MPCs. For example, Vicentini *et al.* [157] post-compressed 3.1 W - 460 fs pulses at 200 kHz repetition rate using fused silica plates in two cascaded MPCs. Frisch *et al.* [154] expanded this work further by cascading three MPCs to compress 200 fs pulses down to 16 fs, but with an overall throughput of 60%.

Fairly quickly, MPCs were scaled up to mJ-energy level, using gas-filled MPCs, studying a variety of geometrical configurations. This allowed kW-scalable Ytterbium (Yb) based amplifiers [161–163] to efficiently reach a few 10s of femtosecond pulse durations, a regime that has been historically dominated by Ti:Sa lasers. Ueffing *et al.* [152] demonstrated for the first time post-compression of 2 mJ - 200 W - 200 fs pulses from a Yb:YAG laser system in a $4f$-geometry, yielding sub-40 fs pulses with a throughput of over 90%. Soon after several attempts were made to test the average power handling capabilities of MPCs, at 500 W [156], 700 W [158] and even at 1 kW [140, 141]. Energy scaling has also been demonstrated at a 10 mJ level [136], 100 mJ [139, 164] and quite recently, at a 200 mJ-level [140]. However, at a 200 mJ input energy level, the MPC was already 10 m long, filled with 90 mbar of Argon. Energy scaling the setup further in a similar geometry would lead to even larger footprint, making it cumbersome to align.

Omar *et al.* [160] proposed another novel compact design of the MPC using concave-convex cell mirrors, where they could demonstrate post-compression of 200 W - 2 mJ - 670 fs pulses in a compact, 60 cm long, air-filled MPC. This design enables large beam sizes on the cell mirrors and mitigates excessive ionization by avoiding to go through a beam focus. The authors could demonstrate compressibility of the pulses down to 130 fs without any degradation of the spatio-temporal pulse quality. Scaling this setup in a vacuum tight, gas-filled MPC to higher pulse energies ($\sim 100\,\mathrm{mJ}$-level) should help to mitigate ionization and maintain a reasonable overall footprint of the setup.

Over the past few years, significant efforts have been devoted to increase the achievable compression factors and reduce the pulse duration, in an attempt to reach the few-cycle or even the single cycle regime. Fritsch *et al.* [154] used a bulk-plate MPC to compress 100 W - 400 fs pulses by a factor of 22, to 18 fs, corresponding to ≈ 5.3 optical cycles at $\lambda = 1030\,\mathrm{nm}$. Balla *et al.* [138] post-compressed even longer input pulses of 1.2 ps by a factor of more than 90, to 13 fs (≈ 4 optical cycles at $\lambda = 1030\,\mathrm{nm}$) in two stages of gas-filled MPCs. Müller *et al.* [137] also used two stages of gas-filled MPCs equipped with dielectrically-enhanced cavity mirrors on a Silicon substrate that was water-cooled to compress 500 W - 200 fs pulses down to 7 fs, corresponding to nearly two-optical cycles at $\lambda = 1030\,\mathrm{nm}$. A multiple-stage approach was adapted in this case to not only maximize the efficiency but also improve the temporal contrast of the pulses for similar overall broadening factor by using suitable dispersion compensation between the stages [142]. Seidel *et al.* [153] adapted a hybrid approach using multiple plates in an MPC, operating in air to compress 1.2 ps pulses down to 40 fs in a single stage. This approach is however limited to lower input pulse energies due to operation in air but nevertheless suppresses adverse features of single-pass spectral broadening in bulk plates. Due to long input pulse duration ranging from several 100 fs up to 1 ps pulse duration, characteristic of Yb-based systems owing to the narrow emission bandwidth, achieving post-compression to the few-cycle regime necessitates two or more post-compression stages, while the demonstration of the single-cycle regime remains pending. The first stage typically involves highly reflective dielectric

mirrors with high damage threshold but supporting moderate spectral bandwidths corresponding to a few tens of femtoseconds. The second stage typically employs larger bandwidth optics in the cavity but at the expense of lower reflectivity and lower damage threshold, yielding few-cycle pulses. It is worth noting that applications that typically require few-cycle or single-cycle laser pulses also impose other stringent requirements on the pulse properties such as high temporal intensity contrast ratio (in case of laser-solid interactions) and waveform control, which to date remains challenging to reliably extract from Yb-based laser system.

Recently, MPC-based post-compression was extended from Yb-based laser systems to Ti:Sa lasers, with compressibility down to the few-cycle regime in a single stage. Rueda *et al.* [150] compressed $290\,\mu\mathrm{J} - 42\,\mathrm{fs}$ pulses from a readily available commercial Ti:Sa system in a single stage to 8 fs (≈ 3 optical cycles at $\lambda = 800\,\mathrm{nm}$), thereby avoiding the first compression stage altogether. However, the throughput of the system was limited to 45% owing to the losses in the cavity due to the limited reflectivity of enhanced silver-coated cell mirrors. At LOA, we have also demonstrated post-compression of a Ti:Sa system directly to few-cycle regime in MPCs at a mJ-level [151], which is detailed in the following section.

Further advancement towards the single-cycle regime targeting MPCs require precisely dispersion-engineered cell mirrors. This has been exploited for self-compression inside an MPC which enabled the authors to avoid an external compressor altogether [165]. Very recently, Karst *et al.* [166] used dispersion-engineered mirrors inside the cavity itself for spectral broadening, reshaping the nonlinear interaction and resulting in a smooth spectrum and consecutively also improving the pulse quality, to a Strehl ratio of higher than 0.96, while compressing 200 fs from a Yb-based laser system, down to 32 fs. However, a second compression stage will have to be installed with dispersion-engineered cell mirrors in this case to investigate the compressibility to the single cycle regime. It also remains to be seen how the characteristic phase oscillations introduced by broadband dispersion compensating mirrors affect the quality of the post-compressed pulses, and if it is possible to circumvent them. Nevertheless, the flexibility offered by cavity mirror design opens the possibility to engineer pulse compression w.r.t. pulse shape, contrast, compression factors, etc.

So far, MPCs have almost exclusively being used for laser post-compression applications, however, other nonlinear phenomenon are being increasingly investigated. To name a few, introducing negative group velocity dispersion for self-compression [165], supercontinuum generation [167], spectral compression [168], Raman wavelength conversion [169], quasi-phase matched four-wave mixing for wavelength conversion [170], free-space quasi phase-matching in SHG [171], and temporal contrast enhancement using nonlinear ellipse rotation (NER) [164, 172, 173] and cross-polarized wave generation (XPW) [173]. All of the above listed nonlinear effects exploit the additional degrees of freedom by introducing a suitable source of nonlinearity inside the MPC to accordingly tailor the output pulse characteristics. The versatility of the MPCs has paved the way for a myriad of opportunities in the field of ultrafast optics, revolutionizing applications across various disciplines from laser-based machining to attosecond science and beyond.

3.4 Post-compression in multipass cells

Together with Louis Daniault (LOA), Rodrigo Lopez-Martens (LOA), Marc Hanna (LCF), and Jean-Francois Hergott (CEA), I built the first MPC prototype at LOA for post-compression of mJ-level 30 fs pulses from a Ti:Sa laser system. Comprehensive simulation assistance for the experiments, along with the all simulated results presented in this chapter, have been graciously provided by Louis Daniault.

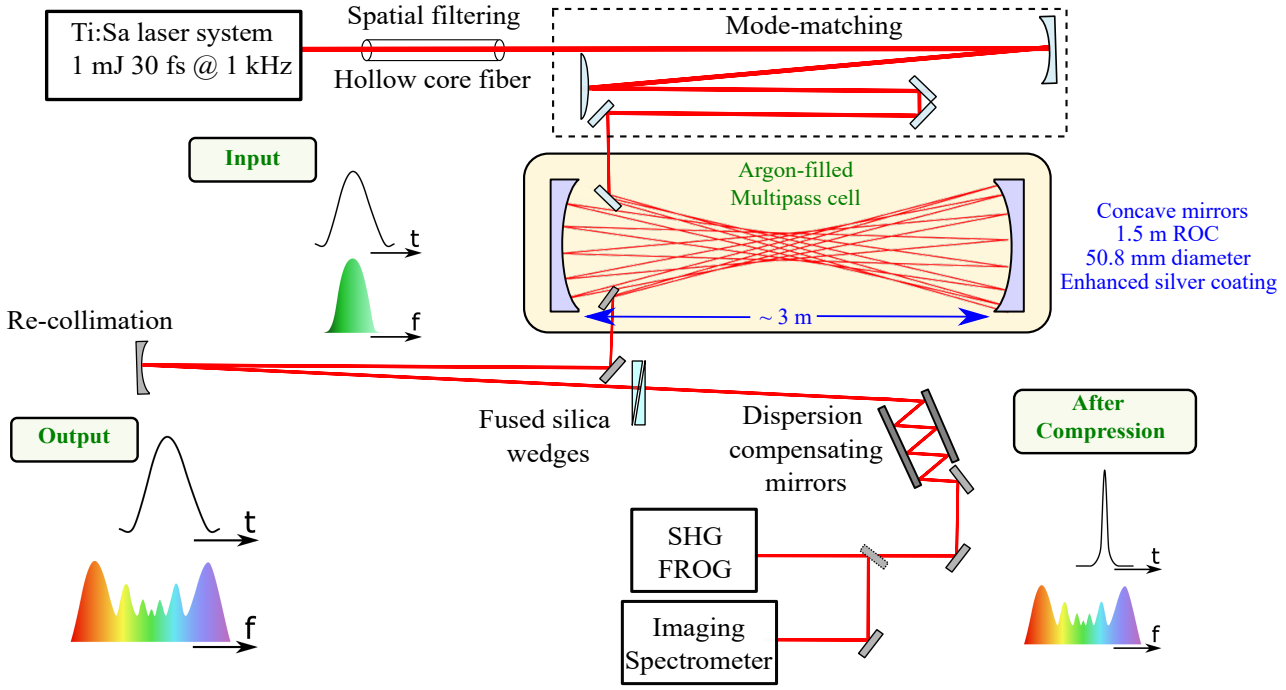

Figure 3.4: A schematic layout of the MPC-based post-compression setup. For clarity, only a few passes in the MPC are represented.

The MPC-based post-compression setup is schematically shown in figure 3.4. A commercial Ti:Sa system (Femtopower, Femtolasers GmbH) was used to seed the MPC, delivering 1.2 mJ - 30 fs pulses at 1 kHz repetition rate. An acousto-optic programmable dispersion filter (Dazzler, Fastlite) integrated in the main amplifier allowed precise control over the pulse spectral phase. To remain on the side of caution for the very first experiments, the amplified beam was spatially-filtered using a 21 cm long $250\ \mu$m inner-core diameter fused silica capillary with a throughput of $\approx 80\%$, making ≈ 1 mJ 30 fs pulses with a near-perfect spatial profile available at the entrance of the MPC.

The Heriott-type MPC consisted of two 50.8 mm diameter enhanced-silver coated mirrors with 1.5 m ROC, separated by $\sim$3 m, yielding a nearly concentric cavity. (3+1)D simulations, i.e. considering (x, y, t and z) were performed to determine the beam size at the waist and on the cell mirrors to nonlinearly match the input beam to the Eigen-mode of the cell. A couple of focusing/diverging optics were used for nonlinear mode-matching, setting the beam size to $480\ \mu$m and 3.1 mm in diameter at the waist and on the mirrors, respectively. This geometry was chosen such that the beam fluence on the mirrors stayed well below their damage threshold, specified to be 100 mJ/cm^2. A small off-axis plane injection mirror coupled the beam into the cavity with each beam pass forming a circular

pattern on the mirror. After the required number of round-trips, the beam is picked off by another small plane off-axis mirror located on the same side as the injection. The 50.8 mm cavity mirror size ensures sufficient distance between the adjacent beam spots on the mirrors and minimizes beam steering losses. The number of passes in the cavity can be varied in even numbers by simply moving the pick-off mirror and can be set to a maximum of 18. Therefore, up to 54 m of propagation length can be folded within an effective 3 m footprint. The MPC itself is operated inside a vacuum-sealed chamber filled with Argon-gas at different pressures. The Dazzler in the main amplifier is used to compensate for dispersion (lenses, windows, air) such that the pulses are FTL in duration at the input of the MPC.

3.4.1 Identification of different propagation regimes

The output spectrum was first studied at different gas pressures for 18 passes through the MPC. The MPC was designed such that at the highest investigated gas pressure of 700 mbar, the input pulse peak power remains at $\approx 30\%$ of the self-focusing critical power. It has been demonstrated that the spatio-spectral homogeneity remains satisfactory even for peak powers above half the critical power [170].

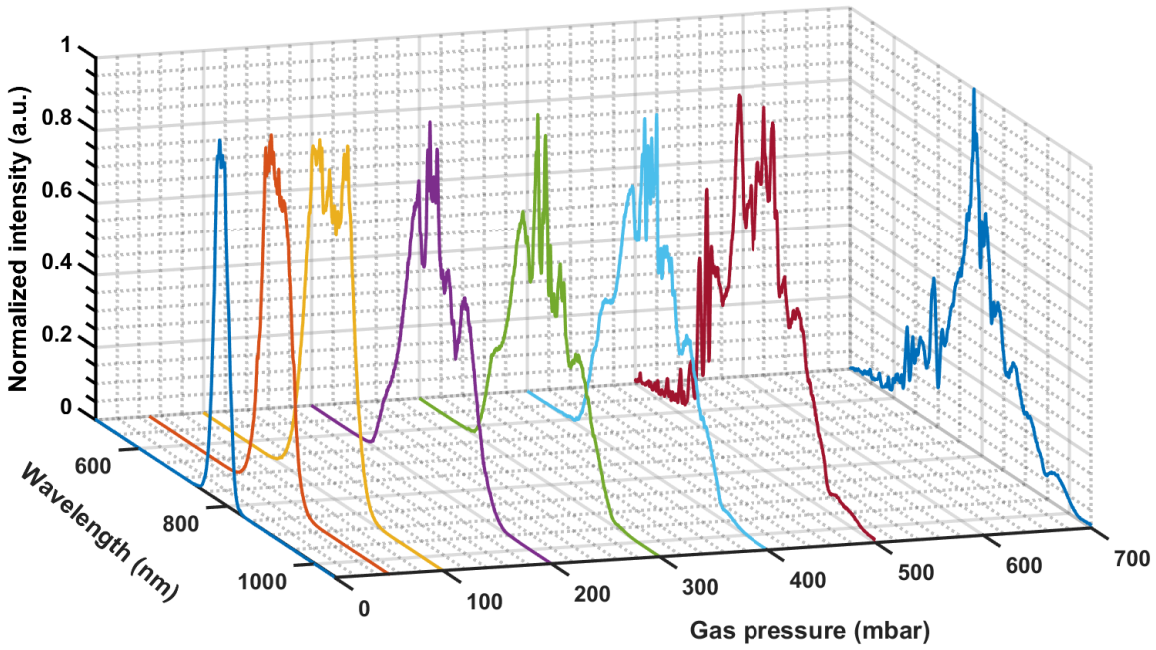

Figure 3.5: Evolution of the normalized spectral shapes with increasing gas pressure in the MPC.

As the pulse propagates in the MPC, the onset of dispersion rapidly decreases the pulse peak power such that the overall self-focusing effects can be simply neglected. Figure 3.5 shows the evolution of output spectral shape obtained for increasing gas pressures, ranging from 0 to 700 mbar and the corresponding RMS spectral widths and FTL pulse durations are shown in figure 3.6. It can be clearly seen that the spectral broadening increases linearly with gas pressure up to ~ 150 mbar, but begins to saturate as the gas pressure is further increased. Gas dispersion is pressure dependent

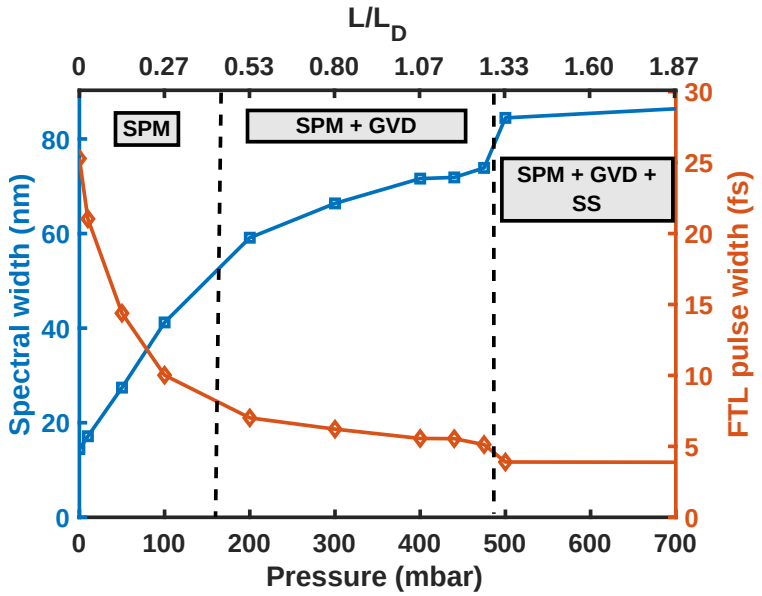

Figure 3.6: Evolution of the RMS spectral and FTL pulse widths with increasing gas pressure in the MPC.

and indeed, plays a crucial role in the broadening process. At lower pressures, pulse propagation in the cell can be considered dispersion free, subjecting all the 18 passes to pure SPM with a constant pulse temporal profile. As a result, the output spectrum broadens linearly and symmetrically with increasing gas pressure in the cell.

Above ~ 150 mbar, the gas dispersion starts to become critical, especially for the last few passes in the MPC, increasing the temporal width of the pulses, and consequently decreasing their peak power, resulting in a saturation of spectral broadening. However, dispersion-assisted spectral broadening leads to much smoother spectral profiles as compared to dispersion-free pure SPM in HCFs where sharp modulations are often seen in the output spectrum [83]. At higher pressures, this effect is further aggravated: gas dispersion effects become significant in the earlier passes in the MPC, and more SPM is accumulated by chirped pulses, favoring the onset of higher-order nonlinear phase, resulting in deteriorated pulse compressibility. Thus, increasing the number of passes at high gas pressures do not necessarily lead to shorter post-compressed pulses.

The interplay between SPM, self-steepening (SS), and gas dispersion induces strong temporal and spectral modulations at excessive gas pressures. In figure 3.5, starting from 475 mbar, the spectral profile exhibits noticeable distortions and a modulated pedestal towards shorter wavelengths. These are clear signs of degradation of output spectral quality and pulse compressibility. The onset of such distortions is very steep when increasing the gas pressure, and shows a tipping point in the pulse spectral quality. It is worth noting that this “tipping point” does not correspond to the critical power above which the beam experiences catastrophic collapse, and the ionization rate of the gas remains sufficiently low to have a noticeable impact under these conditions.

Comprehensive (3+1)D numerical simulations based on the above mentioned experimental conditions were performed by Louis Daniault (LOA). Figure 3.7 shows the simulated on-axis pulse temporal profile after a single pass through the MPC for different gas pressures around this “tipping point”. Sim-

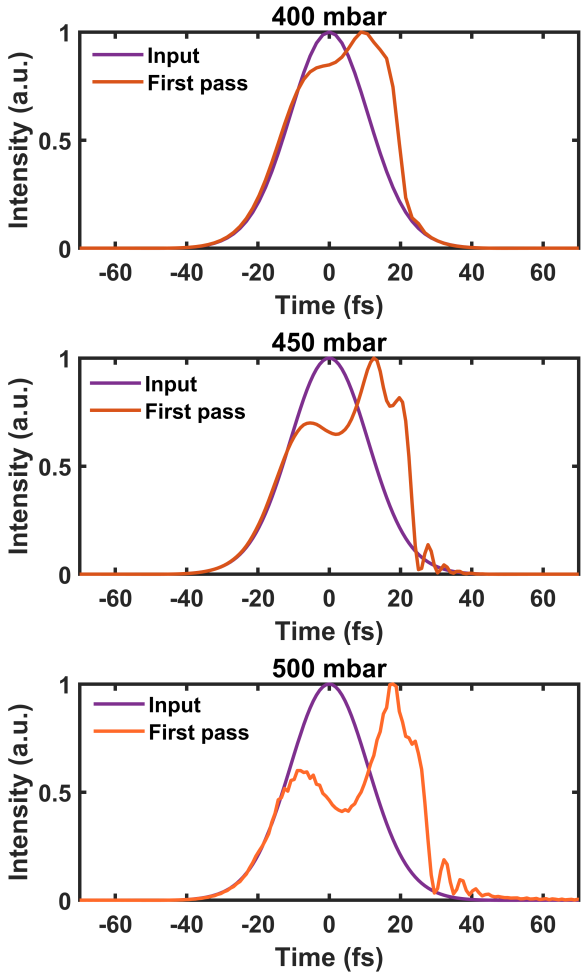

Figure 3.7: Simulated on-axis pulse temporal profile for one pass through the MPC for increasing gas pressure ranging from 400 mbar to 500 mbar.

ulations show the same behavior as observed in the experiments highlighting the impact of excessive SS during the first few passes in the cell. The optical shock of the pulse and the fast modulations of its tailing edge arise quite rapidly at the level of nonlinearity around the “tipping point”, leading to a highly distorted pulse profile. This effect cannot be avoided, for example, by limiting the number of passes since the pulse degradation is most significant in the first pass. Thus, SS imposes a fundamental limit on spectral broadening in the MPCs, regardless of the number of passes and directly depends on: (1) a dimensionless parameter s characterizing the SS, given as, $s = 1/t_0\omega_0$, where t_0 is the FTL input pulse width and ω_0 is the pulse central frequency, and (2) the beam-averaged B-integral accumulated in the first pass. In our experimental conditions, this corresponds to $s \approx 0.02$ and $B \approx 5$ rad.

It should be noted that this behavior is specific to short input pulses (few 10s of femtoseconds), where SS can arise quite rapidly with increasing SPM. Conversely, in the range of 100 fs - 1 ps, the B-integral per pass in the MPC is usually limited to avoid strong spatio-spectral couplings, but SS and gas dispersion have little or no impact. Also, in HCF-based post-compression schemes designed to reach near-single-cycle regime, SS arises rapidly at low B-integrals but can partially compensated by modest ionization [53]. However, this solution is very specific to HCF-based post-compression

and cannot be used in case of MPCs as plasma-induced defocusing effects can disturb the beam caustics throughout the passes.

3.4.2 Results in optimal conditions

The single-stage MPC-based post-compression scheme described above is limited in the acquired B-integral in the first pass by SS and dispersion limits the number of efficient passes. For a particular MPC geometry, the gas pressure and the number of passes in the cell need to be selected carefully, depending on the input pulse energy and duration. Thus, as a trade-off between spectral broadening, pulse compressibility, and MPC transmission efficiency, the number of passes in the MPC was set to 16 and the shortest pulse duration is obtained for 450 mbar of Argon in the cell. In this configuration, the output energy of the MPC is 0.77 mJ compared to 0.98 mJ at its input, yielding a transmission of about 79%. When juxtaposed with the multitude of MPC-based post-compression setups demonstrated previously, typically with throughput exceeding 95% [84], our observed relatively lower cell throughput can be attributed to losses incurred by enhanced-silver coated cell mirrors with a limited reflectivity of 98.5% for each pass over the entire spectral bandwidth. Our reliance on silver mirrors is necessitated by the absence of high-reflectivity dielectric mirrors with near-zero dispersion capable of supporting the nearly-octave-spanning bandwidth of the few-cycle pulses.

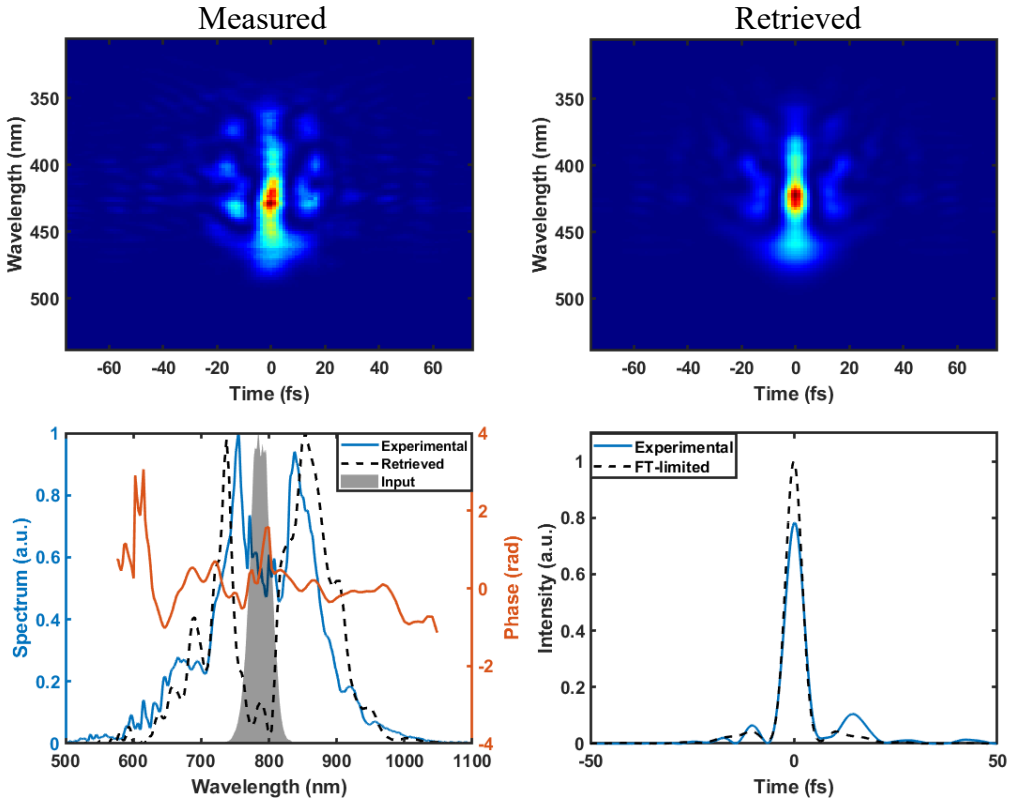

Figure 3.8: Top: measured (left) and retrieved (right) SHG-FROG traces on a 256×256 grid with an error of 11×10^{-3}. Bottom: input, measured, and FROG-retrieved output spectra (left) and pulse temporal profile along with its FTL profile (right).

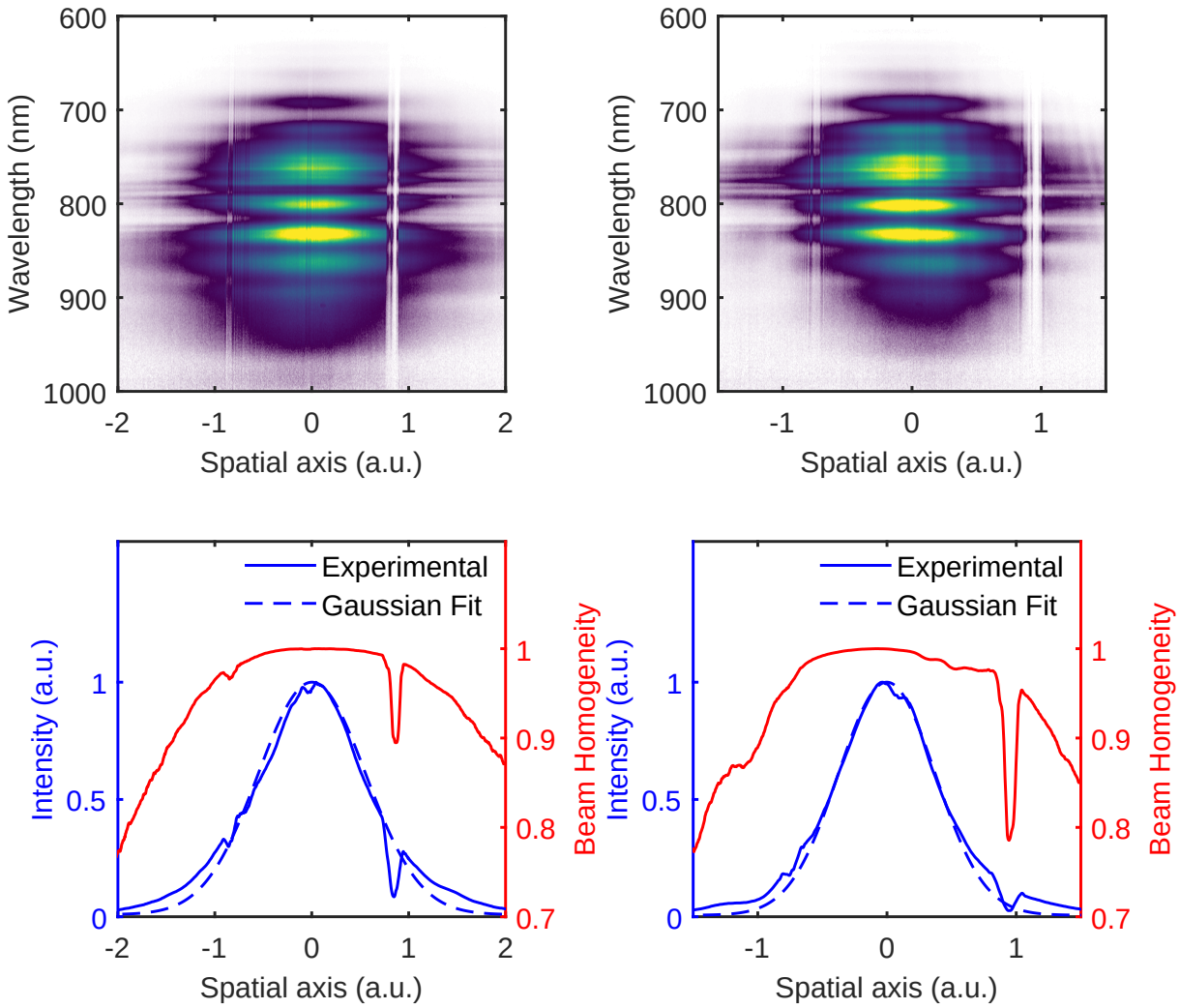

Figure 3.9: (Top) spectrally-resolved beam profile in the horizontal (left) and vertical (right) dimensions and (bottom) output beam profile in arbitrary units in the horizontal (left) and vertical dimensions (right) along with their spectral homogeneity. The sharp dip in the beam profile is due to irremovable dust on the spectrometer slit.

At the output of the MPC, nine pairs of double-angled broadband dispersion compensating mirrors ($-378\,fs^2$ in total, PC42, Ultrafast Innovations), followed by a pair of thin fused silica wedges to compensate for accumulated nonlinear phase and gas dispersion. The compressed pulse energy is measured to be 0.66 mJ including beam transport losses, yielding a 67% overall efficiency for the full post-compression setup. The output spectrum measured using a spectrometer is shown in figure 3.8 along with the one retrieved from by the SHG-FROG device, with an error of 11×10^{-3} on a 256×256 grid. The corresponding measured 5.3 fs pulse intensity profile, to be compared to its FTL duration of 4.7 fs are also presented in figure 3.8. This yields a compression factor of 5.7 and output pulses of ≈ 2 optical cycles at $\lambda = 800\,\text{nm}$. According to the simulations, the beam-averaged B-integral accumulated over 16 passes is $\approx 10\,\text{rad}$. This value is notably higher than the compression factor since in the last few passes in the MPC, chirped pulses experience less spectral broadening for a given B-integral. This configuration is located just before the "tipping point" described above. Higher number of passes and/or higher gas pressure in the cell would lead to worse pulse compressibility, longer output pulse duration with a lower throughput.

Figure 3.9 shows the measured spatio-spectral homogeneity profile in both dimensions, horizontal and vertical. Note that the sharp hole in the beam profile is caused by irremovable dust on the entrance slit of the spectrometer. The overlap of each spectrum $\mathrm{I}(\lambda)$ with the spectrum on-axis $\mathrm{I}_0(\lambda)$ is defined in terms of the V-parameter [134]

$$V = \frac{[\int \sqrt{I(\lambda) I_0(\lambda)} d\lambda]^2}{[\int I(\lambda) d\lambda][\int I_0(\lambda) d\lambda]} \tag{3.10}$$

and is shown in figure 3.9 alongside the beam profile for both dimensions. The output beam exhibits a nearly Gaussian profile with very little degradation and excellent spectral homogeneity, above 99% at the beam FWHM and above 95% at $1/e^2$ in both dimensions.

3.4.3 Summary

Thus, we generated a two-optical-cycle pulses with a Ti:Sa pumped single-stage Argon-filled MPC at a mJ-level, compressing 30 fs - 1 mJ input pulses to 5.3 fs at 0.66 mJ output energy with excellent beam quality and homogeneity. The transmission efficiency of the MPC itself was measured to be 79%, and 67% including the overall post-compression and all the intrinsic losses. The study of the evolution of output spectrum with increasing gas pressure in the cell revealed two major roadblocks to reaching the single-cycle regime: (1) gas dispersion reducing the accumulated B-integral and saturating spectral broadening (nevertheless helps to maintain a smooth spectral shape without significant modulations), and (2) spectral distortion and pulse compressibility deterioration due to SS. Thus, in order to reach the single-cycle regime, we would need careful dispersion management in the cell to partially compensate for the gas dispersion while maintaining a fine balance between SPM and dispersion, and avoiding excessive SS in the first few passes. A complete dispersion-less post-compression scheme would lead to a significant SS and highly unbalanced output spectral shapes. Tailored dispersion throughout the propagation would limit this effect while preserving smooth or weakly modulated spectral shapes. Additionally, the number of passes in the cell need to be re-

stricted to generate the broadest possible spectrum with good temporal compressibility and limited MPC losses.

Furthermore, spatial filtering of the input beam prior to the MPC, although implemented for practical reasons, is not an absolute necessity for achieving compression. In the following sections, the MPC setups discussed are directly seeded without any filtering, while the cavity design is adapted to handle the additional $\approx 20\%$ of available pulse energy.

3.5 Contrast enhancement in multipass cells

In order to reach ultra-high focused intensities in the frame of light-matter interaction experiments [20], most Ti:Sa laser systems rely on some form of nonlinear temporal filtering to suppress the amplified spontaneous emission (ASE) and parasitic pulses surrounding the main pulse peak. Such contrast enhancement techniques include saturable absorbers [174, 175], optical parametric amplifiers [176–178], second harmonic generation [179], plasma mirrors [78, 180], spectrally filtered self-phase modulation (SPM) [181], NER [31–34, 182, 183] and the most widely used XPW [38].

This section details two contrast enhancement techniques: NER and XPW, integrated in an MPC architecture for simultaneous post-compression and temporal contrast enhancement of mJ-energy 30 fs pulses from a Ti:Sa laser system, with compressibility down to the few-cycle duration regime. Comprehensive (3+1)D numerical simulation of the nonlinear process allowed us to accurately reproduced the measured data and pinpoint the role played by the different experimental parameters and find optimized, application-specific configurations for both the techniques.

3.5.1 Nonlinear ellipse rotation

In NER, temporal contrast enhancement is achieved thanks to the intensity-dependent rotation of the polarization ellipse of an ultrashort pulse undergoing nonlinear propagation [28]. Polarizing optics can be used to discriminate the high-intensity pulse peak that experiences nonlinear rotation against the unwanted, unrotated low-intensity ASE pedestal and parasitic side pulses. NER was tested early on for contrast enhancement and spatial mode cleaning in air [33, 34] and in gas-filled hollow fibers [32], the latter having been later shown to enable post-compression down to few-cycle duration with internal conversion efficiencies in the range of 40-55% [184, 185]. Very recently, NER in a gas-filled MPC was first explored through simulations [172] and then experimentally with Yb-lasers both in a gas [164] and in a multi-plate arrangement [153].

NER-MPC setup

A schematic layout of the general MPC-based contrast enhancement setup is shown in figure 3.10. The laser system used in the post-compression experiments described earlier is also employed here but without any spatial filtering. A pair of focusing/diverging optics is used to fulfill the mode-matching conditions for stable MPC operation. A pair of folding mirrors mounted on a translation stage after the telescope is used to tune the position of the beam-waist inside the cell. The MPC geometry remains consistent with the description provided in section 3.4. The MPC is operated in a vacuum-tight

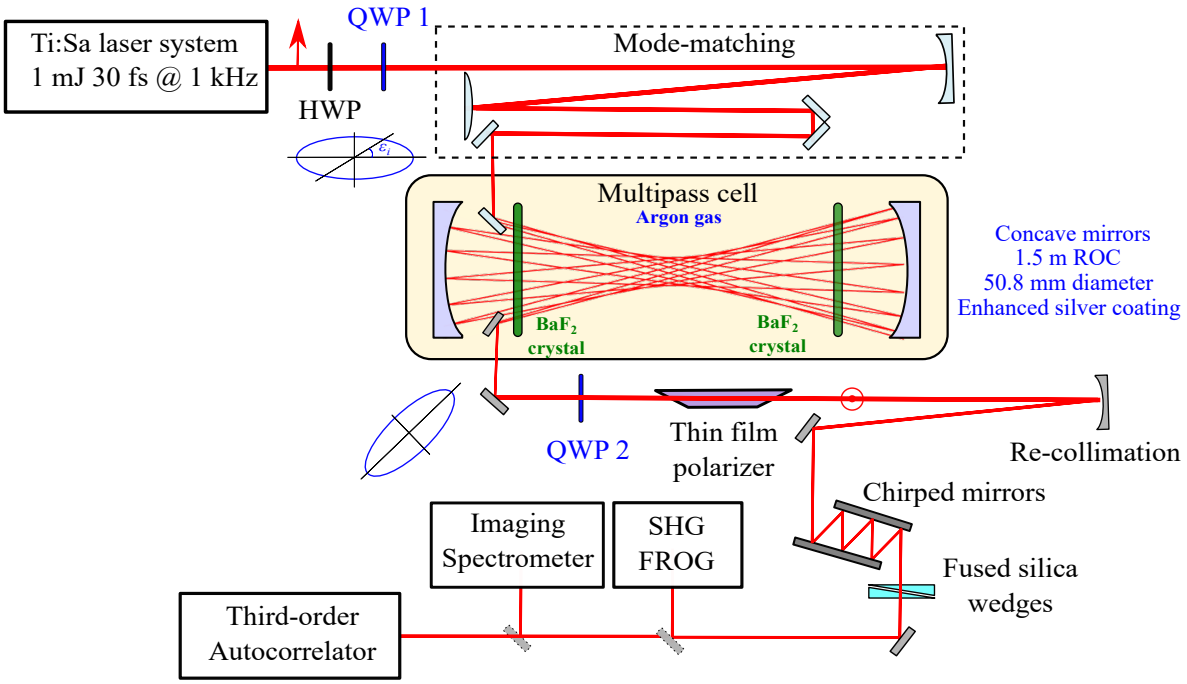

Figure 3.10: Contrast enhancement in MPCs using NER and XPW techniques. Components marked in dark blue and green are used for performing NER and XPW, respectively. For clarity, only a few passes in the cell are represented. HWP: Half-Wave Plate, QWP: Quarter-Wave Plate.

chamber filled with Argon at a controlled pressure. Nonlinear refraction in Argon is taken into account in the simulations to find the appropriate mode-matching conditions and maintain an overall constant beam size on the cavity end-mirrors and at the center of the cavity, which also avoids damaging the optics and minimizes ionization [144, 145]. The beam waist is set to $450\ \mu\mathrm{m}$, corresponding to a 2.9 mm beam diameter on the end-mirrors. The number of passes is set to 12, corresponding to a total propagation length of 36 m.

Elliptical polarization is achieved by inserting a broadband QWP into the collimated beam before entering the mode-matching telescope. A HWP is placed before it to tune the input polarization direction and hence the ellipticity ε_i inside the MPC from 0 (linear) to 1 (circular). Dispersion introduced by the QWP and HWP is pre-compensated with the Dazzler in the main amplifier. A second crossed broadband QWP is used to retrieve linear polarization at the output of the MPC. A low-dispersion broadband thin film polarizer (TFP) (Femtolasers GmbH) with an extinction ratio of 5×10^{-3} filters out the pulse peak rotated by NER at $90°$ with respect to the input polarization, while rejecting the low-intensity unrotated ASE background. Since all the polarizing optics are used are in air, outside the MPC, they do not require precise vacuum compatible motorized mounts and manual continuous rotation mounts with a precision of $0.5°$ or better can be used. The beam size on all the transmissive polarizing optics was $> 10\,\mathrm{mm}$ diameter to avoid any nonlinear effects.

The temporally filtered pulses are then post-compressed using a set of chirped mirrors (up to $-\ 450\ \mathrm{fs}^2$, PC42, Ultrafast Innovations GmbH) and a pair of adjustable thin fused silica wedges. In addition to the previously used diagnostic tools, single-shot SHG-FROG and imaging spectrome-

ter, we also use a high dynamic range third-order cross-correlator (TUNDRA, Ultrafast Innovations GmbH) to detect the ASE pedestal and parasitic pulses over a time window of 200 ps around the main pulse peak.

Maximizing NER efficiency

Internal NER efficiency is defined as the ratio of the energy measured after and before the output polarizer. Maximum NER efficiency is therefore achieved when the polarization ellipse rotates by exactly $90°$, such that transmission through the TFP is maximized. However, the NER angle is time-dependent along the time-varying pulse profile, which leads to a time-dependent transmission through the TFP. Moreover, as the pulses simultaneously experience spectral broadening and chirping through self-phase modulation (SPM), the NER angle also becomes wavelength-dependent, implying that the broadened spectrum is not uniformly transmitted through the polarizer. All these effects combined limit both the energy and the spectral throughput and thus drastically affect post-compression performance.

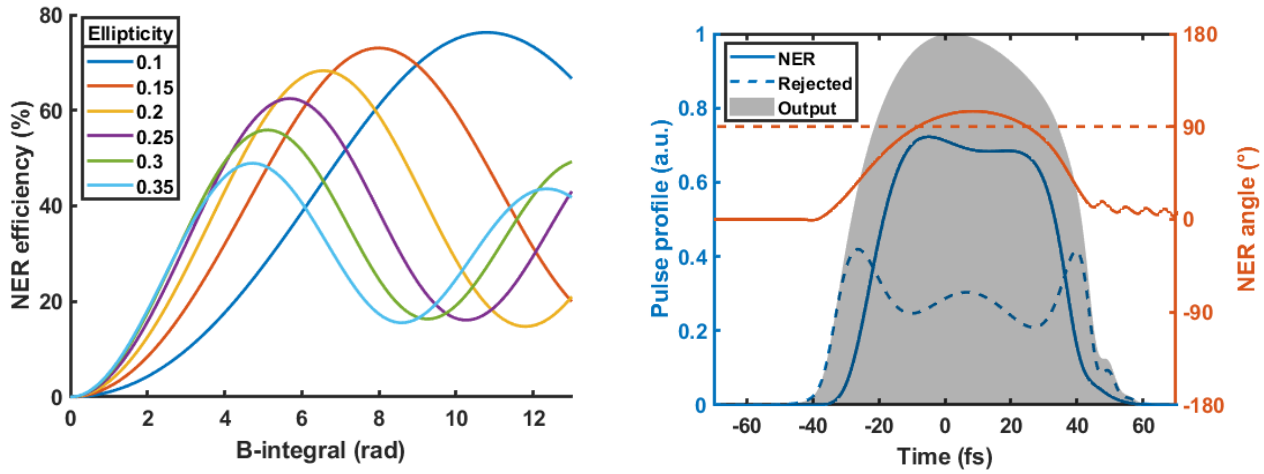

Figure 3.11: Left: Simulated NER efficiency vs. B-integral for various pulse ellipticities. Right: Temporal profile of NER pulse (grayed), transmitted pulse (solid blue) and rejected (dashed blue) pulse by the TFP; time-dependent NER angle (solid red), all simulated for $\varepsilon_i = 0.25$ at maximum efficiency ($B \simeq 6$ rad).

Figure 3.11 (left panel) shows the evolution of internal NER efficiency versus B-integral for different ellipticities, obtained from numerical simulations for a plane-wave 1 mJ, 30 fs pulse propagating in Argon, including SPM, cross-phase modulation (XPM), self-steepening and gas dispersion. One clearly notices that lower ellipticities lead to a reduced spread of NER angles and, when combined with high B-integrals, yield higher throughput. However, our previous work on direct post-compression of 1 mJ 30 fs Ti:Sa pulses in the same MPC configuration showed that the equivalent dispersion-free simulated B-integral cannot be pushed much beyond 6 rad, corresponding to an Argon gas pressure around 400 mbar, where excessive self-steepening effects lead to poor pulse compressibility as seen in section 3.4. In the case of NER, the ellipticity should therefore not be lower than 0.15 and the maximum NER efficiency should not exceed 75%. Fig. 3.11(right panel) shows the simulated time-dependent NER angle during the rise and fall of the pulse along with the transmitted and rejected

pulse profiles for $\varepsilon_i = 0.25$ at maximum efficiency ($B \simeq 6$ rad). The maximum NER angle is above 90°, such that the transmission averaged over the whole pulse profile is maximized.

Evolution of output spectrum with gas pressure

We performed the experiment using $\varepsilon_i = 0.25$ and measured the internal NER efficiency along with the output pulse spectrum for increasing Argon pressures up to 420 mbar, where pulse break-up starts. Figure 3.12 compares the measured data with the results obtained from (3+1)D simulations now including temporal, radial, and polarization dimensions and using measured device losses and the experimental laser pulse spectrum as input. Simulations show excellent agreement with measurements. Experimentally, the spectral bandwidth increases fast at first, then starts flattening out before increasing again around 420 mbar. The effects of pulse break-up can be seen in simulations at higher pressures, with the sudden appearance of wings and deep modulations in the broadened spectrum. The agreement between experiment and simulations is particularly good for the internal NER efficiency versus pressure, which reaches a maximum of 58% at an optimum Argon pressure of $\simeq$ 350 mbar and then rolls off because of the intensity-weighted NER angle exceeding 90°. We now can tune the ellipticity to a lower value, such that the maximum NER efficiency occurs just before pulse break-up around 420 mbar. This should lead to both a higher throughput and a broader spectrum and therefore yield shorter compressed output pulses.

Experimental results at optimum conditions

By setting the Argon pressure to 420 mbar and the pulse ellipticity to $\varepsilon_i = 0.18$, the internal NER efficiency increases from 58% to 69%. The output polarizer is rotated accordingly to preserve the extinction ratio and the output energy drops to 0.49 mJ. Overall efficiency is defined as the ratio of the energy measured after the TFP to the energy measured at the input of the MPC. We obtain an overall NER efficiency of 49%, including losses in the MPC. In this configuration, we obtain, nearly-FTL 5.8 fs pulses (2.2 optical cycles at $\lambda = 800$ nm) as shown in figure 3.13. The reconstructed 5.8 fs pulse profile (solid blue curve) is close to the Fourier-transform-limited profile (FTL, dotted black curve), with a low-intensity pedestal structure limited by the residual phase and spectral modulations introduced by the paired double-angle chirped mirror compressor. The compressor efficiency is measured to be 87%, leading to an overall post-compression efficiency of 43%. Our FROG measurements can produce slightly asymmetric traces, a well-known feature of broadband single-shot 2D acquisition FROG devices, for which slight misalignment can lead to a small virtual pulse front tilt being imprinted onto the measured trace as can be seen in figure 3.13.

Figure 3.14 compares the long-range temporal profiles of input and output pulses measured by the TUNDRA device. The contrast enhancement obtained via NER is at least 3 orders of magnitude, with ASE levels dropping down to $1 : 10^{-11}$ a few ps prior to the pulse peak, and is limited by the extinction ratio of the TFP. The pre-pulse seen at -7.5 ps in the traces for both the input and NER pulses is an inherent artifact of the TUNDRA. The train of post-pulses visible in the NER trace originates from internal reflections within the TFP itself and are not observed when a Glan polarizer is used for extinction. However, the high thickness of a Glan polarizer leads to excessive dispersion and nonlinear effects distorting the output pulse and beam. This is a standard problem encountered in

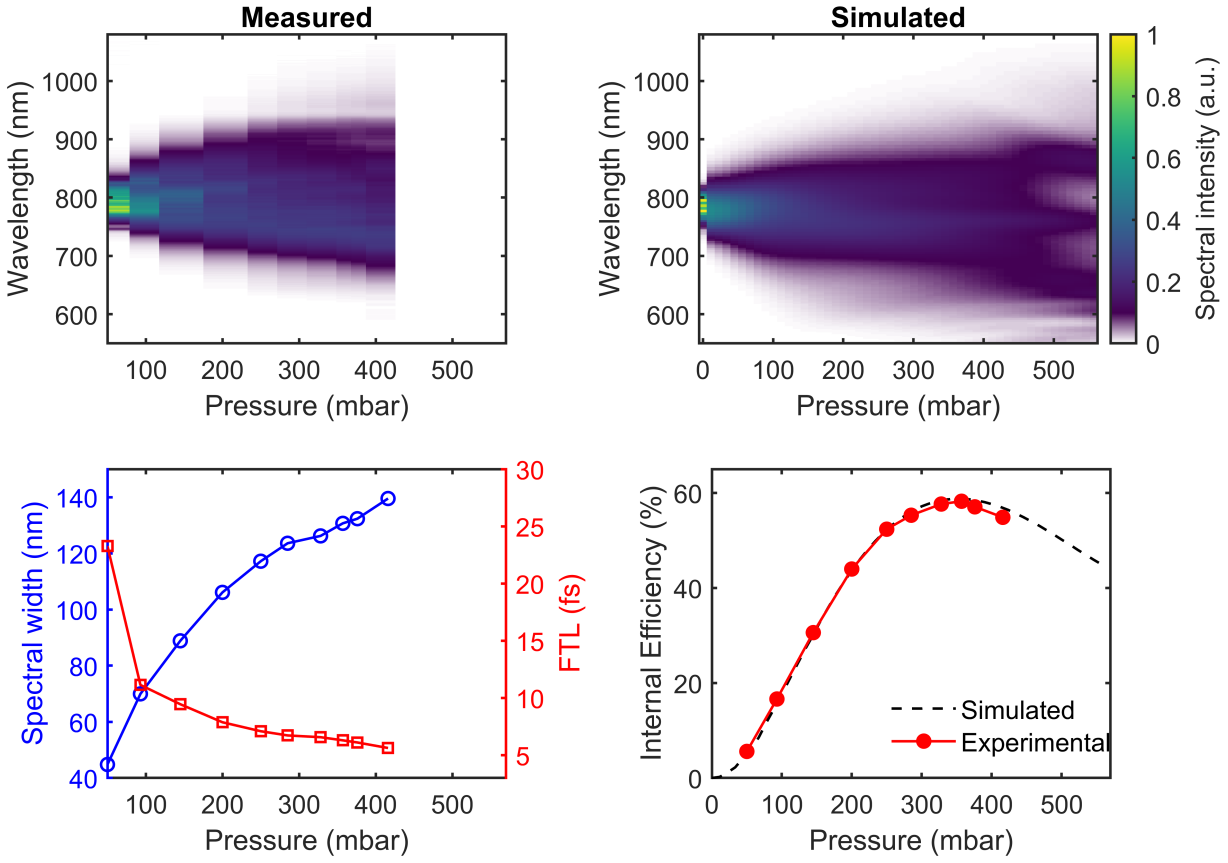

Figure 3.12: Top: evolution of the measured (left) and the simulated (right) transmitted NER spectrum with Argon gas pressure, for $\varepsilon_i = 0.25$. Bottom: variation of the measured spectral width and Fourier-transform-limited (FTL) duration (left) and corresponding experimental NER conversion efficiency with Argon pressure compared to simulated values (right).

all polarization-discrimination based contrast enhancement techniques and the choice of polarizing optics varies according to the targeted application. Finally, the spectrally-resolved beam profile in the horizontal and vertical dimensions and the corresponding V-parameter measured for $\varepsilon_i = 0.18$ are shown in figure 3.15. In both dimensions, the output beam exhibits good spectral homogeneity, $> 98\%$ at FWHM and above $> 85\%$ at $1/e^2$.

These results must be compared to direct post-compression experiments discussed in section 3.4. Under the exact same experimental conditions, albeit with only 16 passes in the MPC, we measured 5.3 fs post-compressed pulses with 67% overall efficiency, dispersive mirror compressor included. The 43% overall transmission measured in the case of NER amply justifies its implementation in an MPC post-compressor as it enables the direct generation of high-contrast few-cycle pulses with moderately higher losses, little compromise on the output pulse duration, and very low added complexity.

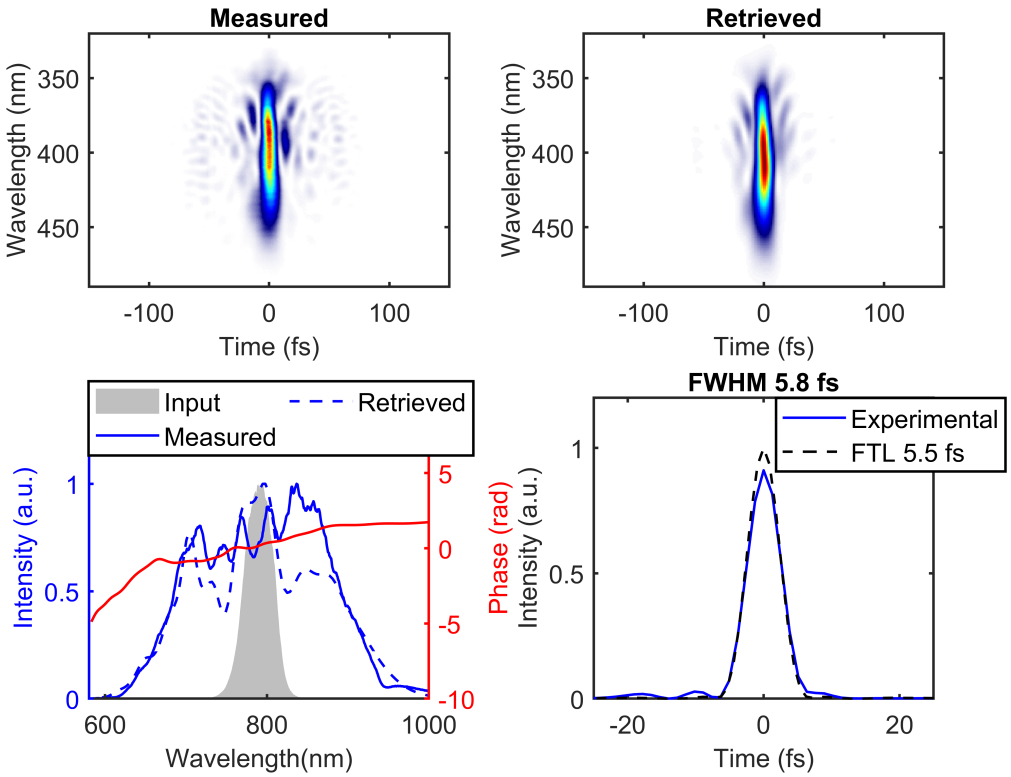

Figure 3.13: Top: measured (left) and retrieved (right) SHG-FROG traces with an error of 72×10^{-4} on a 256×256 grid. Bottom: input and NER spectra (left) and the corresponding temporal profile (right) for $\varepsilon_i = 0.18$.

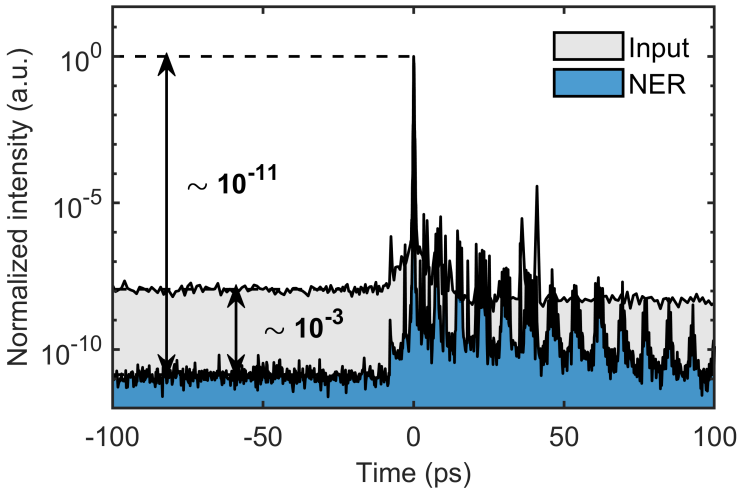

Figure 3.14: Temporal contrast enhancement between input and NER ($\varepsilon_i = 0.18$) pulses measured using a high dynamic range third-order auto-correlator.

3.5.2 Cross-polarized wave generation

XPW generation is a well-established and perhaps the most widely used technique for temporal contrast enhancement in high-energy Ti:Sa lasers. It is a degenerate four-wave mixing process

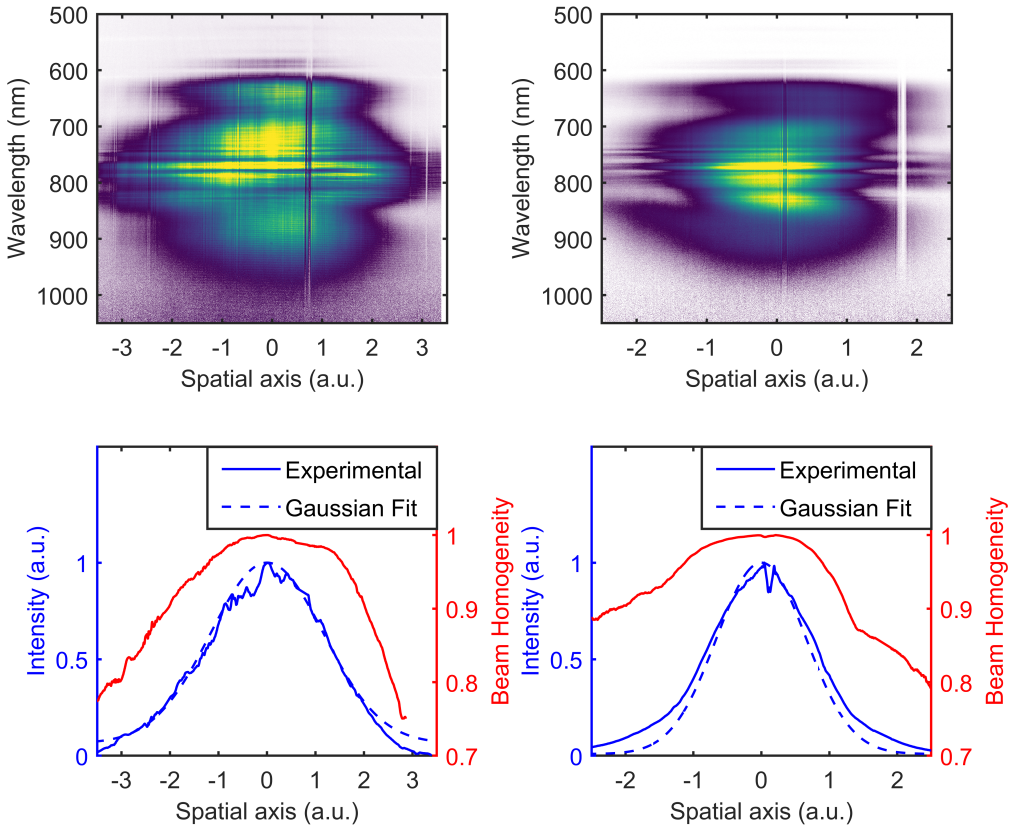

Figure 3.15: (Top) spectrally-resolved beam profile in the horizontal (left) and vertical (right) dimensions and (bottom) output beam profile in arbitrary units in the horizontal (left) and vertical dimensions (right) along with their spectral homogeneity, measured for $\varepsilon_i = 0.18$.

governed by the anisotropy of the real part of the third-order nonlinearity tensor $\chi^{(3)}$. Inside the nonlinear medium, a new orthogonally polarized wave is generated at the same central frequency as the incident wave. Fundamental principle and conventional implementation of this technique are detailed in section 2.1.3. It has been well established that the XPW conversion efficiency depends on the intensity of the pulse incident on the crystal, the thickness of the crystal, the input spatio-temporal pulse quality and its spectral phase [186, 187]. The incident intensity on the XPW crystal is limited by the threshold of white light generation in the crystal (e.g. $\sim 10^{12}$ W/cm^2 for BaF_2 crystals). Using thicker crystals to achieve higher conversion leads to unwanted nonlinear third-order processes that tend to compete with XPW generation, making the XPW beam properties more sensitive to spatial-temporal couplings. The input intensity is also limited by damage due to self-focusing inside the crystal, which tends to reduce its lifetime. So far, the highest demonstrated overall conversion efficiency has been limited to 10-20% using a double thin-crystal configuration [188] and, for mJ energy pulses, some form of spatial filtering or shaping is needed to ensure a smoother or more homogeneous incident spatial beam profile on the crystals [189, 190]. In this section, we discuss the implementation of XPW in the MPC, where the nonlinearity is acquired in small increments and spatially redistributed across the beam for each pass in the MPC.

XPW-MPC setup

The setup for integrating XPW in the MPC is depicted in figure 3.10. Here, no QWPs are needed since the linear polarization direction of the XPW signal can simply be set by the HWP at the MPC input. The chamber is operated under vacuum and two anti-reflection-coated, $600\,\mu$m thick, holographic cut BaF_2 crystals aligned with the same orientation, placed symmetrically with respect to the center of the MPC. This configuration helps to mitigate spatial nonlinear effects and ensures spatio-spectral beam homogeneity. The distance of the crystals from the waist enables the tuning of the nonlinearity for every pass and is set to about 1 m, placing the crystals approximately 50 cm away from the end-mirrors. The chirped mirrors of the output compressor are changed to accommodate the narrower spectral bandwidth typically produced by the XPW process, and to introduce higher dispersion in order to compensate for the total amount of material traversed by the pulses in the BaF_2 plates. The input pulse parameters, output polarizer, and pulse diagnostics all remain the same as for NER.

Nonlinear Mode-matching

In case of XPW, mode matching into the MPC becomes much more complicated. First, for a Gaussian input pulse in space and time, both spatial and temporal pulse profiles of the XPW wave are shortened by a factor of $\sqrt{3}$ because of the cubic nonlinearity. Therefore, both input and XPW beams do not share the same beam-matching conditions and their respective caustics cannot be stabilized together. Moreover, the input pulse peak power is about 5×10^3 times higher than the critical power for self-focusing in BaF_2, under our experimental conditions. Although the BaF_2 plates are thin enough to prevent catastrophic beam collapse, they have to be considered as thin nonlinear lenses that can disturb mode matching and overall propagation in the MPC. Moreover, the repeated energy transfer from the input pulse to the XPW wave leads to changes in the pulse peak power, such that the Kerr lensing experienced through the BaF_2 plates is different for both pulses and for every pass, especially for such high nonlinearity. Material dispersion and reflection losses from the plate surfaces further exacerbate this behavior.

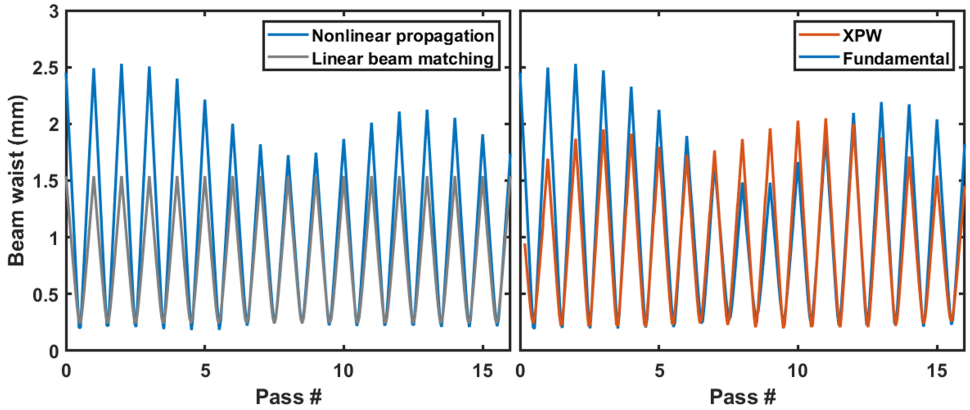

Figure 3.16: Left: Beam caustic of the fundamental wave alone including Kerr lensing in the BaF_2 plates compared to linear mode matching in the MPC. Right: XPW and fundamental beam caustics.

Numerical simulations were performed to determine the best beam matching when including Kerr lensing from the BaF_2 plates. First, it was run for the input fundamental wave alone, while inhibiting

XPW generation. Figure 3.16 shows that the beam caustic of the fundamental wave in the MPC, which is stable for the first few passes and then becomes strongly modulated, illustrating the impact of dispersion on the caustic stability. However, the beam size on the MPC end-mirrors is always larger than that of the linearly matched beam, which excludes any risk of optical damage by design. Excessive ionization at the beam waist, which can occur if the caustic is unstable, is not a concern here as the MPC is operated under vacuum. Second, XPW generation was enabled in the simulation by choosing the proper polarization that maximizes efficiency, as detailed below. The XPW caustic is shown in figure 3.16. It can be seen that the newly created XPW beam in the first BaF_2 plate pass is smaller than the fundamental. As expected, its caustic is highly modulated throughout the MPC, but here again the beam sizes on the mirrors are always larger than in the linear regime. The fundamental beam is more modulated in the presence of XPW generation due to the energy transfer, but the minimum beam size on the mirrors still remains close to that for linear beam matching, thus avoiding optical damages. These simulations show that Kerr lensing in the BaF_2 plates drastically disturbs beam propagation and caustic stability throughout the MPC, but also leads to larger beam sizes on the mirrors, such that the beam fluence systematically remains below the damage threshold of the end-mirrors.

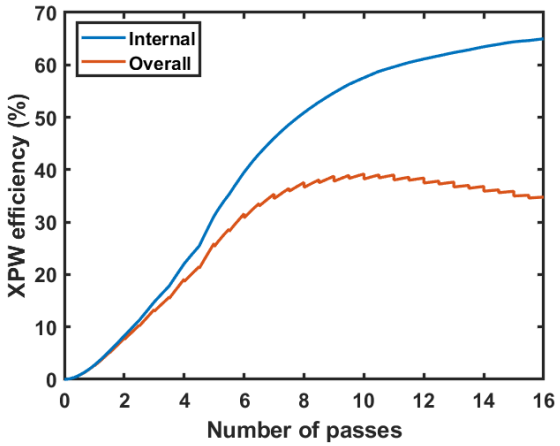

Figure 3.17: Left: Internal (blue) and overall (orange) XPW generation efficiency as a function of number of passes in the MPC.

Experimental results

Figure 3.17 shows the XPW efficiency simulated as a function of the number of passes in the MPC, including reflection losses introduced by the enhanced-silver-coated mirrors ($\sim 1\%$ per bounce) and the BaF_2 crystals ($\sim 3\%$ per MPC pass). The input polarization is set to 64.5° with respect to the optical axes of the BaF_2 crystals, which maximizes XPW conversion efficiency per pass [191]. For 16 passes, the internal XPW efficiency reaches up to 65%, an unprecedented value which cannot be obtained for XPW in free space. This is because the MPC geometry mitigates nonlinear spatial effects and beam distortion, enabling better control over the beam size for every pass and a higher conversion efficiency. However, such a high number of passes through the BaF_2 plates implies higher reflection losses, such that the overall efficiency, calculated as the output XPW power over the input

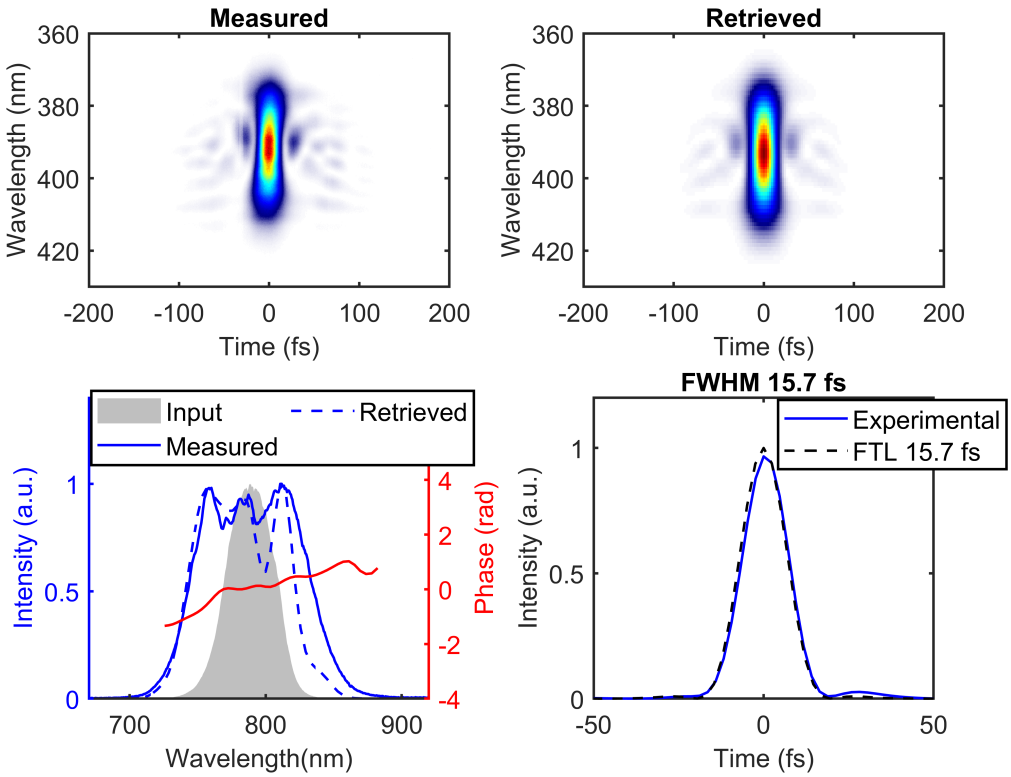

Figure 3.18: Top: measured (left) and retrieved (right) SHG-FROG traces with an error of 46×10^{-4} on a 256×256 grid. Bottom: input and XPW spectra (left) and the corresponding compressed XPW temporal profile (right), for FTL pulses injected into the MPC.

power, rapidly drops. In practice, the number of passes should be limited to 10 passes to maximize the overall efficiency to about 35%, which is still higher than the current state-of-the-art. The beam size is set to $330\ \mu$m at the waist and 4 mm on the end-mirrors in order to fulfill the stability conditions of the MPC. The input pulses are p-polarized and the output TFP is oriented to select the XPW pulses along the orthogonal polarization direction. The XPW pulses are then compressed outside the MPC using a set of chirped mirrors (total dispersion $\simeq -750\ fs^2$, HD58 from Ultrafast Innovations) and a pair of adjustable thin fused silica wedges. By compensating dispersion (entrance window, propagation in air) with the Dazzler in the laser chain, we can inject nearly-FTL 30 fs pulses into the MPC, and obtain $295\ \mu$J total XPW pulse energy, corresponding to 57% internal and 28% overall conversion efficiency, respectively, while taking into account all the losses in the MPC.

The broadened XPW spectrum can be compressed down to 16 fs nearly transform-limited, as shown in figure 3.18. However, as opposed to NER, a fraction of the spectrum in the long-wavelength range measured with the spectrometer could not be retrieved with the FROG. We think that the use of XPW bulk plates in vacuum instead of a gas-filled MPC might play a role and this effect should be investigated further in a dedicated study.

Figure 3.19 shows the spectrally-resolved beam profile measured in both the vertical and horizontal dimensions with the imaging spectrometer, which exhibits a nearly-Gaussian profile in both cases. The homogeneity factor is also shown for both the dimensions in figure 3.19. The beam exhibits excellent spectral homogeneity above 99% at the FWHM and above 95% at $1/e^2$ in both dimensions.

This is a direct advantage of implementing XPW in an MPC, where incremental accumulation of B-integral mitigates spatio-temporal couplings and yields excellent output beam quality.

Figure 3.20 shows the long-range temporal intensity profiles measured with the TUNDRA for both input and XPW pulses. The contrast enhancement is at least 3 orders of magnitude and limited, as for NER, by the polarization extinction capability of the TFP. Several pre-pulses visible before the main pulse peak for both the input and the XPW pulses were confirmed to be inherent artifacts of the TUNDRA. The train of post-pulses visible in the XPW trace originates from the output TFP itself, similar to those observed in the NER measurements.

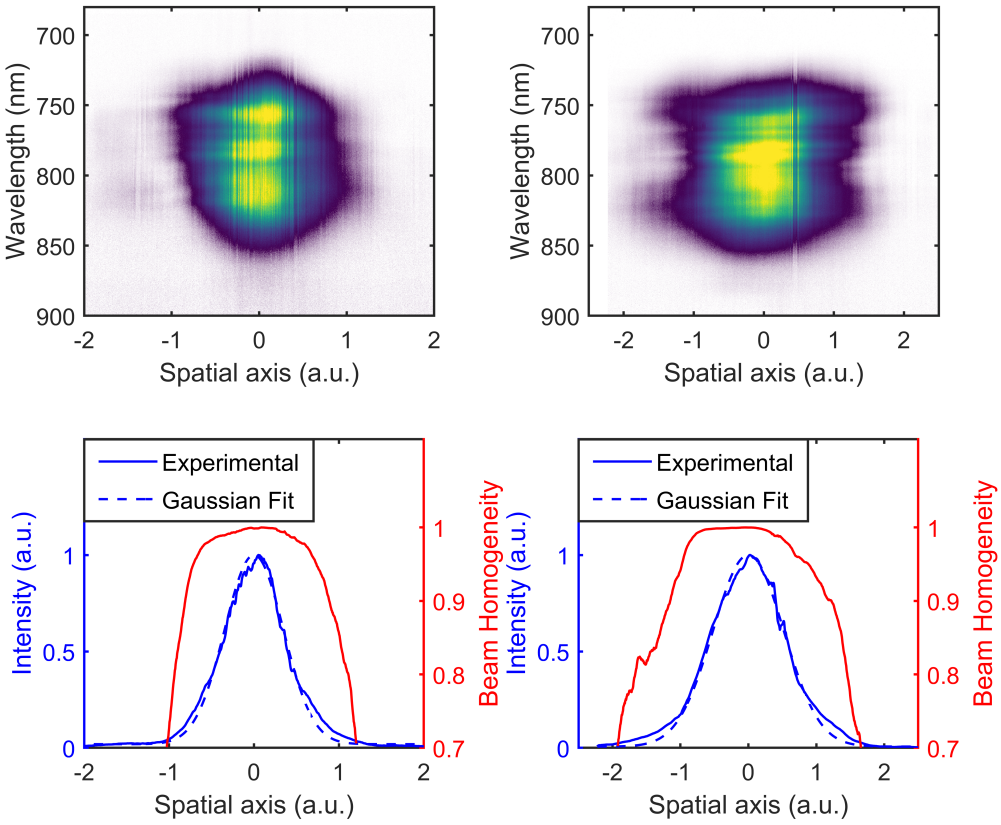

Figure 3.19: Top: measured spatio-spectra traces in horizontal (left) and vertical (right) dimensions; bottom: output beam profile in arbitrary units in horizontal (left) and vertical dimensions (right) along with their spectral homogeneity.

Maximizing XPW efficiency

XPW generation has been shown to be accompanied by significant spatio-temporal reshaping due to interplay between XPM and SPM involving both fundamental and XPW pulses [189, 192]. When an initial -500 fs^2 spectral phase is applied to the input pulses with the Dazzler to globally compensate for the effects of dispersion inside the MPC, the XPW energy increases to 360 μJ, corresponding to 65% internal and 34% overall conversion efficiencies, respectively. To the best of our knowledge, this is the highest conversion efficiency reported so far for XPW generation. However, this increase in conversion efficiency comes at the cost of lower spectral broadening and therefore slightly longer re-

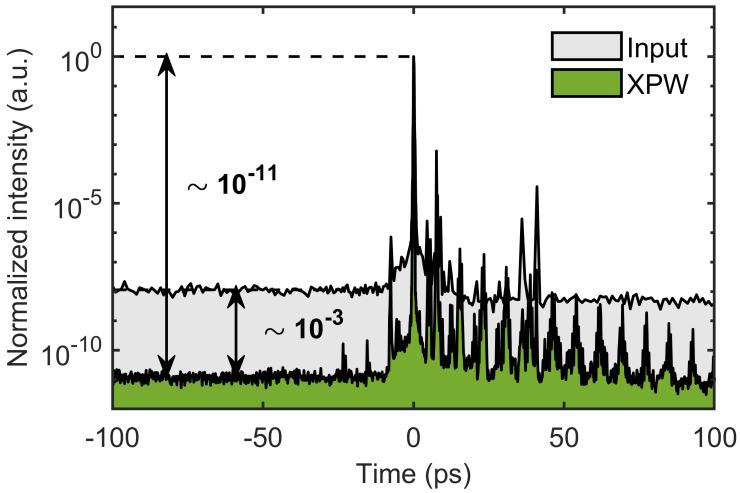

Figure 3.20: Temporal contrast enhancement between fundamental and XPW pulses.

compressed pulses of 20 fs, as shown in figure 3.21. This result is in good agreement with previous studies on the effect of residual chirp on the output spectral behavior [193], where narrower albeit smoother output XPW spectra were observed for negatively chirped input pulses. Finally, spectral homogeneity and contrast enhancement factors similar to the FTL case were measured for negatively chirped input pulses. Overall, the smooth XPW spectrum together with the increased available XPW pulse energy could be particularly useful for efficient seeding of further laser amplification stages in a double chirped pulse amplifier architecture.

3.5.3 Summary

To summarize, we could demonstrate efficient nonlinear temporal compression and cleaning of mJ-energy 30 fs pulses in an MPC using two different third-order nonlinear filtering techniques: XPW and NER. Comprehensive (3+1)D numerical simulations show excellent agreement with the measured data in both cases and enables us to carefully design the MPC architectures so as to obtain the highest conversion efficiencies. In both cases, a contrast enhancement $> 10^3$ could be observed together with near-FTL post-compressed pulse durations.

To the best of my knowledge, this is the first time that XPW has been implemented inside an MPC, exhibiting several advantages over a more conventional free-space setup: (1) record high efficiencies (up to 65% internal and 34% overall), (2) no need for spatial filtering, (3) excellent output beam quality and spectral homogeneity, and (4) relatively higher tolerance to input beam pointing fluctuations. More adapted surface coatings on the nonlinear crystals and cavity end-mirrors should help significantly increase the overall energy throughput and polarization optics with higher extinction ratios could easily increase the contrast enhancement factor ($> 10^3$) by 2-3 orders of magnitude. However, to ensure a stable operation of XPW in an MPC, it is critical to stabilize the caustics due to different mode-matching conditions for the input and the XPW beams. Nevertheless, this approach has the potential to facilitate the designing of efficient and compact devices for spatio-temporal pulse cleaning in high-peak-power laser systems.

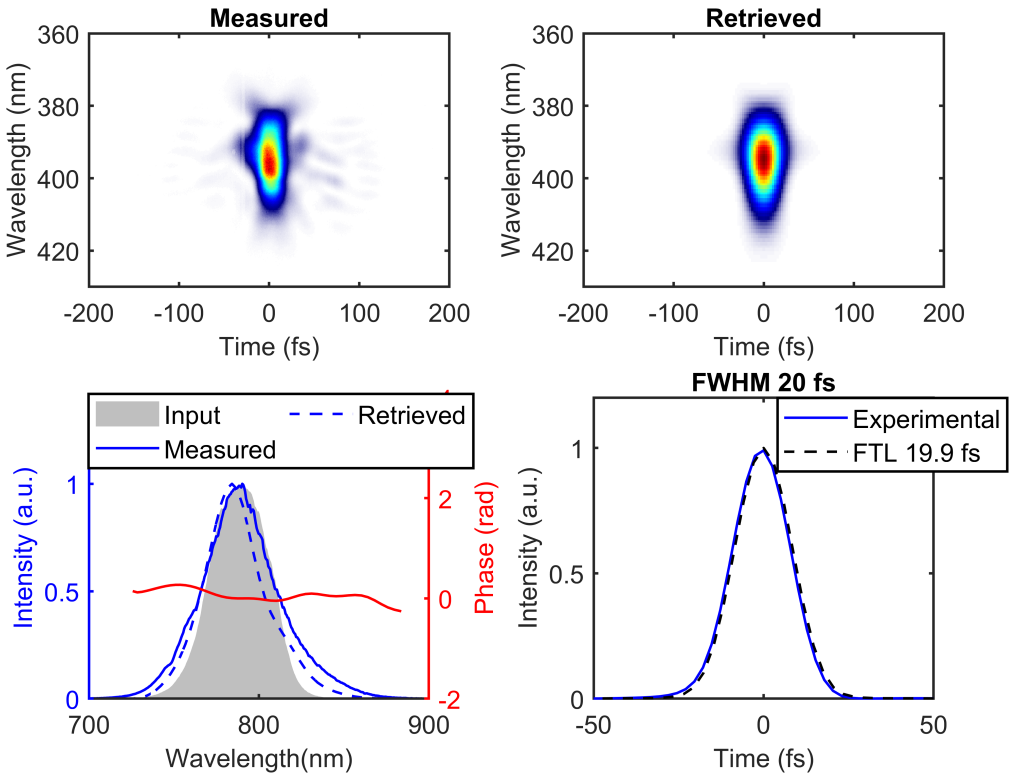

Figure 3.21: Top: measured (left) and retrieved (right) SHG-FROG traces with an error of 65×10^{-4} on a 256×256 grid. Bottom: input and XPW spectral properties (left) and corresponding output XPW temporal profile (right).

To the best of my knowledge, this is also the highest total internal efficiency (up to 69%) reported for NER for 30 fs input pulses. Implementing NER in an MPC architecture with such pulses enables the direct generation of high-contrast few-cycle pulses (< 6 fs) with up to 43% overall efficiency, in a single post-compression stage. The inherent power scalability of MPCs makes this an attractive end-of-chain solution for producing high peak-power few-cycle pulses with high temporal contrast suited to ultra-high intensity laser-matter experiments. Shorter post-compressed pulse duration, down to the single-cycle regime, could in principle be reached using dispersion-engineered coatings, striking a delicate balance between dispersion and self-steepening, to suppress the saturation of Kerr non-linearities, which should enable octave-spanning broadening with high throughput. For this, however, the limitations on pulse compressibility imposed by the residual phase profile of these coatings and ionization remains to be investigated.

3.6 Conclusion

The recent advancements in the MPC technology have greatly enhanced the capabilities of high peak and average power laser systems. As this technique continues to advance, achieving several milestones in laser post-compression, such as high compression factors [138], energy and average power scalability [140], while maintaining excellent output spatio-spectral beam homogeneity [142],

and strong potential for nonlinear spatio-temporal pulse shaping applications [134, 194]. These technological capabilities have opened a wide range of possibilities not only for laser post-compression but also for other nonlinear pulse shaping applications within MPC architectures [84, 195]. Several theoretical studies have provided insights into the nonlinear interaction process and have guided the precise design of the optical systems. Nonlinear mode-matching taking into account the other nonlinear effects that accompany SPM has quickly become a cornerstone for the effective operation of highly nonlinearly driven MPCs [145, 170]. This process is critical as it involves a meticulous setup of initial beam parameters such as waist size, curvature, ensuring beam stability and focus throughout multiple passes within the cell. Other nonlinear effects such as SPM can severely influence the beam caustics, necessitating accurate modeling of nonlinear interactions and precise adjustment of optical design parameters to enhance MPC performance. This ensures leveraging the full potential offered by tailored nonlinear mode-matching for superior control and efficiency.

Thanks to the many practical advantages of MPCs such as discretization of accumulated nonlinearities, versatility, ease to align, robustness against beam pointing fluctuations, their application has expanded from Yb-based laser systems to Ti:Sa systems [150, 151, 173], with the goal of reaching highest peak powers while maintaining the spatio-temporal beam quality. This expansion aims to achieve the highest peak powers while maintaining excellent spatio-temporal beam quality [150, 151, 173]. In this chapter, we demonstrated direct post-compression of mJ-energy level, nearly-FTL 30 fs laser pulses from a Ti:Sa laser system at 1 kHz repetition rate, in an Argon-filled MPC. Additionally, we successfully integrated two third-order nonlinear techniques for laser-contrast enhancement: NER and XPW. A comparison of the performances achieved with each of these these setups is presented in Table 3.1.

Parameters	**Direct post-compression**	**NER-MPC**	**XPW-MPC**
Non-linear medium	Argon gas	Argon gas	Two z-cut, $600\ \mu$m thick BaF_2 crystals
MPC transmission	79%	69% (internal efficiency)	65% (internal efficiency)
Overall post-compression efficiency	67%	43%	64%
Output pulse duration	5.3 fs	5.8 fs	≥ 15.7 fs
No. of optical cycles	2 ($\lambda = 800\,$nm)	2.2 ($\lambda = 800\,$nm)	$\approx 6-8$ ($\lambda = 800\,$nm)
Contrast enhancement	~ 10	$> 10^3$	$> 10^3$

Table 3.1: A comparison of performances obtained from direct post-compression of pulses and contrast enhancement techniques within MPC architectures.

The overall efficiency achieved in direct post-compression experiments is notably high for a few-cycle system, especially in comparison to its HCF-based counterparts, which typically exhibit lower efficiency due to guiding losses. Two primary challenges have been identified in reaching the single-cycle regime: gas dispersion, which limits spectral broadening, and excessive SS, which degrades the pulse quality. These challenges necessitate a nuanced approach to dispersion management in the cell, in order to carefully balance SPM and dispersion, to ensure broad, smoothly shaped spectral shape at the output.

In case of contrast enhancement in MPCs, both the NER and the XPW techniques offer unique advantages and can be easily adapted to suit the specific requirements of the targeted application. Although stabilization of the beam caustics is tricky in case XPW-MPC due to different mode-matching conditions for the input and the XPW beams but it also offers tremendous benefits over free space implementation and warrants further exploration of XPW in MPC architectures. There is further scope for improvement and to minimize the losses in the MPC by: (1) using dispersion engineered highly-reflective coatings for the cell mirrors to avoid saturation of XPW generation in the last few passes in the MPC, (2) improvement of the AR coatings on the BaF2 plates. Depending on the targeted application, this technique can be easily adapted for both “intra-chain” and “end-of-chain” use.

The NER-MPCs offer simultaneous post-compression and contrast enhancement, reaching the few-cycle regime. Such a scheme is more suited for an “end-of-chain” solution. This technique is not best suited for intra-chain use as it yields high spectral broadening which can be problematic for next amplification stages. The overall transmission is comparable to direct post-compression experiments that amply justifies its implementation in an MPC post-compressor as it enables the direct generation of high-contrast few-cycle pulses with moderately higher losses, little compromise on the output pulse duration and very low added complexity. Additionally, single-cycle regime should be accessible with high throughput using dispersion engineered mirror coatings to suppress the saturation of Kerr nonlinearities, while balancing dispersion and self-steepening effects in the cell.

Looking ahead, the prospects for MPC technologies are promising, with potential developments in designing compact devices for spatio-temporal pulse tailoring. Continued research into dispersion-engineered coatings and ionization effects is warranted to enable even shorter post-compressed pulse durations, approaching the single-cycle regime. These future developments will not only enhance the technical capabilities of MPCs but also broaden their practical applications in scientific research and industrial innovation.

Chapter 4

Laser-Plasma interactions: Physical mechanisms

"*I am one with the Force, and the Force is with me.*"

Outline

4.1 Generation of plasmas: Ionization mechanisms 101
4.2 Plasmas: key parameters 104
4.3 Pre-plasma expansion 105
4.4 Ponderomotive force 106
4.5 Laser absorption in plasmas 107
4.6 What is a plasma mirror? 109
4.7 High-harmonic response of plasma mirrors 110
4.7.1 Sub-relativistic regime 110
4.7.2 Relativistic regime 112
4.8 Electron acceleration mechanisms 114
4.8.1 Vacuum laser acceleration 115
4.8.2 Laser wakefield acceleration 117
4.9 Ion acceleration mechanisms 118

4.1 Generation of plasmas: Ionization mechanisms

"Plasma" is the fourth state of matter, often defined as a quasi-neutral gas of charged particles exhibiting collective behavior. When the electromagnetic field of an intense laser pulse interacts with matter (in the form of gas, liquid or solid), it can strip electrons bound to the nuclei, thereby creating ions and free electrons or in other words, a plasma. At $\lambda = 800\,\mathrm{nm}$, the energy of a single photon is $\approx 1.5\,\mathrm{eV}$. Figure 4.1 illustrates some of the "field ionization mechanisms" [196], which are briefly described below.

- **Multi-Photon Ionization (MPI):** In cases where the single-photon energy is less than the ionization potential, electrons can instantaneously absorb the minimum required number of photons for ionization, transiting through a series of short-lived virtual energy states. The theoretical foundation for two-photon ionization was laid by Göppert-Mayer in 1931 [197]. However, since the cross-section of this transition is small, it requires intense sources ($\geq 10^{12}\,\mathrm{W/cm^2}$) that were not available at the time. It was not until the early 1950s that two-photon transitions could be experimentally observed. MPI was formally introduced by Pierre Agostini in 1968 [198].

- **Tunnel Ionization:** In this mechanism, the electrons are ionized by tunneling through the Coulomb barrier which is lowered in the presence of strong laser electric fields. Tunnel ionization strongly depends on the laser electric field as well its central wavelength. The duration of one optical cycle of the laser electric field should be much longer than the time a classical electron with a kinetic energy equal to the binding energy takes to tunnel through the barrier potential. This idea was first introduced by Keldysh and Perelomov [199, 200] in the late 1960s. Additionally, Keldysh introduced the "Keldysh parameter" γ_K, such that if $\gamma_K = \omega_L\sqrt{2E_{ion}/I_L} < 1$ tunnel ionization would dominate [201], where E_{ion} is the ionization potential of the ion.

- **Barrier-Suppression Ionization (BSI):** At high laser intensities when the laser electric field is strong enough to completely suppress the Coulomb barrier for the electron can simply escape classically. The intensity threshold to observe BSI is given as

$$\begin{aligned} I_{BSI} &= \frac{\pi^2 c \varepsilon_0^3 E_{ion}^4}{2e^6 Z^{*2}} \\ &= 4 \times 10^9 \frac{E_{ion}^4 [\text{eV}]}{Z^{*2}} \ [\text{W/cm}^2] \end{aligned} \tag{4.1}$$

Here, Z^* is the degree of ionization. In terms of Keldysh parameter, BSI becomes dominant for $\gamma_K \ll 1$.

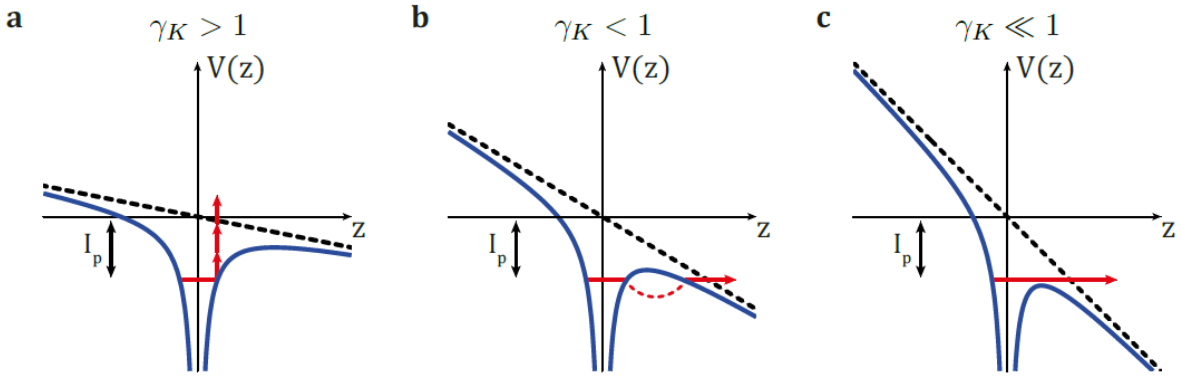

Figure 4.1: Different mechanisms to ionize an atom under the effect of a laser field: Multiphoton ionization (a), tunnel ionization (b), and barrier suppression ionization (c). Reprinted from [202].

Thus, the dominant ionization mechanism depends on the laser intensity, pulse central wavelength, but also on the target material. In our case, we are interested in ionization of fused silica targets, i.e. SiO_2 in amorphous phase, ionized by laser pulses focused down to intensities ranging from 10^{14} to 10^{19} W/cm^2. A fully ionized SiO_2 means 30 electrons per SiO_2 (2.21×10^{22} SiO_2 molecules per cm^3), yielding a peak plasma density of

$$\begin{aligned} n_e &= 30 \times 2.21 \times 10^{22} \ \text{cm}^{-3} \\ &= 6.63 \times 10^{33} \ \text{cm}^{-3} \\ &= 330 \ n_c \end{aligned} \tag{4.2}$$

where n_c is the critical plasma density. In our case, the pulses are relativistic and most of the ionization is attributed to BSI. After the plasma is initiated by BSI, the pulse only interacts with the plasma skin depth δ_D which is significantly shorter than pulse central wavelength, λ_0 for a strongly over-dense plasma. Tables 4.1 and 4.2 list an estimate of ionization energies and corresponding BSI intensities for various ionization states of Silicon and Oxygen respectively, calculated using equation 4.1.

In our relativistic plasma mirror experiments, the Main-pulse intensities range between $\sim 10^{18} - 10^{19}$ W/cm^2. For a peak laser intensity, $I_0 = 1.0 \times 10^{19}$ W/cm^2, assuming that only field ionization mechanisms are present, we can expect to ionize until Si^{12+} and O^{7+}, i.e. 26 electrons per SiO_2,

Ionization	E_{ion} (eV)	I_{IBS} (W/cm^2)
$Si \rightarrow Si^{+}$	8.15	1.8×10^{13}
$Si^{+} \rightarrow Si^{2+}$	16.3	7.0×10^{13}
$Si^{2+} \rightarrow Si^{3+}$	33.5	5.6×10^{14}
$Si^{3+} \rightarrow Si^{4+}$	45.1	1.0×10^{15}
$Si^{4+} \rightarrow Si^{5+}$	167	1.2×10^{17}
$Si^{5+} \rightarrow Si^{6+}$	205	2.0×10^{17}
$Si^{6+} \rightarrow Si^{7+}$	247	3×10^{17}
$Si^{7+} \rightarrow Si^{8+}$	304	5.3×10^{17}
$Si^{8+} \rightarrow Si^{9+}$	351	7.5×10^{17}
$Si^{9+} \rightarrow Si^{10+}$	401	1.0×10^{18}
$Si^{10+} \rightarrow Si^{11+}$	476	1.7×10^{18}
$Si^{11+} \rightarrow Si^{12+}$	523	2.1×10^{18}
$Si^{12+} \rightarrow Si^{13+}$	2440	8.4×10^{20}
$Si^{13+} \rightarrow Si^{14+}$	2670	1.0×10^{21}

Table 4.1: Ionization energies and corresponding BSI intensities for various degrees of ionization of Silicon.

Ionization	E_{ion} (eV)	I_{IBS} (W/cm^2)
$O \rightarrow O^{+}$	13.6	1.4×10^{14}
$O^{+} \rightarrow O^{2+}$	35.1	1.0×10^{15}
$O^{2+} \rightarrow O^{3+}$	54.9	4.0×10^{15}
$O^{3+} \rightarrow O^{4+}$	77.4	9.0×10^{15}
$O^{4+} \rightarrow O^{5+}$	114	2.7×10^{16}
$O^{5+} \rightarrow O^{6+}$	138	4.0×10^{16}
$O^{6+} \rightarrow O^{7+}$	739	2.4×10^{19}
$O^{7+} \rightarrow O^{8+}$	871	3.6×10^{19}

Table 4.2: Ionization energies and corresponding BSI intensities for various degrees of ionization of Oxygen.

yielding a peak plasma density of $n_e = 26 \times 2.21 \times 10^{22}\,\mathrm{cm}^{-3} = 290 n_c$. For an order of magnitude lower intensities, $I_p = 1.0 \times 10^{18}\,\mathrm{W/cm}^2$, we expect to ionize until Si^{10+} and O^{6+}, i.e. 16 electrons per SiO_2, corresponding to $n_e = 16 \times 2.21 \times 10^{22} = 3.5 \times 10^{23}\,\mathrm{W/cm}^2 = 175 n_c$. In our case, the plasma is initiated

by a Prepulse, typically focused down to $\sim 10^{15}\,\mathrm{W/cm^2}$. Carrying out a similar computation for the Prepulse intensities, we get 8 electrons per SiO_2, corresponding to peak electron density, $n_e = 90 n_c$.

Additionally, higher ion charge states can also be produced by collisions with fast electrons with energies $E_k > 2.5\,\mathrm{keV}$ in the plasma bulk. This renders the estimation of plasma ionization state not so straightforward.

4.2 Plasmas: key parameters

Each term in the definition of a plasma: "*a quasi-neutral gas of charged particles exhibiting collective behavior*," highlights a key aspect of plasmas. *Quasi-neutrality* means that for a plasma in equilibrium, the overall charge density is conserved, i.e. $n_e = Z^* n_i$, where n_i is the ion density. Plasma exhibits *collective behavior* due to interaction between the charged particles. Any local pocket of charge concentration in a plasma (for example due to external fields), will give rise to an electrostatic field within the plasma leading to motion of charges that gives rise to a current density which in turn induces a magnetic field. Thus, plasma dynamics are collectively governed by the microscopic fields. A more complete and advanced study of plasmas can be found in textbooks [196, 203–205] and review papers [206, 207]. In this section I will define some of the key parameters which are critical for a quantitative understanding of plasmas, that will be used throughout this manuscript.

Debye Length: It is a fundamental property of nearly all plasmas of interest that are isothermal and follow an exponential density decay (detailed in section 4.3). The Debye length is defined as the characteristic distance over which the electrostatic field from a test charge particle is effectively shielded by the other charged particles in the plasma. The Debye length expression for a quasi-neutral cold plasma can be quickly derived using the Poisson equation and the Boltzmann distribution as [203]

$$\lambda_D = \sqrt{\frac{\varepsilon_0 k_B T_e}{n_e e^2}} \tag{4.3}$$

Plasma frequency: The collective motion of the plasma electrons after perturbation due of an external field is characterized by an oscillation frequency, called the plasma frequency ω_p, defined as [203]

$$\omega_p = \sqrt{\frac{n_e e^2}{m_e \varepsilon_0}} \tag{4.4}$$

Critical density: It is defined as the electron density at which the laser frequency matches the plasma frequency,

$$\begin{aligned} \omega_p = \omega_L &= \sqrt{\frac{n_c e^2}{m_e \varepsilon_0}} \\ \implies n_c &= \sqrt{\frac{m_e \varepsilon_0}{e^2}}\,\omega_L^2 \end{aligned} \tag{4.5}$$

When the electron density exceeds the critical density, $n_e > n_c$, the plasma is said to be over-dense, while $n_e \leq n_c$ for an under-dense plasma.

4.3 Pre-plasma expansion

In *Salle Noire*, we use a time-delayed "Prepulse", $\approx 100\,\mu\mathrm{J}$ energy, 28 fs pulses chirped to ≈ 200 fs (due to transmissive optics in the beam path), focused down to a $\approx 10\,\mu\mathrm{m}$ (at FWHM) spot, reaching intensities $\sim 10^{14} - 10^{15}\,\mathrm{W/cm^2}$ to ionize and heat the target, thereby creating an over-dense plasma with a temperature up to $\approx 100\,\mathrm{eV}$. Owing to the pressure difference, the plasma quickly expands towards vacuum. At a controlled delay after the plasma initiation, the Main-pulse is focused onto the expanding plasma for relativistic laser-plasma interactions. It is well known that the plasma density profile is a crucial parameter in laser-plasma experiments, requiring not only meticulous control but also a through study [69].

The pre-plasma expansion is typically modeled by an isothermal model or a 1D two-fluid model [203, 208], with the following assumptions:

- The plasma consists of ions of charge Ze and electronic charge $-e$. The law of quasi-neutrality is maintained at all times
- There are no external fields. The only field considered is the electric field due to the charge separation in the plasma, $\vec{E} = -\partial V/\partial x$
- The plasma is collisionless
- The ion fluid is cold i.e. $T_{ion} = 0\,\mathrm{K}$
- Electron fluid is assumed to be isothermal with a temperature T_e
- Let $x = 0$ be at the target surface and $x > 0$ is along the target normal direction. At $t = 0$, i.e. before the plasma is initiated, ion density is given as

$$n_i = \begin{cases} n_{i0} & \text{for } x \leq 0 \\ 0 & \text{for } x > 0 \end{cases} \tag{4.6}$$

At $t > 0$, the plasma expands towards vacuum through ion motion. Since the timescale of ion motion is much longer than the timescale at which electrons move, it is reasonable to assume that the electron fluid is at a thermal equilibrium at all times. Thus, we can say that the electron density follows a Boltzmann distribution, given as

$$n_e = n_0 \exp\left(\frac{eV}{k_B T_e}\right) \tag{4.7}$$

Here, $n_0 = Z n_{i0}$ is the electron density in the unperturbed region of the plasma i.e. where $x \to -\infty$; and k_B is the Boltzmann constant. Keeping these assumptions in mind, the equations of conservation of mass and momentum for ions are given as [209]

$$\begin{aligned} \frac{\partial n_i}{\partial t} + c_i \frac{\partial n_i}{\partial x} + n_i \frac{\partial c_i}{\partial x} &= 0 \\ \frac{\partial c_i}{\partial t} + c_i \frac{\partial c_i}{\partial x} &= -\frac{Ze}{m_i} \frac{\partial V}{\partial x} \end{aligned} \tag{4.8}$$

Here, c_i and m_i are the ion velocity and mass respectively. Solving equations 4.7 and 4.8 for $t > 0$, we get

$$n_e = Zn_i = \begin{cases} n_{e0} \exp\left(-\frac{x}{c_s t} - 1\right) & \text{for } x > -c_s t \\ n_{e0} & \text{for } x < -c_s t \end{cases} \tag{4.9}$$

Here, $c_s = \sqrt{Zk_B T_e / m_i}$ is the ion acoustic velocity. Thus, the plasma expands towards vacuum with an exponential decay in the density profile and the gradient scale length, L_g increases linearly with time at velocity c_s, $L_g = c_s t$. The higher the electron temperature, the faster the plasma expands. Figure 4.2 shows the 1D isothermal expansion of a plasma with an initial density $n_{e0} = 330 n_c$, for three different values of L_g: 0, $\lambda_0/10$ and $\lambda_0/4$, where $\lambda_0 = 800\,\text{nm}$ is the pulse central wavelength.

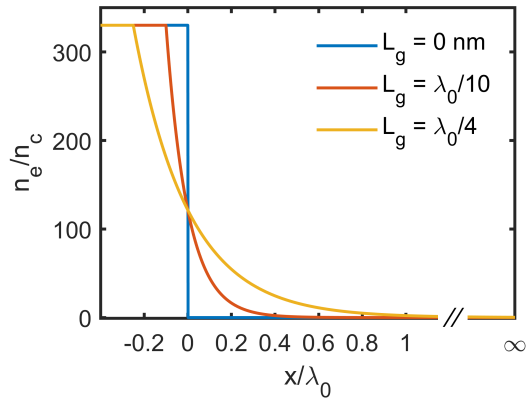

Figure 4.2: 1D isothermal expansion of a plasma with an initial density, $n_{e0} = 330 n_c$, for different gradient scale lengths. Here, $\lambda_0 = 800\,\text{nm}$.

However, it should be noted that this solution diverges when $t \to 0$ or $x \to \infty$. This is because the assumption of quasi-neutrality is reasonable only when $L_g > \lambda_D$ [210]. For $L_g \leq \lambda_D$, the electric fields due to individual charges are screened. A more rigorous approach for $L_g \leq \lambda_D$ would be to replace the hypothesis of quasi-neutrality by the Poisson equation and then solve the resulting equations [208].

4.4 Ponderomotive force

Let us consider an oscillating laser electric field along the x-axis,

$$E_x = E_0 sin(kz - \omega t) \tag{4.10}$$

where E_0 is the amplitude of the laser electric field, k is the wave vector, and ω is the angular frequency. As charged particles, such as electrons, move in this oscillating laser field, they experience an average force towards the decreasing field intensity, proportional to the gradient of the intensity. Understanding the Ponderomotive force is crucial in studying the dynamics of particles in strong laser fields and various plasma physics phenomena. In a classical, non-relativistic case, the time-averaged Ponderomotive force is given as [203]

$$< F_P > \; = -\frac{e^2}{4m\omega^2}\nabla E^2 \tag{4.11}$$

where e is the electronic charge and m is the mass of the charge particle. We can see that the ponderomotive force does not depend on the direction of laser polarization. It isotropically pushes the electrons away from regions of high electric field intensity. Also, the force term is inversely proportional to the mass of the charged particle, m, implying that, as compared to ions, the ponderomotive force will be much stronger for electrons. In the relativistic case, the ponderomotive force exhibits similar dependencies. A complete derivation of the relativistic ponderomotive force can be found in [211].

4.5 Laser absorption in plasmas

In this section, I will briefly describe the three major laser absorption or electron heating mechanisms in plasmas which are often encountered in the literature.

- **Resonant absorption**
  A component of the p-polarized laser electric field along the plasma density gradient, $E(x)$, drives the electrons to oscillate normal to the target, creating a periodic perturbation of the charge density along the gradient scale length. At a certain depth, δ_c in the density gradient, plasma oscillations are resonantly excited when the laser frequency matches the plasma frequency.

  $$\omega_p = \sqrt{\frac{e^2 n_c}{\varepsilon_0 m_e}} = \omega_L \tag{4.12}$$

  In our case, the laser pulses are incident obliquely on the target and will be reflected from $n_e(x) = n_c cos^2(\theta)$ from the surface, as shown in figure 4.3. An evanescent wave tunnels from the $n_e(x) = n_c cos^2(\theta)$ surface to the critical density surface, exciting plasma oscillations. This mechanism is called resonant absorption [212]. For a given angle of incidence, there is an optimal gradient length for which resonant absorption dominates [213]. In our case, $\theta = 55^\circ$ that corresponds to an optimal gradient length $L_g \sim \lambda/5$. In principle, "inverse resonant absorption" is also possible where there is a resonant transfer of energy from the plasma wave to incident laser electromagnetic wave.

- **Brunel absorption or vacuum heating**
  This mechanism was first proposed by Brunel in 1987 in his very famous article titled "Not so resonant, resonant absorption" [214]. Up until this milestone article was published, laser

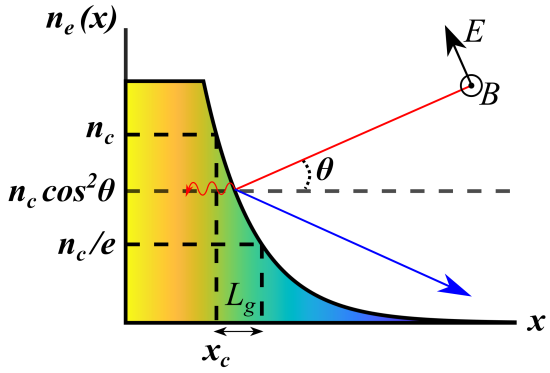

Figure 4.3: Principle of resonant absorption: A p-polarized wave incident at θ w.r.t. the target normal is reflected from $n_c\cos^2\theta$ surface. An evanescent wave tunnels to the critical density surface to excite plasma oscillations.

absorption in over-dense plasmas was largely attributed to resonant absorption [215]. Brunel absorption is critical to understand how the incident laser field can deposit its energy to the plasma, or be "absorbed" without even penetrating it. This model accounts for large absorption rates when p-polarized high intensity lasers ($I > 10^{16}$ W/cm^2) are focused at an oblique incidence onto a sharp density gradient in over-dense plasmas ($L_g \ll \lambda$). Figure 4.4 shows a gradient scale length Vs. intensity map of transition from resonant to Brunel absorption.

In the first half cycle of the laser electric field, the normal component of the field, $E(x)$ pulls the electrons out towards the vacuum. In the next half-cycle, as the laser electric field changes sign, electrons are pushed back into the plasma bulk, where they are screened from the laser field. These "hot electrons", also called **Brunel electrons** propagate ballistically inside the target, depositing their energy in the plasma through collisions. A charge perturbation in the plasma caused by the moving electrons while the ions largely remain static, creates a space-charge field that also pulls the electrons back into the plasma bulk. Energy transfer to electrons largely depends on their excursion length in vacuum. In a crude approximation, an estimation of the excursion length can be given as [214, 216],

$$\frac{d}{\lambda} \simeq \frac{a_0}{2\pi\sqrt{1+a_0^2}} \tag{4.13}$$

where, a_0 is the normalized vector potential. The solid black curve in figure 4.4 represents the location where the excursion length d given by equation 4.13 equals the gradient scale length. The longer the electron excursion length, the more energy electrons gain from the incident field. Brunel absorption also plays a key role in the HHG from over-dense plasmas, which is discussed later in this chapter.

- **$\mathbf{J} \times \mathbf{B}$ heating**
  This mechanism comes into play when the magnetic force ($F_{mag} \sim J \times B$) is comparable or stronger than the electric force ($F_e = eE$). The ponderomotive force (non-averaged) excites

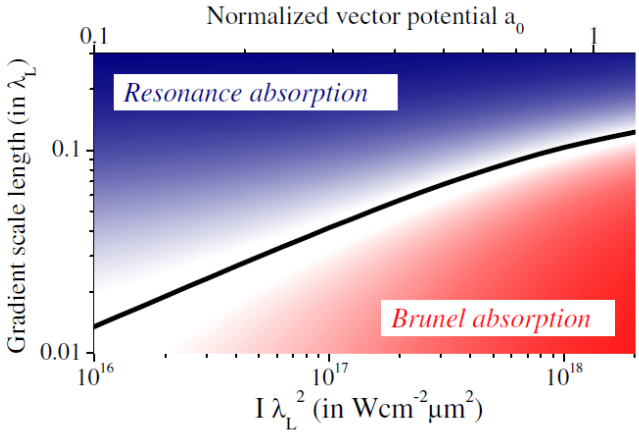

Figure 4.4: Transition from resonance to Brunel absorption as a function of laser intensity and gradient scale length. The solid black line indicates the location where typical electron excursion length equals the gradient scale length L_g. λ_L is the pulse central wavelength. Reprinted from [216].

non-resonant electron oscillations at $2\omega_L$ in the plasma [217, 218]. At normal incidence, Brunel absorption is no longer efficient because the electric field has no direct component towards the density gradient. In case of relativistic lasers, the $J \times B$ term pushes the electrons into the bulk of the plasma where they escape the laser field. This population of **hot electrons** deposit their energy through collisions. The number of electrons being able to escape the laser-field largely depends on the strength of the force. This effect can be observed at very long gradients, $\sim$ several 10s of λ [219].

4.6 What is a plasma mirror?

When an intense femtosecond laser pulse is tightly focused, traditionally, on the surface of an initially-solid target, it generates a thin layer of surface plasma with near-solid density, which under certain conditions becomes highly reflective for the incident laser light and is often called a “plasma mirror” (PM) [22, 78]. When the plasma frequency matches or surpasses that of the incident light, the plasma shields itself from external electromagnetic perturbations, thereby reflecting the incident light almost like a metallic mirror. Figure 4.5 illustrates how the critical density varies with the driving laser wavelength. It is evident that a shorter driving laser wavelength requires a higher plasma density for the plasma to act like a mirror.

There are two fundamental differences between a PM and a conventional metallic mirror. First, depending on the lifetime of the PM, it can dynamically switch between reflective and transmissive states. This is particularly useful for enhancing the temporal contrast of laser pulses [220]. Secondly, because the plasma is in an ionized state, there is inherently no intrinsic limitation of the incident laser fluence and intensity. This is one of the main reasons why PMs are considered as ideal test-beds for studying high-intensity laser-plasma interactions and the associated nonlinear propagation of the intense light in a plasma [22].

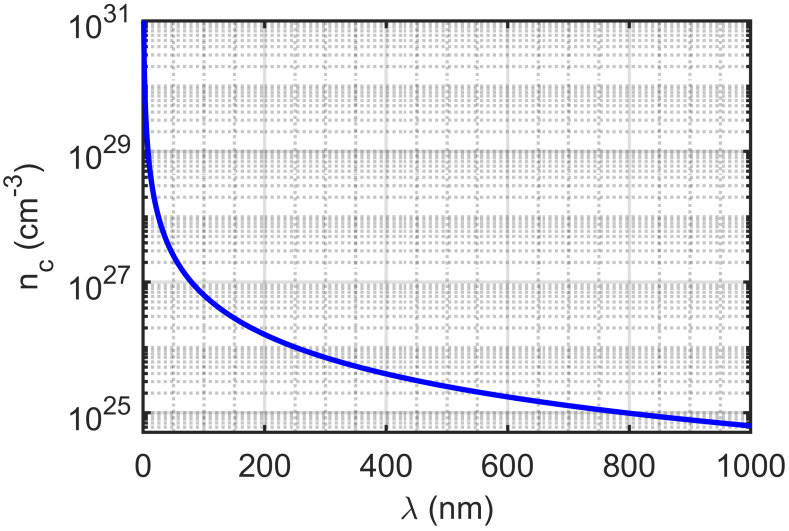

Figure 4.5: Variation of critical density with laser pulse wavelength.

4.7 High-harmonic response of plasma mirrors

High-harmonic generation (HHG) from plasmas was first observed in 1977 by Burnett *et al.* [3] using a CO_2 laser focused on an Aluminium target. A plateau of intense harmonics up to the 11th order were detected but was not immediately understood. The advent of high-contrast high peak power femtosecond lasers [2] subsequently enabled detailed studies on HHG from PMs. These studies have identified and characterized various mechanisms both in theory and experiments that are dominant in either sub-relativistic or relativistic regimes, as discussed below.

4.7.1 Sub-relativistic regime

Resonant absorption

At moderate laser intensities, $I \sim 10^{16} - 10^{17}\,\mathrm{W/cm^2}$, and relatively smooth density gradient scale length, $L_g \approx 0.1 - 0.2\lambda$, the dominant mechanism for HHG is cascaded linear mode conversion of plasma waves, excited through resonant absorption [212, 215, 221]. In this case, a fraction of the laser energy is converted into electrostatic energy in the form of plasma oscillations. For a given angle of incidence on-target θ, there is an optimal gradient scale length L_g, independent of the laser intensity that maximizes resonant absorption [212].

Coherent Wave Emission (CWE)

For moderate to high laser intensities ($I \sim 10^{15} - 10^{18}\,\mathrm{W/cm^2}$), the excursion length of plasma electrons in vacuum exposed to the laser electric field becomes so extensive that it exceeds the gradient scale length. Under these conditions, resonant absorption becomes less effective, and Brunel absorption [214] emerges as the dominant mechanism. The principle of HHG triggered by a Brunel electron dominated mechanism is illustrated in figure 4.6. Once per laser electric field cycle, the Brunel electrons are accelerated away and then back towards the surface plasma, forming an elec-

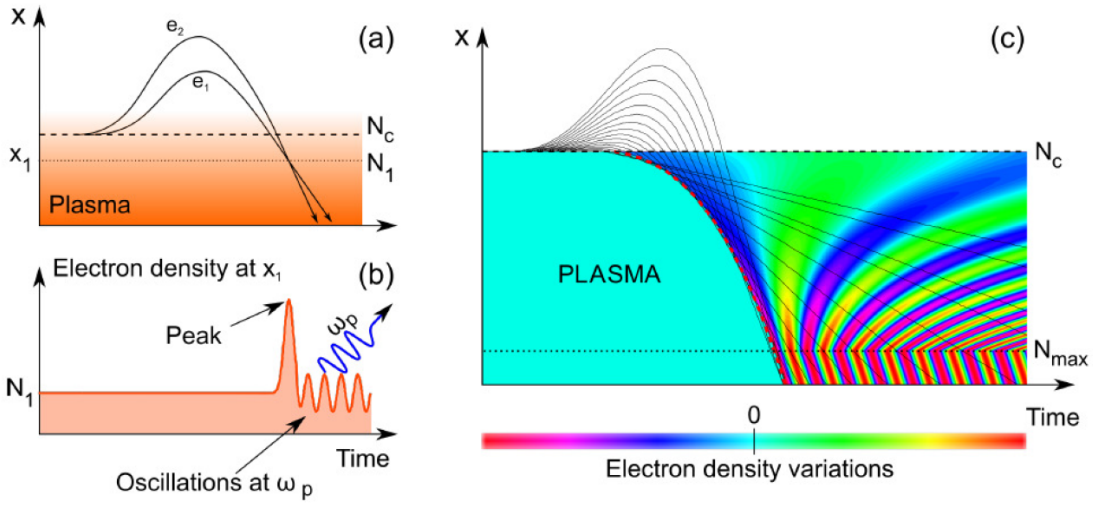

Figure 4.6: CWE-HHG mechanism: Trajectories of two Brunel electrons on the surface plasma are represented in (a). Temporal evolution of the electron density peak, exciting oscillations at the local plasma frequency ω_p, leading to emission of photons at the same frequency (b). Electron density variations in the plasma caused by the crossing of Brunel electrons (c). The solid black line represents the trajectories of Brunel electrons and the dotted red line shows the caustic at which the electron peak appears and triggers plasma oscillations. Reprinted from [222].

tron density peak via collective trajectory crossings, traversing the over-dense part of the plasma density gradient. Once the electrons have passed the critical density surface, they are effectively screened from the laser field, and the kinetic energy accumulated during their vacuum excursion is then transferred to the plasma. The traversing electron density perturbation excites plasma waves in its wake. These plasma waves then emit photons at the local plasma frequency, resulting in the emission of an attosecond light pulse per laser cycle. This HHG mechanism, predominantly driven by Brunel electrons, is referred to as coherent wake emission (CWE). The following are some of the key characteristics of CWE-HHG:

- **Intensity dependence:** The amplitude of the plasma density front excited by the interaction increases linearly with the amplitude of the laser electric field. Since the conversion from plasma oscillations to light is also a linear process, the CWE-HHG signal is expected to behave linearly within the laser intensity range of $a_0 = 0.02 - 0.2$ [20]. This linear relationship has been substantiated through both theoretical analyses and experimental demonstrations

- **Plasma density gradient**: The electron density peak formation and conversion to HHG are optimized for a very steep density gradient, $L_g \sim 0.01\lambda$. As the density gradient length increases, the CWE efficiency rapidly drops [20], while the harmonic chirp, translating to an increased spectral width of the harmonic peak increases [216, 223].

- **Angle of incidence:** Simulations have shown that the CWE-HHG efficiency peaks at an angle of incidence, $\theta \approx 55^\circ$ [20]. At $\theta \to 0^\circ$, the Brunel mechanism does not occur and at $\theta \to 90^\circ$, the laser intensity effectively reduces to zero.

- **Spectral cut-off:** The spectral extent of the emitted harmonics is limited by the maximum plasma frequency

$$\begin{aligned} \omega_p^{\max} &= \sqrt{\frac{n_e^{\max} e^2}{\varepsilon_0 m_e}} \\ &= \omega_0 \sqrt{\frac{n_e^{\max}}{n_e}} \end{aligned} \tag{4.14}$$

  In our experiments, for a fused silica target ionized to Si^{12+} and O^{7+} by BSI, we get 26 electrons per SiO_2. In this case, the CWE-spectral cut-off energy is around 30 eV.

- **Phase properties:** The intensity-dependence of the trajectories of Brunel electrons leads to increasing delays between successive attosecond pulses under the driving pulse envelope, and thus, to frequency broadened negatively chirped individual harmonics [18, 216, 224, 225]. Additionally, an increase in the gradient scale length stretches the spatial distribution of harmonics, thereby increasing the delay between the emission times of different harmonics, consequently, increasing the amplitude of chirp and hence duration of the attosecond pulses [226]. A positively chirped driving pulse can partially compensate the effect and consequently lead to spectrally narrower CWE-harmonics [216, 223, 227].

- **Divergence:** CWE-HHG can be understood as a coherent superposition of point sources, each with a well-defined phase relationship [228]. Since the HHG emission time is intensity-dependent, it typically occurs earlier at the center than at the periphery, which results in a diverging beam [20]. To mitigate this, the focus of the driving laser beam can be positioned beyond the target surface, which helps produce a less divergent XUV beam [226]. However, inhomogeneities on the plasma surface, along with variations in the driving laser's intensity distribution at the focus, contribute to additional XUV wavefront aberrations. The high divergence and aberrations represent a significant limitation of CWE-HHG as an XUV light source, making it particularly challenging to refocus the attosecond pulses. Despite these challenges, there have been successful efforts to reduce beam divergence. For instance, Porat *et al.* achieved a nearly diffraction-limited CWE beam with a divergence of approximately $5\,\mathrm{mrad}$, which is comparable to gas-HHG [229].

4.7.2 Relativistic regime

As the laser intensity crosses the relativistic threshold, $I \geq 10^{18}\,\mathrm{W/cm^2}$ or $a_0 > 1$, HHG was observed beyond the CWE spectral cut-off frequency [20]. Relativistic HHG (RHHG) from the PM was first predicted through numerical simulations and qualitatively understood through a relativistic Doppler shift model, called the "relativistic oscillating mirror" (ROM) [230–235]. At such high intensities, electron jets at the PM surface are accelerated to relativistic velocities, essentially creating a PM surface oscillating at relativistic speeds that lead to a transient but periodic Doppler frequency up-shift of the laser field reflected by the PM. Different analytical approaches have been used to numerically account for the Doppler effect, such as an oscillating step-like plasma interface [231], cancellation of tangential

electric field [233] and vector potential [234] at the surface.

Analytical modeling of RHHG emission has evolved over time. Baeva *et al.* proposed another approach to understand the mechanism, called the Baeva-Gordienko-Pukhov (BGP) theory [233]. The authors provided another analytical description for the ROM-model, in which the sharp spikes in the temporal variation of the Lorentz factor were identified as the key to RHHG emission. This theory could predict the spectral shape of the generated harmonics at moderate relativistic intensities, $I_n \propto n^{-8/3}$, with a threshold of $n_{th} \propto \gamma_{max}^3$, where γ_{max} is the maximum value of the Lorentz factor of the plasma surface. Beyond n_{th} RHHG emission was found to decay exponentially.

Gonoskov *et al.* proposed another model, called the "Relativistic electron spring" (RES) to analytically study a vast range of regimes in laser-plasma interactions [236]. In this model, the authors suggest that at ultra-high intensities ($a_0 \gg 1$) there is a significant energy build-up in the plasma, forming nanoscale electron layers due to ponderomotive force of the laser. When this electron nano-layer is accelerated back towards vacuum, RHHG is coherently emitted. D. an der Brügge *et al.* proposed another model "Coherent synchrotron emission" (CSE) that was similar to RES, but based on the BGP-theory [237]. This model also proposes that the electrons on the surface of PM form nanometric, highly compressed layers that coherently emit synchrotron radiation when they are accelerated perpendicular to their motion. Mikhailova *et al.* also proposed RHHG emission via synchrotron emission [238]. Dromey *et al.* experimentally observed RHHG emission in transmission using nanometric thick carbon foils that was also understood through a synchrotron emission from plasma [239].

Some of the key characteristics of RHHG identified in theory and experiments are as follows:

- **Intensity dependence:** The harmonic generation efficiency and the number of emitted harmonics should increase as the laser intensity increases till $a_0 \sim 10$ and should begin to saturate at ultra-high intensities, $a_0 \sim 100$ [20, 240]. The radiation reaction force [241] also comes into play at such ultra-relativistic intensities, modifying the energy partition between plasma electrons, ions and radiation, thus, modifying the RHHG properties [242]. However, such ultra-high laser intensities are beyond the reach of current laser technology.

- **Plasma gradient scale length:** At steep density gradients where CWE-HHG is optimized, the gyromagnetic effect [243] suppresses RHHG by preventing electrons from escaping the plasma. In experiments and simulations, RHHG has been found to be optimal at relatively softer gradients, $L_g \sim 0.1\lambda$ [69, 202, 244]. When the density gradient scale length is further increased, the onset of a more chaotic regime suppresses RHHG. [202].

- **Angle of incidence:** Thaury *et al.* simulated the effect of angle of incidence on RHHG while maintaining a constant laser intensity on-target, and found an maximum generation efficiency around $\theta_i = 55^\circ$ [20]. At moderate relativistic intensities, electrons involved in RHHG are accelerated by the Brunel mechanism with peak velocities in the outward direction on the Brunel trajectory, proportional to $E_x \propto sim\theta\sqrt{cos\theta}$, which is maximum at, $\theta \approx 55^\circ$. However, the complexity of the interaction process cannot be completely explained by this rather simple calculation.

- **Spectral cut-off:** The spectral cut-off of RHHG has an extremely non-linear dependence on the maximum velocity of the oscillating critical density surface [232, 233]. The spatial compres-

sion of electron nano-sheets in the CSE model plays a crucial rule to determine the spectral extension of RHHG [240]. As mentioned above, the spectral extension begins to saturate only at very high intensities, around $a_0 \sim 100$ [20].

- **Phase properties:** Contrary to CWE-HHG, for moderately relativistic intensities, RHHG correspond to FTL attosecond pulses in the time domain, i.e. the "attosecond" spectral phase of the RHHG should be flat [20, 245, 246]. In principle, if the generated spectrum is broad enough, due to a pristine "attosecond" spectral phase, RHHG can also correspond to zeptosecond pulses in the time domain [232]. In case of ultra-high intensities, $a_0 > 10$, the plasma surface denting can induce an intrinsic chirp with an opposite sign as compared to that of CWE [20]. In case of a multiple optical cycle driving pulse, the emitted train of attosecond pulses is not necessarily periodic and therefore individual harmonics can be chirped, or in other words, the "femtosecond" spectral phase is not necessarily flat [20].

- **Divergence:** If we consider a spatially constant intensity in focus, the RHHG beam emitted should exhibit diffraction-limited divergence for a given harmonic order n, $\theta_n \sim \theta_{las}/n$r [247]. Consequently, the focused intensity of the RHHG beam can in principle exceed the intensity of the driving laser. However, in the experiments, the situation is far from ideal and the space-dependent laser-intensity in the focal plane leads to a focusing of the RHHG beam and increases its divergence [20, 247]. However, if this plasma-denting induced focusing is aberration-free, the emitted XUV beam can be considered to have a diffraction limited spatial quality.

4.8 Electron acceleration mechanisms

Acceleration of electrons from PMs largely depends on the driving laser intensity and plasma gradient scale length. At sub-relativistic intensities ($a_0 < 1$) a fraction of Brunel electrons can escape towards vacuum, leading to observation of an electron beam, between the target normal and specular directions. In this regime, for electrons to be efficiently accelerated towards vacuum, it is preferable to have softer density gradients, $L_g \sim 0.1\lambda$, contrary to what is required for optimal CWE emission, where it is favorable for Brunel electrons to return to the plasma [248]. Under such conditions, another mechanism based on Stochastic heating [249, 250] has been reported by Zhou *et al.* [251]. A small population of electrons injected into the laser field very close to the tail of the pulse, at zero crossings of the laser electric field are exempted from strong ponderomotive forces and only deflected by the weak laser field, undergoing a change in momentum depending on the vector potential associated with the optical cycle. These electrons were observed to have a "streaking pattern" with a narrow energy spread and a duration of about ≈ 200 as.

At relativistic intensities ($a_0 \geq 1$), various electron acceleration mechanisms have been identified in theory and experiments. The dominant mechanism depends critically on the scale length of the plasma density gradient. At extremely steep gradients, $L_g < \lambda$, correlated to the ROM-HHG, acceleration dynamics are driven by the ponderomotive force (discussed above in 4.4) and vacuum laser acceleration (VLA) [252, 253] in which electrons are directly accelerated by the laser electric field in

vacuum. VLA will be discussed in more detail later in this section. At intermediate gradients, $L_g \approx \lambda$, a more chaotic regime sets in and stochastic heating comes into play and electrons in the under-dense part of the plasma gain energy in the interference pattern resulting from the superposition of the incident laser field with the laser field reflected by the over-dense part of the plasma. In this case, the electron dynamics are no longer integrable and get chaotic which can lead to high energy transfer from the laser wave to the electron population [249, 254]. The "streaked" attosecond electron bunches observed at sub-relativistic densities [251] are hard to observe for $a_0 > 1$ as they are overlapped with other electron species.

At much softer gradients in the relativistic regime, $L_g \gg \lambda$, electrons are accelerated to relativistic energies by fields of the order of 1 TV/m, attributed to the laser wakefield acceleration (LWFA) mechanism, with few-cycle driving pulses that can near-resonantly excite a wakefield in a dense plasma [255].

4.8.1 Vacuum laser acceleration

Direct acceleration of electrons to relativistic energies in the laser electric field in vacuum with accelerating fields exceeding 10 TV/m has long been studied both theoretically [211, 252, 253, 256, 257] and numerically [258–261]. The accelerating fields in VLA are at least two orders of magnitude stronger than those in conventional laser-plasma accelerators, underscoring their potential to accelerate electrons to even higher energies. The central idea is to inject free electrons into an ultra-intense laser field such that the they remain in-phase, within a given half optical cycle of the laser field, such that they can constantly gain energy until they exit the focal volume. However, initial experimental demonstrations were rather elusive and fell short of theoretical predictions of high gain [262–266]. For the acceleration to be efficient, electrons have to be injected into the laser field with a high initial velocity and at a precise phase, close to the zero of the electric field. This ensures that the electrons remain in phase with the laser field, maximizing their acceleration duration. The stringent nature of these injection conditions made experimental realization challenging.

Thévenet *et al.* [267] discovered that PMs are ideal tools that inherently meet the injection requirements for VLA. When an ultra-intense laser pulse is reflected off a relativistic PM, at a steep plasma density gradient ($L_g \ll \lambda$), relativistic electrons are expelled towards vacuum close to the specular direction, at specific phases of the reflected laser field (figure 4.7(a)). These electrons, once ejected in vacuum, co-propagate with the reflected laser pulse in vacuum, where they are further accelerated over a distance of the order of the Rayleigh range as shown in figure 4.7(b). This interaction also modifies the angular distribution of electrons. The underlying dynamics of electron injection, their subsequent acceleration and injection phase dependent emission properties have been thoroughly studied by 1D and 2D PIC simulations in [268].

Thévenet *et al.* [267] also identified different populations of electrons emitted from PMs and performed 3D PIC simulations to distinguish VLA electrons properties. They sorted electrons into different groups, depending on the number of laser field cycles, N_{OC} crossed by them. Figure 4.8(a) illustrates trajectories of two different populations: ponderomotively scattered electrons that cross $N_{OC} = 3$ and VLA electrons indicated for $N_{OC} \leq 1$. Their corresponding temporal evolution of the Lorentz factor is shown in figure 4.8(b). We can clearly see that VLA electrons simply "surf" the laser

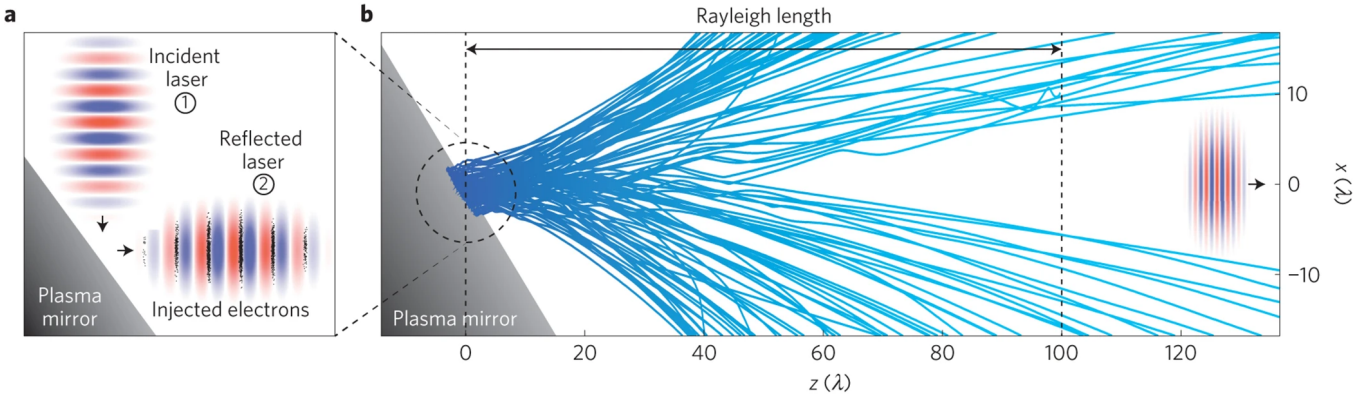

Figure 4.7: A 2D PIC simulation of VLA of electrons using PMs. When an ultra-intense laser pulse (E-field in red-blue) is reflected-off a relativistic PM, relativistic electrons (black dots) are expelled in phase with the laser field (a). These electrons (blue lines) then co-propagate with the laser field and are further accelerated in vacuum (b). Reprinted from [267].

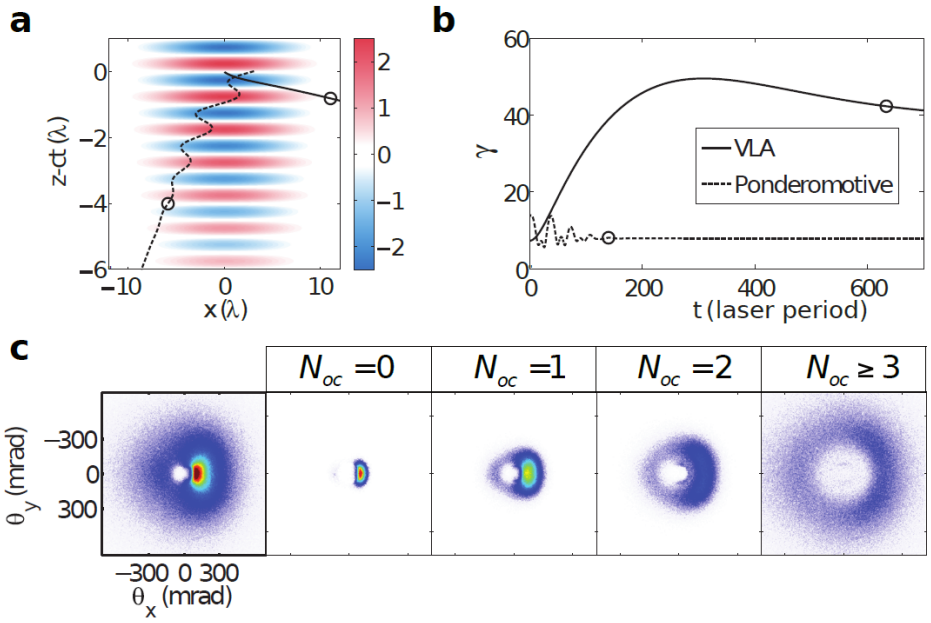

Figure 4.8: 3D PIC simulations of VLA of electrons using PMs. Trajectories of electrons that see different laser field cycles (red-blue), $N_{OC} = 1$ (dashed-black line) and $N_{OC} = 1$ (solid-black line), and the respective points at which they escape the laser field (circled) (a). Temporal evolution of the Lorentz force factor (γ) along these two trajectories (b). Angular electron distribution of various electron populations for different laser field cycles experienced by the electrons. Reprinted from [269].

wavefront in which they were injected, along the direction of polarization of the laser pulse, gaining energy almost throughout its trajectory ($\sim z_R$) before escaping the focal volume. On the other hand, the ponderomotive electrons oscillates initially and is fairly very quickly expelled out of the laser field. Several sub-ensembles of simulated electron beam profiles, from VLA to ponderomotively scattered electrons are shown in figure 4.8(c). Ponderomotive electrons are isotropically scattered around the laser propagation axis, forming a “doughnut” shaped beam profile. VLA electrons, on the contrary

are more localized, concentrated in a bright peak on the edge of the ponderomotive hole, along the laser polarization direction. The authors found that the maximum energy of VLA electrons was twice that of ponderomotive electrons.

When VLA is driven by a linearly polarized pulse, the accelerating fields are transverse, which pushes the electrons off the optical axis, thereby increasing their angular spread. In case of a radially polarized pulse, where at every position, the polarization vector points towards its center, there is a strong longitudinal field component at the focus, with a maximum on the optical axis. Recent work suggests that using radially-polarized pulses at a near-normal incidence on a PM to drive VLA can not only increase the energy gain but also help reduce the divergence of the electron beam [270, 271].

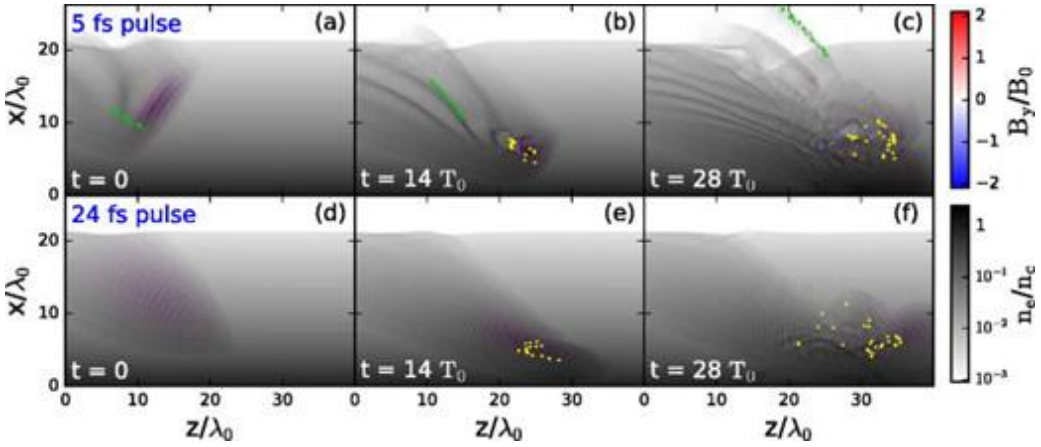

Figure 4.9: 2D PIC simulation of LWFA of electrons and long density gradients ($L_g \geq \lambda$) using few-cycle pulses. Laser $B-$field and electron density for 5 fs (a)-(c) and 24 fs (d)-(f). Green and yellow dots highlight a sample of ejected electrons. Reprinted from [255].

4.8.2 Laser wakefield acceleration

At longer gradient scale lengths ($L_g \geq \lambda$), for few-cycle driving laser pulses, a completely different acceleration regime was experimentally discovered and theoretically modeled by Zaïm *et al.* [255]. Figure 4.9 shows snapshots of 2D PIC simulations of laser magnetic field and electron density for a few-cycle (5 fs) and longer pulses (24 fs) with multiple optical cycles. A high amplitude plasma wave can be seen in the wake of a few-cycle laser pulse with a wavefront that is bent by the plasma density gradient, that is reminiscent of the plasma waves generated by Brunel electrons in the CWE-HHG emission [20]. This characteristic is unique to LWFA on PMs, and is not observed in conventional LWFA. Consequently, in this scenario, the electrons accelerated by LWFA are not emitted in the same direction as the laser propagation. The electron population originating from ionization-injection is trapped and accelerated by these excited plasma waves reaching up to 1 TV/m and pushed out, away from the specular, towards the normal direction. It is worth noting that these plasma waves are completely absent for the case of a 24 fs pulse. This mechanism was only observed for few-cycle pulses ($1-4$ optical cycles) reaching relativistic intensities on-target ($a_0 > 1$). This can be explained by a resonance condition: the laser pulse duration τ is comparable to half the plasma wavelength, $\lambda_p/2$, i.e. $c\tau \approx \lambda_p/2$ [209, 255, 272, 273]. In case of 5 fs pulses, the resonant density corresponds to

$\sim n_c/12.5$, while for 24 fs pulses, the resonant density is $\sim n_c/300$. Additionally, the authors found no influence of the laser polarization or waveform on the emitted electron beam properties.

4.9 Ion acceleration mechanisms

Due to their large inertia, ions cannot be directly accelerated to high energies by the laser electric field. The emission of fast electrons and direct action of the laser Ponderomotive force induces a charge separation. Ions are accelerated by the space-charge field at a time scale typically of the order of $\omega_i^{-1} \sim \sqrt{m_i/m_e}\omega_p^{-1}$.

Laser ion-acceleration is possible from both the front as well as the rear surface of the target. Initial experiments from the 1990s mainly studied ion acceleration from the rear target surface [274]. Acceleration from the front surface could not be explored extensively at first because of poor temporal intensity contrast of then-available CPA lasers. Studies have shown that a low-density pre-plasma generated by the ASE pedestal reduces the laser-to-proton energy conversion [275].

One of the most widely accepted laser-ion acceleration models is target normal sheath acceleration (TNSA) [276]. Other mechanisms have been proposed over time such as radiation pressure acceleration (RPA) [277, 278], collisionless shock-wave acceleration (CSA) [279–282] light-sail acceleration [283–286], relativistic self-induced transparency acceleration [287, 288], breakout afterburner [289, 290], and magnetic vortex acceleration [291, 292]. The complex non-linearity of the interaction makes it difficult to identify the dominating pathway. The co-existence of these pathways in experiments further complicates the understanding of the acceleration scenario. Although these mechanisms offer promising ion beam properties, they generally require stringent laser and/or target parameters.

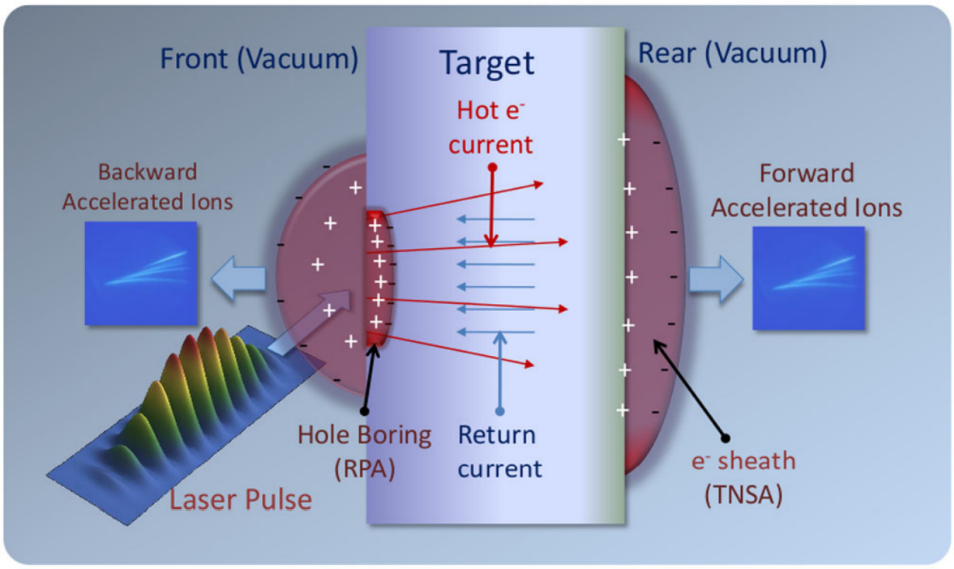

Figure 4.10: A schematic view of the TNSA process. The laser pulse heats up the plasma electrons. The hot electrons set up a negative sheath on both sides of the target, creating a capacitor-like field to acceleration ions. Reprinted from [293].

By far, due to its inherent simplicity, **TNSA** remains the most widely recognized and dominant mechanisms for ion acceleration [276, 294]. The principle of the TNSA process is depicted in figure 4.10. When an intense laser pulse is focused on the surface of the target, an overdense plasma is created on the surface majorly by suppression of the Coulomb potential (see section 4.1) [295]. The acceleration mechanism is driven by the "hot plasma electrons" that leak into vacuum. If the target is relatively thin ($\sim 50\ \mu\mathrm{m}$), electrons penetrate to the rear side of the target, thereby creating a negatively charged sheath on both sides of the target, with thickness typically of the order of the local Debye length, $\lambda_D = \sqrt{\varepsilon_0 k_B T_e / n_i e^2}$. The electron sheath layer gives rise to electrostatic fields along the target normal direction, $\sim$TV/m, strong enough to rapidly ionize atoms and accelerate ions normal to the target surface. The resulting ion trajectories depend on the local orientation of the target surface and the electric field driven by the time-dependent electron density distribution [296]. As the ions start from a cold solid surface, the resulting beam quality is extremely high [293]. The accelerated ion beam has a conical profile with a typical divergence of $\phi_i \sim 10^\circ - 30^\circ$ at FWHM, depending on the target and laser parameters. Typically, ϕ_i decreases with increasing ion energy as well as charge [274, 297–299]. The total ion energy can reach a few percent of the incident laser pulse energy [300]. The maximum ion energy scales unfavorably with the laser intensity. There is no robust scaling law, so the scaling is often determined empirically from experiments. Typically, the ion energy $E_i \propto I^\alpha$, where α ranges between 0.3 and 1 [293]. The ion energy spectrum typically follows a Maxwell-Boltzmann distribution. It is worth noting that protons are the most easily accelerated ion species mainly due to their low charge-to-mass ratio but also because they can shield the accelerating field and prevent acceleration of heavy ions.

Thus far, most of the TNSA-driven ion acceleration studies have been focused on the forward accelerated (in the direction of laser propagation) ion beams emitted from the back-side of thin targets, mainly because backward direction (opposite to the direction of laser propagation) TNSA, i.e. from the front surface of the target is not very efficient due to the screening effect from the generated plasma resulting in less energetic ions as compared to the forward accelerated ions [301], .

Front-surface proton-acceleration studies

In 2007, Ceccotti *et al.* presented a pioneering comprehensive parametric analysis of proton acceleration from over-dense plasmas, drawing a comparison between the proton beams simultaneously emitted from the front and rear side of the target based on their maximum energy, charge, and divergence, across a wide range of laser and target parameters [301]. This work highlighted the significant role of the laser temporal contrast in determining the dominant acceleration mechanism and consequently the properties of the emitted proton beams. Specifically, with oblique incidence on-target and low temporal contrast (around 10^6), acceleration was primarily efficient in the forward direction, predominantly driven by TNSA. Conversely, high-contrast laser pulses (around 10^{10}) even though a factor of two lower in energy as compared to the low-contrast pulses, yielded proton energies approximately twice as high as those in the low-contrast scenario. In this case, proton beams emitted in both directions exhibited similar maximum energies, charge and a narrow divergence of approximately 4.5°. The study also presented results from numerical simulations indicating that the "hot-electron" population driving proton acceleration—such as $J \times B$ heating, resonant absorption, and Brunel absorption—is influential. However, proton energies significantly diminished either when the incidence

on the target was nearly normal or when using s-polarized pulses, conditions under which Brunel absorption is less effective. This investigation clearly demonstrates that high laser temporal contrast is essential for effective proton acceleration from both the front and rear surfaces of the target, further identifying the role of Brunel electrons in the acceleration dynamics.

Hou *et al.* also reported a low-divergence proton beam emitted from the front surface of a thick target, which was driven by obliquely incident mJ-energy 50 fs pulses at 0.5 kHz but with a pulse temporal contrast limited to 10^8, focused to $\sim 10^{18}\,\mathrm{W/cm^2}$. Proton beams of 265 keV could be generated with a 16° spread at FWHM. The higher divergence in this case could be explained by a lower temporal contrast of the driving laser. The authors performed 2D PIC simulations and confirmed that the acceleration mechanism was predominantly driven by the sheath field generated on the front surface, which was further enhanced by ponderomotive forces, $J \times B$ heating, and Brunel absorption.

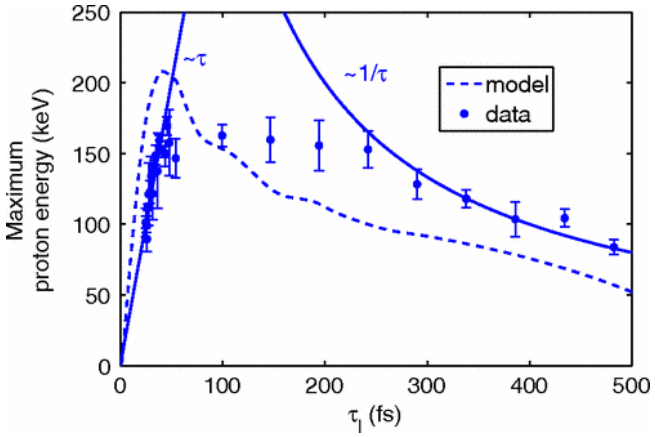

Figure 4.11: Maximum proton energy as a function fo the driving laser pulse duration for a constant pulse energy. Reprinted from [25].

At LOA, Veltcheva *et al.* also conducted a parametric study on proton acceleration, focusing on the emission from the front side of a thick target, using obliquely incident 1 mJ energy, 5 fs pulses at 1 kHz with a temporal contrast of $\sim 10^8$ [25]. The authors presented a theoretical model supported by 2D PIC simulations, where they propose that the acceleration dynamics are largely driven by Brunel electrons and not by thermal electron pressure. They varied the pulse duration from 5 fs to 500 fs, establishing that proton acceleration occurs within the laser pulse duration time, during which the Brunel electrons are driven into and out of the plasma by the laser electric field. This experiment was performed without any control of the plasma density gradient, so at the steepest density gradients limited by the temporal contrast of the laser pulse. At such steep gradients, the Brunel electrons that are pushed back into the plasma beyond the critical density surface are lost to the plasma. Consequently, they do not contribute to the electron thermal pressure, making it unlikely for TNSA to be efficient. Additionally, optimized proton energies observed for a p-polarized laser further validated the significant role of Brunel electrons in this process.

Chapter 5

kHz Relativistic Plasma Mirror Beamline

Outline

5.1 Relativistic plasma mirror beamline: Overview **123**
5.2 kHz Solid target **125**
5.3 Shooting sequence **127**
5.4 XUV detection **129**
5.4.1 XUV Spectrometer 129
5.4.2 Spatial-intensity profile detection 130
5.4.3 Wavefront characterization 132
5.5 Electron detection **133**
5.5.1 Spatial charge distribution 133
5.5.2 Magnetic electron spectrometer 135
5.6 Ion detection **136**
5.6.1 Thomson Parabola Spectrometer 136
5.6.2 Time of flight detector 138
5.7 Plasma density gradient calibration **141**

5.1 Relativistic plasma mirror beamline: Overview

The optical layout of the fully vacuum-integrated kHz relativistic PM beamline is illustrated in figure 5.1. Following the output of the *Salle Noire* laser, we have 3.5 mJ energy p-polarized pulses with tunable pulse duration from 30 fs to sub-4 fs available at 1 kHz repetition rate. These laser pulses are shaped and transported for interaction with a kHz relativistic PM on the surface of an initially-solid target.

Beam expansion: In order to obtain a tight focus and achieve the highest possible intensities on-target, the beam at the output of the laser is first expanded from 25 mm to 38 mm (at $1/e^2$ width) using an afocal telescope (**MCX1** and **MCC1**).

Auxiliary beam or Prepulse: In our experiments, what we call a "Prepulse", is used to prepare a plasma on the surface of the target. The Prepulse is picked-off from the "Main-pulse" beam using a 3" diameter, flat, silver-coated "holey" mirror, **MH1** used at a 45° angle of incidence with a hole size of 12 mm $\times$ 8.5 mm, mounted on a horizontal translation stage. The laser pulse being Gaussian-like, it contains more energy in the center as compared to its periphery. Thus, by changing the point of extraction of the Prepulse, its energy can be varied from $50\ \mu$J to up to $200\ \mu$J. Typically, in our experiments, we set the prepulse energy to $\approx 100\,\mu$J. The Prepulse is sent through a delay line consisting of a retro-reflector mounted on a high precision, low-wobble motorized linear translation stage with a scanning range of $600\,$ps. The retro-reflector rotates the polarization state of the Prepulse, which is remediated by a HWP (**HWP1**) that rotates the major axis of the ellipse back into the p-polarization direction. The Prepulse is also downsized to $\approx 2\,$mm using a Galilean telescope (**L1** and **L2**) and then finally collinearly recombined with the Main-pulse through another holey mirror (**MH2**, identical

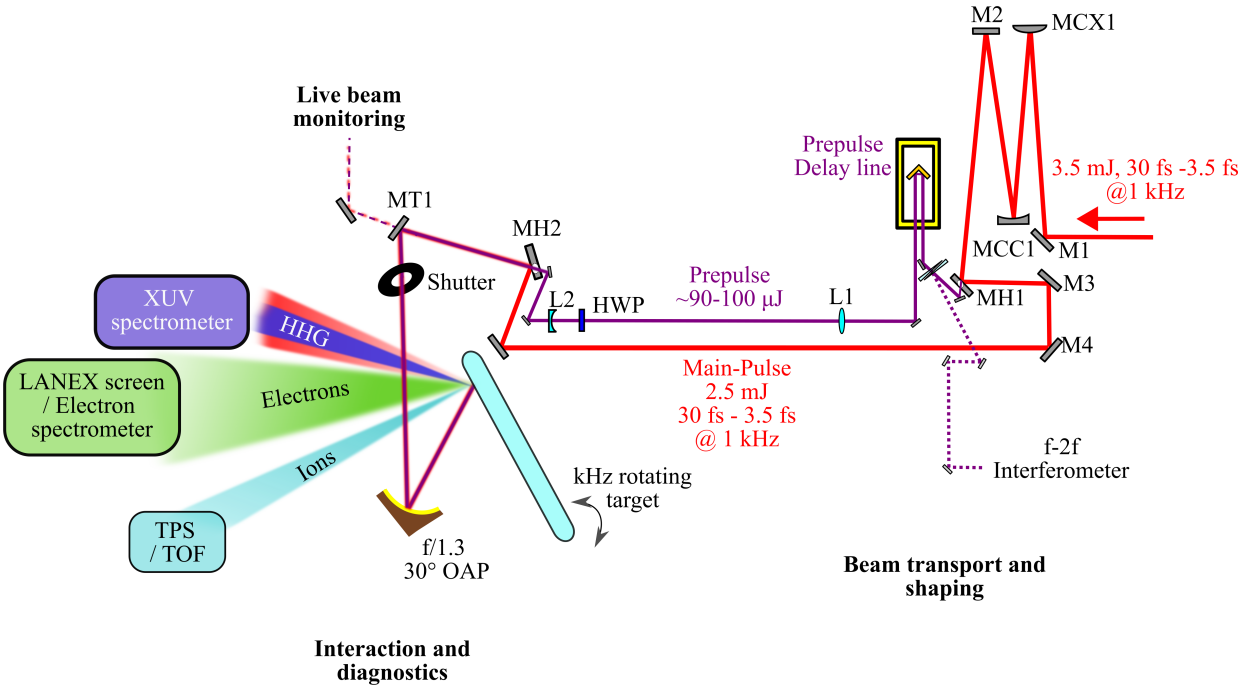

Figure 5.1: Overview of the relativistic PM beamline. MH1 and MH2 are identical "holey mirrors", MCC: concave mirror, MCX: convex mirror, HWP: half-wave plate, MT: partially transmissive mirror, OAP: off-axis parabolic mirror, TPS: Thomson Parabola Spectrometer, and TOF: Time of flight detector.

to **MH1**). Figure 5.2 (left panel) shows the near-field beam profile of the recombined Main-Pulse and Prepulse.

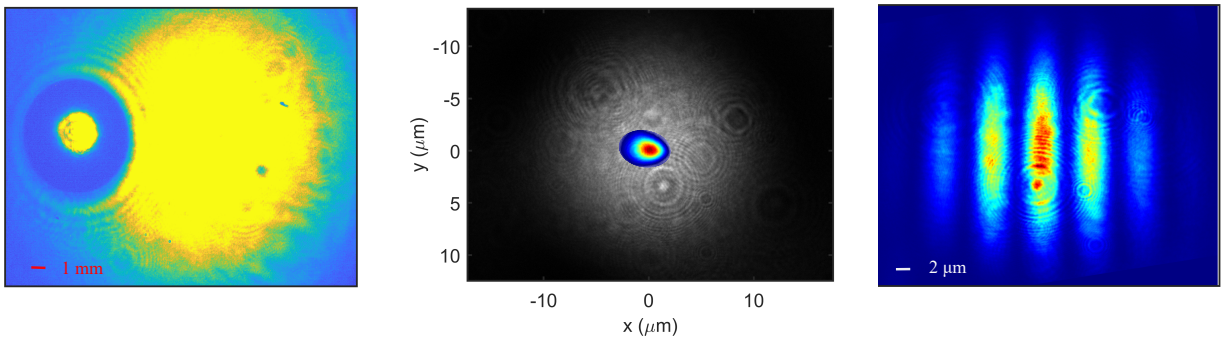

Figure 5.2: A near-field snapshot of the recombined Prepulse and Main pulse (left), on-target Prepulse (gray-scale) and Main-pulse (color scale) spatial beam profiles (center), and the interference fringes observed when the Main-pulse and Prepulse overlap in space and time in-focus (right).

Focusing: The laser pulses are tightly focused onto the target using a protected-silver coated 30° off-axis $f/1.3$ parabolic mirror (OAP), with an effective focal length of $54.4\,\text{mm}$.
Solid target: We use a 5" diameter and 12.5 mm thick, uncoated fused silica (SiO_2) target polished to $\lambda/20$ flatness on both sides, with a 20-10 scratch-dig. Fused silica was chosen mainly because it is low-cost and easily available with high surface quality. A 3D sketch of the kHz solid-target positioner

is shown in figure 5.3. It will be discussed in more detail in section 5.2.

Focal spot imaging: As shown in figure 5.3, an insertable microscope objective is installed to image the laser focal spot onto a CCD camera outside the chamber. We use an infinity corrected, semi-apochromat X40 microscope objective (Olympus) with a 0.51 mm working distance and a numerical aperture of 0.75. Figure 5.2 (center panel) shows the measured Main-pulse and Prepulse beam profiles in-focus.

Temporal overlap or "zero-delay": In order to precisely find the position of the delay line at which the Prepulse overlaps in time with the Main-pulse, we use an interferometric technique in-focus. The focal spot imaging setup described above is used with a narrow-band 800 nm spectral filter in front of the camera, so as to increase the coherence length of the detected laser light. The Main-pulse is reduced in size using an iris such that its fluence is comparable to the Prepulse in-focus. As the two pulses overlap in time, interference fringes appear on the camera as shown in figure 5.2 (right panel).

Laser beam monitoring: A leak from the partially transmissive ($\sim 0.1\%$) mirror (**MT1**) is used to monitor the beam position and angular orientation live while shooting on-target.

Secondary emission diagnostics: This PM beamline has been uniquely engineered to simultaneously detect the emission of HHG in the XUV regime, as well as energetic electrons and proton beams facilitated by dedicated diagnostics, depicted in figure 5.1. Their simultaneous detection enables us to observe direct correlations between the signals whilst ensuring identical interaction conditions on-target. These diagnostics are discussed in more detail later in this chapter.

Reflected near-field beam profile: The secondary diagnostics are complemented with a recording of the near-field profile of the beam reflected off the PM, imaged onto a screen positioned at the entrance of the XUV spectrometer (section 5.4.1) using a CCD camera with a narrow-band 800 nm filter. This diagnostic is useful for several reasons: First, it acts as a preliminary guide to accurately position the laser-focus on-target under vacuum, where the reflected beam is most-intense and more localized when the laser focus is on the target. Second, it is an effective monitoring setup to ensure that the reflected beam is well aligned to the XUV spectrometer. Lastly, this imaging setup is also used for calibration of the plasma density gradient length (section 5.7).

5.2 kHz Solid target

In laser-plasma experiments, the target surface is destroyed every shot and has to be refreshed before the next laser pulse arrives on-target. Performing laser-plasma experiments at kHz repetition rate is no easy feat, primarily because the target has to be refreshed every millisecond while maintaining the same angular orientation and position w.r.t the laser beam in-focus. Since maintaining angular and depth instabilities below $100\,\mu$rad and $2\,\mu$m respectively at a kHz repetition rate were beyond the capabilities of standard rotational platforms available at the time, Borot et al. have developed a precise optical target positioner in the group [302]. A 3D image of the kHz rotating target is shown in figure 5.3. It consists of a rotating and translating target holder featuring an uncoated 5" diameter fused silica (SiO_2) substrate as the target, polished to $\lambda/20$ flatness on both sides. The target surface is scanned with precise control over the shooting position and rotation speed, maintaining adequate spacing between two consecutive laser shots. Once a full circle of shots at a given radius

is completed, the target is translated laterally by typically $100\ \mu$m to commence a new circular shot pattern.

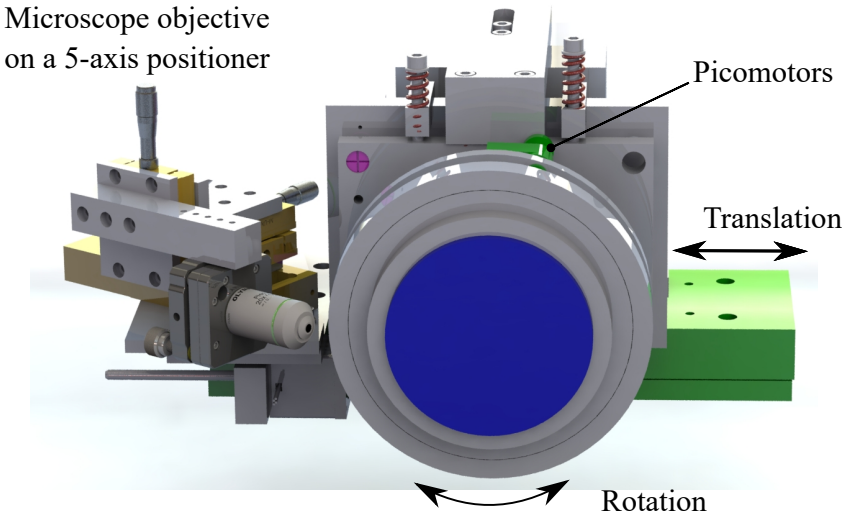

Figure 5.3: A 3D sketch of the kHz target positioner. Target substrate is shown in blue.

Target command-control: It relies on an Arduino micro-controller board which continuously tracks the radial and angular position of shots on-target. The target rotation speed is fixed by the set shot spacing (typically $100\ \mu$m) and has to be adjusted every time the radial shot position on target changes. A LabVIEW-based interface communicates with the target controller and calculates the optimal target motion sequence depending on the chosen shot parameters (desired shot spacing, burst or continuous mode, etc). It also triggers the shot sequence as well as the secondary emission diagnostics. For a $100\ \mu$m spacing between two consecutive shots, a 5" target can accommodate up to 1.3 million consecutive shots per face, which translates to > 20 minutes of continuous operation at 1 kHz. In practice, we shoot in a burst of 100 ms per acquisition and one target substrate lasts up to approximately a month.

Non-invasive target monitoring: To ensure identical interaction conditions shot-to-shot, the moving target surface is non-invasively monitored and stabilized using a Mach-Zehnder interferometer (figure 5.4). A frequency stabilized Helium-Neon (HeNe) laser source (frequency drift $< \pm 3$ MHz) with a coherence length of several hundreds of meters allows to have highly unbalanced interferometer arms and therefore total flexibility in the layout of the Mach-Zhender interferometer around the target holder. The HeNe is collimated to ≈ 1 cm beam size and sent into the Mach-Zhender interferometer, where one arm is reflected-off an unused portion of the target and the second arm is reflected off a fixed flat mirror in the chamber. Both the arms are then recombined with a small horizontal angle between them, resulting in vertical fringes as shown in figure 5.4. The fringe contrast is maximized by balancing the beam intensities of both arms of the interferometer. A CCD camera placed outside the vacuum chamber records the interference pattern online. As the target rotates, the relative change in the orientation and position of the target induces a change in the interference pattern: a deviation in the azimuthal and tangential angle leads to a tilt of the fringes (figure 5.4(b)) and a change of the

fringe spacing (figure 5.4(c)), respectively, and a change in depth leads to a lateral shift in the fringe pattern (figure 5.4(d)).

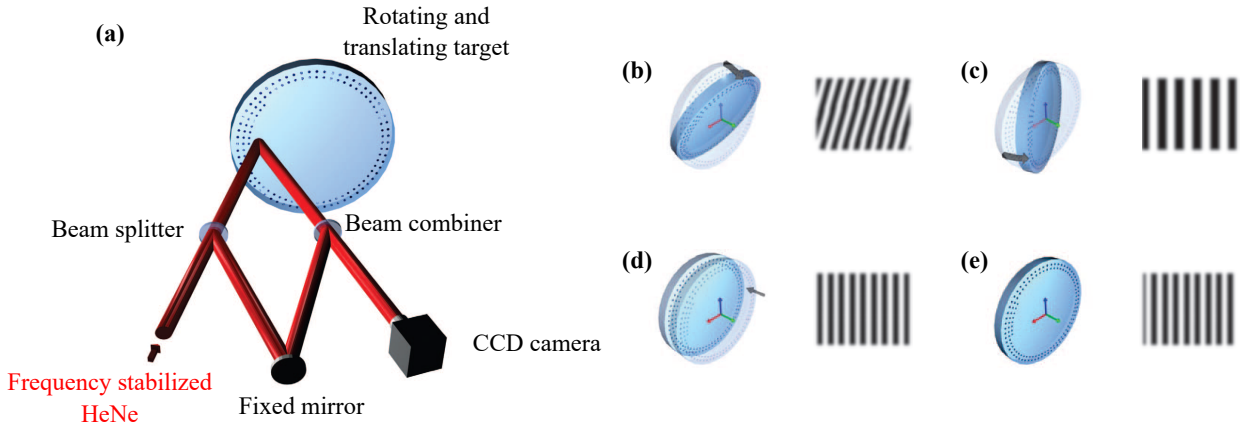

Figure 5.4: A Mach-Zehnder interferometer setup for non-invasive monitoring of the target surface motion (a). Typically recorded interference fringe pattern as a result of change in azimuthal (b), tangential (c), , and depth (d), w.r.t an initial position (e). Adapted from [303].

Passive stabilization: The target holder is equipped with two diametrically opposed linear picomotor actuators, which provide sub-μrad control over the target precession angle. The above mentioned interferometry setup is used to measure and thereby minimize the relative motion of the target surface. Figure 5.5 shows the residual target motion recorded over a few revolutions, measured after the target precession has been minimized. The target surface motion in depth could be minimized to $\approx z_R/5$ peak-to-valley, where $z_R \approx 10\,\mu$m is the Rayleigh range of the driving laser. The angular deviations could be reduced down to $< 80\ \mu$rad peak-to-valley. These measurements were made at the very edge of the target where precession is the greatest and can therefore be considered to be the upper limit in stability. The residual target motion is limited by the mechanical stress induced by the target's rotary bearing and the target surface quality itself.

5.3 Shooting sequence

We use two shutters before the main focusing OAP: (1) "Slow" shutter: a ceramic disc mounted on a slow flip mount with an opening/closing time of ≈ 500 ms, and (2) "Fast" shutter: a high-speed mechanical beam shutter (*Uniblitz*) which is 45 mm in diameter with an opening time of 14 ms and a closing time of 44 ms. The slower ceramic shutter is used to protect the fast shutter from over heating in-between acquisitions due to the laser's high average power (~ 3 W).

Figure 5.6 shows a timing diagram of the shooting sequence. As soon as the target controller receives the command to **SHOOT**, after ensuring that there is adequate space at the radial position of the target to complete the desired shot sequence, the target controller starts accelerating the rotation motor. Once the target is rotating with the desired speed and is at the right shooting position, the slow and the fast shutters are triggered in sequence. Once the fast shutter is completely open, all the diagnostics are triggered for the desired sequence length (typically 100 ms). Finally, both the

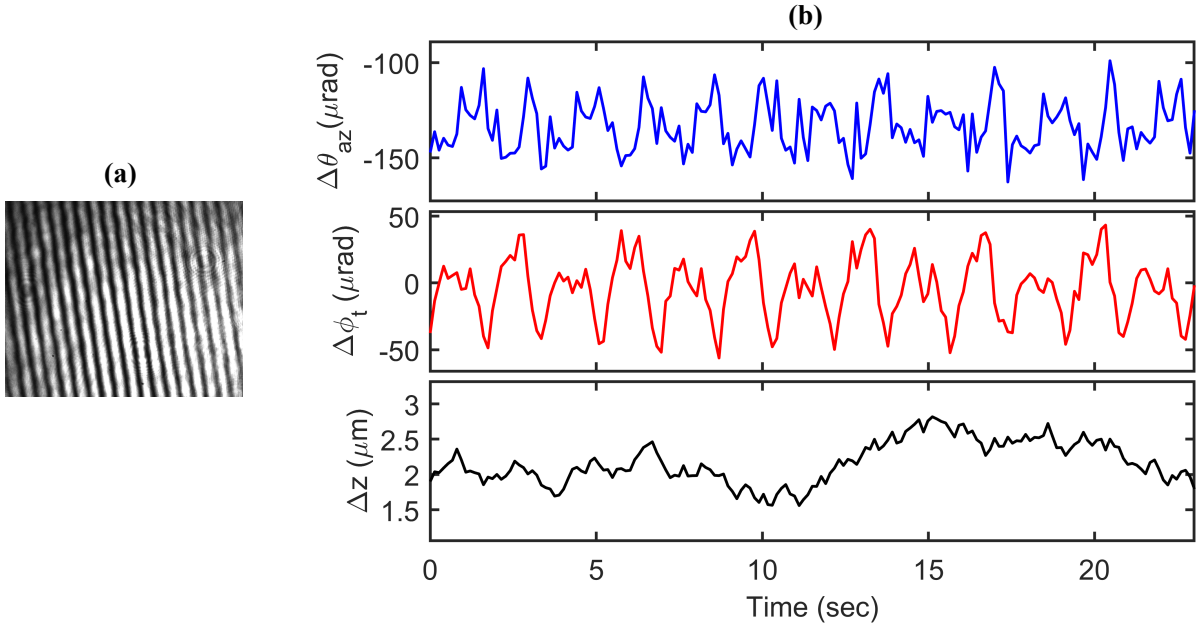

Figure 5.5: Fringes measured using the Mach-Zehnder interferometer (a). Residual target motion measured over a few revolutions in tangential (top), azimuthal (middle) and depth (bottom) (b).

slow and fast shutters are triggered again to their closed position. After the sequence is complete, the target is slowly decelerated and waits for the next command. Once a full circle at a given radius on the target is completed, the target is translated laterally, typically, by 100 μm and the target rotation speed is adjusted according to the new radial position.

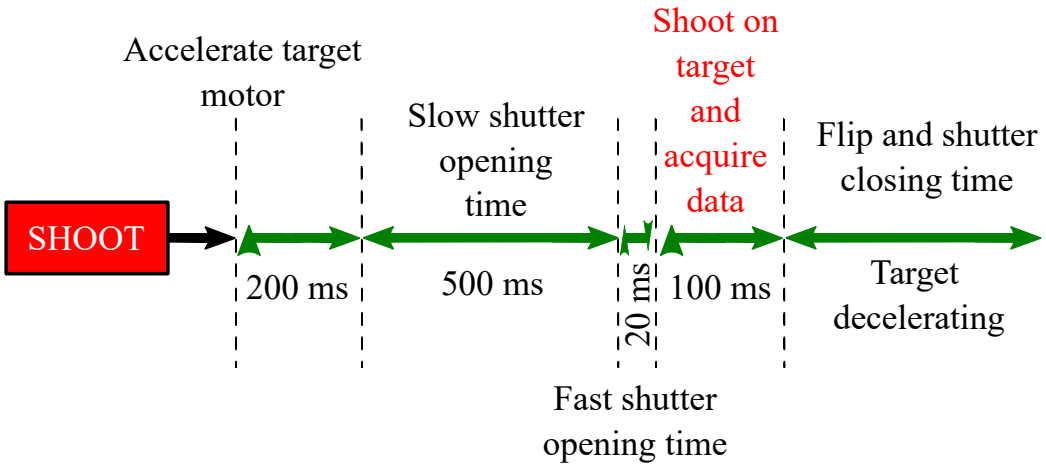

Figure 5.6: Timing diagram of the shooting sequence.

5.4 XUV detection

The HHG in the XUV spectral range emitted in the specular direction is routinely characterized spectrally using a fixed home-built imaging XUV spectrometer. In addition, the XUV spatial-intensity beam profile is measured using an insertable dedicated setup. Within this configuration, the spatial-intensity detector can be exchanged for an XUV wavefront sensor to characterize the wavefront of the XUV beam and estimate its focussability.

5.4.1 XUV Spectrometer

The spectral properties of the HHG emitted in the XUV regime are routinely measured using a fixed home-built imaging XUV spectrometer, illustrated in figure 5.7. It comprises majorly of: (1) a concave grating, (2) a micro-channel pate (MCP) coupled to a Phosphor screen, and (3) a CCD camera. A spatial mask in the form of a rectangular slit is positioned at the entrance of the spectrometer (close to the grating). The entire setup is shielded from ambient light using aluminum plates and foils.

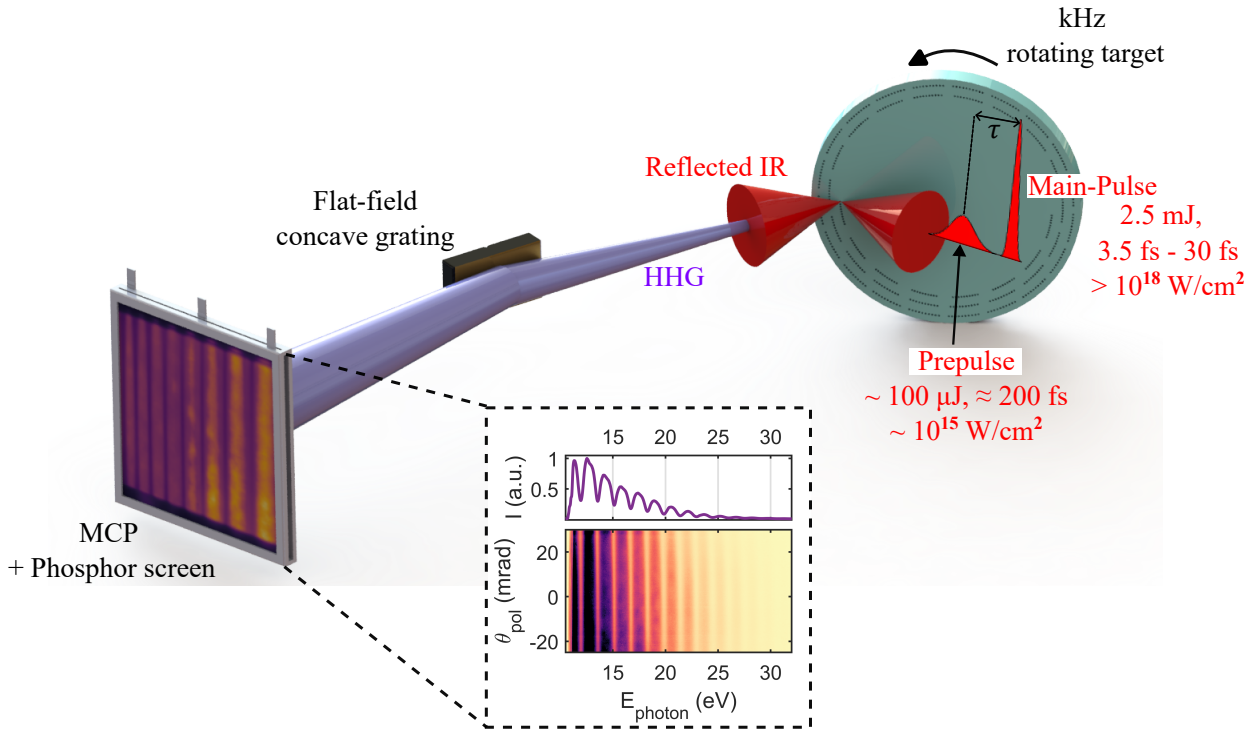

Figure 5.7: A schematic drawing of the XUV spectrometer with an inset showing a typically recorded XUV spectrograph with calibrated energy and divergence axis, and an integrated XUV spectrum is displayed on top.

Detection range: In order to observe the transition between the CWE and ROM regimes, we are particularly interested in detecting HHG around the maximum plasma frequency, ω_p. In our case, for a fully ionized fused silica target, $\omega_p \approx 30\,\text{eV}$. Consequently, the detection range was chosen to be around 10 eV to 56 eV, corresponding to $\lambda = 22\,\text{nm}$ to $124\,\text{nm}$.

Concave grating: We use an aberration corrected flat-field gold coated concave grating from Hitachi (001-0639), with 600 groves/mm, optimized for wavelengths, $\lambda \approx 22 - 124\,\text{nm}$. A high quality gold coating as well as use at a near-grazing incidence angle, $\alpha = 85.3°$ allows for an excellent reflectivity of $\approx 90\%$ in the desired spectral range. The concave grating allows to image in the horizontal dimension the $\approx 1\,\mu$m size HHG source spot on the PM surface, and spectrally disperses it onto an image plane. A flat-field concave grating allows to both focus and disperse light, thereby reducing losses and minimizing defocus in the detector plane. The beam propagation is hardly influenced in the vertical dimension which adds angular resolution to the resulting spectrograph.

MCP and Phosphor screen assembly: The resulting spectrograph is imaged on a large, $93\ \text{mm} \times 75\ \text{mm}$ single-stack MCP (*Photonis Scientific*) placed in the tangential focal plane. The MCP, biased at 1kV, functions as a particle amplifier, turning a single impinging XUV photon into a cloud of electrons. The MCP is time-gated for 200 ns synchronously with the laser pulses to suppress the background signal from longer incoherent plasma emissions. To obtain 200 ns HV pulses, we used to use an HV driver from Quantum Technology (HVP-5LP-1KV-300P-5PS) adapted for our high load capacitance of $\sim 280\ \text{pF}$. However, this driver did not allow for any protection against electrical shorts and eventually had to be replaced with a DC HV driver from Photek (DPS2) coupled to a gating module adapted for a high load capacitance (GM-MCP3-500), capable of gating the MCP to a window as short as 10 ns, thereby further suppressing the detection of background plasma emissions. The MCP is coupled to a glass plate coated with P46 Phosphor, continuously biased at 3 kV to attract electrons and convert them to visible light with a maximum emission at 530 nm. The Phosphor screen has a decay time of $\approx 300\,\text{ns}$ enabling detection at kHz repetition rate while avoiding saturation effects.

CCD camera: The phosphor screen is imaged on a 12-bit CCD camera (PCO Pixelfly QE) placed outside the vacuum chamber. The camera has a maximum quantum efficiency of 65% at $530\ \text{nm}$, features a digital temperature compensation to reduce detection noise, and is hardened against high external magnetic fields. The high dynamic range allows to detect high harmonics near the CWE cut-off, where the signal drops quickly with the harmonic order. Additionally, an Ethernet readout via a PCI board allows a fast serial data up-link.

After the imaging system is carefully calibrated, the x and y coordinates in the MCP plane along the horizontal and vertical dimensions respectively are transformed into nanometers and radians. A typically recorded XUV spectrograph is shown in figure 5.7. Notably, the divergence and the wavelength axes are calibrated while the intensity is remains in arbitrary units.

5.4.2 Spatial-intensity profile detection

Measuring the spatial intensity distribution of the XUV beam is quite challenging as it is difficult to catch the full beam due to its high divergence and the tight space in the interaction chamber. Also, when using detectors like MCPs, they have to be well shielded from electrons emitted from the PM itself as they can traverse through or create a spurious electron avalanche in the MCP channels and hit the phosphor screen, thereby polluting the XUV signal. For the spatial measurement of the XUV beam, after several attempts accompanied with modifications and upgrades each time, we could finally find an arrangement that works. A schematic layout of the measurement setup is

shown in figure 5.8. It was designed such that the spectral and spatial characterization could be made under similar conditions, in particular without opening the chamber. An insertable amorphous Silicon-plate was placed at $\approx 10\,\text{cm}$ from the point of interaction, at a near-grazing incidence angle (tunable, $70° - 80°$), mounted on a motorized linear translation and a rotation stage, steering the reflected XUV beam towards another large MCP coupled to a phosphor screen (VTC Baspik). The MCP has an active area of $96\ \text{mm} \times 96\ \text{mm}$, large enough to measure the full XUV beam profile. The detection resolution is limited by the channel diameter of $15\,\mu\text{m}$. It is biased at 1 kV, time-gated for 250 ns synchronously with the laser pulses using another suitable HV driver adapter for a high load capacitance (Axis Photonique). This MCP is coupled to a K-67 Phosphor screen with a peak spectral response at 550 nm and a decay time of $\approx 1\,\text{ms}$, biased continuously at 4 kV. Although this phosphor screen is slower as compared to the detector screen used in the spectral characterization setup, we were still able to detect at 1 kHz while avoiding saturation effects in a burst shooting mode. The Phosphor screen is finally imaged by a CCD camera through an narrow-band spectral filter at 550 nm.

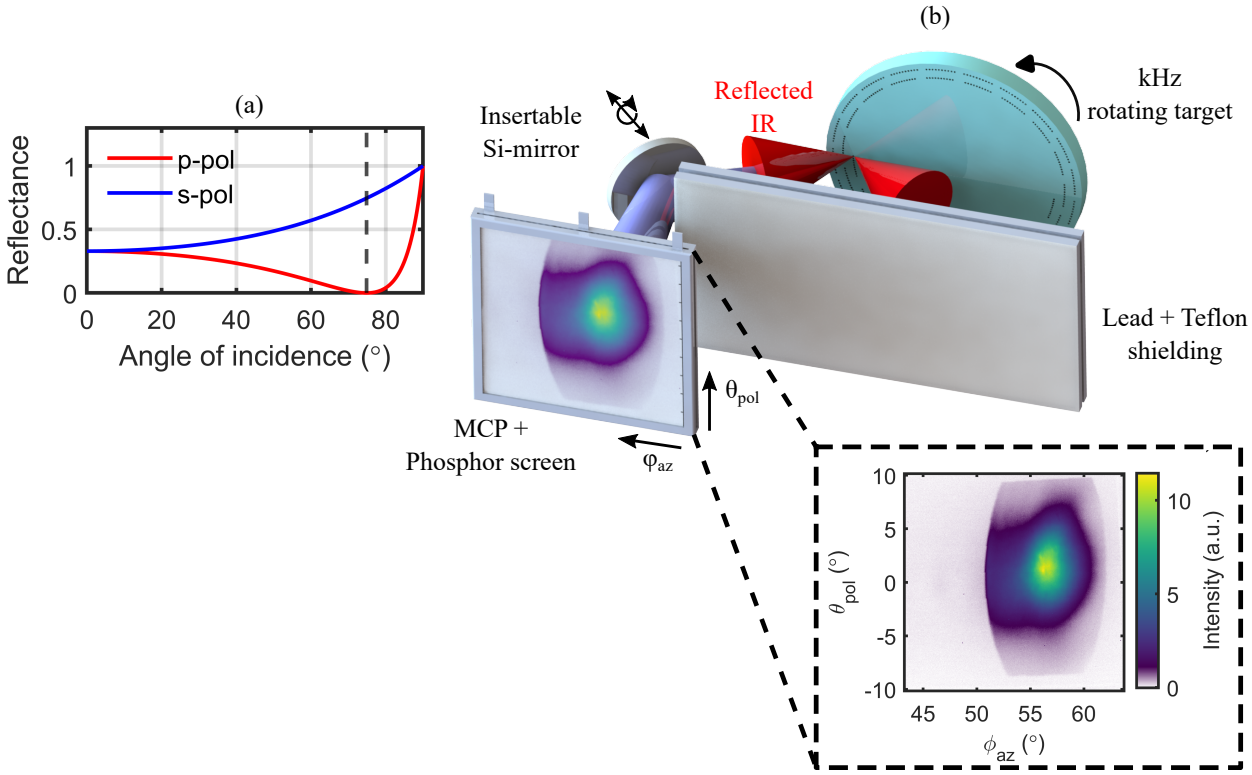

Figure 5.8: Reflectivity of Silicon at 800 nm for incident p-pol and s-pol laser pulses (a). The minimum reflectivity is obtained at the Brewster angle for a p-polarized laser pulses. A 3D sketch of the experimental setup measuring the spatial-intensity profile of the generated XUV beam (b). The Silicon-plate is mounted on a linear translation as well as rotation for accurate positioning. An inset shows a typically recorded XUV beam profile.

It is critical to shield the camera from ambient light. The MCP itself is blind to the reflected IR-visible light (i.e. no primary electrons are created and amplified in response), but in case of a single-stack MCP, SHG upon reflection on the PM can leak through the channels, hitting the phosphor screen which scatters and also partially transmits this light, producing an additional background on

the detector. Also, in case of few-cycle driving laser pulses, the laser spectrum itself overlaps with the Phosphor screen emission. Typically, very thin aluminum filters ($\sim 100-200$ nm thick) are used to block the IR-visible light steered towards the MCP. However, the large size of the detector in our case requires large and thin Al filters are extremely expensive, easily damaged by debris from the target, and make vacuum handling very cumbersome. To avoid using fragile aluminum filters: (1) We use the silicon-plate at near-Brewster angle incidence ($\approx 75°$) to minimize steering of IR light towards the MCP (figure 5.8(a)), (2) we use a narrow-band interferometric filter at 550 nm in front of the camera, and (3) we also use aluminum plates and foil around the MCP and especially between the Phosphor screen and the camera to block any leaks. We also used a 5 mm thick plate of lead, sandwiched between two Teflon sheets to block energetic electrons emitted from the plasma mirror. Teflon plates around the lead plate help to avoid generation of hard X-rays when the electrons impinge on it.

5.4.3 Wavefront characterization

It is essential to accurately and reliably measure the wavefront of the emitted XUV beam as it would determine whether the HHG from the PMs can be refocused and finally be available for end-user experiments. This measurement setup was developed in the framework of a LaserLab campaign with Li LU (Shenzhen Technology University, China) and Philippe ZEITOUN (LOA). The primary objective was to characterize the wavefront of the emitted XUV beam and study its behavior with a wide range of laser-plasma parameters, and finally attempt to correct for the observed aberrations by introducing small aberrations in the driving IR beam.

Li LU and Philippe ZEITOUN developed a high-NA broadband Hartmann XUV wavefront sensor in collaboration with *Imagine Optic* to measure the XUV wavefront for the full spectral band in the XUV as well as for certain filtered harmonic orders, for tightly focused XUV beams [304], which is also suitable in our case.

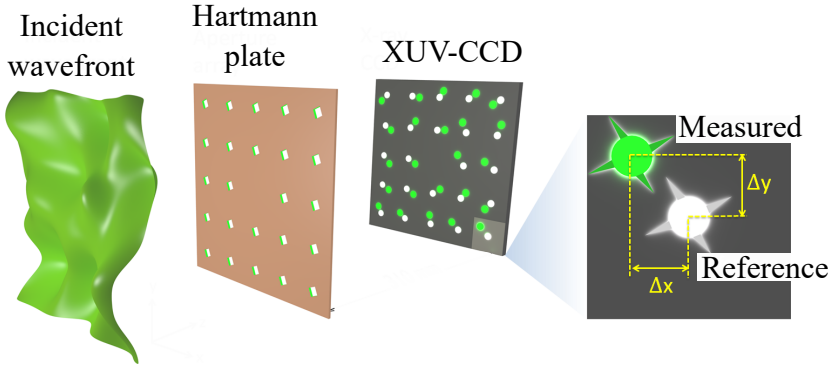

Figure 5.9: Principle of XUV wavefront detection using a Hartmann plate. The distorted wavefront (in green, on left) is incident on a Hartmann plate and the resulting diffraction pattern is recorded on an XUV CCD. The inset on the right shows the deviation of the measured diffraction pattern from the reference, which is used to calculate the wavefront profile. Adapted from [305].

XUV Hartmann sensor: The working principle of a typical Hartmann-type wavefront sensor is illustrated in figure 5.9. The wavefront is sampled by a plate with an array of holes made out of an opaque

material and the transmitted light is typically imaged on a CCD camera. The wavefront of a beam $w(x,y,z_0)$ is defined as a surface perpendicular to its local direction of propagation or the Pointing vector $S(x,y)$, at a position z_0 along the optical axis. The Hartmann plate splits in the incident beam to an array of sub-beams, which then propagate to the camera placed at a distance D. By computing the deviation of the measured centroid of each sub-beam $(\Delta x, \Delta y)_{ij}$ w.r.t to the reference position $(x_r, y_r)_{ij}$, we can determine the local wavefront gradient inside each sub-aperture.

$$\begin{bmatrix} \partial w/\partial x \\ \partial w/\partial y \end{bmatrix}_{ij} = \frac{1}{D} \begin{bmatrix} \Delta x \\ \Delta y \end{bmatrix}_{ij} \tag{5.1}$$

The reconstruction of the wavefront from these local gradients is performed by an optimized computation algorithm from *Imagine Optic* and projected onto a Zernike base.

The high-NA XUV wavefront sensor used in the scope of this work features a Hartmann plate made of Nickel, 36 mm in diameter, with $50\,\mu$m holes arranged with a pitch of $15\,\mu$m. The XUV diffraction pattern is captured by a soft X-ray CCD (Princeton Instruments) with a chip size of $27.6\text{ mm} \times 27.6\text{ mm}$, which is water-cooled to minimize dark-current noise. This configuration gives the sensor a numerical aperture of approximately 0.15. Further technical specifications are detailed in [304]. The sensor itself, with a footprint of approximately $80\text{ mm} \times 120\text{ mm}$, is mounted on a two-axis motorized translation stage for precise beam centering. Additionally, it is supported by a base plate equipped with four picomotor actuators, enabling fine adjustments in orientation and the precise alignment of the central blocked hole in the Hartmann plate with the CCD's center.

To measure the XUV wavefront, the same Silicon-plate steering assembly is used as for the spatial intensity measurement of the XUV beam. The MCP-phosphor detection assembly is simply replaced by the wavefront sensor. A $200\,$nm thick aluminum filter is used at the entrance of the sensor to block the IR radiation, ensuring that the setup is completely light-tight and no ambient light reaches the CCD. The Silicon-plate helps to suppress the IR when it is placed close to the Brewster angle ($\approx 75°$ for $\lambda = 800\,$nm). Additionally, the aluminum filter limits the detection range to $20-50\,$eV or $\lambda \approxeq 25-60\,$nm, which is towards the most energetic harmonics for our experiments.

5.5 Electron detection

5.5.1 Spatial charge distribution

Setup I: Compatible with simultaneous measurement of HHG

The angular electron charge distribution is measured with a $65\text{ mm} \times 60\text{ mm}$ scintillating screen [306] (Gd_2O_2S:Tb, LANEX fast, Carestream), converting electrons into visible light centered around 545 nm. A schematic illustration of the experimental setup for simultaneous detection of HHG and electron angular charge distribution is shown in figure 5.10. The LANEX screen is placed $\approx 20\,$cm from the

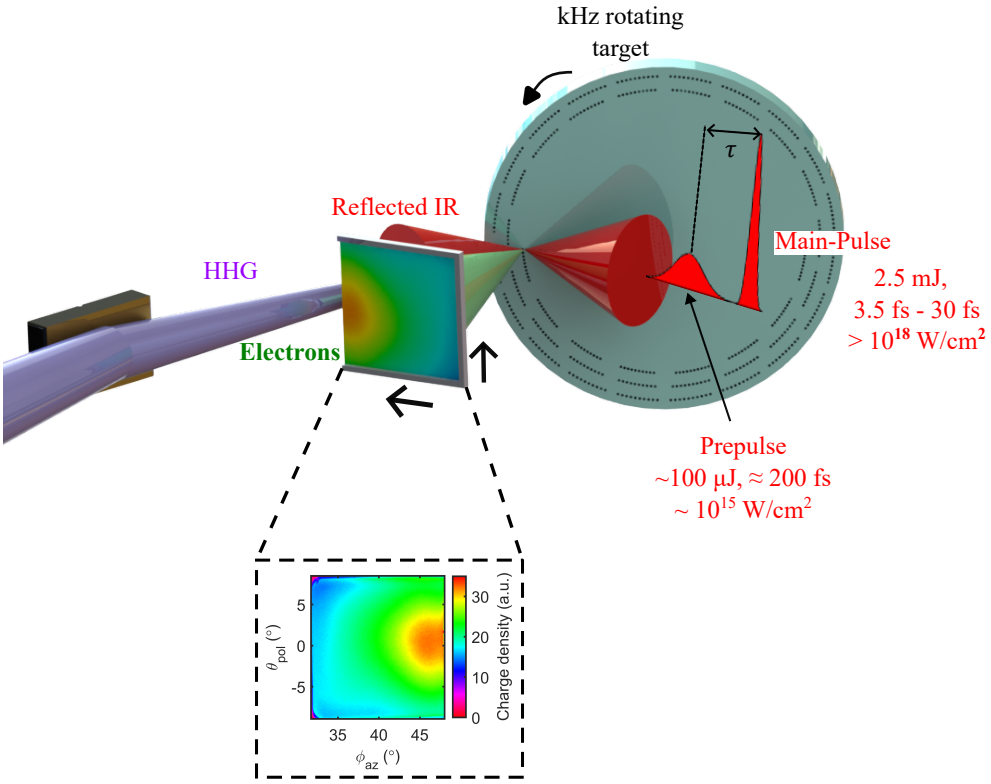

Figure 5.10: Experimental setup for simultaneous spatial detection of electrons and HHG spectrum. The LANEX screen is imaged by a CCD camera. The aluminum shielding from the back of the LANEX screen to the camera are omitted for clarity.

point of interaction, covering a small but sufficient angular range between the target normal and the specular direction, for $30^\circ < \phi_{az} < 50^\circ$, where ϕ_{az} is the angle w.r.t the target normal in the plane of incidence, as depicted in figure 5.10. The size and the placement of the screen was chosen such that the XUV spectrometer is simultaneously operational. The front side of the LANEX screen is covered with a $15\ \mu$m thick Aluminium foil to block visible light and low-energy electrons ($E_k < 150$keV). Detection of low-energy electrons is also suppressed by the substrate of the LANEX screen itself. The green light emission of the LANEX screen is imaged by a CCD camera through an interferometric band-pass filter centered at 545 nm. The decay time of such a LANEX screen is typically $\lesssim 1$ ms [307] and hence, these screens are compatible for operation at a kHz repetition rate.

Setup II: Wide-angular-range electron detection

Alternatively, we have another setup for measuring the angular charge distribution of electrons with a wider angular coverage, where we use a larger LANEX screen to look at the full electron beam (figure 5.11). Here, we use a $177\ \text{mm} \times 60\ \text{mm}$ LANEX screen (regular, Carestream), increasing the detection range to $18^\circ < \phi_{az} < 72^\circ$. However, due to the large size of the screen, the XUV spectrometer is completely blocked, introducing an uncertainty in ascertaining correlations between the electrons and HHG. Nevertheless, it is well established that both the electron emission and HHG in the relativistic regime are optimized when the target is in the laser focal plane, which is already a good indication of their interdependence.

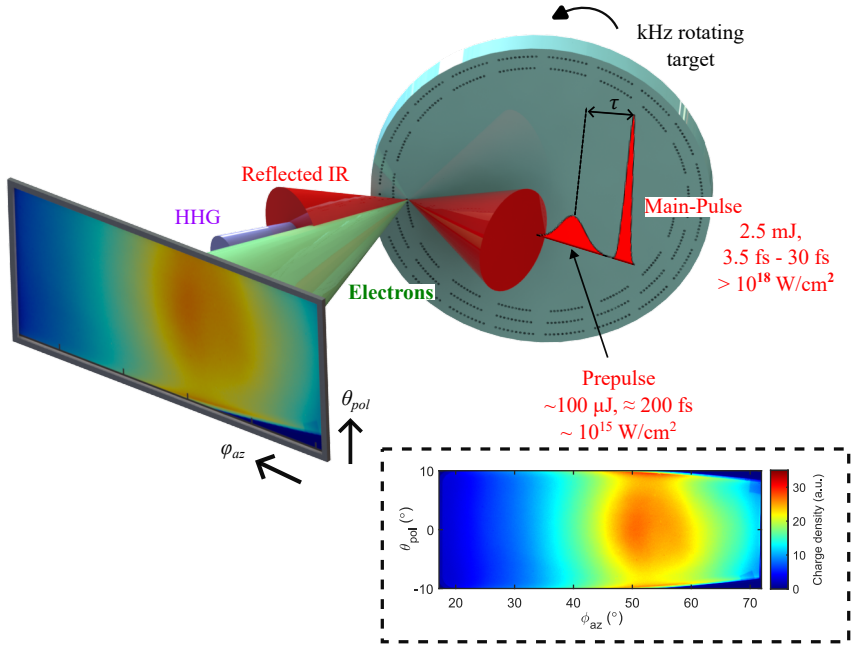

Figure 5.11: Experimental setup for the spatial electron detection with the big LANEX screen covering $18^\circ < \phi_{az} < 72^\circ$. An inset displays a typically recorded electron charge distribution with calibrated θ_{pol} and ϕ_{az} axes. Target normal and specular directions are located at $\phi_{az} = 0^\circ$ and $\phi_{az} = 55^\circ$.

Both the setups described above have not been calibrated for the deposited electron charge. For a proper charge calibration, we need to take into account the response of the LANEX screen, transmission of the interferometric filter as well as the objective lens in front of the camera, ans response of the CCD. Most calibration platforms available use several 10s of MeV electrons. However, in our case, the electron energies are in a few-MeV range, in which the LANEX screen response varies rapidly [306]. Thus, in our case, charge calibration of the detection setup is far from trivial.

5.5.2 Magnetic electron spectrometer

The electron energy spectrum is measured by inserting a purpose-built magnetic electron spectrometer in front of the LANEX screen (setup I). The electron spectrometer design is illustrated in figure 5.12. It comprises of a 0.5 mm pinhole in a Lead-disk located at ≈ 90 mm from the point of interaction, followed by a separately insertable pair of Neodymium magnets ($B_0 \approx 80$ mT over ≈ 20 mm). The pinhole is used to sample the electron beam at a variable angle ϕ_{az} selected by the insertion position with an angular acceptance of $\approx 0.4^\circ$. In order not to block the HHG beam, ϕ_{az} is limited to values $< 40^\circ$, which is often slightly off the electron beam center. The magnetic field map has been measured with a Hall probe and injected into a numerical electron trajectory calculation to calibrate the electron energy Vs the position along the trace of deflected electrons on the LANEX screen (figure 5.13 (left-panel)). The calculated energy-dependent resolution of our electron spectrometer is shown in figure 5.13 (right-panel). An example of a calibrated electron spectrometer trace is depicted in figure 5.12.

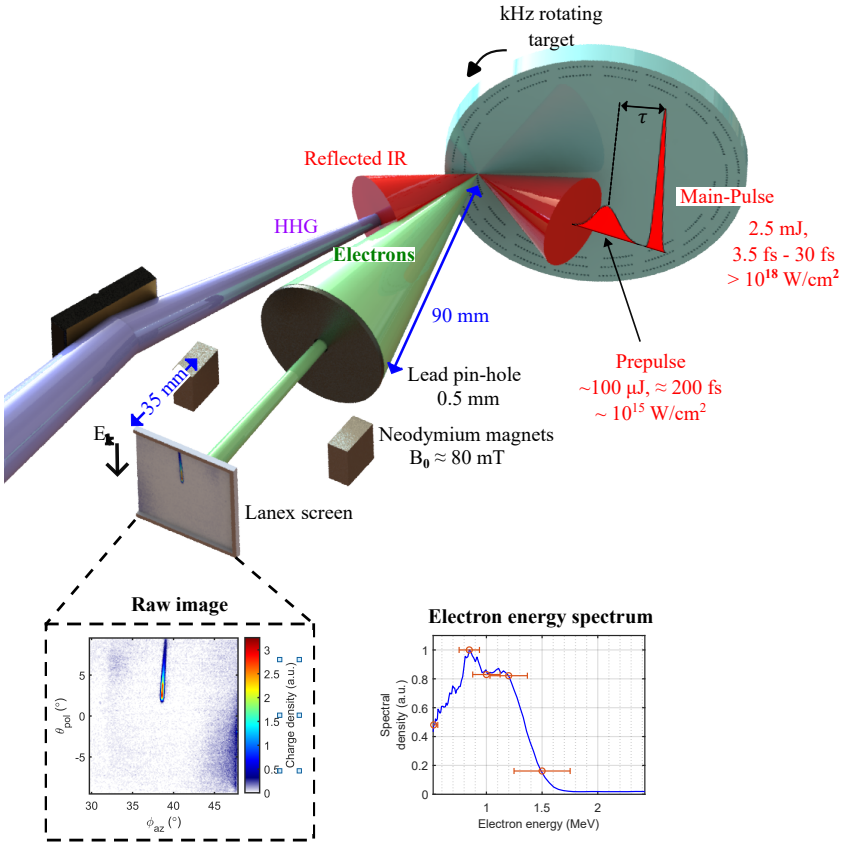

Figure 5.12: Experimental setup for simultaneously measuring the HHG and electron spectra. The pinhole is positioned at variable ϕ_{az}, with $\theta_{pol} = 0°$. A typical raw electron spectrum image recorded after inserting the magnets (bottom-left) alongside the corresponding calibrated electron spectrum (bottom-right). The error-bars are calculated from the simulated energy-dependent resolution of electron spectrometer in figure 5.13. The shielding mechanics around both HHG and electron spectrometers are omitted for the sake of clarity.

5.6 Ion detection

Protons accelerated from the front-side, along the target normal are characterized spectrally and spatially using a fixed Thomson Parabola Spectrometer (TPS) and an insertable, scanning time of flight detector (TOF) respectively. Characterization of the accelerated ions was performed within the framework of another LaserLab campaign, in collaboration with Dan Levy, Victor Malka and Eyal Kroupp (Weizmann Institute). The TPS was designed to be modular with all the components mounted in a separate small chamber and could simply be connected to the main interaction chamber, installed with the help from Dan Levy. The TOF detector was designed and calibrated by Eyal Kroupp.

5.6.1 Thomson Parabola Spectrometer

The TPS is one of the most widely used devices to measure the energy spectrum of ions in the laser-plasma community. It is based on the principle of a mass spectrometer, first introduced by

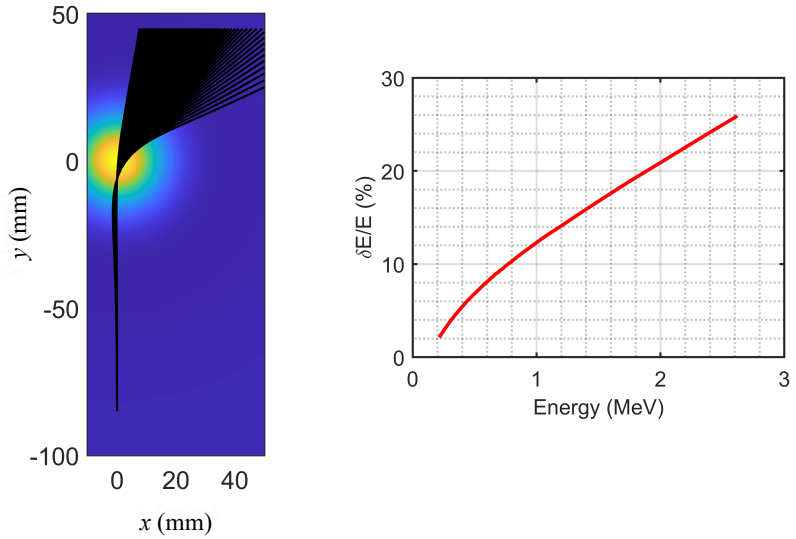

Figure 5.13: Simulated electron trajectories (in black, left panel) and the corresponding energy-dependent resolution of the electron spectrometer (right panel).

J. J. Thomson in 1911 [308]. Depending on their charge-to-mass ratio, ions are dispersed by parallel electric and magnetic fields, tracing a parabolic trajectory on the detector. A TPS consists of five main elements: a filtering pinhole, high voltage electrodes (electric field E), permanent magnets (magnetic field B), a light-emitting screen, and a camera. Figure 5.14 shows a schematic representation of the TPS connected to the main interaction chamber. The proton beam is spatially filtered by a $300\ \mu$m pinhole placed at ≈ 60 cm from the point of interaction, along the target normal direction. An electric field strength, $E = 2$ kV/cm is achieved through a pair of parallel Copper-electrodes raised to 2 kV. Permanent magnets yield an average field strength, $B = 0.32$ T. The dispersed ions are converted to electrons and the signal is amplified by several orders of magnitude by an MCP placed ≈ 210 mm from the far-edge of the magnets. The electrons are accelerated towards a phosphor-coated glass plate coupled to the MCP, emitting light at 545 nm with a decay time of < 1 ms. Finally, the phosphor screen is imaged by a CCD camera outside the TPS vacuum chamber.

A typically recorded raw TPS trace and the corresponding extracted proton energy spectrum is shown in figure 5.14. The origin or the point of "zero-deflection" is the point where the undeviated neutral particles and photons from the source hit the detector. In the small deflection approximation, the coordinates of the deflected particles with a charge-to-mass ratio of Z/M ($M = Am_p$, A is the mass number and m_p is the proton mass), passing through nearly homogeneous electric and magnetic fields, on the detector plane located at a distance D, are given by [309]:

$$x = Ze\frac{E}{E_p}\frac{lD}{2} \text{ and } y = Ze\frac{B}{\sqrt{Am_pE_p}}\frac{lD}{\sqrt{2}} \tag{5.2}$$

where E_p is the kinetic energy of the detected charged particle, l is the length of the electric and magnetic field plates. Due to their smallest Z/M, protons undergo maximum deviation and can be easily identified on the TPS trace. For a fixed value of E and B, all protons fall on the same parabolic trace, on points depending on their kinetic energy. An example of the extracted proton

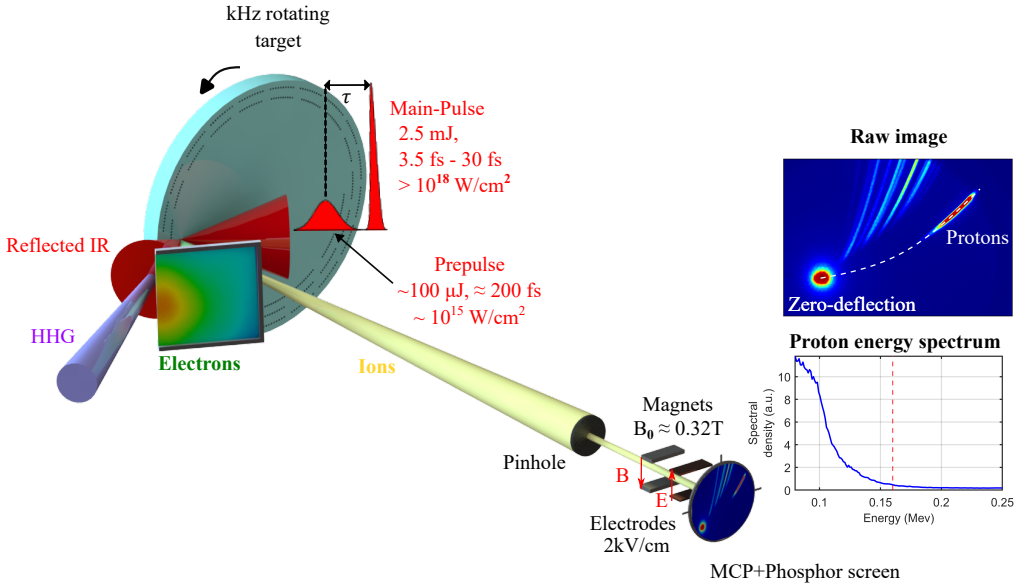

Figure 5.14: TPS experimental setup for measuring the proton energy spectrum along the target normal direction. A typically recorded raw TPS image (top-right) and the corresponding extracted proton energy spectrum (bottom-right). The dotted white line traces the proton trajectory from the point of zero-deflection.

energy spectrum in figure 5.14 is obtained after averaging the values along the proton curve width, after subtraction of a mean background curve which is located in parallel to the signal below it. The cut-off energy is defined as the highest energy where the total signal minus the standard deviation of the background is locally smaller than the total background. The principal source of error in determining the maximum energy is geometric, i.e. the spatial extent of the ion source on the detector which manifests itself in the proton curve width. We find the relative error in our geometry to be, $\Delta E_k/E_k \approx 0.072\sqrt{E_k}\,(\mathrm{MeV})$.

5.6.2 Time of flight detector

The angular profile of the accelerated ion beam is measured with an insertable, scanning TOF detector. A schematic representation of the TOF measurement setup is illustrated in figure 5.15. It consists of a 6 mm diameter MCP biased at 600 V, placed ≈ 37.5 cm from the point of interaction, mounted on a motorized linear translation stage, moving nearly parallel to the target surface. For each stage position, the transient MCP current was read out for 100 consecutive shots using a *KEYSIGHT MSOS804A* 8 GHz oscilloscope capable of individually recording all ~ 100 shots in one acquisition when operated in segmented memory acquisition mode. The TOF-MCP has an angular acceptance of $\approx 0.9^\circ$ which is small enough to neglect the convolution owing to the finite size of the detector.

Figure 5.16 also displays an example TOF trace recorded for 27 fs driving laser pulses, without a prepulse, i.e. $\tau = 0$ ps and at the target normal direction ($\phi = 0^\circ$). The solid blue line shows an average of 100 consecutive shots, smoothed by a rolling average over the response time of the detector (≈ 1 ns). The shaded gray area shows the standard deviation of the shots. The first sharp peak corresponds to the electromagnetic radiation emitted from the laser-plasma interaction and defines

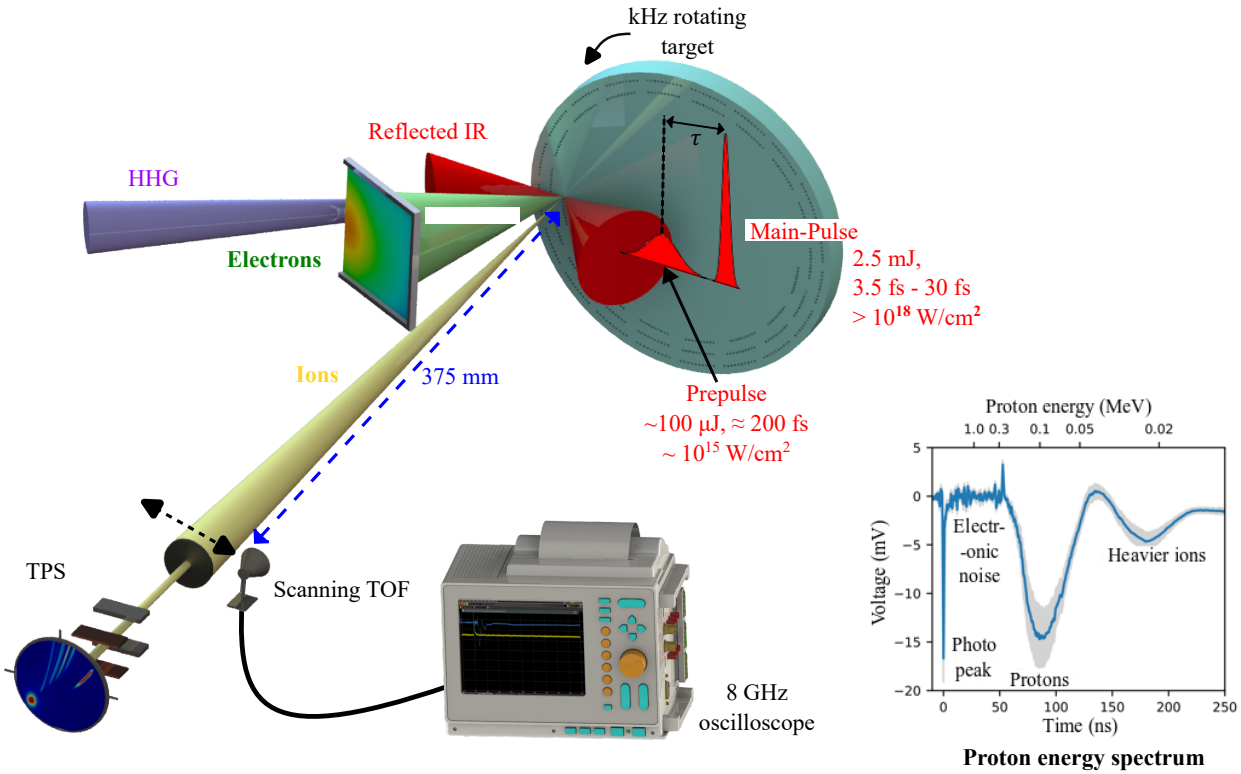

Figure 5.15: Experimental setup for measuring the angular profile of the proton beam using a scanning TOF detector.

the time $t = 0$. The first protons start to arrive at $t \approx 50$ ns, with a peak signal at $t \approx 90$ ns, followed by the heavier ions with a signal peaked at $t \approx 180$ ns. The onset of overlap with the carbon ions' TOF signal gives the lower bound at ≈ 50 keV of the proton energy range for the TOF detector. The noise at ≤ 51 ns was ever-present in all the measurements and is suspected to be due to electrical noise in the read-out circuit. Due to this degradation in signal-to-noise ratio, at energies $\gtrsim 0.3$ MeV, the energy spectrum is more reliably measured with the TPS. Figure 5.16 shows the extracted proton energy spectrum alongside the spectrum extracted from the TPS measured under the same conditions and averaged over 100 consecutive shots. At energies beyond 0.11 MeV the two curves follow together fairly closely, showing a cut-off energy at around 0.25 MeV followed by noise. The decline in the TPS spectrum below 0.11 MeV is due to the signal reaching close to the edge of the MCP.

The TOF detector was calibrated by Eyal Kroupp at Weizmann Institute. A schematic diagram of the calibration setup is shown in figure 5.17(left-panel). It allows to simultaneously record signals from a a ring-like Faraday cup and from the TOF detector. The charge transmitted by the Faraday cup is calculated from first principles and is compared with the TOF signal. Thus, we can estimate the amplification factor of the TOF-MCP. The system is based on a HV Thyratron switch capable of switching at 15 kV at ~ 5 ns. The negative pulse output is connected to a carbon brush emitting electrons at < -3 kV. The radial homogeneity of charge area density was measured by using another Faraday cup, positioned concentrically with the ring-like Faraday cup instead of the TOF detector, thus comparing the signals of the two Faraday cups (accounting for their different areas). Figure

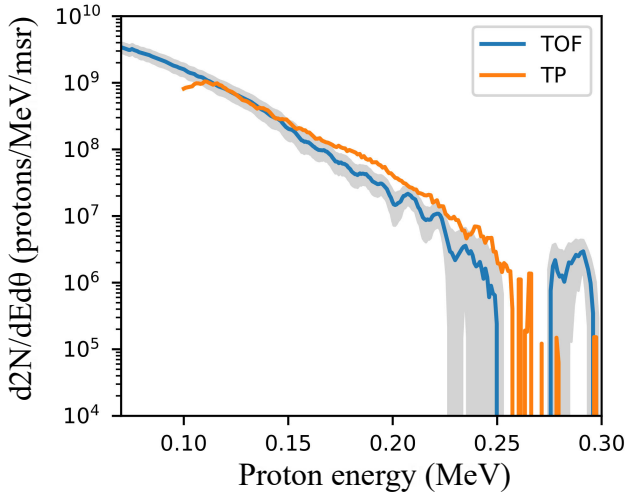

Figure 5.16: A comparison of the proton spectrum recorded with the TPS and the TOF ($\theta = 0°$) under similar driving conditions.

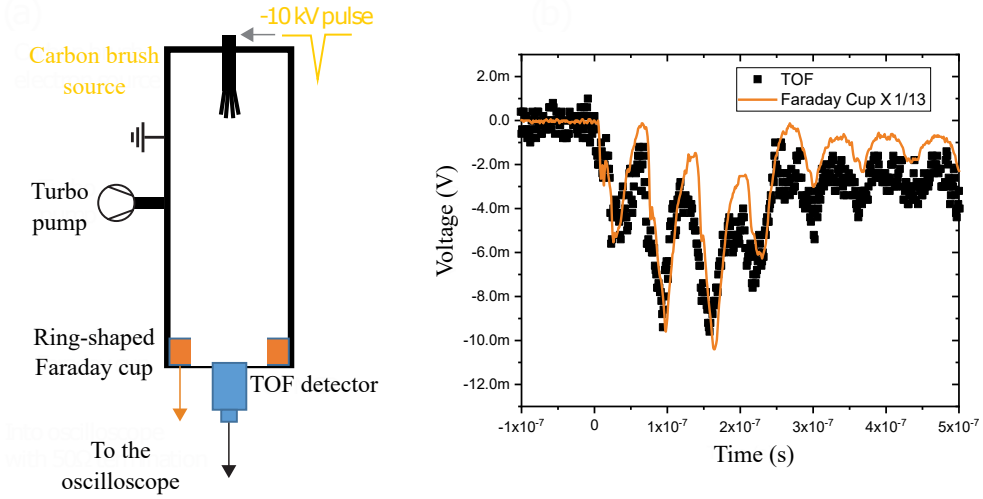

Figure 5.17: Schematic diagram of the calibration setup for the TOF detector (left) Simultaneously measured TOF and the Faraday cup signals. In this shot the Faraday cup signal is divided by 13 to fit the TOF signal. Courtesy of Eyal Kroupp.

5.17(right-panel) shows the simultaneous measurement of both TOF and Faraday cup signals. In order to estimate the MCP amplification factor, we divide the Faraday cup signal by a constant factor so it fits best with the TOF signal. We estimate a 10% fitting uncertainty in deriving this constant, which dominates the other possible sources of error. The MCP amplification factor was found to be 3 ± 0.3.

5.7 Plasma density gradient calibration

The time-delayed Prepulse is focused onto the target to create a near-solid density plasma. Ions govern the inertia while electrons drive the plasma pressure. Due to a thermal imbalance between the plasma (~ 100 eV) and the zero-pressure in the interaction chamber, the plasma expands towards vacuum with a speed c_s. The plasma density gradient scale length, $L_g \approx L_0 + c_s\tau$, is scanned by varying the lead time τ of the Prepulse before the Main-pulse. Here, L_0 is the scale length increase due to the finite temporal contrast of the Prepulse. One way to characterize the plasma density gradient is using the frequency domain interferometry (FDI) [310–314]. In this technique, a femtosecond probe beam is split into two copropagating replicas with an adjustable delay. The first replica is reflected off the bare target surface and the second is reflected after a plasma expansion has been triggered on the target surface. The plasma spatial profile is reconstructed by analyzing the spectral modulations resulting from the interference of the two replica beams using an imaging spectrometer. Due to its interferometric nature, FDI offers an exceptionally high resolution of $\lambda/2000$. However, it is rather complicated to implement experimentally especially in a running PM experiment.

Alternatively, a shearing interferometry based technique, as proposed by Adumi *et al.* [315] and was used in a PM experiment by Jan *et al.* [63] to measure the electron density profile of an expanding plasma. In this method, a separate frequency-doubled probe beam propagates parallel to the target surface a certain delay after the plasma initiation. This technique measures a 2D spatial map of the plasma induced phase shift, enabling the determination of the electron density distribution. Although this technique reveals additional information about shape of the plasma density gradient, it is rather complex to implement in our setup due to the tight focusing geometry.

Spatial Domain Interferometry

In our experiments, we use another technique that was developed in the PCO group a few years ago, called the Spatial Domain Interferometry (SDI) technique [316], illustrated in figure 5.18. It is a fairly simple pump-probe "spatial" interferometry technique. The plasma expansion on the target surface is initiated by the Prepulse or the pump beam. The Main-beam is diffracted through a periodic transmission mask, creating a diffraction pattern in focus such that the 0th-order spot is reflected-off the expanding plasma while the 1st-order spots are reflected-off the bare target surface. The plasma induced phase shift $\Delta\phi$ between the 0th-order and 1st-order spots leads to spatial interference pattern of the reflected probe beam in near-field. The 0th-order of the Main-beam is considered to reflect on the critical-density surface at depth x_{c}, where the electron density is $n_e = n_{\text{c}}\cos^2\theta_i$, with $n_{\text{c}} = \omega_0^2 m_{\text{e}}\varepsilon_0/e^2$, the laser carrier angular frequency ω_0, the electron mass m_{e}, the vacuum permittivity ε_0 and the electron charge e. The phase shift due to the reflection at $x = x_{\text{c}}$ rather than at the initial target-vacuum boundary at $x = 0$ is given by (as in Bragg reflection)

$$\phi = 2\frac{\omega_0}{c}x_{\text{c}}\cos\theta_i. \tag{5.3}$$

Dephasing due to propagation through the low-density tail of the plasma is at least an order of magnitude smaller and is thus neglected. The measured phase shift as a function of the Prepulse lead time τ thus tracks the position of the critical density surface, $x_{\text{c}}(\tau)$. Imposing an exponential

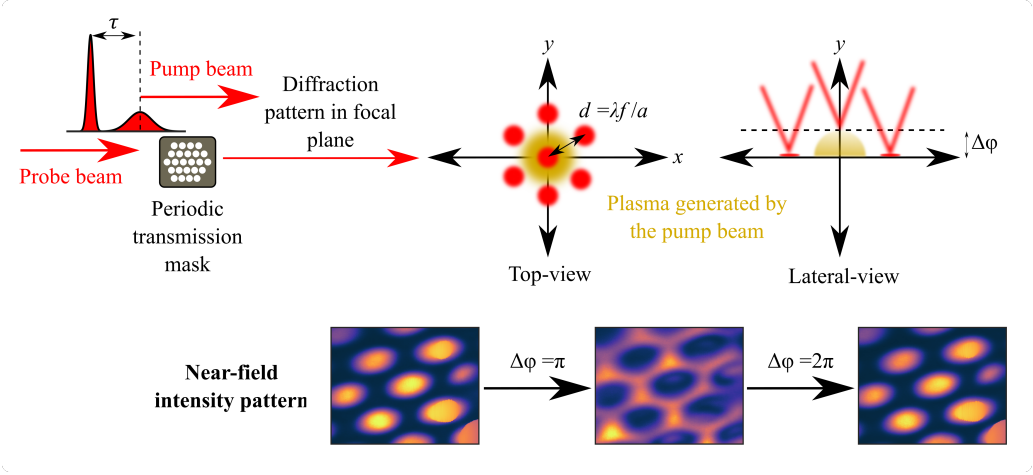

Figure 5.18: Principle of the SDI technique: A pump-beam initiates a plasma in-focus on the target surface. The Main-beam or the probe diffracts through a periodic transmission mask, creating a diffraction pattern in-focus. The phase difference $\Delta\phi$ of the 0th-order spot (reflected-off the expanding plasma) w.r.t. the 1st-order spot (reflected-off the bare-target-surface) leads to an inversion of the near-field intensity profile of the reflected probe beam for $\Delta\phi = n\pi$. Figure inspired from [316].

shape for the plasma density profile (section 4.3), this corresponds to the gradient scale length given as,

$$L_{\text{g}}(\tau) = \frac{x_{\text{c}}(\tau)}{\ln\left[n_0/(n_{\text{c}}\cos^2\theta_i)\right] - 1}. \tag{5.4}$$

Experiment implementation

The experimental implementation of this technique is quite straight forward. We insert a periodic transmission mask of period a (in our case a hexagonal pattern of 3 mm diameter holes with a period $a = 4\,\text{mm}$) into the near-field of the incident Main-beam, as shown in figure 5.18, thus transforming it into a probe beam for SDI. Upon focusing by the OAP, this turns into its far-field diffraction pattern on the target surface. In the paraxial approximation, this is given by the probe beam's spatial Fourier-transform, which is again a hexagonal pattern of "probe spots" (each of the same $\approx 1.8\ \mu$m FWHM size as the main beam focus) with a period $d = \lambda f/a$, where λ is the pulse central wavelength. For $\lambda = 800\,\text{nm}$, we thus obtain $d = 10\,\mu\text{m}$. This means that the central ($0^{\text{th}}-$order) probe spot overlaps with the center of the Prepulse and thus with a nearly homogeneously expanding plasma with which the Main-pulse would interact, while the surrounding hexagon of ($1^{st}-$order) probe spots overlaps with the wings of the $\sim 10\,\mu$m Pre-pulse spot, where the Prepulse fluence F_1 has dropped to $\approx 10\%$ of its peak value F_0.

The expanding plasma thus induces a phase shift $\Delta\phi = \phi_0 - \phi_1$ between the central ($0^{\text{th}}-$order) and the surrounding hexagon of ($1^{st}-$order) probe spots. In the simplest case, the first order spots probe an unaffected target surface, so that $\phi_1 = 0$. In our case however, the first-order spots reflect off an expanding plasma "launched" by a finite local Prepulse fluence of $F_1 \approx 0.1F_0$, with the fluence F_0 at the center of the Prepulse. The local expansion velocity at the location of the first order probe spots, c_{s}^1 is given as, $c_{\text{s}}^1 = \sqrt{F_1/F_0}c_{\text{s}}$. We rely on two assumptions here: (1) 1D isothermal expansion

modeling of the expanding plasma (section 4.3), and (2) the maximum plasma density n_0 is the same everywhere. The gradient scale length at the Pre-pulse center, L_g, is proportional to the measurable phase shift $\Delta\phi$:

$$\begin{aligned} L_\mathrm{g}(\tau) &= \alpha\,\Delta\phi(\tau) \\ \text{with } \alpha &= \frac{\lambda_0/(4\pi\cos\theta_i)}{\{\ln\left[n_0/(n_\mathrm{c}\cos^2\theta_i)\right]-1\}\left(1-\sqrt{F_1/F_0}\right)} \end{aligned} \tag{5.5}$$

$\Delta\phi$ is measured by recording the reflected near-field profile of the probe-beam, on the entrance spatial mask of the XUV spectrometer, imaged through an interferometric band-pass filter around $\lambda_0 = 800\,\mathrm{nm}$. As demonstrated in [316] and also illustrated in figure 5.18, there is an inversion of the near-field intensity pattern every time the phase shift $\Delta\phi = n\pi$, where n is an integer. The inversions in the near-field intensity pattern are tracked by calculating the "SDI-contrast" given as,

$$C = \frac{S_b(\tau) - S_d(\tau)}{S_b(\tau) + S_d(\tau)} \tag{5.6}$$

where S_b and S_d are the integrated signals over selected image areas that are initially (at $\tau = 0$) bright and dark, respectively. As visible in the examples shown in figure 5.19 (left-panel), the SDI contrast oscillates and its extrema mark the times, τ, when the dephasing, $\Delta\phi$, has incremented by π. The resulting dephasing curve, $\Delta\phi(\tau)$, is found to be linear (at least for the first $\approx 20\,\mathrm{ps}$ or so), which through equation 5.5 corresponds to a linearly increasing $L_\mathrm{g} = c_\mathrm{s}\tau$, as expected from the 1D isothermal expansion model. Its slope is easily found by a fit on the linear range of data points and yields the plasma expansion velocity, c_s, that is then used to calibrate the plasma gradient scale length in experiments.

SDI measurement with different pulse durations

Figure 5.19 shows a series of SDI measurements for three different laser pulse durations: 27 fs, 8 fs and 4 fs. The Prepulse fluence on target remains the same, ≈ 50 J/cm^2 and only its intensity varies. The Prepulse travels through a transmissive downsizing telescope and a HWP that add a GDD and a third-order dispersion (TOD) of $\approx 260\,\mathrm{fs}^2$ and $\approx 200\,\mathrm{fs}^3$, respectively. As a consequence, the 27 fs pulse is stretched to 38 fs with a peak intensity of 1.1×10^{15} W/cm^2, the 8 fs pulse is stretched to $\approx 100\,\mathrm{fs}$ with a peak intensity of 0.5×10^{15} W/cm^2, and the 4 fs pulse is stretched to $\approx 200\,\mathrm{fs}$, with a profile dominated by a $\approx 40\,\mathrm{fs}$ spike with a peak intensity of 0.7×10^{15} W/cm^2. As visible in figure 5.19, the three cases lead to very similar expansion velocities, with a variation clearly below the uncertainty of the SDI method itself. Thus, we can safely conclude that the plasma expansion speed c_s is independent of the Prepulse duration in the range covered by our experiments. This intensity independence corroborates the proportionality $c_\mathrm{s} \propto \sqrt{F}$, which is one of the strong assumptions used in the SDI analysis.

The slope of the $\Delta\phi(\tau)$-curves decreases for longer delays, $\tau > 25\,\mathrm{ps}$, indicating a decreasing velocity, c_s, and thus a cooling of the plasma electrons through transfer of energy to the ions. Thus, contrast inversions for $\tau > 25\,\mathrm{ps}$ are not taken into account for the linear-curve-fitting in figure 5.19(right-

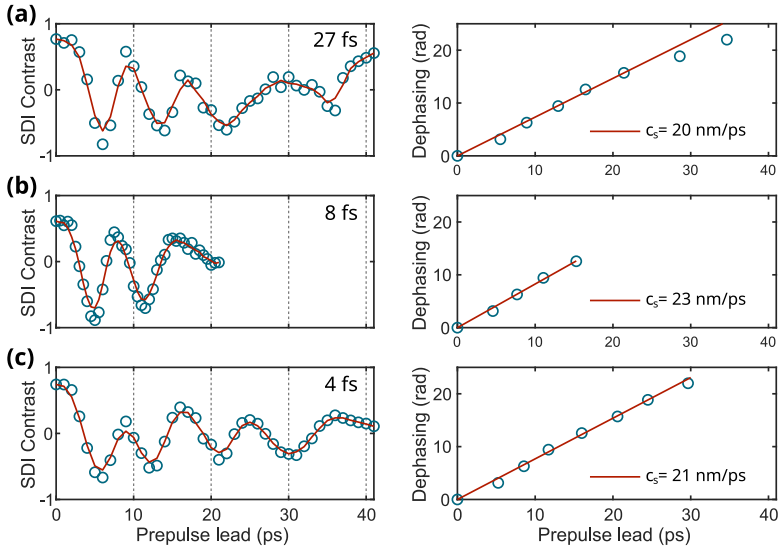

Figure 5.19: Experimentally measured SDI contrast curves (left-panel, raw data points marked by circles and smoothed data by red-lines) and the corresponding extracted dephasing curves (right-panel, extrema are marked by blue-circles and red-line is the linear fit including data points for $\tau < 20$ ps), for 27 fs (a), 8 fs (b), and 4 fs (c) laser pulse durations.

panel). The L_g-values relevant to most of our PM experiments are however reached before these effects set in, such that the linear evolution, $L_g = c_s\tau + L_0$, remains valid. The offset L_0 is estimated to be $< \lambda/50$, since we clearly observe CWE harmonics (discussed in Chapter 6), which are not generated efficiently with longer gradients [20, 216].

Chapter 6

Light and particle radiation from plasma mirrors: Experimental results

Outline

6.1 Correlations between secondary emissions **147**
6.1.1 Anti-correlation between CWE-harmonics and electron emissions 147
6.1.2 Direct correlation between RHHG and electron emissions 149
6.2 LWFA of electrons **152**
6.3 Low-divergence energetic proton beams **154**
6.3.1 Experimental results 154
6.3.2 Analytical model 158
6.3.3 2D PIC simulations 159

This chapter presents the first part of the experimental results obtained using the uniquely designed, well-controlled kHz PM beamline detailed in the preceding chapter, capable of simultaneous detection of all the three secondary emissions: HHG, electrons, and protons. This chapter is structured into three key sections: the first section focuses on the correlations that were observed among the synchronously recorded secondary emissions as a direct benefit of the unique design of this beamline. These correlations are experimentally studied for a wide range of laser and plasma parameters, offering insight into the collective plasma dynamics at play. The second section is dedicated to LWFA of electrons from PMs driven by few-cycle pulses. I performed the experimental studies together with Marie Ouillé (LOA), and analyzed the data with help from Stefan Haessler (LOA).

Finally, the last section of this chapter showcases the observation and physical mechanism behind the emission of a low-divergence MeV-class backward-accelerated proton beam. I conducted the experiments alongside Marie Ouillé, with remote assistance from Dan Levy (Weizmann Institute). I performed the majority of the data analysis, with help from Stefan Haessler. Additionally, Igor Andriyash (LOA) carried out numerical simulations to help us understand the underlying physical mechanisms.

6.1 Correlations between secondary emissions

6.1.1 Anti-correlation between CWE-harmonics and electron emissions

The plasma gradient scale length dependencies of CWE-harmonics and electrons in the case of a Brunel-dominated interaction driven by 30 fs pulses has already been reported [248], studied in great detail and well understood in the scope of Maïmouna Bocoum's thesis work [317]. To ensure that our experimental conditions (laser-plasma parameters) and equipment were in order, we attempted to reproduce the findings reported in [248]. To limit the laser intensity on-target to the sub-relativistic regime, we simply reduced the input beam size to 15 mm by using a spatial mask, which reduces the laser pulse energy from 2.5 mJ to 0.9 mJ on-target. Owing to a smaller input beam, the beam size in-focus increased to $2.8\,\mu\mathrm{m} \times 3.2\,\mu\mathrm{m}$ at FWHM. Correspondingly, for 27 fs, 6.7 fs, and 3.7 fs driving laser pulses, the intensity on-target was reduced to $2.2\times10^{17}\,\mathrm{W/cm^2}$ ($a_0 \approx 0.32$ for $\lambda = 800\,\mathrm{nm}$), $8.9\times10^{17}\,\mathrm{W/cm^2}$ ($a_0 \approx 0.64$ for $\lambda = 800\,\mathrm{nm}$), and $1.6\times10^{18}\,\mathrm{W/cm^2}$ ($a_0 \approx 0.84$ for $\lambda = 780\,\mathrm{nm}$), respectively.

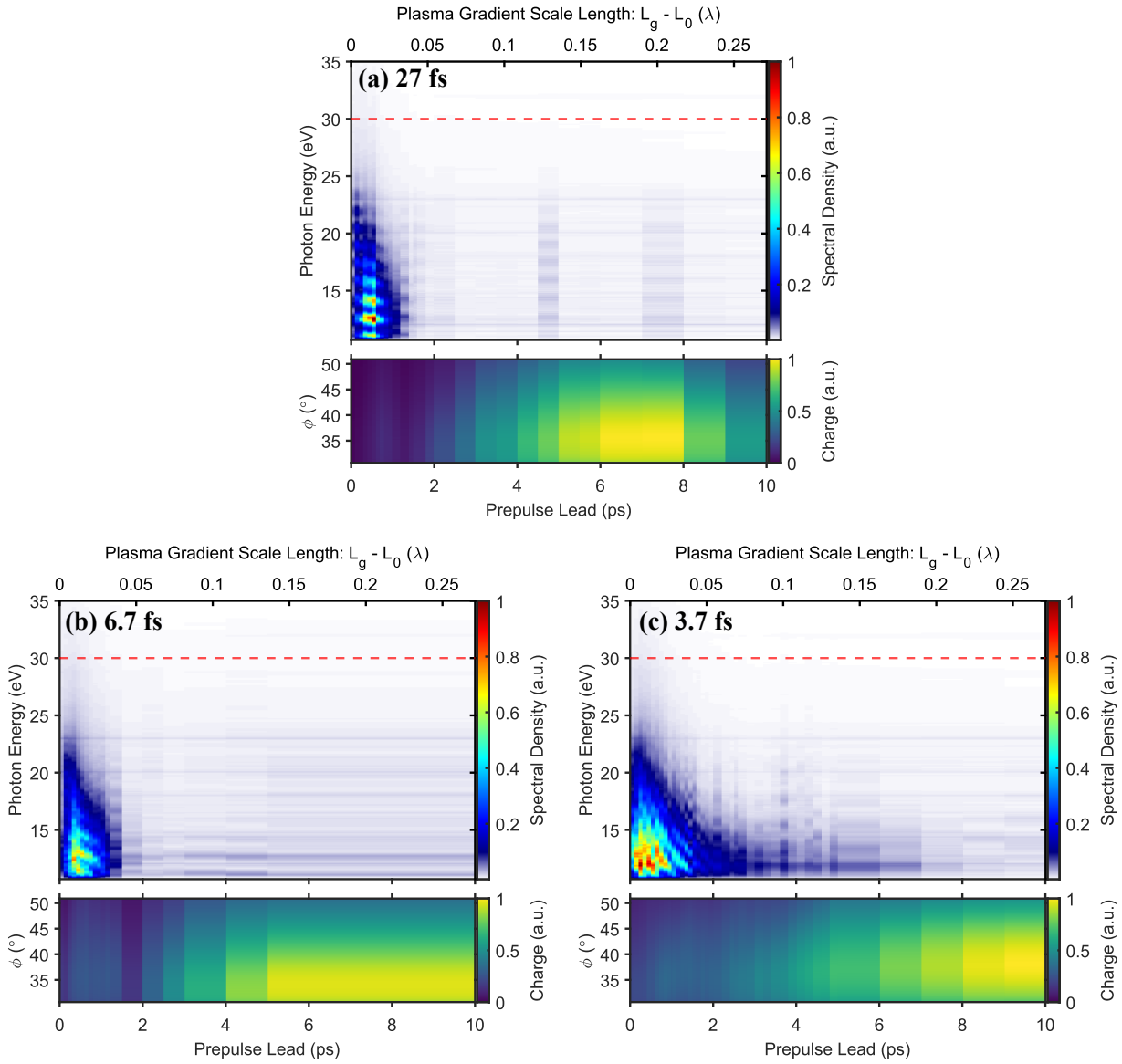

Figure 6.1: Simultaneously recorded vertically integrated HHG spectra (top-panel) and (vertically) integrated electron angular charge distribution in the azimuthal plane (bottom-panel) as a function of varying Prepulse lead time, for different driver pulses: 27 fs (a), 6.7 fs (b), and 3.7 fs (c) while the laser intensity on-target was limited to the sub-relativistic regime using a 15 mm spatial mask. The spectral density and charge for each respective panel has been individually normalized and cannot be directly compared. Each HHG spectrum and electron charge distribution is averaged over 100 consecutive laser shots. The dotted red line marks the CWE-HHG cut-off. The gradient scale length axis is calibrated with an expansion speed of $c_s = 21.7\,\mathrm{nm/ps}$ measured under identical conditions during the same experimental campaign.

The HHG spectrum and electron angular charge distributions were measured with varying pre-pulse lead times of $0-10\,\mathrm{ps}$ (or $L_g - L_0 \approx 0 - 0.27\lambda$, where $\lambda = 800\,\mathrm{nm}$), using the setup described in 5.4.1 and 5.5 for the above-mentioned driving laser pulse durations, as shown in figure 6.1. For all the three driving laser pulse durations, the HHG spectral extension is optimized for the steep-

est, laser-contrast limited plasma density gradients, and then quickly drops as the gradient scale length is increased. This is a well-known characteristic behavior of CWE-HHG in the sub-relativistic regime [216, 248]. Simultaneously recorded angular electron charge distribution was found to be anti-correlated to the CWE-HHG, as previously observed in [248]. For steep density gradients ($L_g < 0.05\lambda$), the Brunel-electrons return into the plasma, exciting plasma waves in the overdense part of the gradient, thus generating harmonics with a high spectral extension. As the gradient scale length is increased to 0.1λ and beyond, the electrons have a longer excursion length, thus gaining more kinetic energy in the space-charge field and finally escape.

It is noteworthy that the spectral position of the harmonic peaks remains stable with gradient length for 27 fs laser pulses, while for 7 fs and 3.7 fs driving pulses, there is a drift seen in the harmonic peak position. However, in figure 6.1(b)-(c), the CEP of the driver laser was unlocked, i.e. CEP was randomly varying from pulse-to-pulse and hence, the waveform effects on HHG in these scans are essentially washed out. The shift in the spectral position of harmonics with gradient scale length is solely the result of dominating Brunel electron dynamics.

6.1.2 Direct correlation between RHHG and electron emissions

For the results presented in this segment, the 15 mm spatial mask, that was previously used, was removed from the beam path, and the full laser energy was focused to reach relativistic intensities on-target.

Figure 6.2(a) displays the results obtained using a 24 fs driving laser pulse focused to 1.9×10^{18} W/cm^2 intensity ($a_0 \approx 0.95$) for a Prepulse lead time span of $\tau = 0 - 10$ ps or a gradient scale length range of $L_g - L_0 = 0 - 0.2\lambda$. The gradient scale length axis is calibrated with an expansion speed of $c_s = 16.1$ nm/ps which was measured on the same day the data presented here was acquired. Two gradient regimes can be clearly identified here: at the shortest gradients, $L_g - L_0 < 0.05\lambda$ where the harmonic peaks are broad, and at relatively softer gradients, $0.05 < L_g - L_0 < 0.2\lambda$ where the harmonics are thinner and well-defined with a maximum spectral extension at $L_g - L_0 \approx 0.1\lambda$. The former is a signature of CWE-HHG where harmonics have increased spectral width due to an inherent chirp as discussed in 4.7.1. The latter is consistent with the theoretical predictions for RHHG as well as with earlier experimental observations with similar multi-cycle driving laser pulses in the relativistic regime [69, 244, 254, 318]. The "thin" feature of harmonics is also in agreement with the theoretical predictions that each harmonic is nearly-FTL.

Simultaneously measured with the harmonics, at softer gradients, we find that the electron emission is directly correlated to the harmonic emission. The presumed RHHG extends till the expected CWE spectral cut-off of 30 eV, however, does not extend beyond it, which is not surprising as the laser intensity in this case is just below the relativistic threshold. We can corroborate this interpretation by using the second dazzler (Daz#2) in the laser chain to add 500 fs^2 of GDD, stretching the pulses to 60 fs, and consequently reducing the laser intensity to 7.7×10^{17} W/cm^2 ($a_0 \approx 0.6$ for $\lambda = 800$ nm). Figure 6.2(b) displays the results obtained with chirped 60 fs pulses. We can see a clear decrease in the spectral width of harmonics at steep gradients, while their spectral extension remains almost the same. This is consistent with the compensation of periodicity of the CWE-attosecond pulse train and an approximately constant CWE-conversion efficiency. A complete disappearance of harmon-

ics at soft density gradients is consistent with the highly non-linear intensity dependence of RHHG. The electrons are still emitted at preferentially softer gradients and the resulting anti-correlation of CWE-HHG and electrons is consistent with the discussion in the previous section.

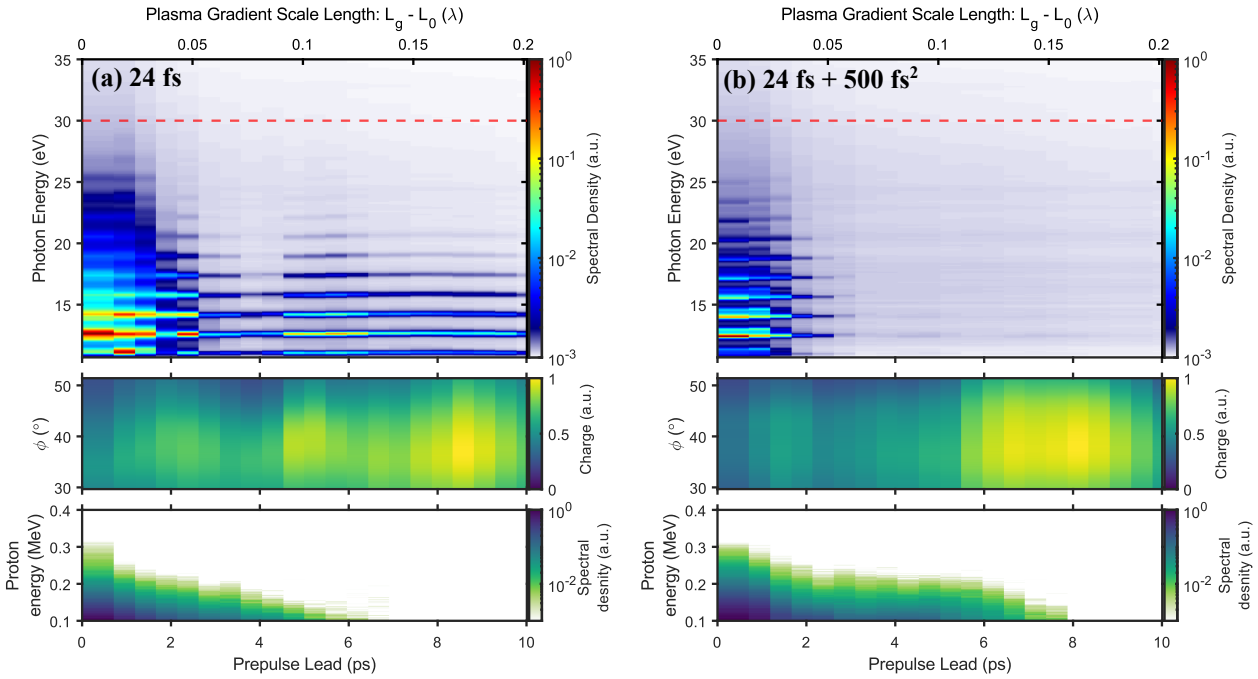

Figure 6.2: Simultaneously recorded vertically integrated HHG spectra (top-panel), (vertically) integrated electron angular charge distribution in the azimuthal plane (middle-panel), and proton energy spectrum measured in the target normal direction $\phi_{az} = 0°$ with the TPS (bottom-panel) for nearly-FTL 24 fs (a) and stretched by adding $500\,\mathrm{fs}^2$ to 60 fs (b). The spectral densities and charge for each respective panel has been individually normalized and cannot be directly compared. Each measurement is averaged over 100 consecutive laser shots. The dotted red line marks the CWE-HHG cut-off. The gradient scale length axis is calibrated with an expansion speed of $c_s = 16.1\,\mathrm{nm/ps}$ measured on the same day.

Reducing the driving pulse duration to 6.3 fs at constant pulse energy increases the intensity on target to 7.2×10^{18} W/cm^2 intensity ($a_0 \approx 1.8$ at $\lambda = 800\,\mathrm{nm}$), leading to results depicted in figure 6.3(a). Similar features as the 24 fs driver laser case can be observed here. There is a quick transition from spectrally broad harmonics at the steepest gradients to a more modulated RHHG spectrum, extending from $L_g - L_0 \approx 0.05\lambda - 0.4\lambda$ with an optimal between $L_g - L_0 \approx 0.05 - 0.1\lambda$ that is directly correlated with electron emission at these gradients. Additionally, we can now observe the spectral extent of the RHHG signal to reach and surpass the CWE cut-off of 30 eV, which is a definitive proof of RHHG emission. As L_g is further increased, the RHHG signal persists till $\approx 0.4\lambda$ but its intensity and spectral extent gradually decreases.

An even shorter 4 fs driving pulses are expected to significantly boost the RHHG signal beyond the CWE cut-off. However, self-steepening effects during post-compression in the HCF reduce the central spectral wavelength to $\lambda \approx 780\,\mathrm{nm}$. Furthermore, such short pulses are extremely sensitive to spatio-temporal couplings that can drastically reduce the achievable peak intensity. On many days we observed a reduced spectral extent of the SHHG spectra generated with 4 fs pulses as compared

to those obtained with 6 - 10 fs pulses, as was the case for the results reported in [64]. Nevertheless, we managed to record the SHHG spectra with 4 fs driving laser pulses as shown in figure 6.3(b). Similar to the results obtained with 6.3 fs pulses, RHHG emission is optimized for gradient scale lengths between $L_g - L_0 \approx 0.05\lambda - 0.15\lambda$, where, now $\lambda = 780\,\text{nm}$.

The harmonic spectral peaks for both 6.3 fs and 4 fs driver pulses presented in figure 6.3 are broader, spectrally overlapping as compared to the 24 fs driver pulse case. This could be a result of a varying temporal structure of the generated very short, 1-3 attosecond-pulse-trains. However, for both of these scans, the CEP of the driver pulses was varying randomly from pulse-to-pulse and any CEP effects on RHHG emission would be washed out. This precludes us from inferring this temporal structure from these spectral features [64].

The angular electron distributions presented in figure 6.3 are directly correlated with RHHG emission but they are emitted closer to the specular direction, with the most intense part of the beam increasingly towards $\phi_{az} \approx 45^\circ - 48^\circ$, as compared to the 24 fs case (figure 6.2(a)), where the electrons were emitted around $\phi_{az} \approx 40^\circ$. This could result from a less efficient ponderomotive scattering of the electrons by the few-cycle laser pulses as compared to the multi-cycle divers.

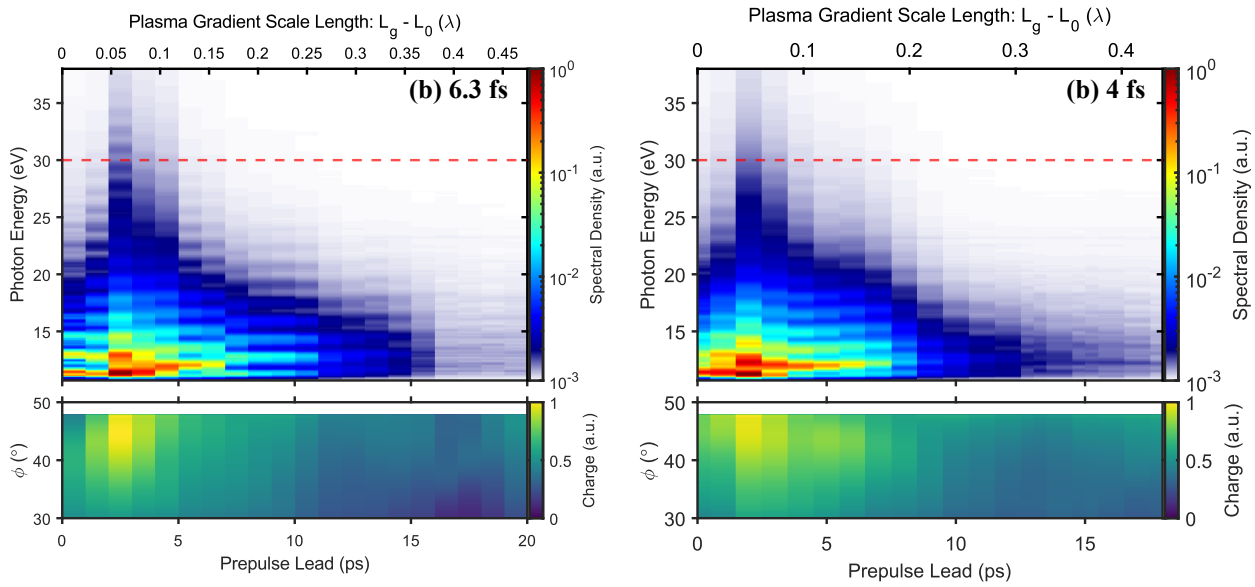

Figure 6.3: Simultaneously recorded vertically integrated HHG spectra (top-panel) and (vertically) integrated electron angular charge distribution in the azimuthal plane (bottom-panel) as a function of varying Prepulse lead time, for relativistic intensity 6.3 fs (a) and 4 fs (b) driver pulses. The spectral density and charge for each respective panel has been individually normalized and cannot be directly compared. Each HHG spectrum and electron charge distribution is averaged over 100 consecutive laser shots. The dotted red line marks the CWE-HHG cut-off. The gradient scale length axis is calibrated with an expansion speed of $c_s = 19\,\text{nm/ps}$ measured on the same day.

Additionally, we could characterize the electron energy spectrum using an insertable magnetic spectrometer, but limited to $\phi_{az} = 40^\circ$ to allow simultaneous measurement of the harmonics spectrum as depicted in figure 6.4. This position does not sample the center of the electron beam, which is located a few degrees closer towards the specular direction. Even though the electron charge is low at the steepest gradients (figure 6.3), we measured a high electron energy of $\approx 1.4\,\text{MeV}$ for 6.3 fs

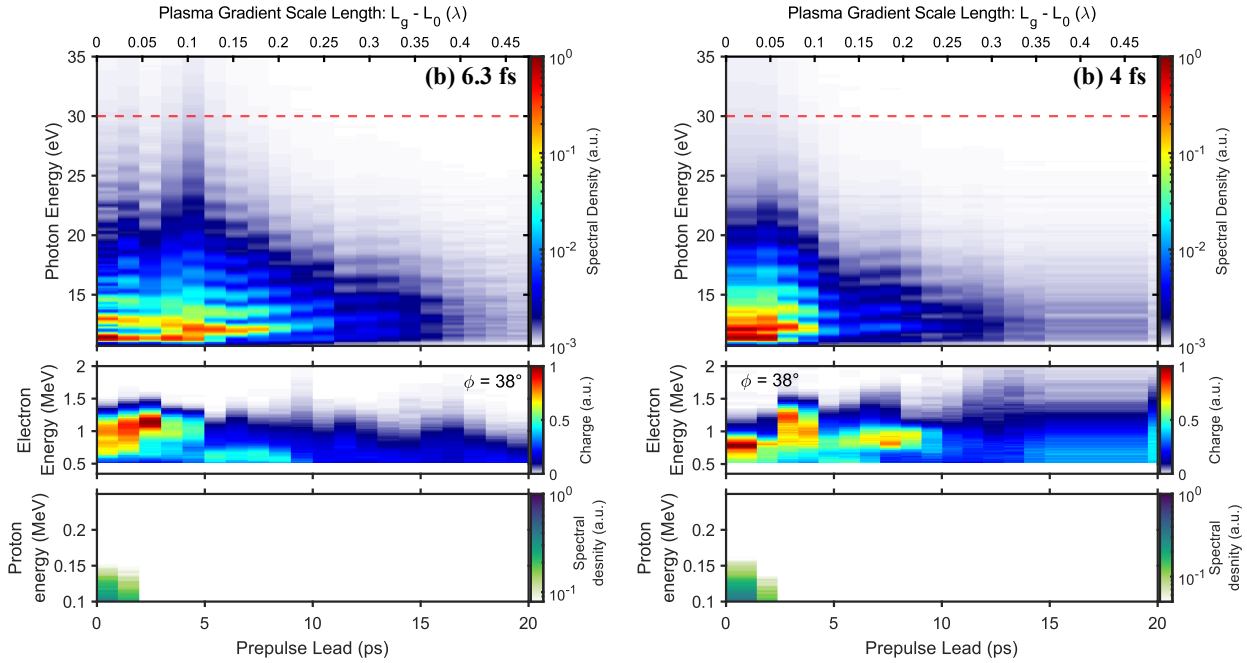

Figure 6.4: Simultaneously recorded vertically integrated HHG spectra (top-panel), electron energy spectrum measured at $\phi_{az} = 38°$ and $\theta_{pol} = 0°$ (middle-panel), and proton energy spectrum measured in the target normal direction $\phi_{az} = 0°$ with the TPS (bottom-panel) as a function of varying Prepulse lead time, for relativistic intensity 6.3 fs (a) and 4 fs (b) driver pulses. The spectral densities and charge for each respective panel has been individually normalized and cannot be directly compared. Each measurement is averaged over 100 consecutive laser shots. The dotted red line marks the CWE-HHG cut-off. The gradient scale length axis is calibrated with an expansion speed of $c_s = 19\,\mathrm{nm/ps}$ measured on the same day.

driving laser pulses and $\approx 1.1\,\mathrm{MeV}$ for 4 fs driver laser pules. At softer gradients, the electron energies further increased to a maximum of $\approx 1.6\,\mathrm{MeV}$, correlated to the RHHG emission. Higher energies and more pronounced gradient dependencies are expected in the center of the electron beam.

6.2 LWFA of electrons

At long plasma gradient scale lengths, $L_g \geq \lambda$, a novel regime for LWFA of electrons from PMs driven by few-cycle pulses was first discovered by Zaïm *et al.* [255], as discussed in section 4.8.2. The emitted electron beam was found to be interesting for several applications given its good stability and beam characteristics [87]. Experimental measurements yielded an integrated electron charge of 100 pC per shot, while simulations indicated electron energies reaching a maximum of 5 MeV.

We could successfully reproduce these results in our experiments. Figure 6.5 shows the measured integrated (along θ_{pol}) electron charge distribution along the azimuthal direction (ϕ_{az}) as a function of the prepulse lead time for three different driving pulse durations. The target normal and specular directions are located at $\phi_{az} = 0°$ and $\phi_{az} = 55°$ respectively. Note that the gradient scale lengths result from a plasma expansion speed of $c_s = 18\,\mathrm{nm/ps}$ as determined for the initial expansion

phase with Prepulse lead times < 20 ps. As discussed in section 5.7, the plasma expansion slows down considerably at longer times. Therefore, true gradient scale lengths are certainly shorter than those indicated here.

As reported in [255], the LWFA regime manifests only for few-cycle driving pulses. For 27 fs driving laser pulses (≈ 10 optical cycles), the emitted electron beam exhibited a clear decay at a prepulse lead time of 150 ps. Conversely, for few cycle driving pulses, 7 fs and 4 fs pulses, a strong robust electron beam emerged in the range of prepulse lead times $150 - 350$ ps. It is important to note that the electron distributions depicted for each driving pulse duration have been individually normalized, hence a direct comparison of the emitted electron charge cannot be drawn between the scans in figure 6.5(b) and 6.5(c). During these scans, for prepulse lead times larger than 20 ps, the simultaneously running HHG and proton spectral diagnostics recorded only background noise signals which are thus not shown. This anti-correlation with the relativistic electron beam corroborates its origin from the under-dense part of the plasma.

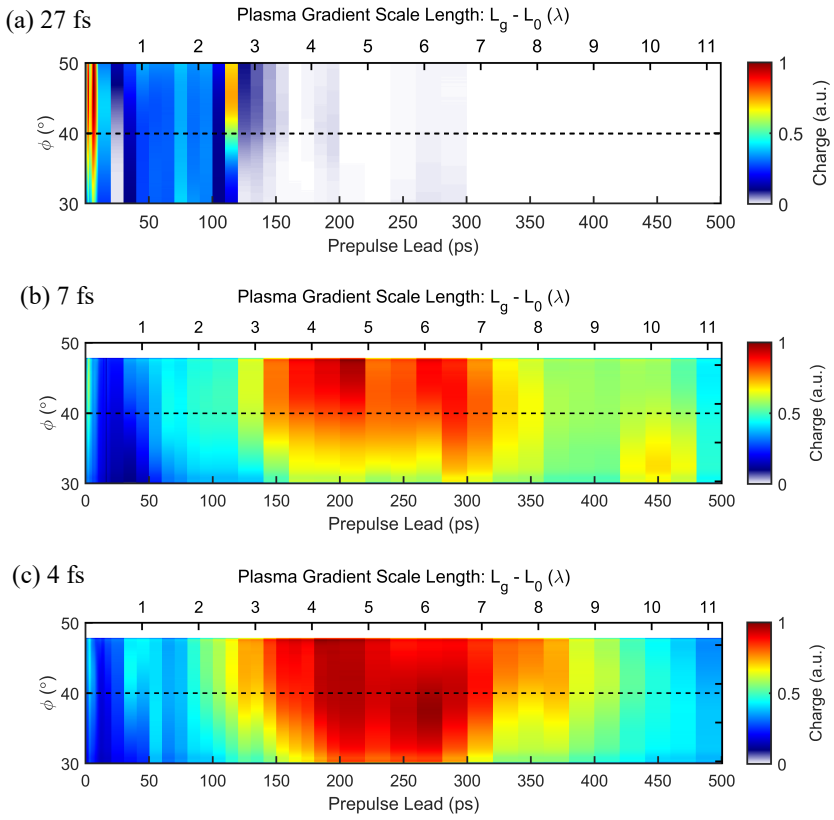

Figure 6.5: Integrated electron spatial charge distribution along the azimuthal direction as a function of plasma gradient scale length for 27 fs (a), 7 fs (b), and 4 fs (c) driving pulse durations. Target normal and specular directions are located at $\phi_{az} = 0°$ and $\phi_{az} = 55°$ respectively. The dotted black line at $\phi_{az} = 40°$ marks the sampling position of the electron spectrometer.

Additionally, we further expanded on the work reported in [255], by experimentally measuring the electron energy spectrum in the LWFA regime. However, our insertable electron spectrometer, detailed in section 5.5.2, was specifically designed to measure electron energies up to $\phi_{az} = 40°$, to

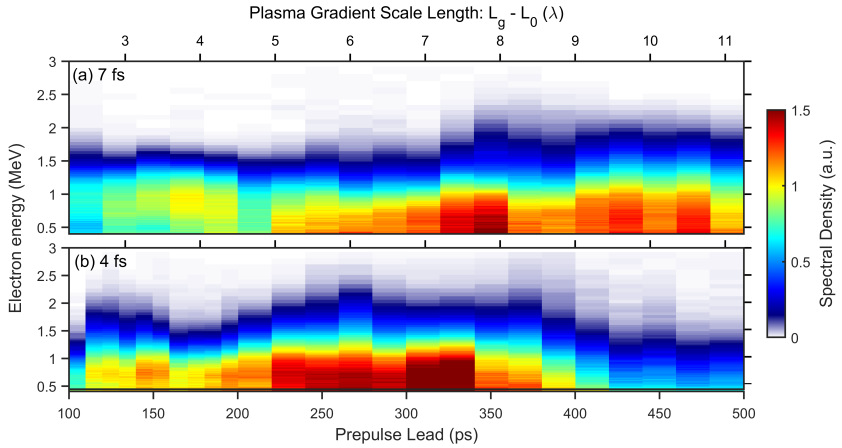

Figure 6.6: Electron energy spectrum measured at $\phi = 40^\circ$ for varying plasma gradient scale length for 7 fs (a) and 4 fs (b) driving laser pulse durations.

simultaneously enable the measurement of the HHG signal. Figure 6.6 shows the electron spectra measured at $\phi_{az} = 40^\circ$ and $\theta_{pol} = 0^\circ$ for a varying prepulse lead time in the range of $100 - 500$ ps, for 7 fs and 4 fs driving pulses. The position at which the electron beam is sampled by the electron spectrometer is indicated by a dotted black line in figure 6.5(b)-(c). In both the cases, electron energies reaching up to 2.6 MeV are observed, which is very close to the value predicted in numerical simulations in [255]. We expect even higher electron energies closer to the specular direction where the most intense part of the electron beam is located at $\phi_{az} \approx 48^\circ$.

6.3 Low-divergence energetic proton beams

Expanding upon Veltcheva *et al.*'s foundational work from 2012 [25], together with Marie Ouillé (LOA), Stefan Haessler (LOA), and in collaboration with Dan Levy (Weizmann Institute), I experimentally investigated proton acceleration from front-side of the solid-targets, with vastly improved laser performance in terms of achievable intensities on-target and temporal intensity contrast ratio. Moreover, we further expanded on Veltcheva *et al.*'s work by not only using a fixed TPS for measuring the energy of the emitted protons but also implementing a scanning TOF detector for a spatial characterization of the proton beam. These diagnostic setups have been detailed previously in 5.6. Thanks to the simulation support from Igor Andriyash (LOA), we could elucidate the underlying physical mechanism through an analytical model that was validated by 2D particle-in-cell (PIC) simulations.

6.3.1 Experimental results

A comprehensive parametric study of proton acceleration from the front-side of a laser-driven PM on the surface of an initially-solid target is presented here. The plasma gradient scale length is varied from $L_g - L_0 = 0 - 0.15\lambda$ by controlling the delay between the Prepulse and the Main-pulse. The driving laser pulse duration is scanned from 30 fs to sub-4 fs by simply varying the gas pressure in the HCF-post compression setup. Additionally, we can stretch the 30 fs pulses to up to ≈ 1.5 ps by

adding GDD with the second Dazzler (Daz#2) in the laser chain. The beam size and energy on-target remained constant throughout this study.

Plasma gradient scale length dependence: Figure 6.7 shows a series of proton energy measurements recorded using the TPS in the target normal direction ($\phi_{az} = 0^{\circ}$) as a function of the gradient scale length, for various driver pulse durations. Each proton energy spectrum displayed here is averaged over 100 consecutive laser shots. It can be observed for all the depicted cases that the maximum proton energy is optimized for the steepest, laser-contrast-limited gradient scale length which corresponds to a "zero-delay" between the Prepulse and the Main-pulse. If there is an optimal gradient length for efficient acceleration of protons, it lies beyond our resolution limit. At such steep gradients, $L_{\mathrm{g}} \ll \lambda$, we know that the plasma dynamics are dominated by Brunel electrons that are pulled and pushed back into the plasma by the laser electric field. The electrons that are lost to the plasma beyond the critical density surface do not contribute to the electron thermal pressure, thereby making TNSA less efficient [24, 25, 301].

Dependence on the driving pulse duration: In figure 6.7, we can clearly see that as the driving laser pulse duration is increased, there is a corresponding rise in the maximum proton energies, suggesting that the maximum proton energies, $E_p^{max} \propto \tau_l$, where τ_l is the driving laser pulse duration. The proton acceleration in this regime is directly driven by the laser-plasma interactions while not strongly depending on the laser intensity. It should be noted that the proton spectral density is displayed in arbitrary units and the proton energy scan for each driving pulse duration is individually normalized, precluding any direct comparison between scans of different driving pulse durations. For $\tau_l < 30\,$fs, the proton energies are optimized at the steepest gradients and as L_{g} is increased, the proton signal quickly decays to a level below our detection limit. However, in the case of $\tau_l \geq 50\,$fs, the maximum proton energies decay to a plateau before completely disappearing around 0.1λ. Staying at the steepest density gradients, if we scan only the driver laser pulse duration, an evolution of the proton peak energy is observed as shown in figure 6.8(b). The proton energies are optimized for $\approx 130\,$fs - $300\,$fs pulses for which a maximum proton energy of 0.48 MeV is observed and then the signal gradually decreases. This observation suggests that protons are accelerated only during the interaction time of the pulse, and therefore, they benefit from a longer driving pulse duration despite the corresponding drop in the laser intensity. However, for $\tau_l > 130\,$fs the proton energy growth switches from $E_p^{max} \propto \tau_l$ to a slow decrease $E_p^{max} \propto I \propto 1/\tau_l$, where I is the driving laser intensity.

Figure 6.9 shows the angle-resolved proton energy spectrum measured with a scanning TOF detector, also averaged over 100 consecutive shots, for four different driving pulse durations, 4 fs, 7 fs, 27 fs, and 200 fs, measured at the steepest plasma density gradients. Interestingly, in all the four cases, a fairly low $\leq 4^{\circ}$ FWHM divergence of the proton beam is observed. This is significantly lower than the proton beam divergence observed in the case of TNSA, ranging from $10^{\circ} - 30^{\circ}$. Additionally, this measured divergence is also significantly lower than the 16° FWHM reported earlier for Brunel-electron driven ion acceleration studies from the front side of the targets [24], which may be the result of a higher temporal contrast ratio of the driving laser in our case. This 1D measurement is well fitted by a Gaussian, and due to the symmetry of the system itself, we expect the beam asymmetry to be

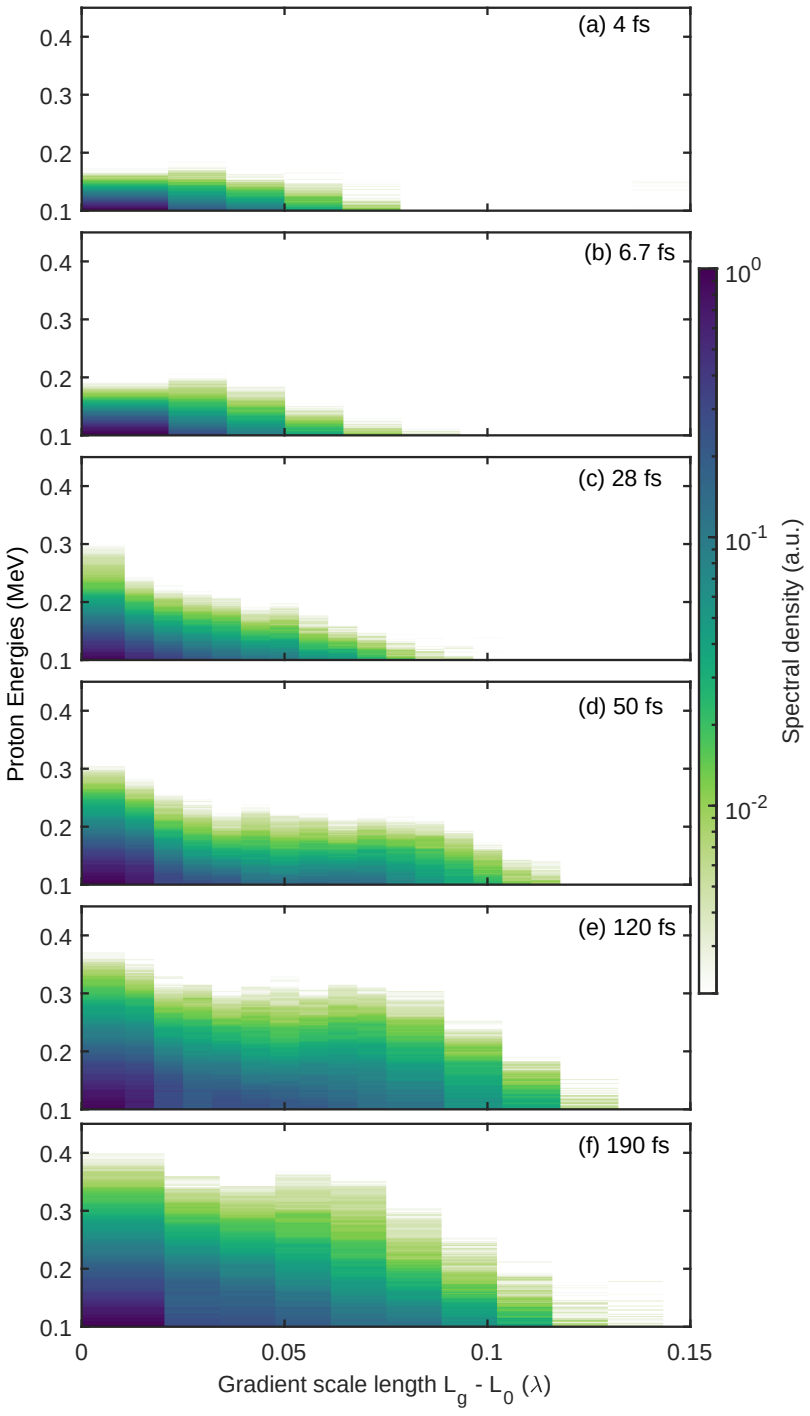

Figure 6.7: Proton energy spectrum measured using the TPS in the target normal direction ($\phi_{az} = 0°$) as a function of the plasma gradient scale length for increasing driving pulse durations: FTL- 4 fs (a), 6.7 fs (b), 27 fs (c), chirped - 50 fs (d), 120 fs (e), and 190 fs (e).

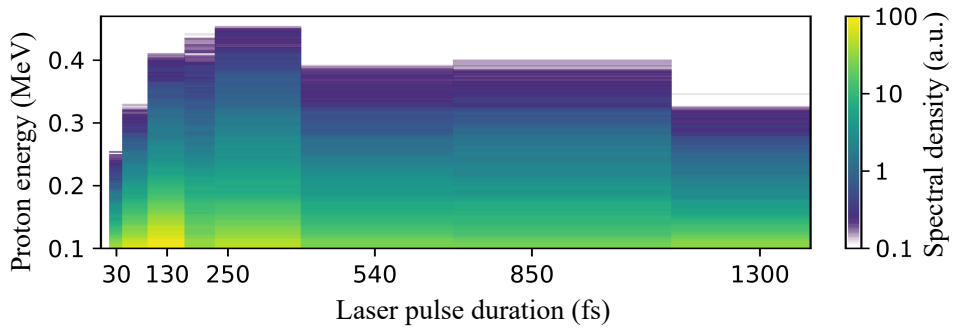

Figure 6.8: Proton energy spectra in the target normal direction ($\phi = 0°$) at the steepest density gradients for increasing driving pulse durations.

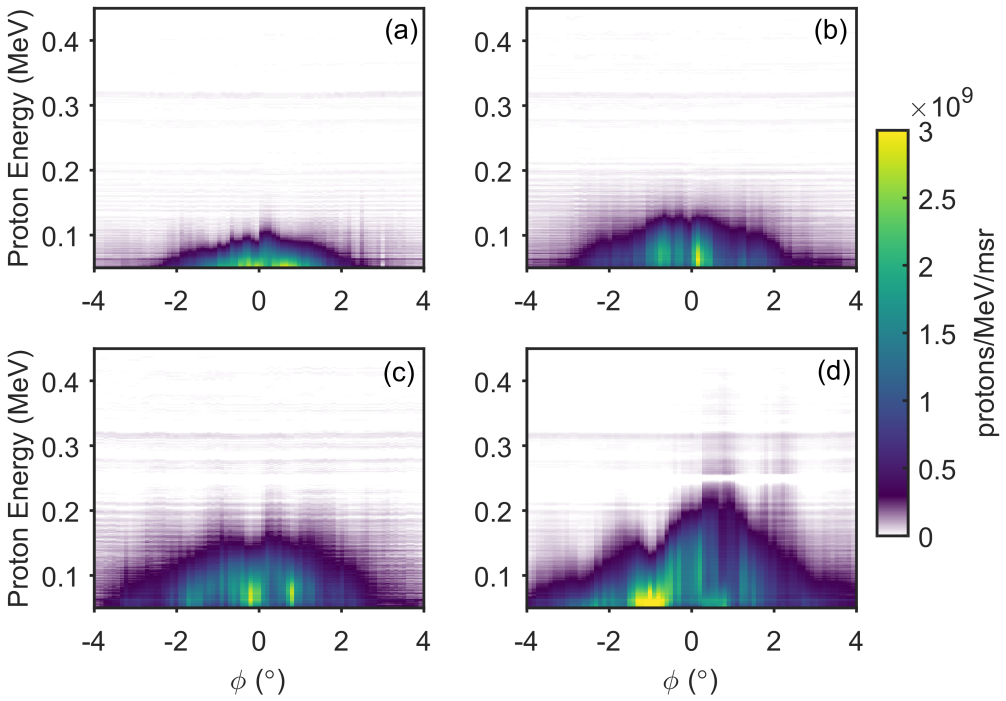

Figure 6.9: Angle-resolved proton spectra measured using a scanning TOF detector for driving pulse durations of 4 fs (a) 7 fs (b), 28 fs (c), and 200 fs (d).

small, as was observed in [24], albeit with a much larger beam divergence. Assuming a 2D Gaussian angular profile, we calculate a total charge (above 0.07 MeV) to be 12 ± 2.4 pC, 34 ± 6.8 pC, 50 ± 10 pC, and 98 ± 20 pC for 4 fs, 7 fs, 27 fs, and 200 fs driving pulses, respectively. Our estimation of a $\approx 20\%$ error originates from uncertainties in the angular TOF distribution measurement and the calibration of the detector.

6.3.2 Analytical model

In the sub-relativistic regime ($a_0 < 1$), when an ultrashort p-polarized pulse is obliquely incident on a near-solid-density plasma, at very short gradients, $L_g \ll \lambda$, the laser field penetrates through a very thin layer of the pre-plasma until it reaches a reflective surface, where $n_e \gtrsim n_c$. The electrons in this layer are driven by the laser-field, being periodically pulled-out and pushed-into the plasma via Brunel absorption [214]. To qualitatively describe this process, we assume a simplified picture where the laser removes electrons up to a depth, $x_0 \gtrsim x_c$, leaving behind a layer of immobile heavy ions that create an electrostatic accelerating field directly related to the value of x_0. Furthermore, we assume that electrons respond instantaneously to the laser-field and are only displaced along the $x-$axis. To correlate electron displacement to the driver laser intensity, we consider that there is a static equilibrium between the radiation pressure of the incident and reflected laser fields, $P_{\text{rad}} = 2cos^2\theta I/c$, and the electrostatic pressure, $P_{\text{es}} \approx \sigma_i^2/\varepsilon_0$ generated by the charge separation. Here, θ is the angle of incidence on-target, I is the incident laser intensity, ε_0 is the vacuum permittivity, and $\sigma_i = e\int_{x_0}^{\infty} n_e dz$ is the area charge density of the ions estimated via the capacitor model. The pressure balancing condition yields,

$$\begin{aligned} P_{\text{rad}} &= P_{\text{es}} \\ \frac{2cos^2\theta I}{c} &= \frac{\sigma_i^2}{\varepsilon_0} \\ \implies \sigma_i &= \sqrt{\frac{2cos^2\theta I\varepsilon_0}{c}} \\ &= \varepsilon_0 E_0 cos\theta \end{aligned} \tag{6.1}$$

where $E_0 = \sqrt{2I/\varepsilon_0 c}$ is the laser electric field amplitude. In this case, for an exponentially decaying pre-plasma profile (section 4.3), the penetration depth is given as

$$x_0 \approx L_g\ ln\left(\frac{en_e L_g}{2cos\theta}\sqrt{\frac{c}{\varepsilon_0 I}}\right) \tag{6.2}$$

The spatio-temporal distribution of the accelerating field can then be estimated using a thin-charged-disk model where the size of the charged ion disk is determined by the projected laser spot-size of $R_i = R_l/cos\theta$:

$$E_z(t,z) = \frac{E_0(t)cos\theta}{2}\left[1-\exp\left(-\frac{x-x_0}{L_g}\right)\right]\left(1-\frac{x}{\sqrt{x^2+R_i^2}}\right) \tag{6.3}$$

The second and third factors on the right side of the equation 6.3 account for the field distribution within the pre-plasma and the 3D field geometry, respectively. These geometric factors can be discarded in the limit when the acceleration length is short compared to the laser field-scale R_i but longer than L_g. In this case, the maximum proton energies are given as

$$E_p^{max} = \sqrt{\frac{ln\,2}{\pi}} \frac{e^2}{m_p c \varepsilon_0} \frac{W \tau_l}{R_i^2} \tag{6.4}$$

where W and τ are the laser energy and pulse duration, respectively. Notably, the accelerating field in equation 6.3 vanishes for $x \gtrsim R_i/2$, thereby limiting the acceleration time to $2\tau_l$. This also imposes a validity condition on equation 6.4 as

$$\sqrt{E_p^{max}}\tau_l \lesssim R_i \sqrt{m_p}/2 \tag{6.5}$$

This condition defines the case when protons reach the vanishing field by the end of the interaction time, thereby defining the optimal acceleration regime. Applying equation 6.5 to equation 6.4, we obtain the scaling:

$$E_p^{opt} = \left(\sqrt{\frac{2ln\,2}{\pi m_p}} \frac{e^2}{4c\varepsilon_0} \frac{W}{R_i} \right)^{2/3} \tag{6.6}$$

which suggests that the maximum cut-off energy is determined solely by the laser energy and the spot-size. Thus, this work paves the way to the production of low-divergence, MeV-class protons at a high repetition rate.

6.3.3 2D PIC simulations

To verify the validity of this analytical model and to understand it in more detail, 2D PIC simulations were performed using the WARPX code [319]. In the simulations, a 3 mJ laser pulse focused down to a $1.8\,\mu$m spot on a pre-plasma of $L_g = 8\,$nm with an exponentially decaying profile was considered. Figure 6.10(a) compares the maximum proton energy for various pulse durations measured in the experiment, simulations, and provided by equation 6.2 and 6.3 of the analytical model and its limiting case in equation 6.5 discussed above. Both the simulated and the measured maximum proton energies follow the predicted flat scaling with the driver pulse duration as predicted by the analytical model.

Figure 6.10(b)-(d) displays the simulated spectral-angular distribution of the emitted protons. For $\tau_l = 30\,$fs, all the protons remain nearly collimated, but in the case of $\tau_l = 100\,$fs, the proton beam develops a higher divergence for lower energy protons which is further exacerbated for the $\tau_l = 250\,$fs case. This is a clear signature of the onset of the TNSA regime that is also visible in the experimental TOF measurements. Figure 6.11(a) identifies the "proton peak" and "heavy ion" peaks in the measured TOF traces for the case of 27 fs and 200 fs driver pulses. For 27 fs pulses, the signal between the two "peaks" falls nearly to zero, suggesting a spatial separation of the protons from the heavy ion species, contrary to the 200 fs driver pulse case where the signal between the two peaks is significant, indicating an overlap of ions and lower energy protons. The simulated TOF traces of oxygen ions and protons for a 100 fs driver pulse depicted in figure 6.11(b) exhibit a similar behavior. The proton signal falls abruptly in the time-range where ions and protons overlap, which corresponds to the degradation of the low angular divergence observed in figure 6.9. It is worth noting that this TNSA-induced degradation of proton beam divergence is massively more pronounced in simulations (figures 6.10(b)-(d)) than in experiments (figure 6.9). This could be attributed to the specificity of

the simulated 2D geometry. The considered proton acceleration is essentially one-dimensional and should not in principle, significantly depend on the transverse dimensions. Nevertheless, 2D PIC simulations have been shown to greatly enhance the TNSA process and result in twice more efficient acceleration compared to the full 3D geometry [320].

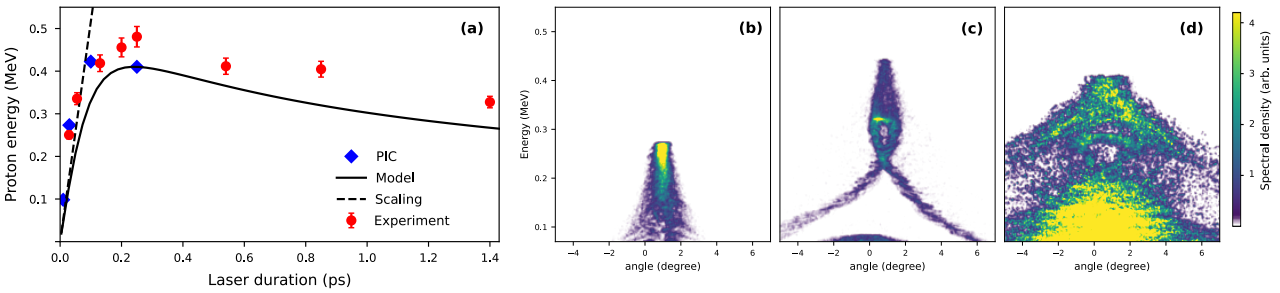

Figure 6.10: Scaling of the maximum proton energy with the driving laser pulse duration, comparing the results obtained in experiments, PIC simulations, calculated through the analytical model (equations 6.3 and 6.2), and the limiting case scaling law (equation 6.4) (a). Simulated spectral-angular distributions of protons for 30 fs (b), 100 fs (c), and 250 fs (d) driving laser pulse durations. Courtesy of Igor Andriyash.

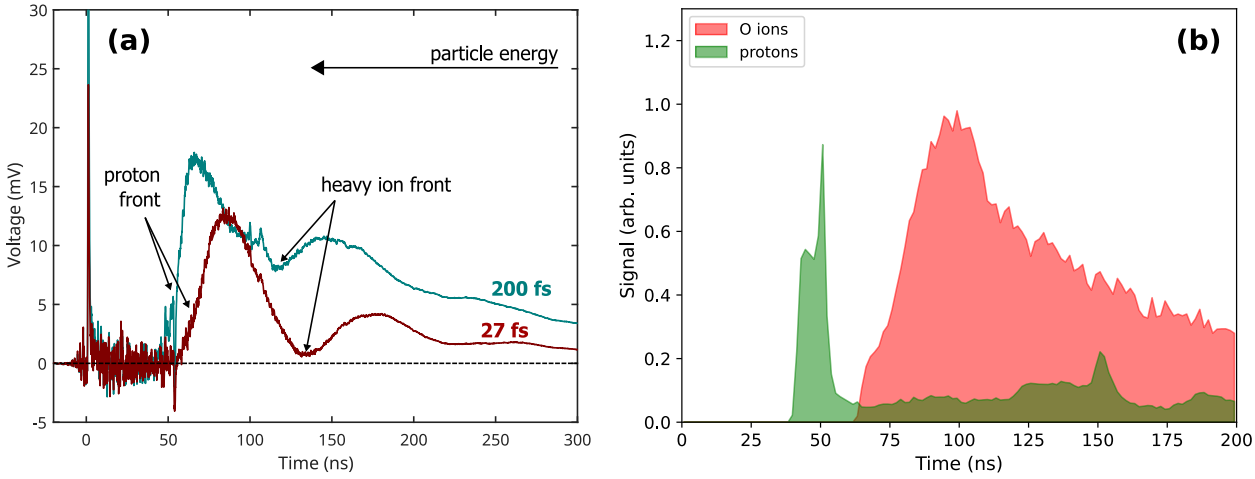

Figure 6.11: Measured TOF signal for 28 fs and 250 fs driving laser durations (a). Simulated TOF measurement of oxygen ions and protons for 100 fs driving laser pulse (b). Courtesy of Igor Andriyash.

The acceleration mechanism identified here may be referred to as radiation pressure-assisted Coulomb explosion (RPACE). The low-divergence feature of RPACE can only be exploited for “short” driver pulse durations that subsequently limit the maximum proton energy that can be obtained. Additionally, one may expect TNSA efficiency to increase with driving laser energy where the electron temperature grows, imposing further limitations on the efficiency of RPACE. However, this process is governed by multiple parameters, such as laser intensity, pulse duration, and also ion composition. For a given driver laser pulse energy and focusing geometry, an optimal pulse duration can be found that preserves the proton beam quality while allowing to scale the maximum proton energy. One

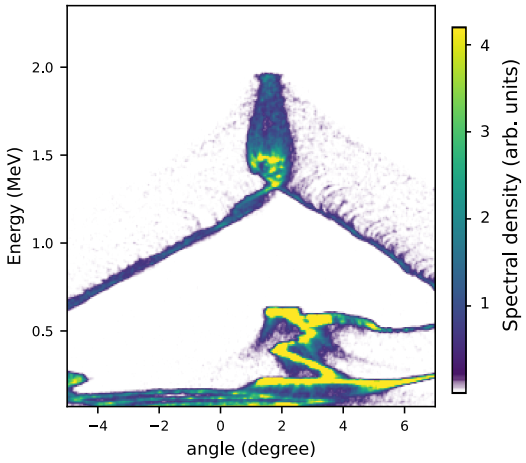

Figure 6.12: Simulated final angular-spectral distribution of protons for a 30 mJ energy 70 fs pulse. Courtesy of Igor Andriyash.

such case is simulated and displayed in figure 6.12 indicating a maximum proton energy of $\approx 2\,\mathrm{MeV}$ for a 30 mJ - 70 fs pulses focused down to a $2.5\,\mu\mathrm{m}$ spot on-target. This value is in very good agreement with the maximum proton energy of 1.9 MeV predicted by the analytical model in equation 6.5. Higher energy protons remain well-collimated while $E_p < 1.4$ MeV suffer TNSA-induced increased divergence. We anticipate that in full 3D geometry, this threshold should be well below 1 MeV.

Chapter 7

Waveform-controlled relativistic plasma mirror emissions

"*Better is the enemy of good*"

Outline

7.1 State-of-the-art **165**
7.2 CEP effects on RHHG and relativistic electrons **167**
7.2.1 Varying plasma gradient scale length 167
7.2.2 At the optimal gradient scale length 167
7.2.3 From spectral measurements to temporal insights 170
7.2.4 Correlated behavior of relativistic electrons 172
7.3 Wide-range electron angular-charge detection **174**
7.4 XUV wavefront **175**
7.4.1 Silicon plate calibration 176
7.4.2 Wavefront sensor calibration 177
7.4.3 At the optimal gradient scale length 178
7.4.4 CEP effects 179

This chapter is dedicated to the experimental results obtained by implementing sub-cycle control of relativistic PMs driven by waveform-controlled near-single cycle laser pulses, with the goal of generating isolated attosecond pulses (IAP) on-demand and simultaneously observing the correlated behavior of electrons. First, I will briefly review of the current state-of-art to generate IAPs from PMs, followed by the experimental results obtained using the *Salle Noire* beamline. The waveform control in the *Salle Noire* laser was implemented by the previous PhD student in the group, Marie Ouillé. I conducted these experimental studies together Marie Ouillé and analyzed the data with help from Stefan Haessler.

The last section of this chapter focuses on the wavefront measurement of the XUV harmonics to determine their focussability. These measurements were performed as part of a LaserLab campaign in collaboration with Li Lu (Shenzhen Technology University) and Philippe Zeitoun (LOA). I performed the experiments with Chaoneng Wu and Mingyuan Shi (Shenzhen Technology University) and the preliminary data analysis on these measurements with support from Philippe Zeitoun and Chaoneng Wu.

7.1 State-of-the-art

Ever since the pioneering demonstration of the feasibility of attosecond pulses in 2001 [11, 321], the field of attosecond science has rapidly advanced, attracting significant attention within the scientific community. To date, the most widely used and matured route for producing attosecond pulses remains HHG in atomic and molecular gases [12], which has been used successfully to unveil the atomic and electronic dynamics in ultrafast processes [322–325]. Advancements in laser technology facilitated the generation of CEP-stable and intense few-cycle laser pulses [83], which were almost immediately exploited to time-gate the generation process and produce isolated attosecond pulses (IAP) in the XUV regime [98, 326]. Nevertheless, inherent limitations imposed by the generation

process itself constrain the IR-to-XUV conversion efficiency to $\sim 10^{-4}$ for photon energies below 30 eV [327, 328], whereas for higher photon energies the efficiency drops to $\sim 10^{-6}$ [329, 330], limiting the attosecond pulse energies to ~nJ to a few μJ. PMs driven at relativistic intensities have long been recognized as a promising route for generating bright attosecond pulses and ultrashort electron bunches [331], with anticipated percent-level conversion efficiencies [238]. Moreover, attosecond pulses generated from PMs were predicted to have high spatial coherence [247, 332] and measured to have a nearly-FTL pulse profile [245].

Owing to the better suitability of IAPs over attosecond pulse trains (APT) for real-time imaging of fundamental electronic processes [322, 323, 333, 334], significant efforts have been dedicated to gate the generation process to produce IAPs from PMs. Some of the proposed and experimentally used techniques are detailed below:

- **Attosecond lighthouse:** First proposed by Vincenti *et al.* [335] and experimentally demonstrated in the PCO group in 2012 [336], this technique involves rotating the wavefront of the driving laser pulses by introducing a pulse-front tilt perpendicular to the polarization plane, so that the emitted attosecond pulses are separated in space, with each "atto-beamlet" emitted at a CEP-dependent angle.

- **Polarization gating:** This technique involves creating a short gate window, wherein only the dominant field cycle i.e. at the peak of the pulse envelope is p-polarized and contributes to efficient RHHG on PMs [337–339]. Originally employed in gas-HHG, this approach relaxes the constraints on the driving laser pulses, allowing to use multi-cycle pulses to generate IAPs.

- **Non-collinear gating:** This technique was also initially proposed [340] and exploited for gas-HHG [341]. More recently, its potential has been investigated through simulations for relativistic PMs [342]. In this method, two identical temporally separated laser pulses, are focused on a PM with a 2θ angle between them. Attosecond pulses are emitted in the direction of the incident wavefront that rotates over time due to the non-collinear nature of the interaction. This rotation results in the propagation of each atto-beamlet in a different direction, effectively separating them in space.

However, all these techniques share a common drawback of being costly in terms of the required driving intensity. Alternatively, a more direct and energy-efficient method of generating IAPs is to temporally gate the interaction on the surface of PMs by using CEP-controlled few-cycle or ideally, near-single-cycle driving laser pulses. Although technologically challenging, producing high-quality CEP-stabilized near-single-cycle pulses has been pursued, and IAPs generated via this mechanism have been reported where the generated XUV spectrum is recorded while measuring the fluctuating CEP of the driving laser pulses in parallel [62–64].

Kormin *et al.* [62] enhanced the contrast of 5.1 fs - 40 mJ pulses generated by the "*Light-Wave Synthesizer*" (LWS) system [343] using a PM and focused the pulses to $\sim 10^{20}$ W/cm^2, obliquely on a relativistic PM at 1 Hz repetition rate. The authors relied on data binning and CEP-sorting, which revealed a linear shift of the harmonic spectral peak positions. At a specific CEP value, a train of three attosecond pulses was emitted with the central pulse 30% more intense than the satellite pulses.

Jahn *et al.* [63] used 7 fs - 25 mJ pulses at 10 Hz repetition rate from an OPCPA-based laser system [344], focused to $\sim 10^{19}$ W/cm^2 obliquely on a relativistic PM. In this case too, the authors employed CEP-tagging and data-binning techniques. They observed a CEP-dependent shift of the harmonic peaks along the energy axis and an overall harmonic yield that was higher for the case when an IAP was emitted.

In the PCO group, Böhle *et al.* [64] used 3.5 fs - 2.6 mJ energy laser pulses at 1 kHz, focused tightly to $\sim 10^{19}$ W/cm^2 onto a rotating target. At the time, CEP control was not successfully implemented in the *Salle Noire* laser chain. The authors could observe an XUV continuum corresponding to the production of an IAP while relying on data-binning and post-processing. An isolation degree (defined as the main-to-satellite pulse temporal intensity ratio) of ≈ 10 was predicted via simulations without any spectral filtering.

Thanks to the recent upgrades of the *Salle Noire* laser system, we now have full, and, more importantly, reliable control over the CEP of the driving laser pulses at 1 kHz. As a result, we have gained the capability to produce IAPs on-demand, paving the way for attosecond pump-probe experiments with (allegedly) bright IAPs at kHz repetition rate.

7.2 CEP effects on RHHG and relativistic electrons

7.2.1 Varying plasma gradient scale length

Figure 7.1 displays a series of scans for different Prepulse lead times (or plasma gradient scale lengths) for varying CEP values of the 3.6 fs driver pulse focused to 1.3×10^{19} W/cm^2 on-target, corresponding to $a_0 \approx 2.4$. Concurrently, a plasma expansion speed of 18.6 nm/ps was determined during the same experimental campaign under similar interaction conditions. The CEP values are measured relative to an unknown offset.

We observe a distinct CEP-dependent shift of the harmonic peaks along the energy axis for all the depicted gradient scale lengths, particularly pronounced for the steepest gradient scale length (figure 7.1(a)). This observation echoes with the findings previously reported in the sub-relativistic regime with 5 fs pulses [345] and relatively recently, in the relativistic regime [62, 63].

7.2.2 At the optimal gradient scale length

There is clearly an optimal gradient scale length corresponding to a Prepulse lead time of 2 ps at which the spectral extent of the generated harmonics is maximized and the CEP effects are most pronounced. We observe a CEP-dependent transition from a very modulated spectrum around a CEP value of 0 rad to a quasi-continuous XUV spectrum at an offset of π, around a CEP value of -3 rad (figure 7.1(c)).

Figure 7.2(top-panel) provides a closer look into the CEP scan for the optimal gradient length case, laying out the angularly-resolved HHG spectrograph for different CEP values. To mitigate any experimental bias, the CEP was varied randomly throughout this scan. Two extreme cases are highlighted atop the HHG spectrographs, depicting the integrated XUV spectra at an offset of π and showcasing the consistent trend. For a CEP value of -2.5 rad, a highly modulated XUV spectrum is

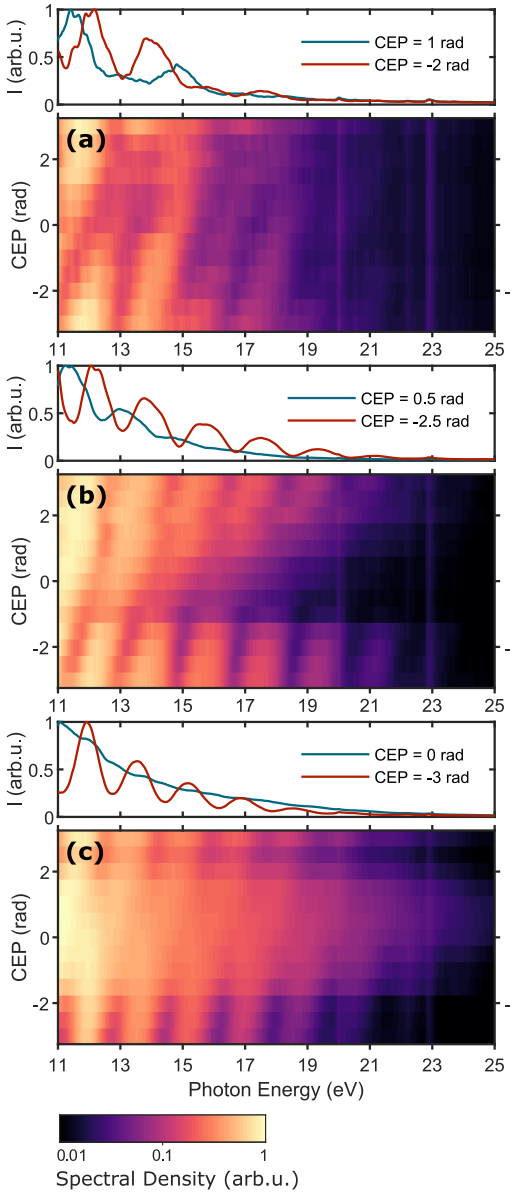

Figure 7.1: Vertically-integrated HHG spectra as a function of the relative CEP of the driver pulse, for different Prepulse lead times: without the Prepulse i.e the Main pulse is directly focused onto the target and the Prepulse arrives after the interaction (a), 1 ps (b), and 2 ps (c). Above each frame are two line-out spectra measured for opposite laser waveforms (π CEP offset). Each data acquisition is averaged over 100 consecutive laser shots (100 ms). The CEP is measured relative to an arbitrary unknown offset. The Prepulse lead times can be translated to gradient scale lengths using an expansion speed of $c_s = 18.6\,\mathrm{nm/ps}$ measured during the same campaign.

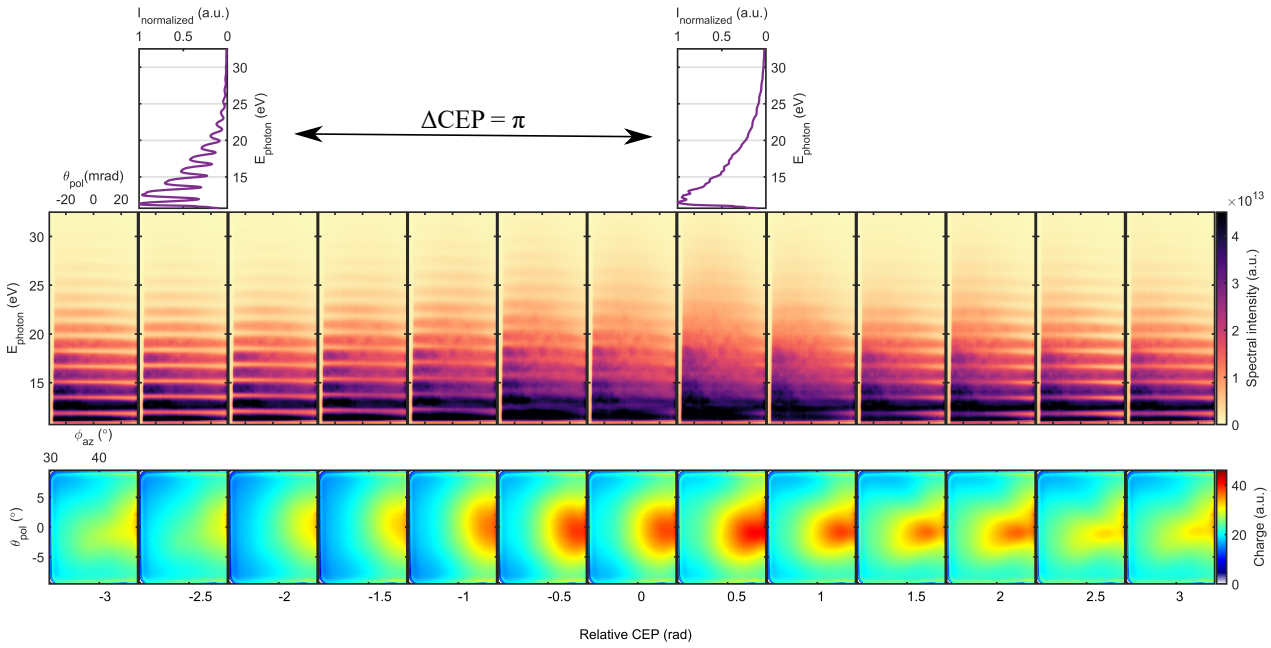

Figure 7.2: Simultaneously recorded of angularly-resolved HHG spectrograph (top-panel), electron charge distributions (bottom-panel) for varying CEP values measured at a Prepulse lead time of 2 ps that prepares the optimal gradient scale length. The CEP values measured relative to an arbitrary offset and were varied randomly during this scan to avoid any experimental bias. Each measurement is averaged over 2 consecutive acquisitions of 100 shots, i.e. 200 shots.

observed, whereas at an offset of approximately π (CEP value of 0.5 rad), a nearly continuous XUV spectrum is measured. Moreover, the integrated harmonic yield is $\approx 20\%$ higher in the case of the quasi-continuous spectrum compared to the modulated case.

It is important to acknowledge that while the scans depicted in Figures 7.1 and 7.2 originate from the same experimental campaign, they were acquired on different experimental days. Consequently, they are susceptible, albeit minimally, to day-to-day fluctuations in energy and CEP stability within the laser chain. Nevertheless, the CEP effect on HHG spectra as well as electron beam profile was reproducible from day-to-day.

Figure 7.3 showcases the angularly-resolved XUV spectrograph and the spatial intensity profile of the XUV beam, both acquired on the same day, using a 4 fs driver pulse. It's important to emphasize that although the spectral and spatial measurements were not simultaneous, they were conducted consecutively, maintaining the same interaction conditions throughout. The XUV beam exhibits a divergence of approximately $\approx 75\ \text{mrad} \times 95\ \text{mrad}$ across the scan. It's noteworthy that no spectral filtering was applied for this measurement; instead, the spectral filtering was solely the result of the response range of the MCP and the reflectivity of the Silicon plate used in the measurement setup (see Section 5.4.2). Consequently, the measured signal is dominated by the 6th harmonic ($\approx 10\,\text{eV}$), explaining the observed high divergence.

A similar trend is observed in the measured XUV spectrograph in figure 7.3 compared to the scan in figure 7.2, as emphasized by the two integrated XUV spectra atop the HHG spectrographs. At a CEP value of -1 rad, corresponding to a quasi-continuous XUV spectrum, a more intense XUV beam

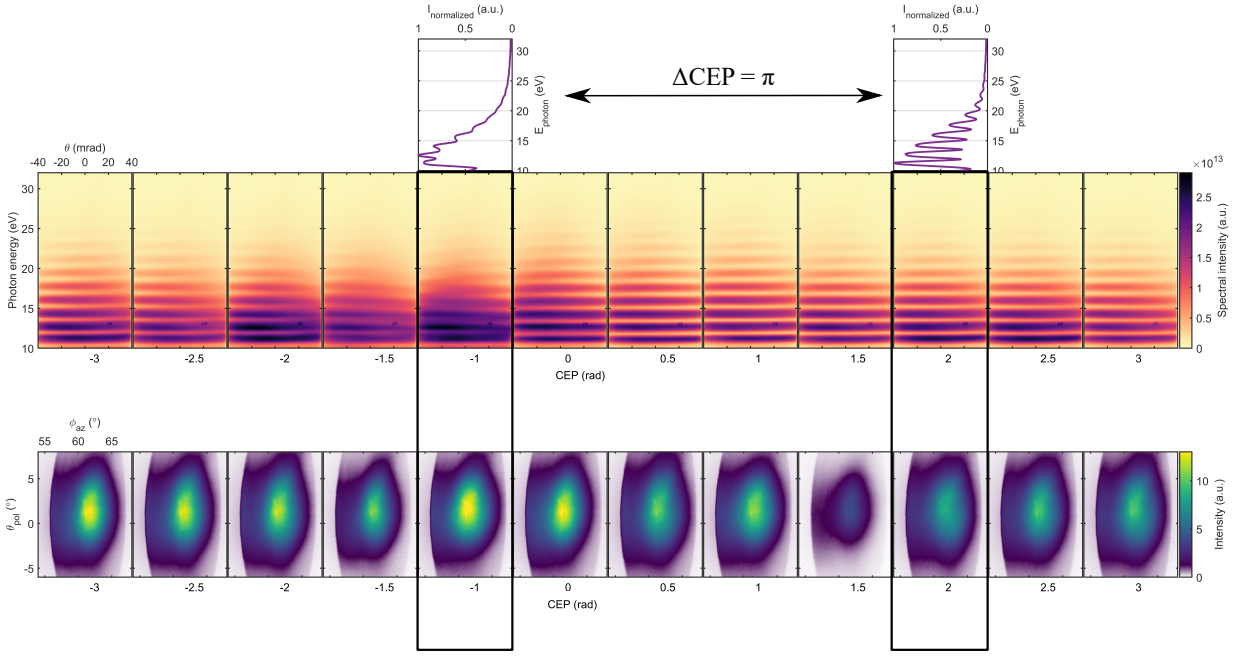

Figure 7.3: Angularly-resolved HHG spectrograph (top-panel) and spatial-intensity profile of the XUV beam (bottom-panel) recorded for a varying CEP of the 4 fs driver pulse, at the optimal density gradient length. Each image is averaged over 100 consecutive shots. It should be noted that these scans were not measured synchronously, but consecutively, albeit under the same experimental conditions.

is observed, while at an offset of π, the harmonic yield is significantly lower. Nevertheless the beam size remains approximately the same.

Hence, we can now control not only the spectral emission properties of the HHG and consequently the temporal structure (whether 1 or 2 attosecond pulses are generated, discussed in the next section), but also selectively enhance the energy of the emitted attosecond pulse on demand. However, the observed increase in measured energy should be further validated through dedicated experimental investigations.

7.2.3 From spectral measurements to temporal insights

Thanks to the 2D PIC simulations performed by Maxence Thévenet, we could translate our spectral measurements into a temporal domain and obtain the temporal structure of the generated attosecond pulses. The simulation parameters were chosen to closely resemble our experimental conditions: a 3.5 fs pulse with a pulse central wavelength of $\lambda = 800$ nm, focused to a spot size of $\omega_0 = 1.5$ μm, to a peak intensity of 8.5×10^{18} W/cm^2, resulting in $a_0 = 2$. The laser pulses were focused obliquely ($\theta_i = 55°$) onto a plasma with an exponentially decaying density profile, at a gradient scale length of $L_g = 0.1\lambda$ and a peak plasma density of $n_e = 400 n_c$.

Figure 7.4 presents the simulated incident and reflected laser magnetic field profiles for four distinct CEP cases: CEP $= 0$, corresponding to the “maximal push” when the electrons are efficiently pushed into the plasma; CEP $= \pi/2$, indicating two distinct push-pull cycles; CEP $= \pi$, represent-

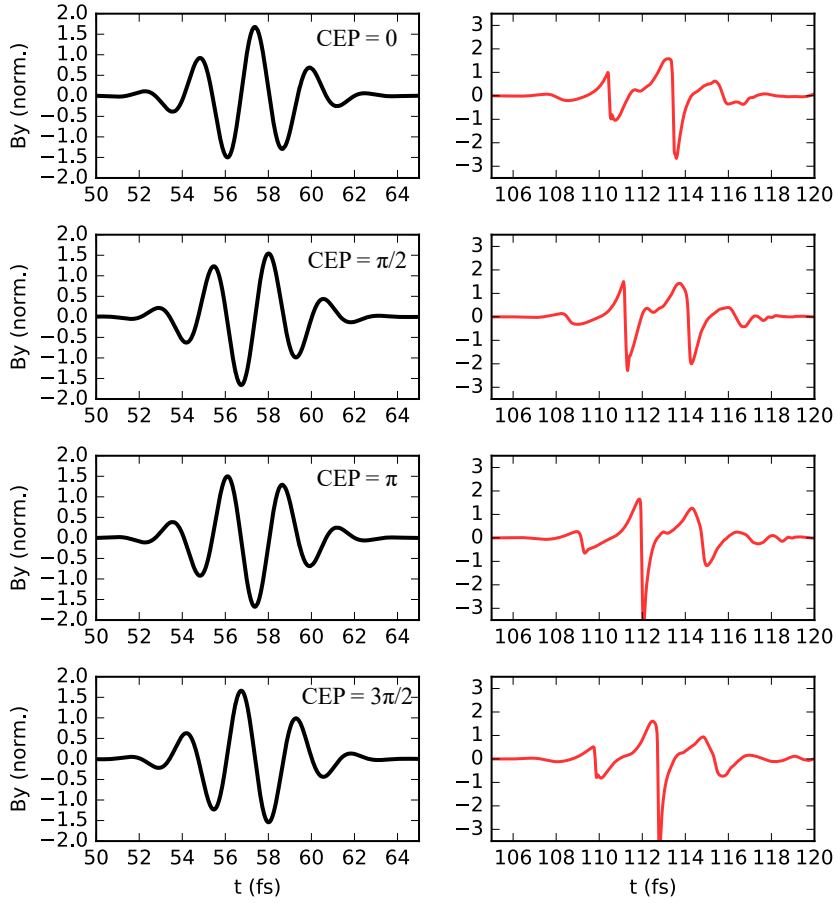

Figure 7.4: Results of 2D PIC simulations. Magnetic field of the incident (left-panel) and the reflected laser pulse (right-panel) for CEP values of 0 (a), $\pi/2$ (b), π (c), and $3\pi/2$ (d). Courtesy of Maxence Thévenet.

ing an "maximal pull" case, when the electrons are efficiently pulled out towards vacuum; and CEP $= 3\pi/2$, a single effective field cycle corresponding to the optimal push-pull scenario. Evidently, the latter two cases result in the strongest temporal compression of a single dominant field cycle in the reflected field profile. The enhanced peak fields observed in these cases cannot be explained by the simple ROM model, where RHHG results from merely a phase-modulation. However, models such as the relativistic electron spring [236, 346, 347] and coherent synchrotron emission [237, 238] provide better explanations, suggesting that RHHG arises from the re-emission of energy stored within the plasma.

The simulated pulse intensities corresponding to the reflected field profiles in figure 7.4 were obtained through a Hilbert transform, as depicted in Figure 7.5(b). When the CEP value is $\pi/2$, two push-pull cycles occur in the incident laser field (Figure 7.4), resulting in the emission of two attosecond pulses in time, corresponding to a highly modulated XUV spectrum (Figure 7.5).

At a CEP offset of π, the optimal push-pull case of a CEP value of $3\pi/2$, a single dominant optical cycle emerges. Within this cycle, two equally intense half cycles of the incident laser field occur in the correct sequence: electrons are initially pushed into the plasma and then pulled out towards vacuum.

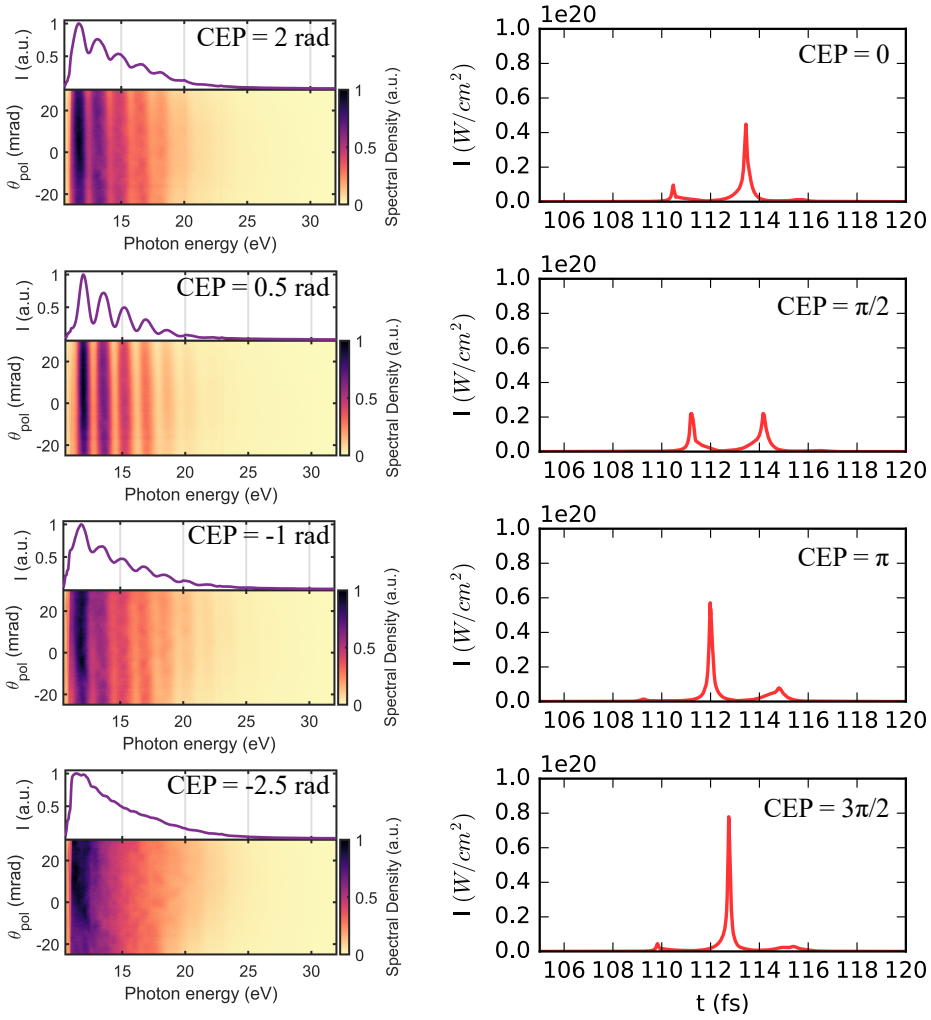

Figure 7.5: Experimentally measured XUV spectra for four relative CEP values separated by $\approx \pi/2$: 2 rad, 0.5 rad, -1 rad, and -2.5 rad, measured w.r.t. an arbitrary CEP offset, at the optimal gradient scale length (left-panel). Each spectrum image is averaged over 200 consecutive laser shots. The simulated intensity profiles of the reflected attosecond pulse for four absolute CEP values separated by $\pi/2$: 0, $\pi/2$, π, $3\pi/2$. Simulated traces provided by Maxence Thévenet.

This sequence generates a dominant push-pull cycle conducive to efficient synchrotron emission. In the optimal scenario, an isolated attosecond pulse, 350 as in duration, is generated with a 10-fold isolation degree, containing approximately 35% of the incident pulse energy (assuming symmetry around the beam propagation) without any spectral filtering.

7.2.4 Correlated behavior of relativistic electrons

We have previously seen that in direct correlation with the RHHG emission, optimized at the same plasma density gradients, relativistic electrons are emitted from PMs. They are injected at a specific phase in the reflected laser field, undergo acceleration [267], and are emitted in sub-femtosecond bunches [251].

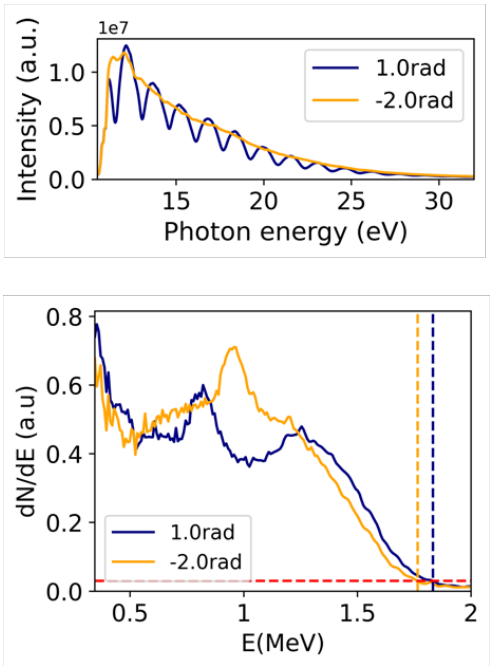

Figure 7.6: Simultaneously acquired integrated HHG (top) and electron (bottom) spectra for two different relative CEP values, separated by $\approx \pi$. The electron spectra were measured at $\phi_{az} = 39°$.

Figure 7.2 depicts the angular charge distribution of electrons recorded simultaneously with the HHG spectra for varying CEP of the driver laser pulses. At the CEP value of -2.5 rad, corresponding to a modulated XUV spectrum (or emission of two attosecond pulses in the temporal domain), a diffused and isotropic electron beam profile is recorded, resembling ponderomotive scattering of the electrons by the laser. In contrast, when an XUV continuum corresponding to an IAP is observed, a highly localized electron beam with higher charge is emitted with a clear charge density peak close to the specular direction ($\phi_{az} = 55°$). Notably, a higher integrated electronic charge aligns with a higher harmonic yield.

Furthermore, the measurement of CEP-dependent electron energy spectra confirms the influence of the CEP of the driver pulse on the acceleration mechanism. Figure 7.6 illustrates the simultaneously measured HHG and electron energy spectra for two distinct CEP values separated by approximately π, obtained under similar experimental conditions. At a relative CEP value of 1 rad, a modulated HHG spectrum indicates the presence of two push-pull cycles. Correspondingly, two peaks are observed in the electron spectrum around 0.7 MeV and 1.3 MeV, respectively. Conversely, at a CEP offset of approximately π, where we observe an XUV continuum and expect a dominant push-pull cycle, only one peak is visible in the electron spectrum at around 1 MeV. These observations could signify the phase-locked injection and subsequent VLA of either one (in the case of an absolute CEP of $3\pi/2$) or two (in the case of an absolute CEP of $\pi/2$) presumed sub-femtosecond relativistic electron pulses. These electron energy measurements were made on a small part of the electron beam sampled by a pinhole located slightly off the electron charge peak due to the constraints imposed by our measurement setup. We expect to observe higher electron energies towards the center of the electron beam and also expect this CEP effect to be more pronounced. This should

be confirmed in future experiments with an adapted diagnostic design.

Nonetheless, our observation represents the first experimental evidence of sub-cycle control of electron emission from PMs.

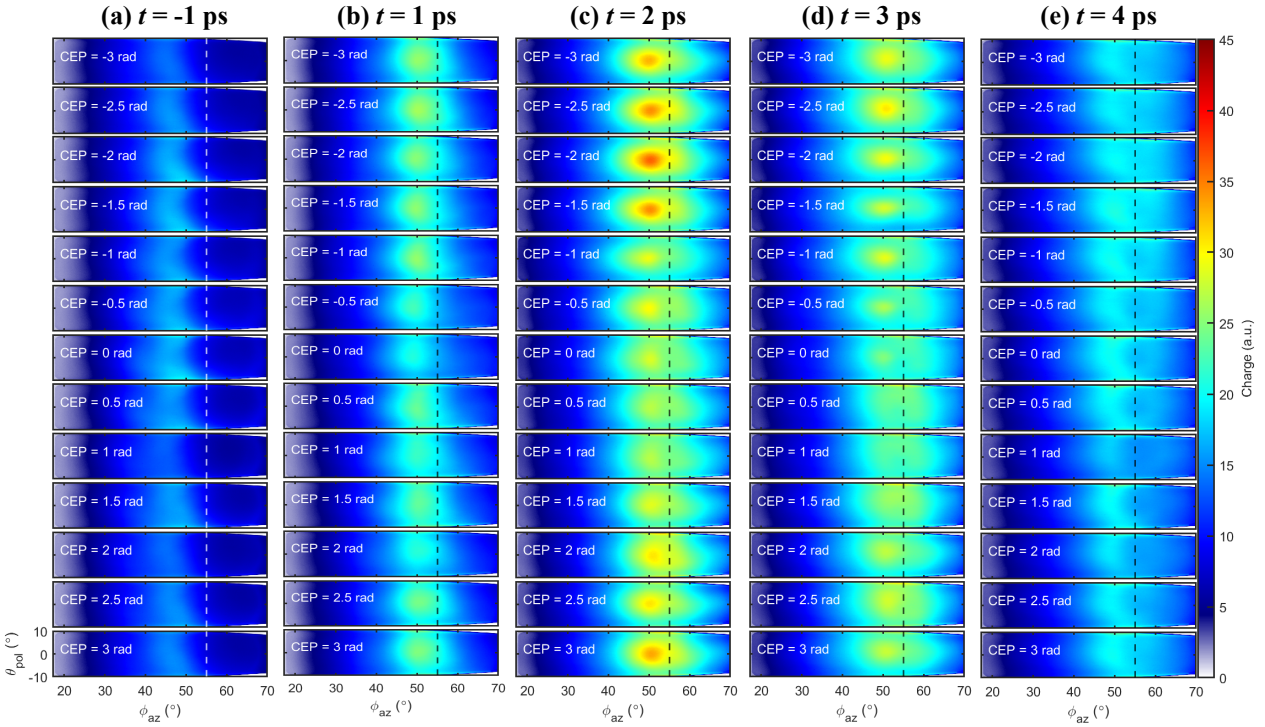

Figure 7.7: Angular-electron charge distribution scan over randomized CEP for different Prepulse lead times: $\tau = -1$ ps i.e. the Prepulse arrives after the Main-pulse (a), $\tau = +1$ ps (b), $\tau = +2$ ps (c), $\tau = +3$ ps (d) and $\tau = +4$ ps (e). The Prepulse lead times can be translated to the gradient scale length using a plasma expansion speed of $c_s = 16.1$ nm/ps. The dotted black line marks the specular direction at $\phi = 55°$.

7.3 Wide-range electron angular-charge detection

In an effort to fully characterize the electron beam while measuring the angular charge spread for $\phi_{az} > 55°$, we dedicated two entire experimental days to measurements with a larger LANEX screen (setup II in 5.5). It is important to note that with this setup, simultaneous detection of the HHG spectrum is not feasible, introducing some uncertainty in correlating observations with the HHG and ensuring identical interaction conditions compared to the previous results outlined in this chapter. Nonetheless, both electrons and RHHG are optimized when the laser focal plane coincides with the target, which provides a promising indication.

Figures 7.7 illustrates randomized CEP scans while capturing the complete electron beam profile obtained for 3.6 fs driver pulses at various Prepulse lead times, converted to gradient scale length using a plasma expansion speed of $c_s = 16.1$ nm/ps, measured during the same experimental campaign. Figure 7.7(a) depicts electron beam profiles recorded for different CEP values with the Main-Pulse directly focused on the target, while the Prepulse follows. Here, the gradient scale length is the

steepest and limited by the laser contrast. Interestingly, no clear CEP effect is discernible on the angular-charge distribution in this scan. However, as a Prepulse is introduced for controlling the interaction, CEP effects become more apparent, particularly noticeable with Prepulse delays of 1 ps, 2 ps, and 3 ps. As the Prepulse lead time is further increased to 4 ps, the CEP effects again become less pronounced. At the optimal gradients, as observed in our previous experiments where clear XUV continua was obtained, we observe the highest electron charge at a relative CEP of -2 rad, located at $\phi_{az} \approx 50°$. At a CEP offset of $\approx \pi$, we see a decrease in the peak electron charge and the electron distribution looks more centro-symmetric, likely due to the ponderomotive scattering by the laser.

Under optimal conditions identified in simulations, an absolute CEP value of $3\pi/2$, corresponds to a maximum push-pull scenario at focus where the electrons remain in-phase with the reflected laser field and experience VLA, as previously discussed in 4.8.1. The electrons gain the highest kinetic energies via VLA and are finally expelled away from the reflected laser field, towards the normal direction in the plane of polarization. Conversely, a CEP offset of π yields two less intense push-pull cycles, resulting in lower kinetic energy electrons. Here, the ponderomotive force dominates, causing the electrons to be isotropically pushed away from the high-field region, manifesting as a ring-like structure. However, this should be verified through PIC simulations.

7.4 XUV wavefront

Now that we can routinely generate IAPs on demand, the next challenge is to refocus them for applications. In order to estimate their focussability, we attempted to measure the wavefront of the emitted XUV beam. These measurements were conducted as a part of a LaserLab campaign in collaboration with Li Lu (Shenzhen Technology University, China) and Philippe Zeitoun (LOA).

However, measuring the wavefront of the XUV beam poses significant challenges for several reasons:

1. The tight focusing geometry results in a highly divergent reflected XUV beam as visible in figure 7.3, making it difficult to capture the full beam.

2. Effective shielding against both electrons and X-rays is imperative to record any exploitable data. Additionally, the emission of relativistic electrons from the PMs creates a hostile environment for electronics, necessitating comprehensive shielding measures. As depicted in Figure 7.8, a stark disparity is evident between the captured Hartmanngrams with and without adequate shielding. The presence of small bright spots, indicative of hotspots contaminating the XUV signal, is notably amplified in the absence of proper shielding. Mitigating these residual hotspots can be easily achieved through the application of a high-frequency filter in the Fourier-space with varying window-size, ensuring their removal without compromising the fidelity of the XUV signal through excessive averaging.

3. Certain fixed diagnostics, like the XUV spectrometer, are essential to retain so as to allow signal optimization. However, this limits the available space within the chamber for positioning the wavefront sensor optimally. Despite this spatial constraint, the XUV spectrometer serves a

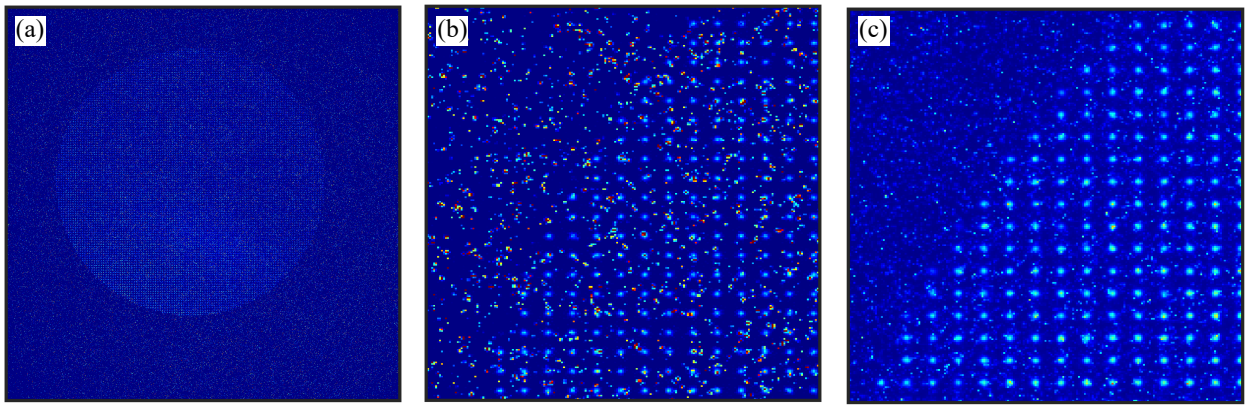

Figure 7.8: Raw images of the complete Hartmanngram (a) and a magnified view (b) captured with the wavefront sensor acquired prior to the implementation of appropriate shielding. Magnified raw image of the Hartmanngram after the appropriate shielding was installed (c).

crucial role by providing a stable reference point for alignment and signal calibration. Furthermore, it enables comparison with past measurements conducted under analogous conditions, ensuring consistency and reliability of the experimental measurements.

4. The task of directing the entire beam towards the wavefront sensor and achieving precise alignment demands several degrees of motorization, often necessitating micrometric precision. This challenge is further compounded the low beam height of 89 mm in the interaction chamber. Designing motorized stages that are both compact and robust to support the weight of the wavefront sensor as well as the lead-shielding around it, while offering the required scanning range and resolution poses an engineering challenge.

It took several attempts spanning over nearly two years to devise a setup capable of capturing the full beam with the required precision. Details of previous attempts at the wavefront measurements can be found in Marie Ouillé's thesis work [67].

7.4.1 Silicon plate calibration

In the wavefront measurement setup (see 5.4.3), a Silicon plate is used to steer the emitted XUV beam towards the wavefront sensor. To accurately estimate the wavefront of the XUV beam, it is crucial to thoroughly examine the flatness of the Silicon plate and the aberrations it introduces in the measurements. Typically, calibration involves measuring the wavefront of a known reference beam before and after deflection by the Silicon plate. For reliability, it is often preferred to perform calibrations at the same wavelength as the measurements. In the XUV regime, low-divergence beams from gas-HHG sources are commonly used. However, lacking such a source in our lab, for a preliminary analysis we adopted an alternative approach, using a Helium-Neon source for calibration of the Silicon plate, using a Shack-Hartmann wavefront sensor (HASO, Imagine Optic). The reflective nature of the Silicon plate in the visible spectral region provides flexibility, unlike multi-layer mirrors that require calibration at specific XUV wavelengths.

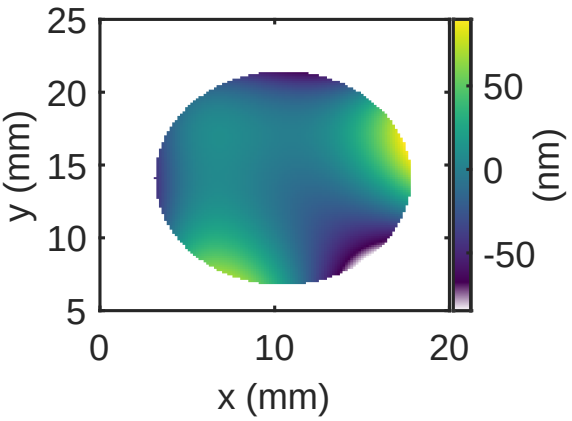

Figure 7.9: Silicon plate surface map showing all aberrations, excluding tilts and defocus.

Aberrations	RMS value (nm)
0° - Astigmatism	3.6143
45° - Astigmatism	-16.0389
0° - Coma	4.4912
90° - Coma	3.4638
Spherical	-2.9871
0° - Trefoil	15.1852
90° - Trefoil	-11.74

Table 7.1: A Zernike decomposition of the Silicon plate map

These calibration measurements were conducted by André Kalouguine (LOA). A meticulous raster scan of the mirror surface was performed and the calculated slopes were stitched while maintaining a required overlap between consecutive positions. Figure 7.9 shows a map of the Silicon plate and the corresponding major aberrations projected onto a Zernike-base are presented in table 7.1.

The preliminary calibration measurements ensured that the mirror maintains $> \lambda/20$ flatness ($\lambda = 633$ nm), with an overall 26 nm RMS. It is imperative to compare these calibration results with the measurements using a reliable XUV source for a better resolved Silicon plate surface map. For the preliminary XUV wavefront reconstruction results presented in this section, the Silicon plate surface map has not been considered. The aberrations introduced by this plate will be addressed once it is calibrated with a reliable XUV source.

7.4.2 Wavefront sensor calibration

The high-NA wavefront sensor used for these measurements was calibrated immediately prior to the experiments at the Nanolite beamline at CEA-Saclay. Stefan Haessler, David Gauthier (CEA), Willem Boutou (CEA), and Li Lu (SZTU), with remote support from Xu Liu (CEA) conducted these calibration measurements using the gas-HHG source at Nanolite. A $2\,\mu$m pinhole, positioned approximately 1.2 m from the sensor, produced an almost perfect spherical wavefront. To compensate for the lost flux, long acquisition times of approximately seven minutes were performed. *Imagine Optic* generated a suitable calibration file to compute the measured wavefront.

Due to the space constraints at the Nanolite beamline, these calibration measurements could only be performed on-axis. This means the wavefront reconstructions are most reliable when the central blocked hole in the Hartmann plate is aligned with the center of the chip, ensuring no significant tilts are present. This limitation adds further constraints to our wavefront measurements. Nevertheless, to test our new wavefront measurement setup, we proceeded with the measurements, hoping to improve the calibration protocol in future experiments.

7.4.3 At the optimal gradient scale length

Figure 7.10 presents the wavefront reconstruction results obtained for a 4.1 fs driver laser pulse focused onto the relativistic PM at the optimal gradient scale length for RHHG. This acquisition was averaged over 100 consecutive laser shots.

The 200 nm thick aluminum filter in front of the wavefront sensor, spectrally selects harmonics below ≈ 70 nm. In the measured spectral range, a beam divergence of ≈ 45 mrad is inferred from figure 7.10. This is significantly lower than what was measured in our direct spatial beam profile measurements (figure 7.3). This discrepancy makes sense because, in the spatial measurements, the spectrum starts from 100 nm, whereas here we restrict it further to 70 nm. The divergence of the XUV beam decreases with increasing harmonic order, which explains why we observe a lower beam divergence here.

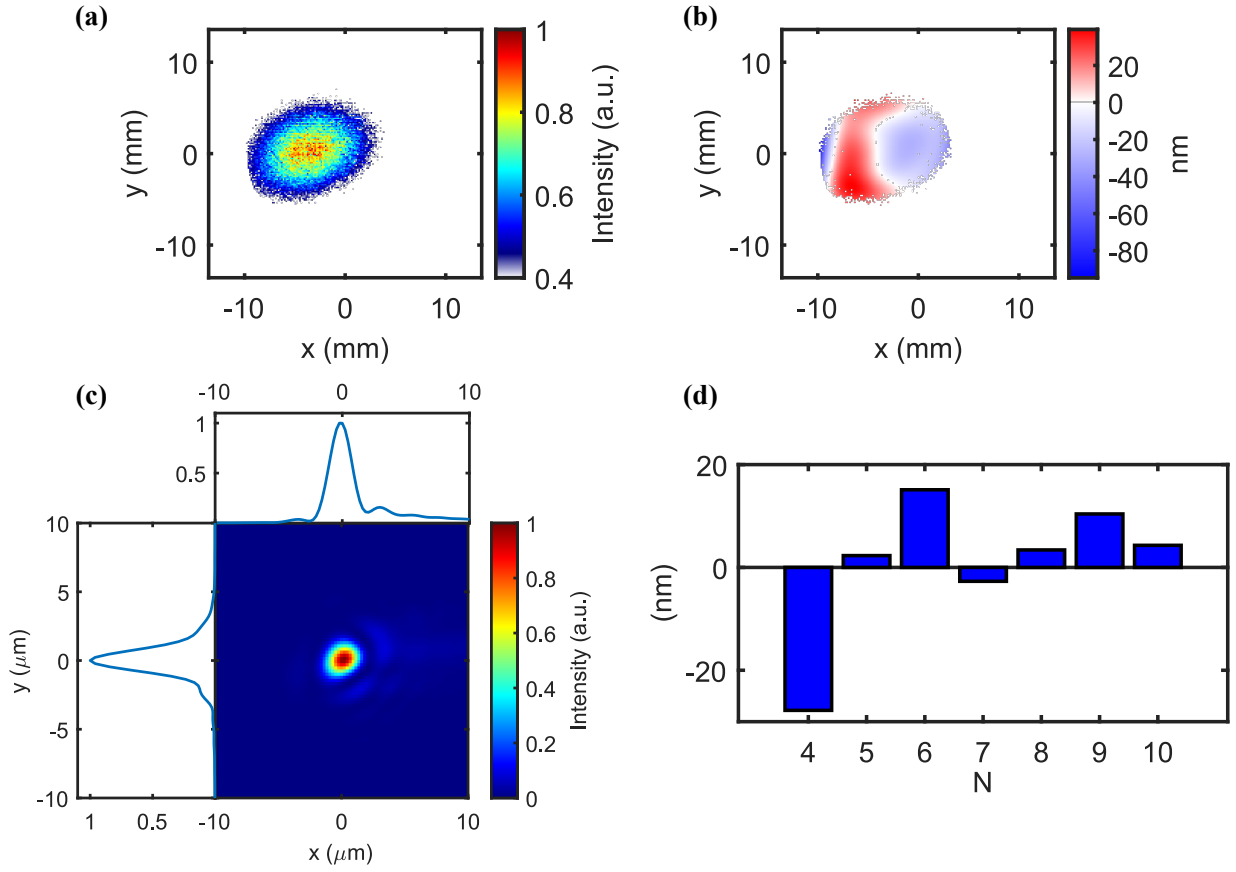

Figure 7.10: Measured XUV beam profile (a) and the reconstructed wavefront (b), excluding the tilts and defocus, for a 4.1 fs driver laser pulse, measured at the optimal plasma gradient scale length for RHHG. These measurements are averaged over 100 consecutive laser shots. The corresponding PSF (c) and the wavefront projected onto a Zernike-base (d), for $N = 4 - 10$, corresponding to 0° - Astigmatism, 90° - Astigmatism, 0° - Coma, 90° - Coma, spherical, 0° - Trefoil, and 90° - Trefoil aberrations, respectively. N is defined according to the Noll's sequential indices.

The reconstructed wavefront (figure 7.10 (b)) exhibits 22 nm RMS and a 100 nm peak-to-valley distortions. When projected onto a Zernike base (figure 7.10(d)), we can see ≈ 28 nm 0° - Astigma-

tism is the dominant aberration, closely followed by $\approx 15\,\mathrm{nm}\ 0^\circ$ - Coma, and $\approx 10\,\mathrm{nm}\ 0^\circ$ - Trefoil. This could be inherited from the driver laser pulse. If we directly calculate the PSF (figure 7.10(c)) from the reconstructed wavefront (figure 7.10(b)), we obtain a Strehl ratio of 0.706. However, it is important to note that the calibration of the steering Silicon plate has not been included in this wavefront reconstruction. Therefore, the wavefront decomposition, the Strehl ratio and the absolute beam quality cannot be conclusively determined until this calibration is completed.

7.4.4 CEP effects

Even though the lack of a proper calibration of the Silicon plate prohibits us from making any absolute claims about the measured wavefront, we can nevertheless reliably study a relative change in the wavefront with the CEP of the driver laser pulses. Figure 7.11 presents the variation of the overall wavefront RMS as well as projection onto the Zernike base for $N = 4 - 8$. Each data point in this figure is averaged over 100 consecutive laser shots. The CEP was randomly varied to avoid any experimental bias. Moreover, owing to the limitation imposed by the restricted calibration of the wavefront sensor, we ensured that the blocked central hole of the Hartmann plat was well aligned with the center of the CCD chip to ensure that no tilts were present in the measurement.

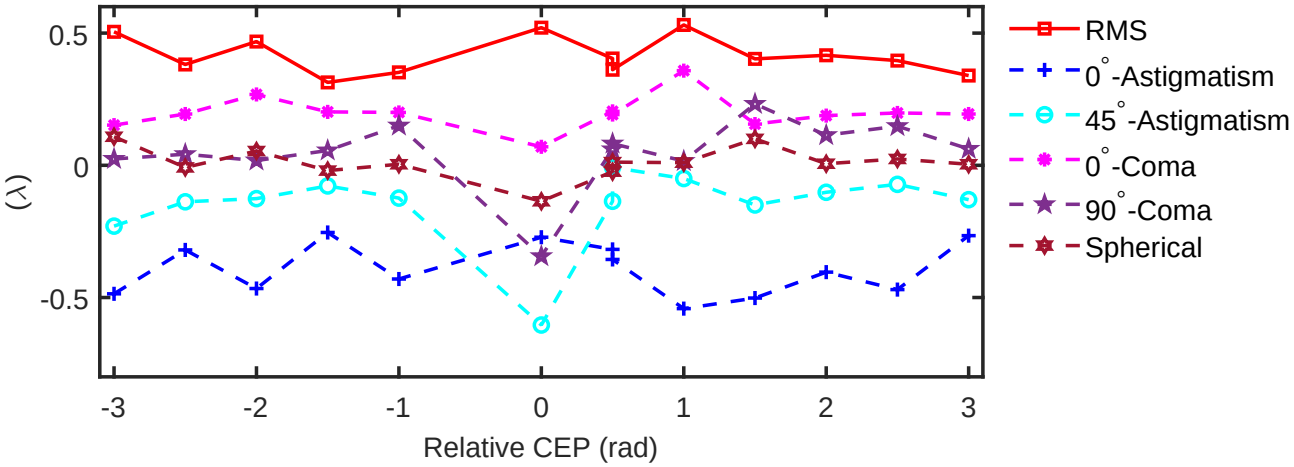

Figure 7.11: Variation of the overall wavefront RMS and the dominant aberrations with the CEP of the driving 4.1 fs laser pulses at the optimal gradient scale length for RHHG. Each data point is averaged over 100 consecutive laser shots. The CEP was randomly varied to avoid any experimental bias. Here, $\lambda = 50\,\mathrm{nm}$. The CEP $= 2\,\mathrm{rad}$ case corresponds to the XUV spectral continuum generation.

From figure 7.11, we can infer that the measured wavefront of the XUV beam exhibits minimal variation with the CEP of the driver laser pulses. This suggests that in our moderately relativistic regime, significant CEP-dependent plasma denting is not observed. However, it is imperative to confirm this through simulations.

Nevertheless, it's crucial to emphasize that the analysis of these wavefront measurements should be reassessed once the silicon is calibrated with a reliable XUV beam.

Conclusion and outlook

This thesis builds upon a long history of development of the *Salle Noire* beamline, with a two-fold objective. The first part of the thesis was dedicated to enhancing the *Salle Noire* laser performance by augmenting the available pulse energy, while also improving the stability and reliability of the source properties, particularly the pulse-to-pulse CEP, and achieving more consistent day-to-day performance.

Chapter 1 reviews the fundamentals of ultrafast optics and lasers. Chapter 2 provides a brief overview of the *Salle Noire* laser architecture as inherited from my predecessors in 2019, identifying various components in the chain that could be upgraded to enhance source properties. The second half of chapter 2 described design and implementation of a cryogenically-cooled multi-pass Ti:Sa amplifier, which increased the available pulse energy after the second CPA from $8.5\,$mJ to up to $12\,$mJ. However, due to the peak-power handling limitations of the current HCF-based post-compression setup, the peak power after the amplifier was reduced to match the previous configuration. While awaiting an upgrade of the post-compression setup, the new amplifier nevertheless significantly improved pulse-to-pulse energy stability and, most importantly, reduced the CEP noise at the end of the chain by at least a factor of two, all while maintaining an excellent temporal intensity contrast ratio. Additionally, an extension-arm was implemented on the post-compression setup to ensure long-term operation without damaging optics. At the end of the chain, we can routinely deliver on-target 2.5 mJ energy, tunable 30 fs to 3.5 fs (~ 1.5 optical cycle) pulses with a temporal contrast of $> 10^{10}$, and a residual CEP noise of $\sim 200\,$mrad RMS, at 1 kHz repetition rate.

Scaling the HCF-based post-compression setups for higher peak powers necessitates the use of larger fiber core diameters and lengths, which can quickly become impractical. I developed a power-scaled HCF-based post-compression setup for Li Lu (Shenzhen Technology University or SZTU), as detailed in Appendix A, capable of handling twice the input energies as compared to the one in *Salle Noire*. However, scaling the energy handling by a factor of two increased the overall footprint of the setup from 7 m (*Salle Noire*) to 15 m (SZTU), rendering it already very cumbersome.

In search of alternative solutions for laser post-compression suitable for *Salle Noire* that can produce near-single cycle pulses with waveform-stability, while maintaining a practical footprint and ease of use, Chapter 3 explores a different post-compression scheme: gas-filled-MPCs. These have emerged as an appealing alternative to HCF-based schemes, due to their high throughput, easy handling, high compression factors, and easy power and energy scalability, while maintaining an excellent output beam quality [84, 348]. We demonstrated post-compression at 1 mJ energy level, down to the few-cycle regime in an Argon-filled MPC. Additionally, we conducted a systematic study

of the different propagation regimes, identifying the roadblocks and potential solutions to reaching the single-cycle regime. This work culminated in an article reported in [151]. An energy-scaled MPC-based post-compression setup should enable full exploitation of the available pulse energy in *Salle Noire*. With the added benefit of an overall higher throughput of the MPCs, it should significantly boost the on-target pulse energy. Motivated by the versatility of the MPCs, we integrated two third-order nonlinear techniques with the MPC architecture for temporal contrast enhancement: NER and XPW. In each case, we could achieve a contrast enhancement of at least 10^3, with record high efficiencies, also reported in [173].

The second part of this thesis was dedicated to using the *Salle Noire* laser to drive relativistic PMs on the surface of initially-solid targets to generate highly energetic particle beams (ions and electrons) and harmonic radiation in the XUV region, corresponding to attosecond pulses ($1\ as\ = 10^{-18}$ s) in the time domain. Chapter 4 briefly reviews the fundamentals of laser-plasma interactions, discussing the HHG emission in the sub-relativistic and relativistic intensity regimes. Additionally, it provides a brief overview of the electron and proton acceleration mechanisms relevant to our experimental conditions.

Chapter 5 details the technical aspects of the kHz relativistic PM beamline in detail, uniquely designed to simultaneously detect three emissions from the relativistic PMs: HHG, electrons and protons. Building upon the previously implemented diagnostics, we introduced additional diagnostic tools to expand the characterization of secondary emissions. Some of these advancements have been reported in [349]. Notably, we implemented an electron spectrometer, a scanning TOF detector for characterizing the angular-spectral spread of protons, and a setup to measure the spatial beam profile and wavefront.

The experimental investigations of relativistic PM emissions unfolds across chapters 6 and 7. In Chapter 6, we delve into the correlations and consequently the underlying electron dynamics, derived from the simultaneous measurements of HHG, electrons, and protons. This approach allows for the observation of direct correlations among these secondary emissions, all while ensuring identical interaction conditions on-target. These experimental studies were conducted systematically, over a wide range of laser and plasma parameters. Notably, we demonstrated RHHG at 1 kHz repetition rate, correlated to the emission of relativistic energy electrons. These findings were detailed in [350]. Additionally, we measured the electron energy spectrum in the laser wakefield acceleration regime (at long gradients), confirming the theoretical predictions by Zaïm *et al.* [255]. Furthermore, we generated nearly-collimated MeV-class proton beams from the front-side of the targets. The high-beam quality obviates the need for additional collimating devices. These proton beams were found to be highly suitable for ion implantation [351, 352] and production of radioisotopes for positron emission tomography [353]. We have detailed this work in a separate publication [354].

The experimental findings detailed in chapter 7 demonstrate sub-cycle control of relativistic PM emissions (RHHG and electrons) at kHz repetition rate. We can now routinely generate, on-demand via CEP control of the driver pulse, XUV continua and relativistic electrons peaked at 1 MeV. Numerical simulations conducted by Maxence Thévenet allowed us to correlate the generated XUV spectral continuum with a bright, isolated attosecond pulse. We performed a comprehensive parameter study to fully characterize and optimize the spatio-spectral properties of the emitted XUV attosecond pulses. Initial steps were taken to characterize the spatial beam profile and wavefront of the XUV beam, es-

sential for determining its focussability and designing an appropriate XUV beam transport system for future applications. For a complete spatio-temporal characterization of the XUV source, future work should include energy and pulse duration measurements as part of the diagnostic toolkit.

The work presented in chapter 7 marks a significant technological advancement towards realizing a plasma-based (bright) attosecond light source. With the design of the *Salle Noire* laser, targeting the λ^3- regime, we can produce attosecond pulses and particle beams at a kHz repetition rate. This capability enables the collection of large datasets, facilitating statistical studies while exploring a high-dimensional parameter space in a reasonable time-frame. Additionally, it opens the possibility for closed-loop automated optimizations [61], all while keeping the footprint of the beamline manageable on a lab-scale.

Potential avenues to explore

Power-scaling RHHG at ELI-ALPS, Hungary

The conceptualization and commissioning of the RHHG beamline at the ELI-ALPS facility in Szeged, Hungary, organized in collaboration with Ardop Industries, represent a significant transfer of our expertise from LOA. This beamline will be primarily driven by the SYLOS 3 laser system, a new generation of OPCPA laser at ELI-ALPS, delivering 120 mJ energy, waveform-controlled 7 fs pulses (≈ 2 optical cycles) at a 1 kHz repetition rate. A detailed summary of the beamline design is provided in the Appendix B.

Towards the end of my thesis, we conducted some of the first shots on-target with another laser from the SYLOS family, the SEA laser, delivering 15 mJ, 12 fs pulses at 10 Hz repetition rate. Despite identifying a few technical issues that need solving, we successfully obtained an HHG spectrum. This beamline holds great promise as it provides access to intensity regimes beyond the capabilities of the *Salle Noire* laser system, enabling the generation of (higher-energy) and (shorter-duration) isolated attosecond pulses. By utilizing relativistic PMs to their full potential, this beamline is poised to pioneer new applications.

Additionally, a secondary SHHG beamline is planned for installation at ELI-ALPS, to be driven by a PW-laser [355]. Post-compressing the PW-laser [356] would enable the combination of temporal gating with a high photon yield, leveraging both the temporal resolution and intensity advantages for advanced research applications.

Liquid plasma mirrors

Relativistic PMs have long been recognized as a promising source of intense attosecond pulses [20]. However, the experimental challenges associated with them have limited the number of researchers in this area to a handful worldwide. Two major inherent limitations of working with solid-target-based PMs are the inability to shoot continuously due to significant refresh times, leading to a restriction to mostly single-shot acquisitions (0.1 - 10 Hz) or burst modes, such as our case of 100 ms bursts at 1 kHz. Additionally, the limited surface area of the targets restricts the shooting time, further complicating operations.

Another significant challenge is the debris generated from the solid targets, which is detrimental to critical and expensive optics. Consumable glass plates are often placed in front of crucial optical components to shield them from debris. We attempted to use AR-coated $300\,\mu\mathrm{m}$ thick optical-quality

fused silica plates to shield the main focusing OAP, which is the most critical optic in close proximity to the target. However, this approach failed with near-single-cycle pulses, as the debris shield severely degraded the pulse quality. This debris issue adds another layer of complexity to the already challenging experimental setup. These challenges have limited the experimental studies of PM emissions to understanding the generation mechanisms [20, 216, 226, 239] and plasma dynamics [62, 254, 345].

A PM based on flat liquid-sheet targets [357] offers a solution to overcome all the above-mentioned limitations. This target provides (1) a self-refreshing rate of > 20 kHz, (2) exceptional control over steering the XUV beam by simply rotating or tilting the target, (3) versatility in terms of target thickness and size, and (4) exceptional stability owing to the laminar flow. To date, liquid-sheet targets have been used to accelerate protons [358, 359] and electrons [360], or as PMs for contrast enhancement [361]. Recently, for the first time, Kim *et al.* [362] demonstrated HHG from a liquid-sheet PM in both CWE and ROM regimes, paving the way for the development of bright attosecond pulses at high repetition rates.

In the PCO group, another PhD student, Antoine Cavagna, has developed two liquid-sheet target setups in close collaboration with Enam Chowdhury and Milo Eder (OSU). One of these targets has been commissioned in the ELI-ALPS beamline, as discussed in Appendix B. The second target has now replaced the solid-target setup in the *Salle Noire* beamline. Consequently, we now have the capability to continuously generate isolated attosecond pulses. Additionally, the ability to generate sub-micrometer thick liquid sheets will allow us to generate harmonics in transmission via the CSE [239] and/or accelerate protons to high energies.

Perspectives

Plasma mirrors as a potential path to the Schwinger limit

Quantum electrodynamics (QED), a cornerstone of modern physics, is widely regarded as the most precisely tested physical theory. In the strong field regime, QED predicts that when large amplitude electromagnetic fields are applied, the interaction of photons with the fermionic quantum vacuum becomes significant. This interaction regime is characterized by effects such as production of magnetic monopoles, polarization of vacuum affecting light propagation, and the light-induced creation of particle-antiparticle pairs from the vacuum, often referred to as the "optical breakdown of the vacuum." In simple terms, the vacuum is not empty space, but is filled with short-lived pairs of particles and anti-particles. In the presence of **strong** electromagnetic fields exceeding the so-called Schwinger limit – an electric field amplitude of $E_0 = 1.32 \times 10^{18}$ V/m, corresponding to an intensity of $I = 4.7 \times 10^{29}$ W/cm^2 [363] – these particles separate from their antiparticle counterparts within the pair lifetime and continue to exist as long as they do not encounter their counterparts again.

Access to the strong-field QED (SF-QED) regime on a lab-scale holds the key to discovering new physics beyond the standard model. It will profoundly impact our understanding of phenomena related to astrophysical relativistic plasma states [364], such as black holes and magnetars, and pave the way for the design of next generation particle colliders, such as TeV Lepton colliders [365].

Manifestations of the Schwinger effect have long been investigated analytically and numerically, and researchers have been on the lookout for its experimental evidence. Advancements in laser technology, particularly the advent of Peta-Watt (PW) class laser systems, have realized the potential of achieving light intensities of 10^{23} W/cm^2 [366], at which matter transforms into an ultra-relativistic plasma. This has positioned ultra-intense laser pulses and laser-driven plasmas in the race to provide evidence for the Schwinger effect. Bamber *et al.* [367] at SLAC (USA) used a relativistic beam of electrons ($E = 46.6$ GeV) with an intense laser pulse ($I \sim 10^{18}$ W/cm^2) and detected approximately 100 positrons resulting from pair creation via the Breit-Wheeler effect. However, this scheme relies on the initial presence of fermions, making it unsuitable for investigating some effects related to the interaction of extreme fields with pure quantum vacuum, one of the most intriguing aspects of SF-QED, and in particular, the Schwinger effect.

The present intensity record of 10^{23} W/cm^2 held by the PW-class system at CoReLs (South Korea) is still at least six orders of magnitude below the Schwinger limit. Thus, exploring the Schwinger effect with the current generation of high-power lasers requires conceptual breakthroughs. The relativistic λ^3-approach has been identified as an alternative way to reach ultra-relativistic intensities [368]. Another approach is to combine the multi-PW class laser technology with "curved relativistic plasma

mirrors" (CRM) [369], illustrated in figure 7.12. The multi-PW beam is focused to $\sim 10^{23}$ W/cm^2 on a CRM, leading to RHHG corresponding to attosecond pulses in the time domain. Due to plasma denting, these pulses are then focused slightly after the reflection from the CRM, boosting the intensity by several orders of magnitude (assuming an aberration-free CRM). Researchers have now converged towards a feasible experimental scheme supported by reliable 3D PIC simulations [21, 370–372], awaiting an experimental attempt to investigate light-vacuum interactions.

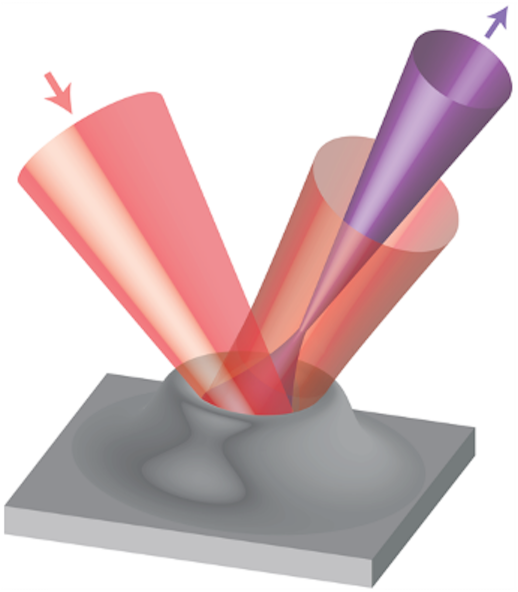

Figure 7.12: Principle of a CRM: Radiation pressure and/or pre-shaped targets create a curved plasma surface, that focuses the generated harmonic beam. Reprinted from [21].

Application of attosecond pulses to proton-boron fusion

The quest for a controlled-fusion reactor for practical applications has been ongoing for nearly a century, dating back to the discovery of nuclear fusion in the 1920s [373, 374]. Despite the significant physics and engineering challenges associated with fusion reactors for energy production, the field has attracted considerable interest and substantial investment over the past century. This is primarily because fusion relies on fuel that is abundant in nature and does not produce dangerous radioactive by-products. In layman's terms, nuclear fusion is often referred to as the "cleanest" energy source. Beyond energy production, nuclear fusion has gathered interest for its potential applications in space propulsion [375] and the development of high-temperature semiconductor chips [376], with the promise of overcoming existing technological limits and challenges.

Recently, the achievement of ignition and a target gain greater than unity in an inertial fusion experiment at the National Ignition Facility (NIF, USA) has provided significant impetus to this field [377]. The inertial fusion confinement (ICF) relies on compression and ignition of spherical target-shells filled with deuterium-tritium fuel using multiple laser beams. The produced energy is released in the form of neutrons and radiation, which is converted into heat in the chamber wall to potentially drive a power plant.

Another long-standing grail of nuclear fusion for future energy production is the proton-boron (pB)

fusion reaction, which has the highly attractive characteristic of not producing any neutrons. This means minimal activation of materials in a potential future reactor and, consequently, lower amounts of radioactive waste. Therefore, the pB reaction seems to have a wider ecological acceptance [374].

Ribeyre *et al.* [58] have proposed the use of high-energy (~ 1 Joule), single-cycle attosecond pulse ($\tau \sim 33$ as) to increase the efficiency of the pB fusion reaction. They investigate the interaction of single-cycle attosecond pulse with a solid-density pB target and, backed by numerical simulations, claim that using a single-cycle pulse, proton and boron ions can be accelerated over a longer distance, thus gaining more kinetic energy. This attosecond route to proton-boron fusion has the potential to achieve similar results compared to magnetic confinement fusion and ICF. While the claims are ambitious and the technological challenges to produce a 1 Joule - 33 as are humongous to say the least, this approach represents an exciting avenue for research in nuclear fusion.

Appendix A

Power scaling of HCF-based laser-post compression

During my thesis, I designed a HCF-based post-compression setup for Li Lu (Shenzhen Technology University or SZTU, China) in collaboration with Yi Liu (University of Shanghai for Science and Technology, China). The newly minted Ti:Sa based laser system from *Amplitude*, installed at SZTU, delivers waveform-controlled 18 mJ energy 25 fs pulses centered at $\lambda = 800\,\mathrm{nm}$, at 1 kHz repetition rate. The high temporal contrast of the laser pulses is ensured by an optical parametric chirped pulse amplifier (OPCPA) front end [378]. Considering the power scaling laws discussed in section 2.1.5, I designed the post-compression setup, drawing significant inspiration from the *Salle Noire* setup. This new design is capable of handling twice the input energy compared to the original *Salle Noire* configuration.

Compared to the *Salle Noire* laser, the SZTU laser carries ≈ 2 times the peak power. First, in order to make sure that the peak power remains well below the critical power for self-focusing ($P < P_{cr}$), the nonlinear index $n_2 \propto p$ (gas pressure) is lowered by a factor of 2 by decreasing the gas pressure in the fiber. Secondly, to stay well below the photo-ionization threshold, the fiber inner core diameter has to be scaled, $D_{\mathrm{SZTU}} = \sqrt{2} D_{SN} = 758\,\mu\mathrm{m}$ (SN: Salle Noire). To allow for some breathing room, the core diameter was conservatively increased to $D_{\mathrm{SZTU}} = 900\,\mu\mathrm{m}$ and proportionally, the length of the fiber was increased to $L_{\mathrm{SZTU}} = 6\,\mathrm{m}$. A schematic layout of the HCF-based post-compression setup planned for SZTU is illustrated in figure A.1. Currently, the vacuum chambers are being fabricated, and optics and optomechanics are simultaneously being procured. This setup is expected to be installed and fully functioning by autumn 2024.

Incoupling chamber: The design of this chamber is very similar to the one in *Salle Noire* (figure 2.10). First, a set of 10 dispersion-compensating mirrors ($\sim 2500\ \mathrm{fs}^2$, HD58, Ultrafast Innovations) compensate for the residual pulse GDD as well as the dispersion introduced by the entrance window. A QWP changes the polarization to circular to reduce the intensity at the fiber entrance to avoid excessive ionization and obtain more stable spectral broadening. Next, a downsizing telescope (M1 and M2 in figure A.1) reduces the beam size from 30 mm to 9.6 mm at $1/e^2$ width. Finally, the beam is focused at the entrance of the fiber using the mirror M3 to $2\omega_0 = 0.64 \times 900\ \mu\mathrm{m} = 576\,\mu\mathrm{m}$ in order to couple maximum energy to the EH_{11} mode of the fiber. Table A.1 lists the specifications of all the

critical optical components in the incoupling chamber.

A piezo-electric-based fast beam stabilization system will be implemented to maintain consistent beam pointing in the far-field. An active mirror positioned at the chamber's entrance will adjust based on correction signals from a PSD that monitors a leak from mirror M1. The beam profile and the position in the far-field will be continuously monitored through a leak from mirror M4, outside the vacuum chamber. The final CPA of the laser system includes a beam stabilization loop, ensuring stable pointing at the entrance of the incoupling chamber. Therefore, we anticipate that stabilization in the far-field alone will be adequate for achieving the desired performance level.

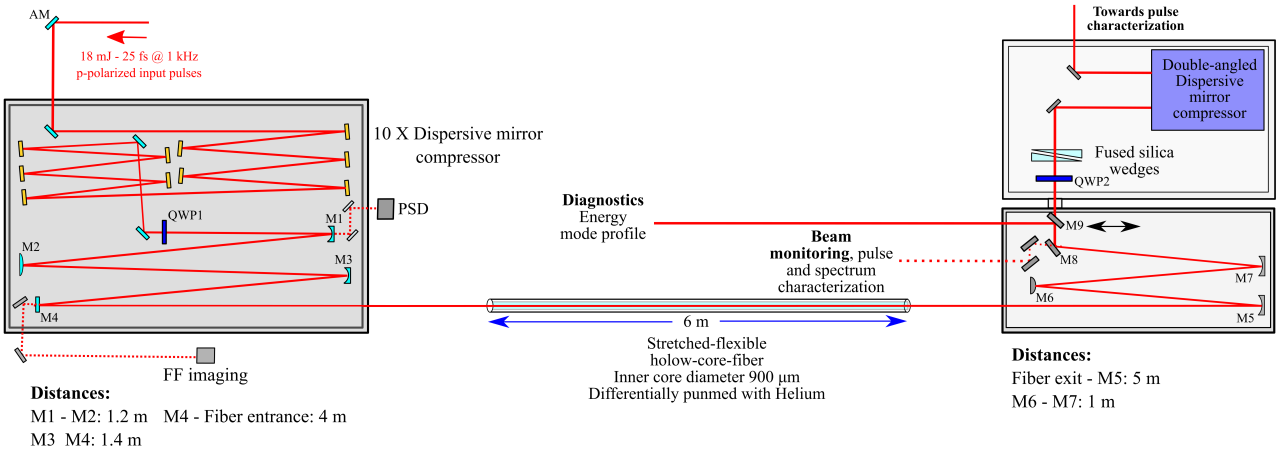

Figure A.1: Power scaled HCF-based compression setup design. AM: active mirror, PSD: position sensitive device, QWP: Quarter-wave plate.

Optical component	Substrate	Coating
M1	2" diameter, concave mirror with ROC = -3.5 m, back-surface polished for imaging	Highly-reflective dielectric coating for $\mathrm{AOI} = 0°$
M2	2" diameter, convex mirror with $\mathrm{ROC} = 1.1\,\mathrm{m}$	Highly-reflective dielectric coating for $\mathrm{AOI} = 0°$
M3	2" diameter, concave mirror with $\mathrm{ROC} = -10.8\,\mathrm{m}$	Highly-reflective dielectric coating for $\mathrm{AOI} = 0°$
M4	1" diameter, flat mirror	Highly-reflective, high LIDT, dielectric coating for $\mathrm{AOI} = 0°$
QWP1	2" diameter, zero order QWP	AR-coated for $\mathrm{AOI} = 0°$

Table A.1: Specifications for the critical optical components in the incoupling chamber of the SZTU post-compression setup. The labels for these optical components correspond to those specified in figure A.1. All the AR coatings are specified for $\lambda = 800\,\mathrm{nm}$ corresponding to the input spectrum. ROC: Radius of curvature, AOI: angle of incidence, and QWP: quarter-wave plate.

Stretched-flexible HCF: A stretched-flexible fiber with an inner core diameter of $D = 900\,\mu\mathrm{m}$ and a length of $L = 6\,\mathrm{m}$ is being developed by Yi Liu (University of Shanghai for Science and Technology, China). The fiber will feature a conical taper at the entrance to protect from slight beam misalignment, and a "Z-lock" at the fiber exit to absorb vibrations and maintain the fiber exit position when the fiber is pumped or filled with gas.

Outcoupling chamber: This chamber is also similar in design to the one in *Salle Noire*. The diverging beam after the fiber is first collimated to 8.8 mm and then up-sized using a telescope to 20.5 mm at $1/e^2$ width. Another QWP cancels the retardation introduced by the QWP at the input and rotates the beam back to p-polarization. The last mirror at 45° sends the beam out through a transparent window and into a compression chamber, where the compression will be finished off with a set of dispersion-compensating mirrors ($\sim 240\,\mathrm{fs}^2$, PC1332, Ultrafast Innovations). A leak from this last mirror is used to monitor the drifts in beam pointing continuously. This is an upgrade from the *Salle Noire* setup, where continuous beam monitoring is not possible directly after the HCF. An insertable mirror (M9) directs the beam close to the fiber entrance for mode-optimization and diagnostics. Table A.2 lists the specifications of all the critical components in the outcoupling chamber.

Optical component	**Substrate**	**Coating**
M5	1" diameter, concave mirror with ROC = -10 m	Enhanced silver coating
M6	1" diameter, convex mirror with $\mathrm{ROC} = 1.5\,\mathrm{m}$	Enhanced silver coating
M7	2" diameter, concave mirror with $\mathrm{ROC} = -3.5\,\mathrm{m}$	Enhanced silver coating
M8	2" diameter, flat mirror	Partially transmissive (0.1%) enhanced silver coating
QWP2	30 mm clear aperture, air-spaced QWP	AR-coated for $\lambda = 450 - 1000\,\mathrm{nm}$

Table A.2: Specifications for the critical optical components in the outcoupling chamber of the SZTU post-compression setup. The labels for these optical components correspond to those specified in figure A.1. QWP: Quarter-wave plate.

Comprehensive (3+1)D simulations were performed to test the performance of this system for a 25 fs - 18 mJ energy, circularly polarized Gaussian pulse at the input. The pressure gradient in the fiber was modeled as $p(z) = p_{out}\sqrt{z/L}$, where p_{out} is the pressure in the outcoupling chamber. The simulations take into account ionization as well as self-focusing during propagation through the fiber. Finally, at the output, for $p_{out} = 570$ mbar, we can obtain near single-cycle pulses, 3.4 fs, as shown in figure A.2. This setup looks promising for generating high energy near single-cycle pulses that will be used to drive attosecond science studies.

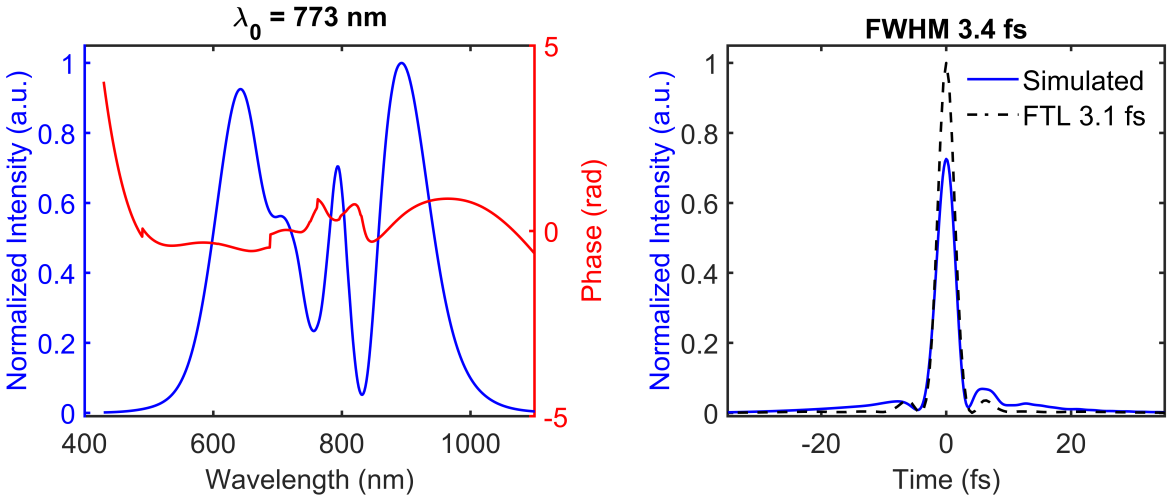

Figure A.2: Simulated pulse spectral intensity and phase (left) and temporal intensity profiles (right) for 18 mJ - 25 fs Gaussian input pulses undergoing self-phase modulation in the power-scaled HCF-based post-compression setup. Courtesy of Louis Daniault (LOA).

Appendix B

RHHG-beamline at ELI-ALPS: Conception and implementation

"To boldly go where no one has gone before ! "

Outline

B.1 RHHG beamline: General description 194
B.2 VC1: Laser contrast enhancement 196
B.3 VC2: Beam shaping and diagnostics 200
B.4 VC3: RHHG 204
B.5 First results and next challenges 207

The SYLOS-RHHG beamline at ELI-ALPS facility in Szeged, Hungary, was first conceptualized in 2016 to deliver attosecond pulses in the XUV spectral region along with synchronized IR driving laser pulses for pump-probe end-user experiments. The initial design of the beamline was conceptualized in 2015 in the PCO group, by Stefan Haessler, with support from Rodrigo Lopez-Martens and the PhD students in the group at the time, Maïmouna Bocoum and Frederik Böhle. Finally, the final design and implementation of this beamline was attributed to Ardop Industries, Bordeaux, France, in 2021, with the commissioning scheduled for 2023-2024. My PhD was organized in collaboration with Ardop to transfer the expertise and technical know-how for the design and implementation of this beamline. In the initial phase of the project, I contributed by consulting on the design of the crucial elements of the beamline, especially the beam-shaping, and diagnostics for plasma mirror emissions, an area of expertise I developed during my thesis work at LOA. Once the beamline design was approved by ELI, Ardop procured all the necessary mechanical and optical components. The installation of the beamline began in early 2023. With assistance from ELI-ALPS staff, and a few other members of the PCO group and Ardop, I installed the crucial components, aligned the complete beamline, and performed the initial shots to demonstrate RHHG at ELI-ALPS.

The RHHG beamline, installed in the medium shielded target area (MTA) at ELI, has been designed to be driven by the single-cycle laser systems (SYLOS) developed by EKSPLA and Light Conversion [379]. Although majorly designed to be driven by the most recently installed SYLOS 3

laser, this beamline is also compatible with the other SYLOS family members as well, such as the SYLOS alignment laser (SEA) and SYLOS 2. The key specifications of the three SYLOS laser systems are specified in table B.1. The design of the RHHG beamline has been inspired from *Salle Noire*, scaled to accommodate the unprecedented SYLOS laser parameters.

Parameters at the laser output	**SEA**	**SYLOS 2**	**SYLOS 3**
Repetition rate	10Hz	1 kHz	1 kHz
Central wavelength	825 nm	891 nm	825 nm
Pulse duration	12 fs	7 fs	8 fs
Strehl ratio	0.93	0.77	0.80
Peak power	3.2 TW	4.8 TW	15 TW
Pulse energy	42 mJ	32 mJ	120 mJ
Energy stability	0.87%	1.2%	0.7%
Beam profile	Top-hat	Top-hat	Top-hat
Beam size at FWHM	60 mm	60 mm	60 mm
Beam clear aperture	100 mm	100 mm	100 mm
CEP stability	-	210 mrad	200 mrad
Temporal contrast at 10 ps	10^{10}	10^{10}	10^{9}
Beam pointing instability (in the units of diffraction limited beam divergence)	< 0.15	< 0.15	< 0.15
Polarization	Linear horizontal	Linear horizontal	Linear horizontal

Table B.1: SYLOS laser specifications. SEA: SYLOS alignment laser.

B.1 RHHG beamline: General description

The SYLOS laser is dispatched through a beam transport system equipped with active beam stabilization and relay imaging, to ensure delivery of a stable high quality beam at the entrance of the RHHG beamline. A 3D model highlighting the key elements of the beamline is depicted in B.1. The

beamline comprises of four main sub-systems housed in four dedicated vacuum chambers (VC).

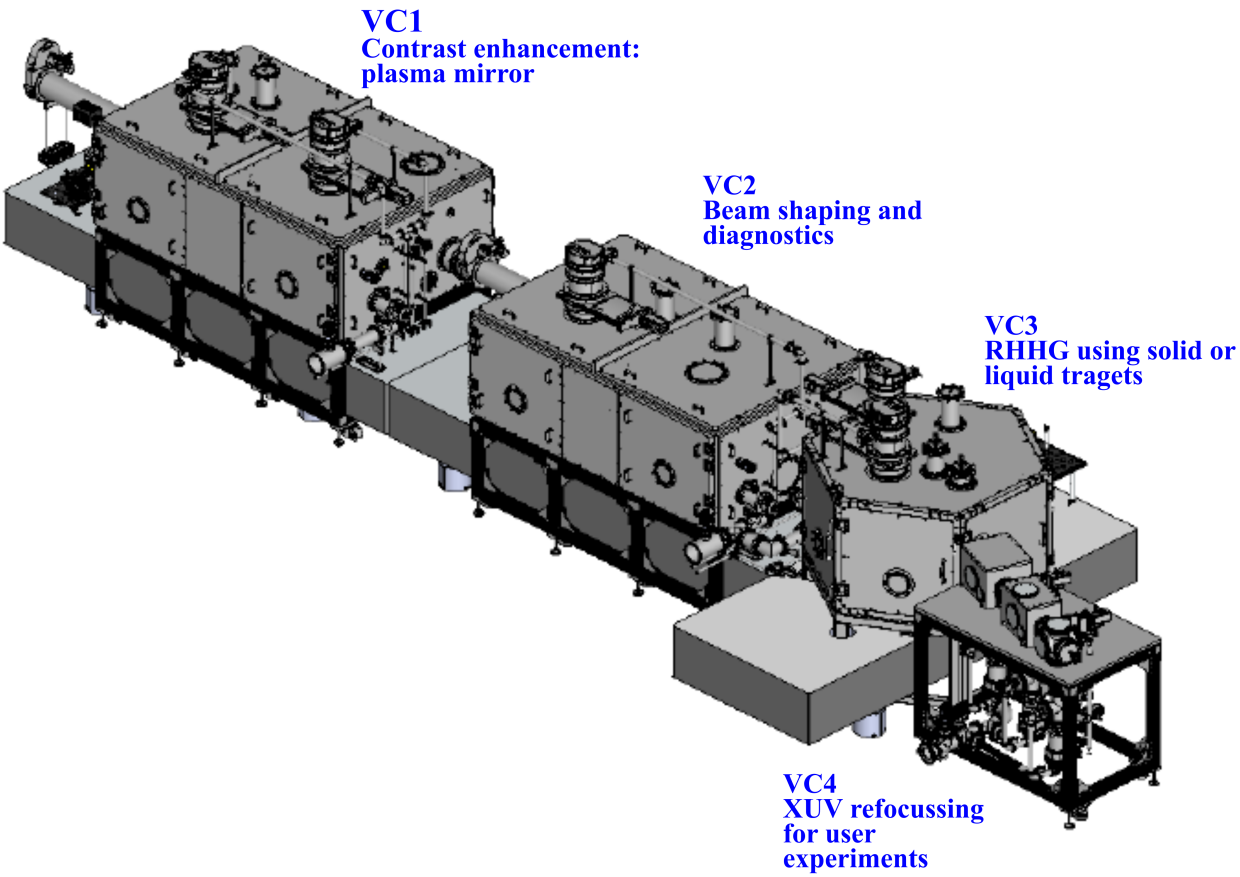

Figure B.1: A 3D layout of the RHHG beamline at ELI-ALPS. Reprinted from the SYLOS-RHHG Technical design report. VC: Vacuum chamber.

- **VC 1:** An insertable single-pass PM device [78] based on liquid-sheet target technology [357, 361] has been implemented for laser contrast enhancement by up to two orders of magnitude. The PM can also be bypassed, sending the beam unchanged directly to the next sub-system.
- **VC 2:** The beam is compressed using a set of dispersion-compensating mirrors. A Deformable mirror (DM) shapes the spatial wavefront and optimizes the focal spot. The laser pulse duration is characterized online using a vacuum-integrated D-Scan device [94]. An auxiliary IR beam, analogous to the Prepulse in *Salle Noire*, is sampled from the main laser beam using a "holey-mirror." This auxiliary beam is time-delayed and then recombined with the Main-laser beam to prepare a suitable plasma density gradient downstream on target.
- **VC 3:** The beam is initially sampled using a partially-transmissive mirror for online beam monitoring and wavefront detection. This chamber is primarily dedicated to generating XUV attosecond pulses and their spatio-spectral characterization. This sub-unit has been designed to be compatible with both solid and liquid targets, allowing for future developments. Additionally, as a secondary probe into laser-plasma interactions, the emitted relativistic electrons are characterized both spatially and spectrally.

- **VC 4:** The generated XUV attosecond pulses are refocused and characterized for end-user experiments.

A detailed description of the first three sub-systems to which I mostly contributed are presented in the following sections.

B.2 VC1: Laser contrast enhancement

VC1 can operate in two configurations: (1) a high-contrast (HC) mode, where a liquid-sheet target-based PM device is used to enhance the temporal contrast of the laser pulses [361, 380] by at least two orders of magnitude, and (2) a low-contrast (LC) mode, which simply by-passes the PM device and directs the beam unaltered to the next sub-system.

Figure B.2(top-panel) shows the top-view of the optical layout of VC1. The beam enters the chamber from the left at a height of 200 mm from the breadboard. **VC1.ATT1** and **VC1.ATT2** are a pair of **mirror-wedge arrangement** for attenuating the beam. A snapshot of the different operation modes of the attenuator is depicted in figure B.3. Each attenuator comprises of a 6" inch diameter glass 15°-wedge with an enhanced-silver coated highly-reflective (HR) back surface. The uncoated front surface of the wedge has low reflectivity (LR), attenuating the beam to $\approx 1\%$ at a 45° angle of incidence (see figure B.3(right panel)). To switch between the full-energy and attenuated positions, the mirror-wedge is rotated by 165° around the center of a small circle positioned such that both the LR and HR surfaces are tangent to it. The beam rejected by the mirror-wedge is transmitted through the LR-surface, reflected back by the HR-surface, to exit almost normal to the LR-surface. The rejected beam is directed towards a beam-dump positioned on the ceiling of the chamber (figure B.4). Safely dumping the laser energy, especially when dealing with 120 mJ laser pulses at a 1 kHz repetition rate, requires careful design. Together with Matthieu Veinhard (Ardop), I designed the beam-dumps to ensure that even the full-energy SYLOS 3 laser beam can be safely blocked within the chamber. The beam-dump utilizes a water-cooled absorber made of V40S (PRIMES) material, which is rated to dissipate 8 kW with less than 1% reflection. The absorber is installed at a grazing incidence angle in a curved-elbow tube to reduce the incident laser fluence further.

For a p-polarized incident laser beam, a series of attenuators (VC1.ATT1 and VC1.ATT2) at a 45° angle of incidence allow us to switch between transmission of 97% (HR-HR), 0.01% (HR-LR) and 0.0001% (LR-LR). The attenuators are mounted on a precise rotation stage and motorized tip-tilt mounts for repeatability.

An insertable **slow beam shutter** with an activation time of ≈ 500 ms is installed between the mirrors VC1.M1 and VC1.M2 as a safety mechanism to block the beam if necessary, capable of withstanding the unattenuated laser beam over long times. It is simply a 6" diameter mirror directing the beam upwards, towards another beam-dump on the ceiling of VC1. The slow shutter is followed by a 90 mm diameter **fast beam shutter** (CS90HS1T0L-EC, Uniblitz) comprising of 6 blades (figure B.5) with an opening time of ~ 50 msec, useful to work in bursts of several milliseconds. The shutter can withstand a laser fluence up to $100\ \mathrm{mW/mm^2}$.

HC mode: The **liquid-sheet target** target was developed by another PhD student in the PCO group,

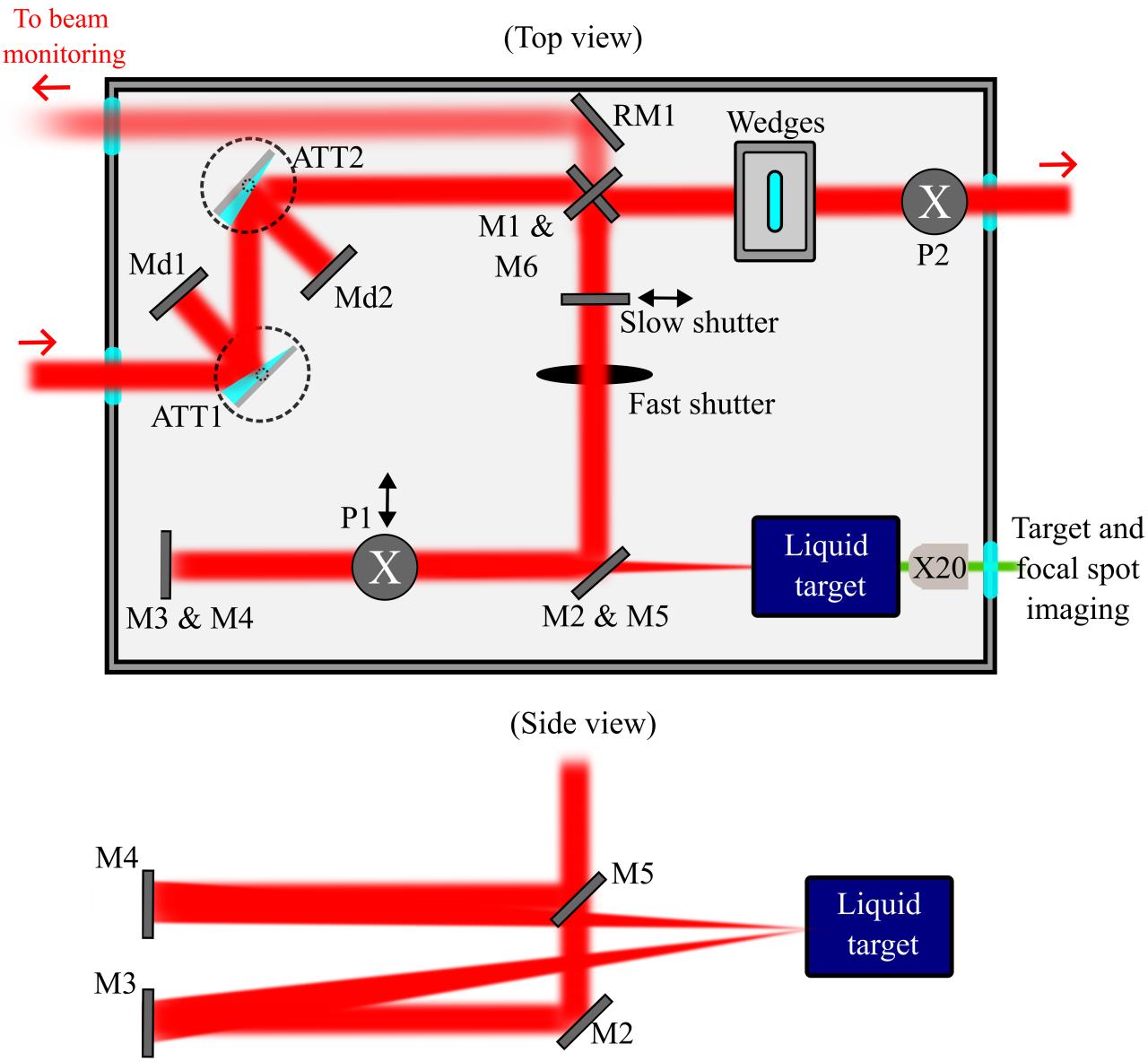

Figure B.2: The optical layout of VC1: Top-view (top-panel) and side-view (bottom-panel) of the optical layout of VC1. ATT1 and ATT2 are attenuator-mirror arrangements, mirrors Md1 and Md2 deflect the beam upwards to the beam dumps, insertable periscope P1 can be used to by-pass the PM, M3 and M4 are OAP mirrors, M6 is a partially-transmissive mirror, periscope P2 lowers the beam height from 462.8 mm to 200 mm. All the labeled components will referenced in the text with the prefix VC1.

Antoine Cavagna, in close collaboration with Enam Chowdhury and Milo Eder, from the Ohio State University (OSU, USA). A flat liquid-sheet target is formed by two obliquely colliding jets created using thin capillaries [357]. Ethylene glycol was chosen as the target material due to its low partial vapor pressure (0.01 mbar), making it more "vacuum-friendly". However, ethylene glycol's high viscosity requires a high-pressure-rated syringe pump (SYRIXUS 65x, Teledyne LABS, ≈ 70 ml capacity and rated for 20,000 PSI or 1380 bars) to push the liquid through the capillaries. While other glycol

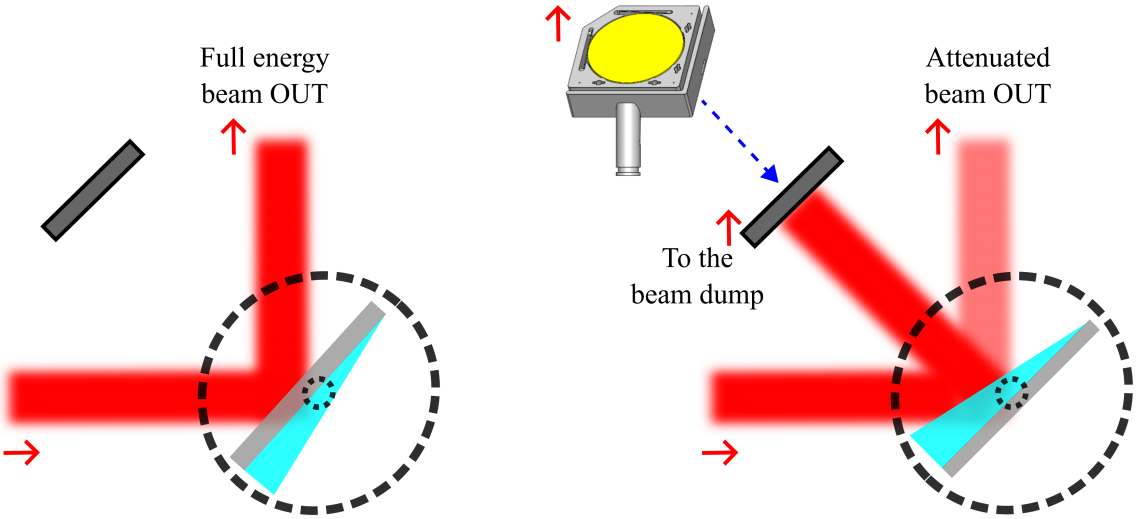

Figure B.3: Reflective mirror-wedge attenuator geometry.

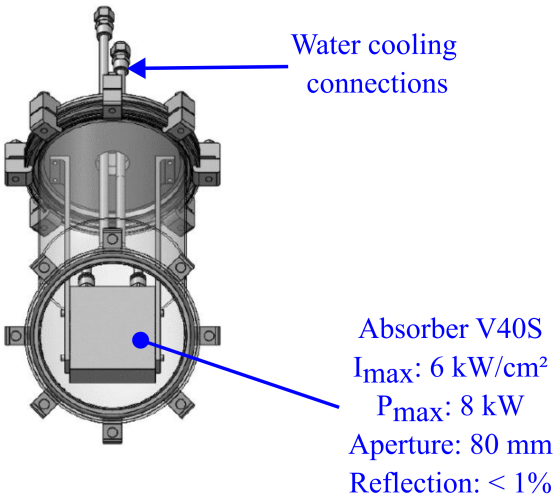

Figure B.4: A 3D layout of the beam-dumps installed on the ceiling of the vacuum chambers.

variants like tetra- and penta-ethylene glycol have even lower partial vapor pressures, their higher viscosity poses a challenge for use with these syringe pumps. Although these glycol variants could potentially be used, limitations in the maximum pressure rating of the pumps and available tubing restrict us to thicker targets. A dedicated study should be conducted to investigate the suitability of these glycol variant targets if ultra-high vacuum is necessary for any future applications.

In the current configuration, we use $50\ \mu\mathrm{m}$ inner diameter fused silica capillaries, resulting in the formation of a target $\approx 2\ \mathrm{mm}$ long, $\approx 500\ \mu\mathrm{m}$ wide and $\approx 1\ \mu\mathrm{m}$ thick at a pressure of approximately $100\ \mathrm{bar}$. The dimensions of the target can be adjusted by varying the circulating pressure and the inner diameter of the capillaries. To facilitate precise positioning of the target relative to the incoming beam and to steer the reflected beam under vacuum conditions, the two jets are mounted on five-axis translation stages, allowing adjustments in x, y, z, θ, and ϕ. Liquid collection is accomplished



Figure B.5: An image of the VC1 Fast shutter comprising of 6 blades with a damage-threshold of $100\ \mathrm{mW/mm^2}$.

by a funnel-shaped "catcher" positioned directly beneath the target. A $1/4$" tube, connected to the catcher, facilitates the removal of the liquid from the chamber using a gradual 15° slope, where it is then recycled utilizing a peristaltic pump. To further minimize the exposure time of liquid within the vacuum chamber, an "inverted funnel" shaped catcher can be implemented, particularly for applications targeting ultra-high vacuum environments.

Our current setup operates continuously for approximately $40-50$ minutes, limited by the cylinder size of the syringe pump and the corresponding pump pressure and flow rate. Upon depletion of the storage cylinder, the pump refills within approximately two minutes and can restart automatically. To eliminate this downtime, two syringe pumps can be interfaced with a single controller. When one pump refills, the other takes over the operation, ensuring continuous functionality. This enhancement can be considered in the future.

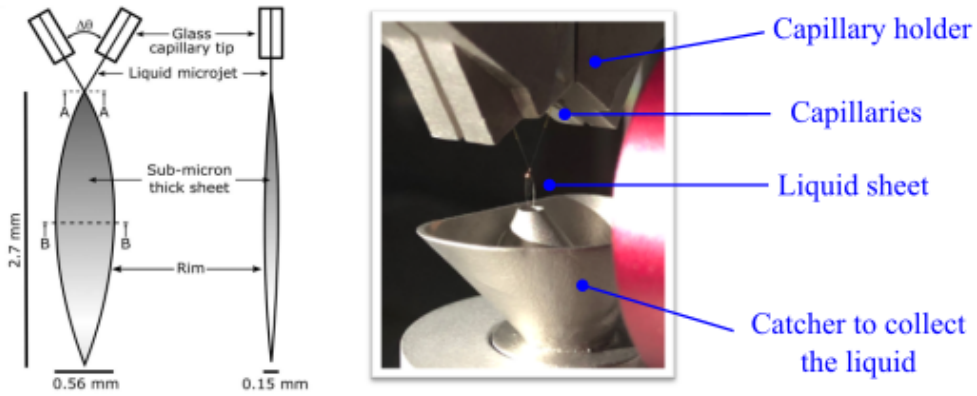

Figure B.6: The principle of thin liquid sheet formation using two obliquely colliding jets. A perpendicular view (left-panel) and a view within the plane of sheet formation (middle-panel) of the liquid-sheet are displayed. Reprinted from [357]. A picture of the liquid sheet target in action (right-panel). A catcher positioned beneath the target collects the liquid which is then collected in a reservoir outside the chamber.

An optimized regime for the operation of a single-pass PM is at a few $100\ \mathrm{J/cm^2}$ incident laser fluence, at a near normal incidence and s-polarization [381] so as to minimize losses due to Brunel [214]

and resonant absorption [212]. The 60 mm diameter (at $1/e^2$) top-hat input SYLOS beam is smoothly focused to $\approx 26\ \mu\mathrm{m}$ (at FWHM) on the liquid-sheet target using a 5° OAP with an effective focal length of 150 cm (**VC1.M3**). The pre-pulses and the preceding ASE pedestal are either transmitted or create a surface plasma, upon which the Main-pulse is reflected, thereby increasing the pulse contrast. A side view of the focusing geometry is shown in figure B.2(bottom). The on-target intensity is limited by the fact that the input pulses are not fully compressed but have a residual $800\ \mathrm{fs}^2$ GDD. A vertical plane of incidence makes the beam s-polarized on the plasma mirror, minimizing the laser absorption and thereby increasing the reflectivity of the PM. The reflected beam is then re-collimated to 60 mm diameter (same as the input beam) by a similar OAP (**VC1.M4**) placed at ≈150 cm from the target, right above VC1.M3, at a height of 462.8 mm from the breadboard.

A 0.1% leak of the beam from **VC1.M6**, propagates outside the chamber through VC1.RM1 and a transparent window for **beam monitoring**, tracking the beam position and the angular orientation. This beam monitoring setup is also useful the evaluate the spatial beam quality, collimation, beam position angle after reflection from the PM.

LC mode: The mirrors VC1.M4, VC1.M5, and the PM can be simply by-passed by inserting the periscope **VC1.P1**, such that the beam path from the mirror VC1.M5 onwards remains the same and the beam passes through the chamber unaltered.

Finally, we have a pair of thin AR-coated fused silica wedges to fine tune the pulse compression and to introduce pulse-front tilt by rotating the second wedge useful for the attosecond lighthouse [335, 336] experiments. These wedges are also used to scan the dispersion for characterizing the pulses using the D-Scan [94] device installed in VC2, discussed in the next section. The periscope **VC1.P2** at the end of VC1 lowers the beam height back to 200 mm.

B.3 VC2: Beam shaping and diagnostics

The second sub-system, VC2, is dedicated to controlling the spatio-temporal waveform shape, temporal pulse characterization (vacuum integrated) and most importantly the generation of a pump pulse or what we call an auxiliary pulse (analogous to the Prepulse in *Salle Noire*-PM experiments) with a controlled time-delay w.r.t. the Main-pulse, to prepare a suitable plasma on the surface of the target.

Figure B.7 illustrates the intricate optical layout of VC2, where the beam enters from the left side, positioned 200 mm above the breadboard. The pulses are first compressed by a set of eight dispersion-compensating mirrors ($\sim 800\ \mathrm{fs}^2$, identical to the SYLOS compressor, which is bypassed for beam transport. A 150 mm clear aperture enhanced-silver coated DM (VC2.DM, ILAO Star 250, Imagine Optic) installed at a 45° angle of incidence corrects for the distortions in the pulse wavefront induced by nonlinear or thermal effects. Refer to figure B.8 for a visual representation of the DM, comprised of 52 stepper motor actuators arranged in a concentric elliptical pattern.

The wavefront error is measured in VC3 (as described in section B.4) using a HASO wavefront sensor (Imagine Optic), which then transmits a correction signal to the DM. As demonstrated in figure B.9, this corrective action results in a significant reduction of residual aberrations to below approximately $30\ \mathrm{nm}$ RMS, consequently enhancing the Strehl ratio of the calculated Point Spread

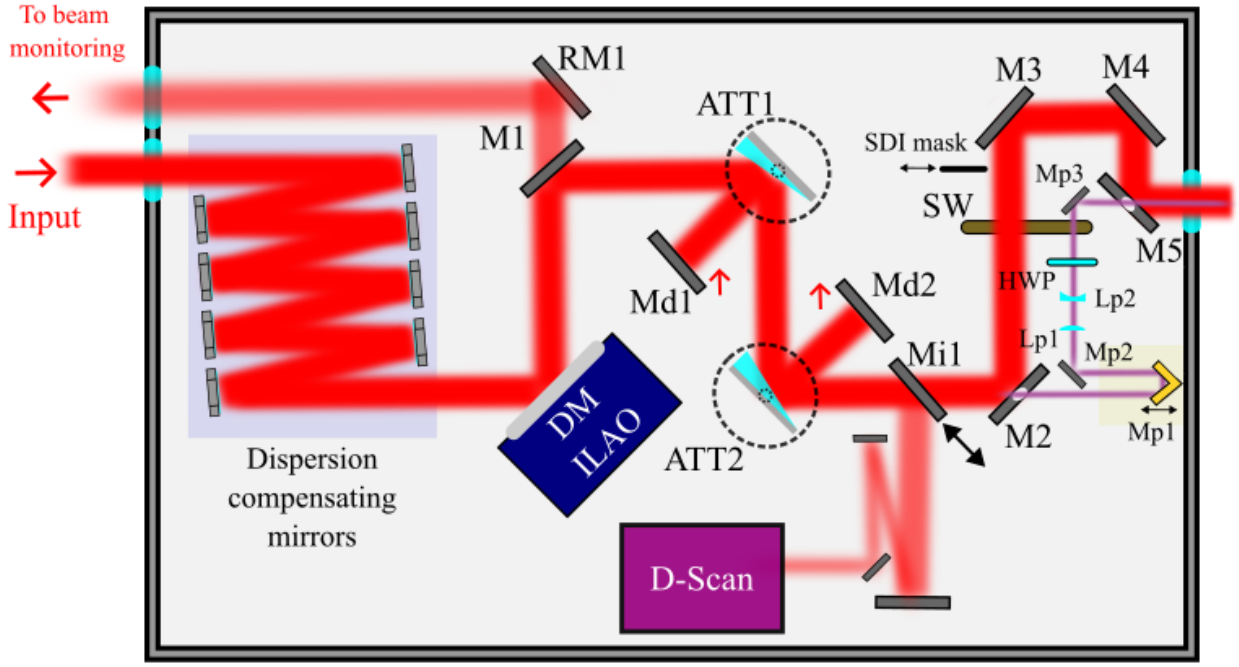

Figure B.7: The optical layout of VC2. M1 is a partially-transmissive enhanced silver-coated mirror (0.1% transmission), ATT1 and ATT2 are the attenuator-mirror arrangements, M2 and M5 are "holey" mirrors for generation of the auxiliary pulse and its recombination with the Main-pulse respectively, mirrors Md1 and Md2 deflect the beam upwards to the beam-dumps, and Mp1 is a retro-reflector mounted on a delay line. All the labeled components will be referenced in the text with the prefix VC2. DM-ILAO: Deformable mirror, SW: Shutter Wheel, HWP: Half-Wave Plate.

Function (PSF) to exceed 0.95. This DM is also equipped with a PharAO tool (Imagine Optic) for focal spot optimization on-target (described in section B.4). Given its pivotal role in the beamline, the DM plays a critical part in ensuring the delivery of high spatio-temporal quality pulses on-target, thereby maximizing achievable intensities on-target.

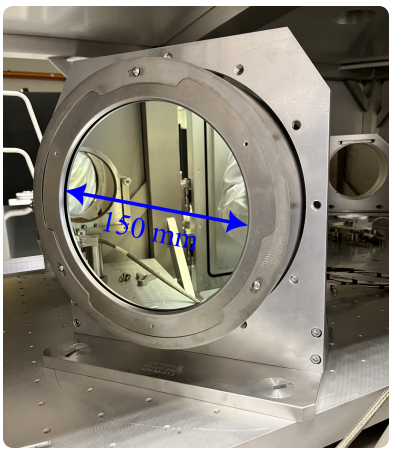

Figure B.8: A picture of the Deformable mirror

After the DM, the beam is reflected off a 0.1% transmissive silver-coated mirror, **VC2.M1**. The

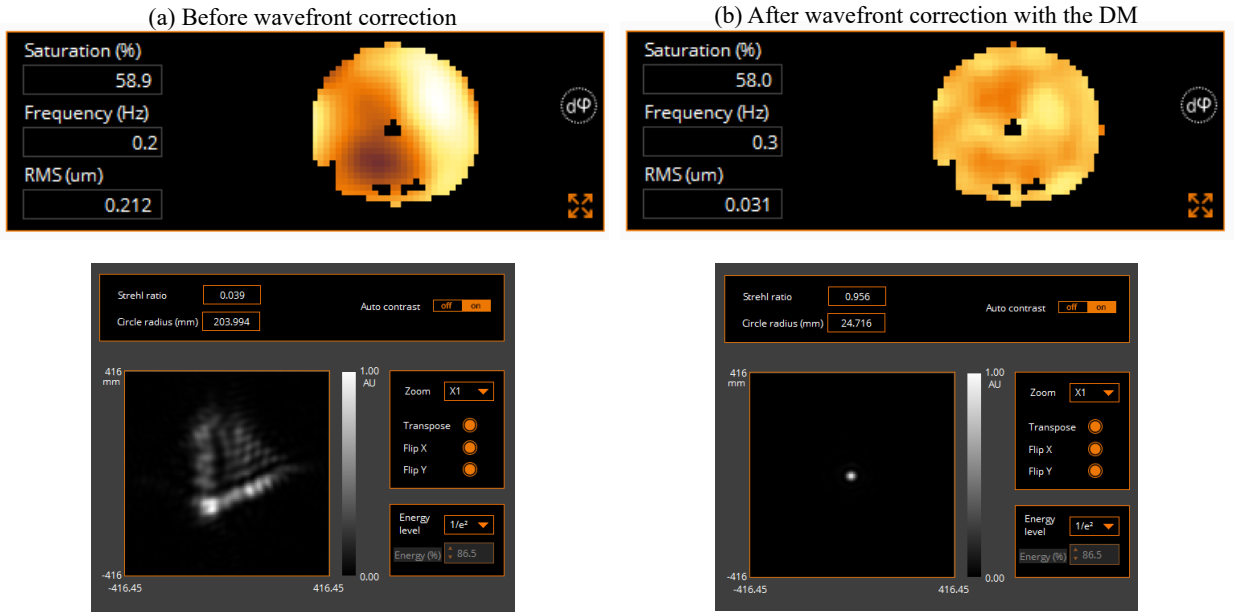

Figure B.9: Screenshots of wavefront measurements (top-panel) and the corresponding PSF (bottom-panel) without (a) and with (b) wavefront correction with the DM.

leak from VC2.M1 is used for beam monitoring outside VC2. Following, we have two sets of mirror-attenuator arrangements (VC2.ATT1 and VC2.ATT2), identical to the ones in VC1. Both the attenuator mirrors are mounted on a rotation stage with both the tip-tilt motorized for facilitating alignment under vacuum. When the beam is incident on the LR-surface, the mirrors VC2.Md1 and VC2.Md2 direct the beam up, towards the dedicated water-cooled beam-dumps installed on the ceiling of VC2. An insertable mirror VC2.Mi1 is used to direct the attenuated beam towards a vacuum-integrated SHG-**D-Scan** device [94] (Sphere Photonics) to characterize the pulses temporally and spectrally. The wedge-pair assembly installed at the end of VC1 is used to scan the dispersion. Figure B.10 shows the SEA's measured spectral and temporal intensity profiles using the D-Scan device in VC2. The SEA pulses are slightly longer in duration as compared to the SYLOS 2 and SYLOS 3 laser systems, nearly at the detection limit of this D-Scan device. Nevertheless, a vacuum integrated pulse characterization allowed for a reliable pulse measurement without risking pulse deterioration by propagation through a transmissive elements (windows, etc) or in the air (outside the chamber).

When the mirror VC2.Mi1 is retracted out of the beam path, the beam is incident on a **holey mirror, VC2.M2** with a 5 mm hole in the center of the mirror to pick-up the auxiliary beam. For a 60 mm beam diameter, a 5 mm hole yields a relative power of 0.7% between the Prepulse and the Main-Pulse. For the SYLOS 3 laser, a $\sim 830\ \mu$J auxiliary beam is extracted from a 120 mJ incident beam. The auxiliary pulse goes through a delay line consisting of a retro-reflector mounted on a low wobble horizontal translation stage with a 50 mm travel range, configured such that the auxiliary pulse can arrive 100 ps before or 100 ps after the Main-pulse. The auxiliary beam is downsized to 3 mm and recombined with the Main through another **holey mirror VC2.M5**. A HWP compensates for the rotation of polarization by the three bounces in the retro-reflector, rotating the polarization back to p-orientation. The transmissive optics used in the auxiliary beam path stretches the pulse in time.

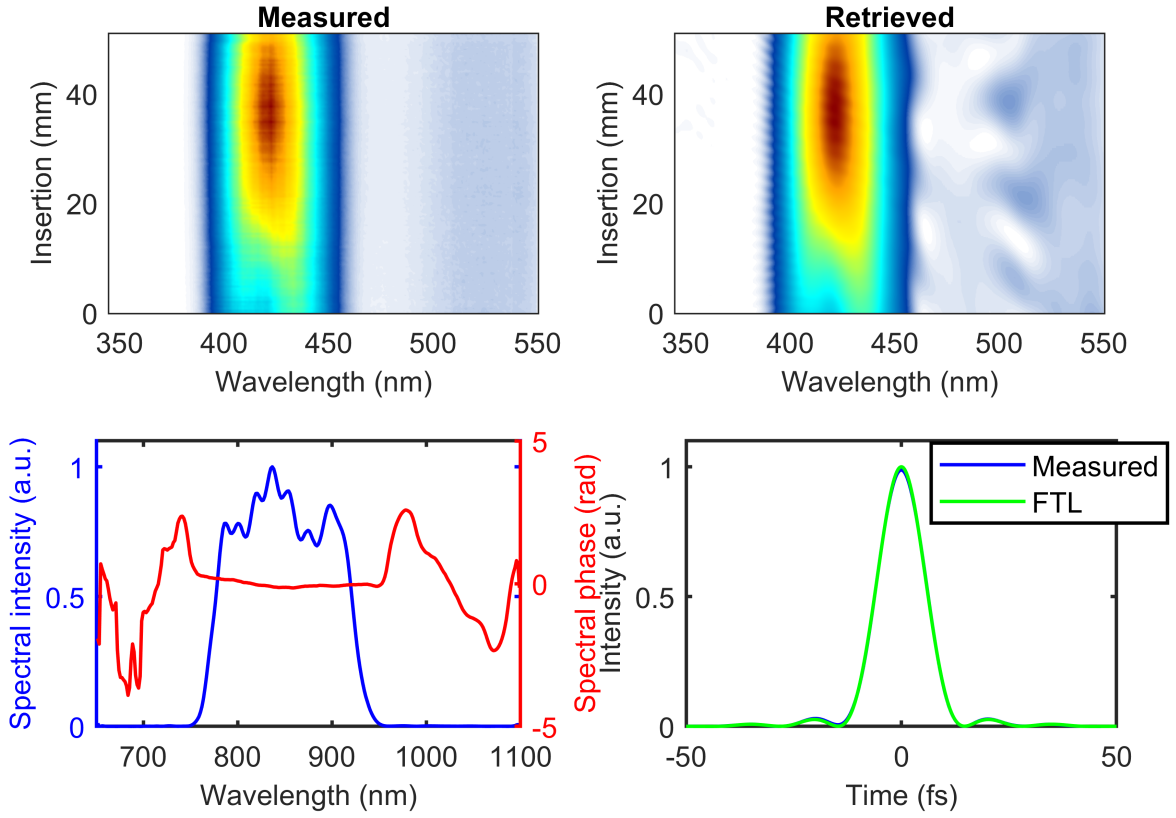

Figure B.10: (Top) Measured (left) and retrieved (right) D-scan traces. (Bottom) The retrieved spectral intensity and phase (left) and the corresponding measured temporal and FTL pulse intensity profile, yield 12.6 fs pulse duration at FWHM.

For example, a 7 fs SYLOS 3 pulse will be stretched to ≈ 170 fs.

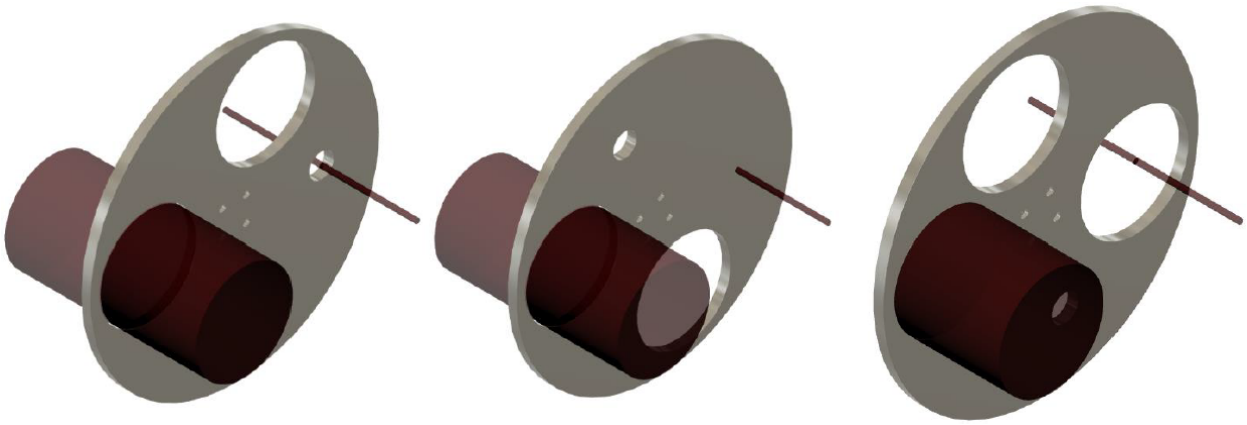

Figure B.11: A 3D view of the three SW configurations: (left) both the Main-pulse and the auxiliary pulse are allowed to pass through completely, (middle) only the Main-pulse passes through, and (3) the auxiliary pulse is allowed to pass through while the Main-pulse is reduced to 25 mm by an aperture. Reprinted from the SYLOS-RHHG Technical design report.

The **Shutter wheel** (SW, figure B.11) common to both the auxiliary and the Main-pulse beam

path works in four different configurations: **VC2.SW.(1)** allows both the Main and the auxiliary beams to pass through completely, **VC2.SW.(2)** blocks the auxiliary beam and allows the Main-pulse to pass through, and **VC2.SW.(3)** that allows the auxiliary beam to pass through unchanged while reduces the Main-beam in size using a 25 mm aperture and attenuated in energy using neutral densities to match the prepulse intensity in-focus. The configuration **VC2.SW.(1)** is the standard operational configuration, **VC2.SW.(2)** allows to image the Main-pulse focal spot in VC3 and **VC2.SW.(3)** is used to find the temporal overlap between the auxiliary and the Main-pulse in-focus, described in detail in section B.4. Additionally, before recombination of the auxiliary pulse with the Main-pulse, a **periodic intensity mask** can be inserted in the Main-pulse beam path, between the mirrors VC2.M2 and VC2.M3 to perform an SDI measurement on-target in VC3 [316]. The mask is 100 mm in diameter, with periodically spaced holes 2 mm in diameter with a pitch of 3 mm. The principle of the SDI technique has been described previously in this manuscript, in section 5.7.

B.4 VC3: RHHG

This sub-system is dedicated to the relativistic laser-plasma interactions, focused on the detection of RHHG as well as energetic electrons emitted from the PMs. A schematic representation of the optical layout of VC3 is illustrated in figure B.12. The recombined Main-pulse and the auxiliary pulse enter the chamber from left at a height of 200 mm from the optical breadboard. The beam is sampled through the mirror **VC3.M2** ($\approx 1\%$) and sent outside to a diagnostic bench for beam monitoring and wavefront characterization. Depending on the mode of operation (LC or HC), the beam is sent to a periscope comprising of a flat enhanced-silver coated mirror and a 90° OAP, setting the beam height to 420 mm from the optical breadboard in VC3.

LC mode: The 60 mm top-hat beam is "softly" focused onto the target to a $7\,\mu\mathrm{m}$ spot-size at FWHM using a 6" diameter, aluminum-substrate, enhanced-silver coated 90° OAP with an effective focal length, $f = 400$ mm. For 120 mJ - 7 fs SYLOS 3 laser, assuming there are no spatio-temporal couplings, we can reach intensities as high as $2 \times 10^{19}\,\mathrm{W/cm^2}$, corresponding to $a_0 \approx 3.2$ at $\lambda = 825\,\mathrm{nm}$.

HC mode: In this case, we employ a tight-focusing geometry using a 4" inch diameter, aluminum-substrate, enhanced-silver coated 90° OAP with an effective focal length, $f = 100$ mm, focusing the 60 mm diameter top-hat beam down to $1.8\,\mu\mathrm{m}$ spot-size at FWHM. Assuming a 70% throughput of the contrast enhancement setup, we can reach an on-target intensity of $2.2 \times 10^{20}\,\mathrm{W/cm^2}$, corresponding to $a_0 \approx 10.5$ at $\lambda = 825\,\mathrm{nm}$.

Target: VC3 is compatible with both the liquid-sheet target setup discussed in B.2 and a solid target setup for laser-plasma interactions. The solid target setup is similar to the one in the *Salle Noire* beamline, described in 5.2. A picture of the solid target positioner installed at ELI along with the focal spot imaging setup is depicted in figure B.13. Developed by SourceLAB (*SL-ST-1000*), this solid target is an upscaled and improved version, offering ultra-high positioning precision, with residual motion below $2\,\mu\mathrm{m}$ peak-to-valley, which can be further reduced to approximately $200\,\mathrm{nm}$ using a 3-piezo-based active stabilization loop. The positioner can accommodate targets up to 200 mm in diameter, allowing for a total shooting time of 52 minutes at a 1 kHz repetition rate. For the solid target, a 2 cm thick, 200 mm diameter disc of BK7, polished to approximately λ flatness on both sides, is

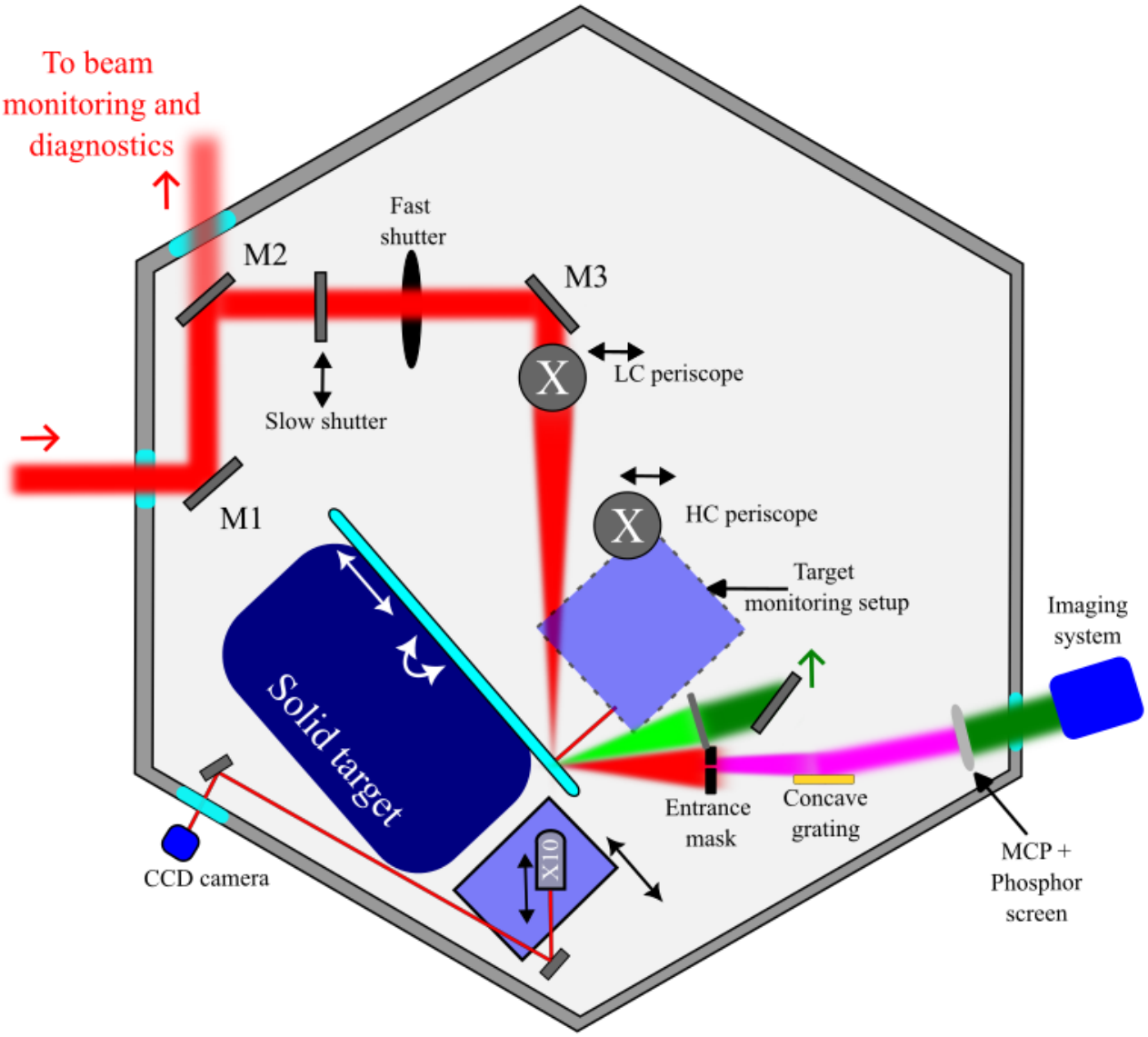

Figure B.12: The optical layout of VC3. M2 is a partially-transmissive enhanced silver-coated mirror (0.1% transmission). All the labeled components will be referenced in the text with the prefix VC3. LC: low-contrast, HC: high-contrast.

used. Obtaining large targets with higher surface quality is challenging; therefore, this specification was chosen as a good compromise, balancing cost and performance.

To characterize the relativistic PM emissions, a range of diagnostics were designed and are briefly described below. Leveraging the experience gained at LOA, I contributed to the design of these diagnostics and was responsible for their installation and alignment in VC3.

XUV-spectrometer: The overall design of the XUV spectrometer is similar to the one in the beamline at LOA, discussed in 5.4.1, but with a higher angular acceptance range. The RHHG in the XUV spectral range is dispersed horizontally by an aberration-corrected, grazing-incidence, flat-field concave grating (Shimadzu 30-006, $N = 600\,\mathrm{groves/mm}$), optimized for a wavelength range of 20-80 nm

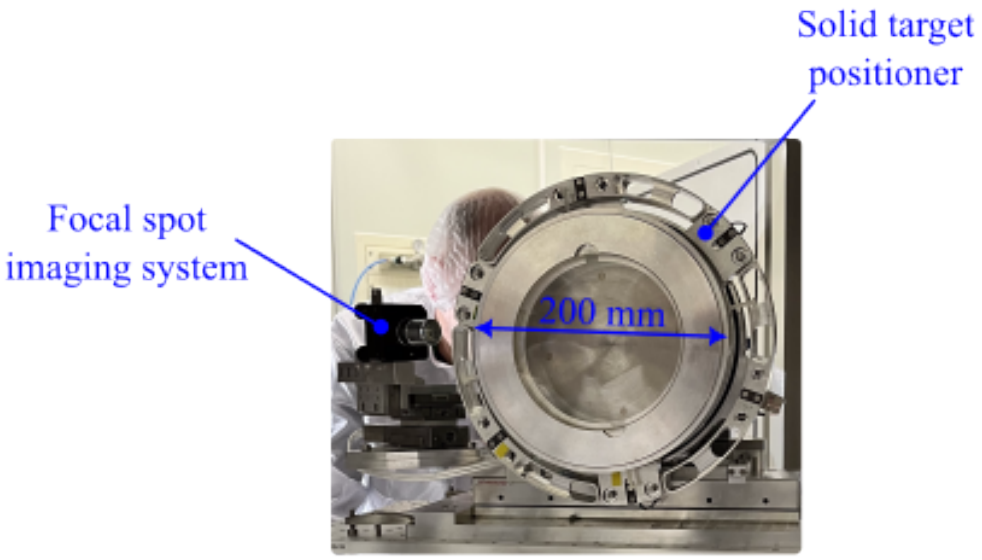

Figure B.13: The solid target positioner and the focal spot imaging setup.

and placed approximately $237\,\mathrm{mm}$ from the point of interaction. The XUV beam retains its divergence along the vertical dimension. The resulting spectrograph is imaged on a 70 mm diameter single-stack MCP-Phosphor screen assembly (Hamamatsu), using a triggered CCD camera (PCO Panda 4.2).

Electron detection: A LANEX screen (Carestream) is used to image the spatial charge distribution of electrons emitted from the target, close to the reflected specular direction. The LANEX screen is covered with $15\,\mu\mathrm{m}$ thick aluminum foil to block visible light. Both the aluminum foil and the substrate of the LANEX screen itself block low-energy electrons with $E_k < 150\,\mathrm{eV}$. A mirror behind the LANEX screen directs the emitted green light upwards, where a dedicated triggered CCD camera on the ceiling of VC3 images the screen through a transparent window. To measure the energy spectrum of the electrons, a pinhole and a pair of Neodymium magnets can be inserted in front of the LANEX screen. The spectrometer has been designed with a non-ferromagnetic yoke made of aluminum pieces, leading to an in-homogeneous magnetic field in the gap along the entrance pinhole axis. Although using a ferromagnetic yoke would improve the magnetic field homogeneity, aluminum is preferred to avoid the activation of heavy elements in the path of high-energy electrons. This approach has been successfully implemented in various spectrometer designs, including the one at LOA.

SDI for plasma density gradient calibration: A periodic intensity mask is introduced in the Main-pulse beam path in VC2, transforming the Main-pulse to a “plasma expansion probe”. The periodic mask creates a pattern of hexagonally arranged spots in-focus. The separation between the zeroth-order and the fist-order is given by, $\Delta = \lambda_0 f/a$, where a is the spacing two holes of the mask. In this configuration, only the zeroth-order is phase-shifted as the probe pulse is reflected, and this ultimately leads to intensity modulations in the Main beam near-field. Using the SDI technique [316], by recording successive inversions in the reflected near-field intensity pattern, the plasma expansion speed and hence the gradient scale length at respective time-delays can be retrieved. The near-field pattern in recorded by inserting a glass diffuser in front of the entrance mask of the grating. The glass diffuser is imaged by a dedicated CCD camera on the VC3 ceiling, installed right above the diffuser.

B.5 First results and next challenges

We conducted initial experiments on the RHHG beamline at ELI-ALPS using the SEA laser, which delivers approximately 15 mJ energy, 12 fs laser pulses at 10 Hz repetition rate. For this first attempt, we bypassed the contrast enhancement setup in VC1, allowing the beam to pass through unaltered. Despite this, the excellent contrast of the SEA laser enabled us to achieve the highest possible intensities on-target using the HC-focusing geometry, given the available laser energy.

A liquid target setup was employed for this campaign, offering numerous degrees of freedom for steering the generated XUV beam. As a result, we successfully detected some harmonics using the XUV spectrometer. However, during this process, we identified several, albeit minor, issues that need to be addressed before the beamline can become fully operational and ready for user access.

Figure B.14 shows a raw image of the recorded XUV spectrograph. The dotted black lines indicate the positions of the recorded harmonic peaks. The strong signal near the first dotted line on the low-energy side is likely due to a leak from the 0th-order diffraction, which was not completely blocked after the grating. The elevated background signal is attributed to ambient plasma emissions. The change in sharpness of the harmonic peaks from low-energy to high-energy suggests that the MCP was not completely parallel to the focusing plane of the grating. Ensuring that the MCP surface is parallel to the focusing plane should not only improve the image quality but also enhance the detection efficiency, particularly for the high-energy harmonics.

To ensure reliable signal detection and avoid missing signals due to triggering issues, the MCP was powered in DC mode. Using high-voltage pulses of approximately 50 ns duration to pulse the MCP should significantly reduce the plasma emission background. Additionally, some background patterns resemble the shape of the mask at the input of the XUV grating, suggesting that we are observing an X-ray image of the entrance mask. Therefore, increasing the mask thickness is necessary to prevent spurious signals from polluting the XUV spectrum.

Thus, we successfully demonstrated HHG from PMs at ELI-ALPS for the first time. Although the signal is not entirely clean, it is nevertheless promising and has helped us identify potential issues that need to be resolved for the next attempt.

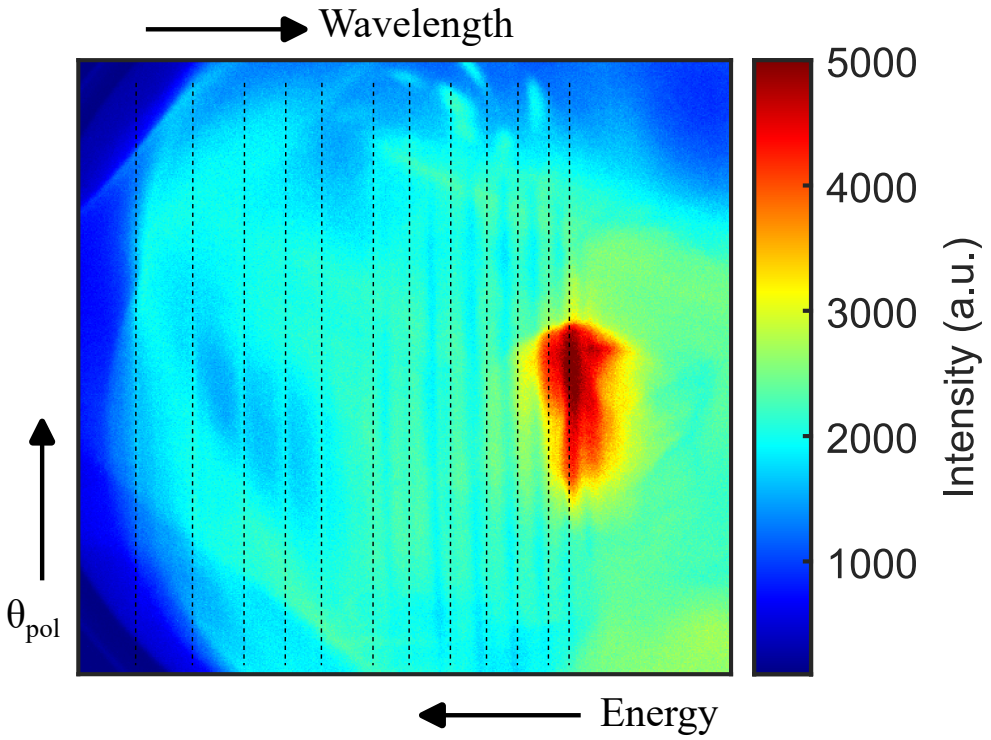

Figure B.14: Raw HHG spectrograph. The dotted black lines mark the position of the visible harmonic peaks.

List of publications and conference Contributions

Publications:

- **Lightwave-controlled relativistic plasma mirrors**
  M. Ouillé, **J. Kaur**, Z. Cheng, S. Haessler, and R. Lopez-Martens, *ArXiv preprint* **arXiv:2406.06396** (2024)

- **Optical ionization effects in kHz laser wakefield acceleration with few-cycle pulses**
  J. Monzac, S. Smartsev, J. Huijts, L. Rovige, I. A. Andriyash, A. Vernier, V. Tomkus, V. Girdauskas, G. Raciukaitis, M. Mackevičiūtė, V. Stankevic, A. Cavagna, **J. Kaur**, A. Kalouguine, R. Lopez-Martens, J. Faure, *ArXiv preprint* **arXiv:2406.17426** (2024)

- **Simple few-shot method for spectrally resolving the wavefront of an ultrashort laser pulse**
  S. Smartsev, A. Liberman, I. A. Andriyash, A. Cavagna, A. Flacco, C. Giaccaglia, **J. Kaur**, J. Monzac, S. Tata, A. Vernier, V. Malka, R. Lopez-Martens, and J. Faure, *Optics Letters* **49, 8** (2024)

- **High repetition rate relativistic laser–solid–plasma interaction platform featuring simultaneous particle and radiation detection**
  J. Kaur, M. Ouillé, D. Levy, L. Daniault, A. Robbes, N. Zaïm, A. Flacco, E. Kroupp, V. Malka, S. Haessler, and R. Lopez-Martens, *Review of Scientific Instruments* **94, 11** (2023)

- **Simultaneous nonlinear spectral broadening and temporal contrast enhancement of ultrashort pulses in a multi-pass cell**
  J. Kaur, L. Daniault, Z. Cheng, O. Tourneur, O. Tcherbakoff, F. Réau, J.-F. Hergott, and R. Lopez-Martens, *Journal of Physics: Photonics* **6 015001** (2023)

- **Relativistic high-harmonic generation and correlated electron acceleration from plasma mirrors at 1 kHz repetition rate**
  S. Haessler, F. Böhle, M. Bocoum, M. Ouillé, **J. Kaur**, D. Levy, L. Daniault, A. Vernier, J. Faure, and R. Lopez-Martens, *Ultrafast Science* **22 (9893418)** (2022)

- **Third-order nonlinear femtosecond optical gating through highly scattering media**
  M. Bocoum, Z. Cheng, **J. Kaur**, and R. Lopez-Martens, *Physical Review A* **106, L051501**

(2022)

- **Carrier-envelope phase controlled dynamics of relativistic electron beams in a laser-wakefield accelerator**
  L. Rovige, J. Monzac, J. Huijts, I. A. Andriyash, A. Vernier, **J. Kaur**, M. Ouillé, Z. Cheng, V. Tomkus, V. Girdauskas, G. Raciukaitis, J. Dudutis, V. Stankevic, P. Gecys, R. Lopez-Martens, and J. Faure, *The European Physical Journal Special Topics* **1-12** (2022)

- **Low divergence proton beams from a laser-plasma accelerator at kHz repetition rate**
  D. Levy, I. A. Andriyash, S. Haessler, **J. Kaur**, M. Ouillé, A. Flacco, E. Kroupp, V. Malka, and R. Lopez-Martens, *Physical Review Accelerators and Beams* **25, 9, 093402** (2022)

- **Waveform Control of Relativistic Electron Dynamics in Laser-Plasma Acceleration**
  J. Huijts, L. Rovige, I. A. Andriyash, A. Vernier, M. Ouillé, **J. Kaur**, Z. Cheng, R. Lopez-Martens, and J. Faure, *Physical Review X* **12, 1, 011036** (2022)

- **Single-stage few-cycle nonlinear compression of milliJoule energy Ti: Sa femtosecond pulses in a multipass cell**
  L. Daniault, Z. Cheng, **J. Kaur**, J.-F. Hergott, F. Réau, O. Tcherbakoff, N. Daher, X. Délen, M. Hanna, and R. Lopez-Martens, *Optics Letters* **46, 20, pp 5264-5267** (2021)

Conference contributions:

- **Sub-cycle control of kHz relativistic plasma mirror emissions**
  J. Kaur, *Forum de la Communauté Ultrarapide du plateau de Saclay (FOCUS #3)* in Gif-sur-Yvette, Île de France **(Invited)**

- **Temporal contrast enhancement of femtosecond laser pulses in a multipass cell**
  J. Kaur, L. Daniault, Z. Cheng, J. F. Hergott, F. Réau, O. Tcherbakoff, and R. Lopez-Martens, *Optica Advanced Solid State Lasers (ASSL) Congress 2023* in Tacoma, Washington, US **(Invited)**

- **High-fidelity few-cycle pulse generation via nonlinear ellipse rotation in a multipass cell at the mJ-level**
  J. Kaur, L. Daniault, Z. Cheng, J. F. Hergott, F. Réau, O. Tcherbakoff, and R. Lopez-Martens, *Ultrafast Optics (UFO) XIII 2023* in Bariloche, Argentina **(Contributed)**

- **Waveform control of relativistic laser-matter interactions**
  J. Kaur, M. Ouillé, Z. Cheng, S. Haessler, J. Huijts, L. Rovige, A. Vernier, I. Andriyash, J. Faure, and R. Lopez-Martens, *Ultrafast Optics (UFO) XIII 2023* in Bariloche, Argentina **(Contributed)**

- **Pulse compression down to the few-cycle regime via non-linear ellipse rotation in multi-pass cells**
  J. Kaur, L. Daniault, Z. Cheng, J. F. Hergott, F. Réau, O. Tcherbakoff, and R. Lopez-Martens, *International Committee on Ultra-high Intensity Lasers (ICUIL) conference 2022* in Jeju Island, South Korea **(Contributed)**

- **Near-single-cycle relativistic optics**
  J. Kaur, M. Ouille, Z. Cheng, S. Haessler, and R. lopez-Martens, *Plasmas in super-intense laser fields 2022* in Erice, Italy **(Poster)**

- **Route to attosecond control of relativistic plasma mirrors**
  J. Kaur, M. Ouille, Z. Cheng, S. Haessler, and R. Lopez-Martens, *Europhotonics Spring school 2022* in Sitges, Spain **(Invited)**

- **Cross-polarized wave generation in multi-pass cells**
  J. Kaur, L. Daniault, Z. Cheng, J. F. Hergott, F. Réau, O. Tcherbakoff, and R. Lopez-Martens, *High-Intensity Lasers and High-Field Phenomena (HILAS) 2022* paper JTh6A.2, in Budapest, Hungary **(Contributed)**

- **Simultaneous measurements of high-order harmonics, accelerated electrons and protons emitted from relativistic plasma mirrors**
  J. Kaur, D. Levy, M. Ouillé, I. Andriyash, E. Kroupp, V. Malka, J. Faure, S. Haessler, and R. Lopez-Martens, *Conference on Lasers and Electro-Optics (CLEO) 2021* paper FTu1K.2, in OSA Technical Digest **(Contributed)**

Bibliography

[1] T. H. Maiman. Stimulated optical radiation in ruby. *Nature*, 187(4736):493–494, Aug 1960.

[2] D. Strickland and G. Mourou. Compression of amplified chirped optical pulses. *Optics Communications*, 55(6):447–449, 1985.

[3] N. H. Burnett, H. A. Baldis, M. C. Richardson, and G. D. Enright. Harmonic generation in CO2 laser target interaction. *Applied Physics Letters*, 31(3):172–174, 08 1977.

[4] A. McPherson, G. Gibson, H. Jara, U. Johann, T. S. Luk, I. A. McIntyre, K. Boyer, and C. K. Rhodes. Studies of multiphoton production of vacuum-ultraviolet radiation in the rare gases. *Journal of the Optical Society of Amercia B*, 4(4):595–601, Apr 1987.

[5] M Ferray, A L'Huillier, X F Li, L A Lompre, G Mainfray, and C Manus. Multiple-harmonic conversion of 1064 nm radiation in rare gases. *Journal of Physics B: Atomic, Molecular and Optical Physics*, 21(3):L31, Feb 1988.

[6] M. Nisoli, P. Decleva, F. Calegari, A. Palacios, and F. Martín. Attosecond electron dynamics in molecules. *Chemical Reviews*, 117(16):10760–10825, Aug 2017.

[7] A L'Huillier, K J Schafer, and K C Kulander. Theoretical aspects of intense field harmonic generation. *Journal of Physics B: Atomic, Molecular and Optical Physics*, 24(15):3315, Aug 1991.

[8] P. B. Corkum. Plasma perspective on strong field multiphoton ionization. *Physical Review Letters*, 71:1994–1997, Sep 1993.

[9] K. J. Schafer, B. Yang, L. F. DiMauro, and K. C. Kulander. Above threshold ionization beyond the high harmonic cutoff. *Physical Review letters*, 70:1599–1602, Mar 1993.

[10] J. M. Schins, P. Breger, P. Agostini, R. C. Constantinescu, H. G. Muller, G. Grillon, A. Antonetti, and A. Mysyrowicz. Observation of laser-assisted auger decay in argon. *Physical Review Letters*, 73:2180–2183, Oct 1994.

[11] M. Hentschel, R. Kienberger, Ch. Spielmann, G. A. Reider, N. Milosevic, T. Brabec, P. Corkum, U. Heinzmann, M. Drescher, and F. Krausz. Attosecond metrology. *Nature*, 414(6863):509–513, Nov 2001.

[12] P. Agostini and L. F. DiMauro. The physics of attosecond light pulses. *Reports on Progress in Physics*, 67(6):813, May 2004.

[13] P. B. Corkum and F. Krausz. Attosecond science. *Nature Physics*, 3(6):381–387, Jun 2007.

[14] J. Biegert, F. Calegari, N. Dudovich, F. Quéré, and M. Vrakking. Attosecond technology(ies) and science. *Journal of Physics B: Atomic, Molecular and Optical Physics*, 54(7):070201, jun 2021.

[15] S. Ghimire, A. D. DiChiara, E. Sistrunk, P. Agostini, L. F. DiMauro, and D. A. Reis. Observation of high-order harmonic generation in a bulk crystal. *Nature Physics*, 7(2):138–141, Feb 2011.

[16] A. Flettner, T. Pfeifer, D. Walter, C. Winterfeldt, C. Spielmann, and G. Gerber. High-harmonic generation and plasma radiation from water microdroplets. *Applied Physics B*, 77(8):747–751, Dec 2003.

[17] T. T. Luu, Z. Yin, A. Jain, T. Gaumnitz, Y. Pertot, J. Ma, and H. J. Wörner. Extreme–ultraviolet high–harmonic generation in liquids. *Nature Communications*, 9(1):3723, Sep 2018.

[18] Y. Nomura, R. Hörlein, P. Tzallas, B. Dromey, S. Rykovanov, Zs. Major, J. Osterhoff, S. Karsch, L. Veisz, M. Zepf, D. Charalambidis, F. Krausz, and G. D. Tsakiris. Attosecond phase locking of harmonics emitted from laser-produced plasmas. *Nature Physics*, 5(2):124–128, Feb 2009.

[19] U. Teubner and P. Gibbon. High-order harmonics from laser-irradiated plasma surfaces. *Reviews of Modern Physics*, 81:445–479, Apr 2009.

[20] C. Thaury and F. Quéré. High-order harmonic and attosecond pulse generation on plasma mirrors: basic mechanisms. *Journal of Physics B: Atomic, Molecular and Optical Physics*, 43(21):213001, 2010.

[21] F. Quéré and H. Vincenti. Reflecting petawatt lasers off relativistic plasma mirrors: a realistic path to the schwinger limit. *High Power Laser Science and Engineering*, 9:e6, 2021.

[22] C. Thaury, F. Quéré, J.-P. Geindre, A. Levy, T. Ceccotti, P. Monot, M. Bougeard, F. Réau, P. d'Oliveira, P. Audebert, R. Marjoribanks, and Ph. Martin. Plasma mirrors for ultrahigh-intensity optics. *Nature Physics*, 3(6):424–429, Jun 2007.

[23] N. Naumova, I. Sokolov, J. Nees, A. Maksimchuk, V. Yanovsky, and G. Mourou. Attosecond electron bunches. *Physical Review Letters*, 93:195003, Nov 2004.

[24] B. Hou, J. Nees, J. Easter, J. Davis, G. Petrov, A. Thomas, and K. Krushelnick. Mev proton beams generated by 3 mJ ultrafast laser pulses at 0.5 khz. *Applied Physics Letters*, 95(10):101503, 2009.

[25] M. Veltcheva, A. Borot, C. Thaury, A. Malvache, E. Lefebvre, A. Flacco, R. Lopez-Martens, and V. Malka. Brunel-dominated proton acceleration with a few-cycle laser pulse. *Physical Review Letters*, 108:075004, Feb 2012.

[26] M. J. Clerk. A dynamical theory of the electromagnetic field. *Philosophical transactions*, 155, 1865.

[27] E. Schrödinger. Non-linear optics. *Proceedings of the Royal Irish Academy. Section A: Mathematical and Physical Sciences*, 47:77–117, 1941.

[28] R. W. Boyd. *Nonlinear Optics, Third Edition*. Academic Press, Inc., USA, 3rd edition, 2008.

[29] Q. Lin and G.P. Agrawal. Vector theory of cross-phase modulation: role of nonlinear polarization rotation. *IEEE Journal of Quantum Electronics*, 40(7):958–964, 2004.

[30] J.-L. Tapié and G. Mourou. Shaping of clean, femtosecond pulses at 1.053 μm for chirped-pulse amplification. *Optics Letters*, 17(2):136–138, Jan 1992.

[31] K. Sala and M. C. Richardson. A passive nonresonant technique for pulse contrast enhancement and gain isolation. *Journal of Applied Physics*, 49(4):2268–2276, 1978.

[32] D. Homoelle, A. L. Gaeta, V. Yanovsky, and G. Mourou. Pulse contrast enhancement of high-energy pulses by use of a gas-filled hollow waveguide. *Optics Letters*, 27(18):1646–1648, Sep 2002.

[33] M. P. Kalashnikov, E. Risse, H. Schönnagel, A. Husakou, J. Herrmann, and W. Sandner. Characterization of a nonlinear filter for the front-end of a high contrast double-cpa ti:sapphire laser. *Optics Express*, 12(21):5088–5097, Oct 2004.

[34] A. Jullien, F. Augé-Rochereau, G. Chériaux, J.-P. Chambaret, P. d'Oliveira, T. Auguste, and F. Falcoz. High-efficiency, simple setup for pulse cleaning at the millijoule level by nonlinear induced birefringence. *Optics Letters*, 29(18):2184–2186, Sep 2004.

[35] D. C. Hutchings, J. S. Aitchison, and J. M. Arnold. Nonlinear refractive coupling and vector solitons in anisotropic cubic media. *Journal of the Optical Society of America B*, 14(4):869–879, Apr 1997.

[36] N. Minkovski, S. M. Saltiel, G. I. Petrov, O. Albert, and J. Etchepare. Polarization rotation induced by cascaded third-order processes. *Optics Letters*, 27(22):2025–2027, Nov 2002.

[37] N. Minkovski, G. I. Petrov, S. M. Saltiel, O. Albert, and J. Etchepare. Nonlinear polarization rotation and orthogonal polarization generation experienced in a single-beam configuration. *Journal of the Optical Society of America B*, 21(9):1659–1664, Sep 2004.

[38] A. Jullien, O. Albert, F. Burgy, G. Hamoniaux, J.-P. Rousseau, J.-P. Chambaret, F. Augé-Rochereau, G. Chériaux, J. Etchepare, N. Minkovski, and S. M. Saltiel. 10^{10} temporal contrast for femtosecond ultraintense lasers by cross-polarized wave generation. *Optics Letters*, 30(8):920–922, Apr 2005.

[39] A. Einstein. Zur Quantentheorie der Strahlung. *Physikalische Zeitschrift*, 18:121–128, 1917.

[40] A. L. Schawlow and C. H. Townes. Infrared and optical masers. *Physical Review*, 112:1940–1949, Dec 1958.

[41] P. Moulton. Ti-doped sapphire: tunable solid-state laser. *Optics News*, 8(6):9–9, Nov 1982.

[42] R. Dabu. Femtosecond laser pulses amplification in crystals. *Crystals*, 9(7), 2019.

[43] L. Xu, G. Tempea, A. Poppe, M. Lenzner, Ch. Spielmann, F. Krausz, A. Stingl, and K. Ferencz. High-power sub-10-fs ti: sapphire oscillators. *Applied Physics B: Lasers & Optics*, 65(2), 1997.

[44] H. Burton, C. Debardelaben, W. Amir, and T. A. Planchon. Temperature dependence of ti:sapphire fluorescence spectra for the design of cryogenic cooled ti:sapphire cpa laser. *Optics Express*, 25(6):6954–6962, Mar 2017.

[45] H. Eilers, U. Hömmerich, and W. M. Yen. Temperature-dependent beam-deflection spectroscopy of ti3+ -doped sapphire. *Journal of the Optical Society of America B*, 10(4):584–586, Apr 1993.

[46] St. Burghartz and B. Schulz. Thermophysical properties of sapphire, aln and mgal2o4 down to 70 k. *Journal of Nuclear Materials*, 212-215:1065–1068, 1994. Fusion Reactor Materials.

[47] A. C. DeFranzo and B. G. Pazol. Index of refraction measurement on sapphire at low temperatures and visible wavelengths. *Applied Optics*, 32(13):2224–2234, May 1993.

[48] F. Planchon. *Solutions globales et comportement asymptotique pour les équations de Navier-Stokes*. Thèse de doctorat, École Polytechnique, Palaiseau, France, 1996. Sciences et techniques communes.

[49] T. A. Planchon, F. Burgy, J.-P. Rousseau, and J.-P. Chambaret. 3d modeling of amplification processes in cpa laser amplifiers. *Applied Physics B*, 80(6):661–667, May 2005.

[50] P. Albers, E. Stark, and G. Huber. Continuous-wave laser operation and quantum efficiency of titanium-doped sapphire. *Journal of the Optical Society of America B*, 3(1):134–139, Jan 1986.

[51] P. F. Moulton. Spectroscopic and laser characteristics of ti:al2o3. *Journal of the Optical Society of America B*, 3(1):125–133, Jan 1986.

[52] A. Shirakov, Z. Burshtein, Y. Shimony, E. Frumker, and A. A. Ishaaya. Radiative and non-radiative transitions of excited ti3+ cations in sapphire. *Scientific Reports*, 9(1):18810, Dec 2019.

[53] M. Ouillé, A. Vernier, F. Böhle, M. Bocoum, A. Jullien, M. Lozano, J.-Ph. Rousseau, Z. Cheng, D. Gustas, A. Blumenstein, P. Simon, S. Haessler, J. Faure, T. Nagy, and R. Lopez-Martens. Relativistic-intensity near-single-cycle light waveforms at khz repetition rate. *Light: Science & Applications*, 9(1):47, Mar 2020.

[54] G. Mourou. Nobel lecture: Extreme light physics and application. *Reviews of Modern Physics*, 91:030501, Jul 2019.

[55] V. Yanovsky, V. Chvykov, G. Kalinchenko, P. Rousseau, T. Planchon, T. Matsuoka, A. Maksimchuk, J. Nees, G. Cheriaux, G. Mourou, and K. Krushelnick. Ultra-high intensity- 300-tw laser at 0.1 hz repetition rate. *Optics Express*, 16(3):2109–2114, Feb 2008.

[56] H. Kiriyama, M. Mori, A. S. Pirozhkov, K. Ogura, A. Sagisaka, A. Kon, T. Zh. Esirkepov, Y. Hayashi, H. Kotaki, M. Kanasaki, H. Sakaki, Y. Fukuda, J. Koga, M. Nishiuchi, M. Kando, S. V. Bulanov, K. Kondo, P. R. Bolton, O. Slezak, D. Vojna, M. Sawicka-Chyla, V. Jambunathan, A. Lucianetti, and T. Mocek. High-contrast, high-intensity petawatt-class laser and applications. *IEEE Journal of Selected Topics in Quantum Electronics*, 21(1):232–249, 2015.

[57] J. Rothhardt, G.. K Tadesse, W. Eschen, and J. Limpert. Table-top nanoscale coherent imaging with xuv light. *Journal of Optics*, 20(11):113001, oct 2018.

[58] X. Ribeyre, R. Capdessus, J. Wheeler, E. d'Humières, and G. Mourou. Multiscale study of high energy attosecond pulse interaction with matter and application to proton–boron fusion. *Scientific Reports*, 12(1):4665, Mar 2022.

[59] J. Doyen, A. T. Falk, V. Floquet, J. Hérault, and J.-M. Hannoun-Lévi. Proton beams in cancer treatments: Clinical outcomes and dosimetric comparisons with photon therapy. *Cancer Treatment Reviews*, 43:104–112, 2016.

[60] J. Faure, B. van der Geer, B. Beaurepaire, G. Gallé, A. Vernier, and A. Lifschitz. Concept of a laser-plasma-based electron source for sub-10-fs electron diffraction. *Physical Review Accelerators and Beams*, 19:021302, Feb 2016.

[61] A. Döpp, C. Eberle, S. Howard, F. Irshad, J. Lin, and M. Streeter. Data-driven science and machine learning methods in laser-plasma physics. *arXiv*, arXiv:2212.00026, 2023.

[62] D. Kormin, A. Borot, G. Ma, W. Dallari, B. Bergues, M. Aladi, I. B. Földes, and L. Veisz. Spectral interferometry with waveform-dependent relativistic high-order harmonics from plasma surfaces. *Nature Communications*, 9(4992), 2018.

[63] O. Jahn, V. E. Leshchenko, P. Tzallas, A. Kessel, M. Krüger, A. Münzer, S. A. Trushin, G. D. Tsakiris, S. Kahaly, D. Kormin, L. Veisz, V. Pervak, F. Krausz, Z. Major, and S. Karsch. Towards intense isolated attosecond pulses from relativistic surface high harmonics. *Optica*, 6(3):280–287, Mar 2019.

[64] F. Böhle, M. Thévenet, M. Bocoum, A. Vernier, S. Haessler, and R. Lopez-Martens. Generation of XUV spectral continua from relativistic plasma mirrors driven in the near-single-cycle limit. *Journal of Physics: Photonics*, 2(3):034010, Jul 2020.

[65] A. Jullien, A. Ricci, F. Böhle, J.-P. Rousseau, S. Grabielle, N. Forget, H. Jacqmin, B. Mercier, and R. Lopez-Martens. Carrier-envelope-phase stable, high-contrast, double chirped-pulse-amplification laser system. *Optics Letters*, 39(13):3774–3777, Jul 2014.

[66] P. Tournois. Acousto-optic programmable dispersive filter for adaptive compensation of group delay time dispersion in laser systems. *Optics Communications*, 140(4):245–249, 1997.

[67] M. Ouillé. *Génération d'impulsions laser proches du cycle optique en durée pour l'interaction laser-matière relativiste à haute cadence*. Theses, Institut Polytechnique de Paris, May 2022.

[68] T. Oksenhendler, S. Coudreau, N. Forget, V. Crozatier, S. Grabielle, R. Herzog, O. Gobert, and D. Kaplan. Self-referenced spectral interferometry. *Applied Physics B*, 99(1):7–12, Apr 2010.

[69] S. Kahaly, S. Monchocé, H. Vincenti, T. Dzelzainis, B. Dromey, M. Zepf, Ph. Martin, and F. Quéré. Direct observation of density-gradient effects in harmonic generation from plasma mirrors. *Physical Review Letters*, 110:175001, Apr 2013.

[70] N.V. Didenko, A.V. Konyashchenko, A.P. Lutsenko, and S.Yu. Tenyakov. Contrast degradation in a chirped-pulse amplifier due to generation of prepulses by postpulses. *Optics Express*, 16(5):3178–3190, Mar 2008.

[71] J Itatani, J Faure, M Nantel, G Mourou, and S Watanabe. Suppression of the amplified spontaneous emission in chirped-pulse-amplification lasers by clean high-energy seed-pulse injection. *Optics Communications*, 148(1):70–74, 1998.

[72] S. Fourmaux, S. Payeur, S. Buffechoux, P. Lassonde, C. St-Pierre, F. Martin, and J. C. Kieffer. Pedestal cleaning for high laser pulse contrast ratio with a 100 tw class laser system. *Optics Express*, 19(9):8486–8497, Apr 2011.

[73] H. Yoshida, E. Ishii, R. Kodama, H. Fujita, Y. Kitagawa, Y. Izawa, and T. Yamanaka. High-power and high-contrast optical parametric chirped pulse amplification in β-bab2o4 crystal. *Optics Letters*, 28(4):257–259, Feb 2003.

[74] C. Dorrer, I. A. Begishev, A. V. Okishev, and J. D. Zuegel. High-contrast optical-parametric amplifier as a front end of high-power laser systems. *Optics Letters*, 32(15):2143–2145, Aug 2007.

[75] A. Dubietis, G. Jonušauskas, and A. Piskarskas. Powerful femtosecond pulse generation by chirped and stretched pulse parametric amplification in bbo crystal. *Optics Communications*, 88(4):437–440, 1992.

[76] M. Aoyama, T. Harimoto, J. Ma, Y. Akahane, and K. Yamakawa. Second - harmonic generation of ultra-high intensity femtosecond pulses with a kdp crystal. *Optics Express*, 9(11):579–585, Nov 2001.

[77] J. Buldt, M. Müller, R. Klas, T. Eidam, J. Limpert, and A. Tünnermann. Temporal contrast enhancement of energetic laser pulses by filtered self-phase-modulation-broadened spectra. *Optics Letters*, 42(19):3761–3764, Oct 2017.

[78] H. C. Kapteyn, M. M. Murnane, A. Szoke, and R. W. Falcone. Prepulse energy suppression for high-energy ultrashort pulses using self-induced plasma shuttering. *Optics Letters*, 16(7):490–492, Apr 1991.

[79] A. Lévy, T. Ceccotti, P. D'Oliveira, F. Réau, M. Perdrix, F. Quéré, P. Monot, M. Bougeard, H. Lagadec, P. Martin, J.-P. Geindre, and P. Audebert. Double plasma mirror for ultrahigh temporal contrast ultraintense laser pulses. *Optics Letters*, 32(3):310–312, Feb 2007.

[80] Zhang C.-M., Wang J.-L., Li C., Chen X.-W., Leng Y.-X., Lin L.-H., Li R.-X., and Xu Z.-Zh. Pulse temporal cleaner based on nonlinear ellipse rotation by using BK7 glass plate. *Chinese Physics Letters*, 25(7):2504–2507, Jul 2008.

[81] A. Jullien, O. Albert, G. Chériaux, J. Etchepare, S. Kourtev, N. Minkovski, and S. M. Saltiel. Two crystal arrangement to fight efficiency saturation in cross-polarized wave generation. *Optics Express*, 14(7):2760–2769, Apr 2006.

[82] T. Brabec and F. Krausz. Nonlinear optical pulse propagation in the single-cycle regime. *Physical Review Letters*, 78:3282–3285, Apr 1997.

[83] P. Simon T. Nagy and L. Veisz. High-energy few-cycle pulses: post-compression techniques. *Advances in Physics: X*, 6(1):1845795, 2021.

[84] A.-L. Viotti, M. Seidel, E. Escoto, S. Rajhans, W. P. Leemans, I. Hartl, and C. M. Heyl. Multi-pass cells for post-compression of ultrashort laser pulses. *Optica*, 9(2):197–216, Feb 2022.

[85] M. Nisoli, S. De Silvestri, and O. Svelto. Generation of high energy 10 fs pulses by a new pulse compression technique. *Applied Physics Letters*, 68(20):2793–2795, 05 1996.

[86] T. Nagy, M. Forster, and P. Simon. Flexible hollow fiber for pulse compressors. *Applied Optics*, 47(18):3264–3268, Jun 2008.

[87] F. Böhle. *Near-single-cycle laser for driving relativistic plasma mirrors at kHz repetition rate - development and application.* Phd thesis, Université Paris-Saclay, 2017.

[88] C. Vozzi, M. Nisoli, G. Sansone, S. Stagira, and S. De Silvestri. Optimal spectral broadening in hollow-fiber compressor systems. *Applied Physics B*, 80(3):285–289, Mar 2005.

[89] X. Chen, A. Jullien, A. Malvache, L. Canova, A. Borot, A. Trisorio, C. G. Durfee, and R. Lopez-Martens. Generation of 4.3 fs, 1 mj laser pulses via compression of circularly polarized pulses in a gas-filled hollow-core fiber. *Optics Letters*, 34(10):1588–1590, May 2009.

[90] S. Ghimire, B. Shan, C.-Y. Wang, and Z. Chang. High-energy 6.2-fs pulses for attosecond pulse generation. *Laser Physics*, 15:838–842, 06 2005.

[91] A. Malvache, X. Chen, C. G. Durfee, A. Jullien, and R. Lopez-Martens. Multi-mj pulse compression in hollow fibers using circular polarization. *Applied Physics B*, 104(1):5–9, Jul 2011.

[92] A. Suda, M. Hatayama, K. Nagasaka, and K. Midorikawa. Generation of sub-10-fs, 5-mj-optical pulses using a hollow fiber with a pressure gradient. *Applied Physics Letters*, 86(11):1–3, March 2005. Copyright: Copyright 2008 Elsevier B.V., All rights reserved.

[93] F. Böhle, M. Kretschmar, A. Jullien, M. Kovacs, M. Miranda, R. Romero, H. Crespo, U. Morgner, P. Simon, R. Lopez-Martens, and T. Nagy. Compression of cep-stable multi-mj laser pulses down to 4 fs in long hollow core fibers. *Laser Physics Letters*, 11(9):095401, jun 2014.

[94] M. Miranda, C. L. Arnold, T. Fordell, F. Silva, B. Alonso, R. Weigand, A. L'Huillier, and H. Crespo. Characterization of broadband few-cycle laser pulses with the d-scan technique. *Optics Express*, 20(17):18732–18743, 2012.

[95] L. Xu, Ch. Spielmann, A. Poppe, T. Brabec, F. Krausz, and T. W. Hänsch. Route to phase control of ultrashort light pulses. *Optics Letters*, 21(24):2008–2010, Dec 1996.

[96] F. Lücking. *Carrier-Envelope Phase Control for the Advancement of Attosecond Pulse Generation*. Phd thesis, Ludwig-Maximilians-Universität, July 2014.

[97] M. Kakehata, Y. Fujihira, H. Takada, Y. Kobayashi, K. Torizuka, T. Homma, and H. Takahashi. Measurements of carrier-envelope phase changes of 100-hz amplified laser pulses. *Applied Physics B: Lasers and Optics*, 74(SUPPL.):S43–S50, June 2002.

[98] A. Baltuška, Th. Udem, M. Uiberacker, M. Hentschel, E. Goulielmakis, Ch. Gohle, R. Holzwarth, V. S. Yakovlev, A. Scrinzi, T. W. Hänsch, and F. Krausz. Attosecond control of electronic processes by intense light fields. *Nature*, 421(6923):611–615, Feb 2003.

[99] C. Li, E. Moon, and Z. Chang. Carrier-envelope phase shift caused by variation of grating separation. *Optics Letters*, 31(21):3113–3115, Nov 2006.

[100] A. Golinelli, X. Chen, B. Bussière, E. Gontier, Pierre-Mary Paul, O. Tcherbakoff, P. D'Oliveira, and Jean-Francois Hergott. Cep-stabilized, sub-18 fs, 10 khz and tw-class 1 khz dual output ti:sa laser with wavelength tunability option. *Optics Express*, 27:13624, 04 2019.

[101] A Börzsönyi, R S Nagymihály, and K Osvay. Drift and noise of the carrier–envelope phase in a ti:sapphire amplifier. *Laser Physics Letters*, 13(1):015301, Nov 2015.

[102] A. S. Wyatt, T. Witting, A. Schiavi, D. Fabris, P. Matia-Hernando, I. A. Walmsley, J. P. Marangos, and J. W. G. Tisch. Attosecond sampling of arbitrary optical waveforms. *Optica*, 3(3):303–310, Mar 2016.

[103] Y. Zhang, P. Kellner, D. Adolph, D. Zille, P. Wustelt, D. Würzler, S. Skruszewicz, M. Möller, A. M. Sayler, and G. G. Paulus. Single-shot, real-time carrier-envelope phase measurement and tagging based on stereographic above-threshold ionization at short-wave infrared wavelengths. *Optics Letters*, 42(24):5150–5153, Dec 2017.

[104] W. Cho, J.-u. Shin, and K. T. Kim. Reconstruction algorithm for tunneling ionization with a perturbation for the time-domain observation of an electric-field. *Scientific Reports*, 11(1):13014, Jun 2021.

[105] S. B. Park, K. Kim, W. Cho, S. In Hwang, I. Ivanov, C. H. Nam, and K. T. Kim. Direct sampling of a light wave in air. *Optica*, 5(4):402–408, Apr 2018.

[106] M. Kurucz, S.Tóth, R. Flender, L. Haizer, B. Kiss, B. Persielle, and E. Cormier. Single-shot cep drift measurement at arbitrary repetition rate based on dispersive fourier transform. *Optics Express*, 27(9):13387–13399, Apr 2019.

[107] T. Fuji, A. Apolonski, and F. Krausz. Self-stabilization of carrier-envelope offset phase by use of difference-frequency generation. *Optics Letters*, 29(6):632–634, Mar 2004.

[108] T. Fuji, J. Rauschenberger, A. Apolonski, V. S. Yakovlev, G. Tempea, T. Udem, C. Gohle, T. W. Hänsch, W. Lehnert, M. Scherer, and F. Krausz. Monolithic carrier-envelope phase-stabilization scheme. *Optics Letters*, 30(3):332–334, Feb 2005.

[109] J. Rauschenberger, T. Fuji, M. Hentschel, A.-J. Verhoef, T. Udem, C. Gohle, T. W. Hänsch, and F. Krausz. Carrier-envelope phase-stabilized amplifier system. *Laser Physics Letters*, 3(1):37, Sep 2005.

[110] Jörn Stenger and Harald R. Telle. Intensity-induced mode shift in a femtosecond laser by a change in the nonlinear index of refraction. *Optics Letters*, 25(20):1553–1555, Oct 2000.

[111] A. Golinelli. *Development of an original 10 kHz Ti : Sa regenerative cavity allowing 17 fs CEP stable 1 kHz TW-class amplification or wavelength tunability*. Theses, Université Paris Saclay (COmUE), January 2019.

[112] J.F. Hergott, P.M. Paul, O. Tcherbakoff, P. Demengeot, M. Perdrix, F. Lepetit, D. Garzella, D. Guillaumet, M. Comte, O. Gobert, and P. d'Oliveira. Carrier-envelope phase stabilization of a grating based chirped pulse amplified laser at 17 mj, 1 khz using regenerative and cryo-cooled amplifiers. In *2011 Conference on Lasers and Electro-Optics Europe and 12th European Quantum Electronics Conference (CLEO EUROPE/EQEC)*, pages 1–1, 2011.

[113] F. Lücking, V. Crozatier, N. Forget, A. Assion, and F. Krausz. Approaching the limits of carrier-envelope phase stability in a millijoule-class amplifier. *Optics Letters*, 39(13):3884–3887, Jul 2014.

[114] J. Huijts, L. Rovige, I. A. Andriyash, A. Vernier, M. Ouillé, J. Kaur, Z. Cheng, R. Lopez-Martens, and J. Faure. Waveform control of relativistic electron dynamics in laser-plasma acceleration. *Physical Review X*, 12:011036, Feb 2022.

[115] P. P. Sorokin and M. J. Stevenson. Stimulated infrared emission from trivalent uranium. *Physical Review Letters*, 5:557–559, Dec 1960.

[116] C. Bowess. Liquid nitrogen cooled ruby laser. US Patent 3339150, August 1967. Patent number 3339150.

[117] P.A. Schulz and S.R. Henion. Liquid-nitrogen-cooled ti:al_2o_3 laser. *IEEE Journal of Quantum Electronics*, 27(4):1039–1047, 1991.

[118] J. Seres, A. Müller, E. Seres, K. O'Keeffe, M. Lenner, R. F. Herzog, D. Kaplan, C. Spielmann, and F. Krausz. Sub-10-fs, terawatt-scale ti:sapphire laser system. *Optics Letters*, 28(19):1832–1834, Oct 2003.

[119] S. Backus, R. Bartels, S. Thompson, R. Dollinger, H. C. Kapteyn, and M. M. Murnane. High-efficiency, single-stage 7-khz high-average-power ultrafast laser system. *Optics Letters*, 26(7):465–467, Apr 2001.

[120] M. Pittman, S. Ferré, J. P. Rousseau, L. Notebaert, J. P. Chambaret, and G. Chériaux. Design and characterization of a near-diffraction-limited femtosecond 100-tw 10-hz high-intensity laser system. *Applied Physics B*, 74(6):529–535, Apr 2002.

[121] V. Ramanathan, J. Lee, S. Xu, X. Wang, L. Williams, W. Malphurs, and D. H. Reitze. Analysis of thermal aberrations in a high average power single-stage Ti:sapphire regenerative chirped pulse amplifier: Simulation and experiment. *Review of Scientific Instruments*, 77(10):103103, 10 2006.

[122] T. A. Planchon, W. Amir, C. Childress, J. A. Squier, and C. G. Durfee. Measurement of pump-induced transient lensing in a cryogenically-cooled high average power ti:sapphire amplifier. *Optics Express*, 16(23):18557–18564, Nov 2008.

[123] D. C. Brown, S. Tornegård, J. Kolis, C. McMillen, C. Moore, L. Sanjeewa, and C. Hancock. The application of cryogenic laser physics to the development of high average power ultra-short pulse lasers. *Applied Sciences*, 6(1), 2016.

[124] T. Oksenhendler, S. Coudreau, N. Forget, V. Crozatier, S. Grabielle, R. Herzog, O. Gobert, and D. Kaplan. Self-referenced spectral interferometry. *Applied Physics B*, 99(1):7–12, 2010.

[125] D. Herriott, H. Kogelnik, and R. Kompfner. Off-axis paths in spherical mirror interferometers. *Applied Optics*, 3(4):523–526, Apr 1964.

[126] D. Kaur, A. M. de Souza, J. Wanna, S. A. Hammad, L. Mercorelli, and D. S. Perry. Multipass cell for molecular beam absorption spectroscopy. *Applied Optics*, 29(1):119–124, Jan 1990.

[127] A. Owyoung, C. W. Patterson, and R. S. McDowell. Cw stimulated raman gain spectroscopy of the $v1$ fundamental of methane. *Chemical Physics Letters*, 59(1):156–162, 1978.

[128] W. R. Trutna and R. L. Byer. Multiple-pass raman gain cell. *Applied Optics*, 19(2):301–312, Jan 1980.

[129] D. R. Herriott and H. J. Schulte. Folded optical delay lines. *Applied Optics*, 4(8):883–889, Aug 1965.

[130] J. Schulte, T. Sartorius, J. Weitenberg, A. Vernaleken, and P. Russbueldt. Nonlinear pulse compression in a multi-pass cell. *Optics Letters*, 41(19):4511–4514, Oct 2016.

[131] S. Hädrich, M. Kienel, M. Müller, A. Klenke, J. Rothhardt, R. Klas, T. Gottschall, T. Eidam, A. Drozdy, P. Jójárt, Z. Várallyay, E. Cormier, K. Osvay, A. Tünnermann, and J. Limpert. Energetic sub-2-cycle laser with 216 w average power. *Optics Letters*, 41(18):4332–4335, Sep 2016.

[132] C. Jocher, T. Eidam, S. Hädrich, J. Limpert, and A. Tünnermann. Sub 25 fs pulses from solid-core nonlinear compression stage at 250 w of average power. *Optics Letters*, 37(21):4407–4409, Nov 2012.

[133] F. Emaury, C. J. Saraceno, B. Debord, D. Ghosh, A. Diebold, F. Gèrôme, T. Südmeyer, F. Benabid, and U. Keller. Efficient spectral broadening in the 100-w average power regime using gas-filled kagome hc-pcf and pulse compression. *Optics Letters*, 39(24):6843–6846, Dec 2014.

[134] J. Weitenberg, A. Vernaleken, J. Schulte, A. Ozawa, T. Sartorius, V. Pervak, H.-D. Hoffmann, T. Udem, P. Russbüldt, and T. W. Hänsch. Multi-pass-cell-based nonlinear pulse compression to 115 fs at 7.5 µj pulse energy and 300 W average power. *Optics Express*, 25(17):20502–20510, August 2017.

[135] L. Lavenu, M. Natile, F. Guichard, Y. Zaouter, X. Delen, M. Hanna, E. Mottay, and P. Georges. Nonlinear pulse compression based on a gas-filled multipass cell. *Optics Letters*, 43(10):2252–2255, May 2018.

[136] M. Kaumanns, V. Pervak, D. Kormin, V. Leshchenko, A. Kessel, M. Ueffing, Y. Chen, and T. Nubbemeyer. Multipass spectral broadening of 18 mj pulses compressible from 1.3 ps to 41 fs. *Optics Letters*, 43(23):5877–5880, Dec 2018.

[137] M. Müller, J. Buldt, H. Stark, C. Grebing, and J. Limpert. Multipass cell for high-power few-cycle compression. *Optics Letters*, 46(11):2678–2681, Jun 2021.

[138] P. Balla, A. Bin Wahid, I. Sytcevich, C. Guo, A.-L. Viotti, L. Silletti, A. Cartella, S. Alisauskas, H. Tavakol, U. Grosse-Wortmann, A. Schönberg, M. Seidel, A. Trabattoni, B. Manschwetus, T. Lang, F. Calegari, A. Couairon, A. L'Huillier, C. L. Arnold, I. Hartl, and C. M. Heyl. Postcompression of picosecond pulses into the few-cycle regime. *Optics Letters*, 45(9):2572–2575, May 2020.

[139] M. Kaumanns, D. Kormin, T. Nubbemeyer, V. Pervak, and S. Karsch. Spectral broadening of 112 mj, 1.3 ps pulses at 5 khz in a $\lg_{10}$ multipass cell with compressibility to 37 fs. *Optics Letters*, 46(5):929–932, Mar 2021.

[140] Y. Pfaff, G. Barbiero, M. Rampp, S. Klingebiel, J. Brons, C. Y. Teisset, H. Wang, R. Jung, J. Jaksic, A. H. Woldegeorgis, M. Trunk, A. R. Maier, C. J. Saraceno, and T. Metzger. Nonlinear pulse compression of a 200 mj and 1 kw ultrafast thin-disk amplifier. *Optics Express*, 31(14):22740–22756, Jul 2023.

[141] C. Grebing, M. Müller, J. Buldt, H. Stark, and J. Limpert. Kilowatt-average-power compression of millijoule pulses in a gas-filled multi-pass cell. *Optics Letters*, 45(22):6250–6253, Nov 2020.

[142] E. Escoto, A.-L. Viotti, S. Alisauskas, H. Tünnermann, I. Hartl, and C. M. Heyl. Temporal quality of post-compressed pulses at large compression factors. *Journal of the Optical Society of America B*, 39(7):1694–1702, Jul 2022.

[143] R. M. Kaumanns. *Generation of energetic femtosecond pulses at high average power*. PhD thesis, March 2020.

[144] M. Hanna, N. Daher, F. Guichard, X. Délen, and P. Georges. Hybrid pulse propagation model and quasi-phase-matched four-wave mixing in multipass cells. *Journal of the Optical Society of America B*, 37(10):2982–2988, Oct 2020.

[145] M. Hanna, L. Daniault, F. Guichard, N. Daher, X. Délen, R. Lopez-Martens, and Patrick Georges. Nonlinear beam matching to gas-filled multipass cells. *OSA Continuum*, 4(2):732–738, Feb 2021.

[146] A. Couairon, E. Brambilla, T. Corti, D. Majus, O. de J. Ramírez-Góngora, and M. Kolesik. Practitioner's guide to laser pulse propagation models and simulation. *The European Physical Journal Special Topics*, 199(1):5–76, Nov 2011.

[147] P.-A. Belanger and C. Pare. Self-focusing of gaussian beams: an alternate derivation. *Applied Optics*, 22(9):1293–1295, May 1983.

[148] J. Weitenberg, T. Saule, J. Schulte, and P. Rußbüldt. Nonlinear pulse compression to sub-40 fs at 4.5 μ j pulse energy by multi-pass-cell spectral broadening. *IEEE Journal of Quantum Electronics*, 53(6):1–4, 2017.

[149] J. Song, Z. Wang, R. Lv, X. Wang, H. Teng, J. Zhu, and Z. Wei. Generation of 172 fs pulse from a nd: Yvo4 picosecond laser by using multi-pass-cell technique. *Applied Physics B*, 127(4):50, Mar 2021.

[150] P. Rueda, F. Videla, T. Witting, G. A. Torchia, and F. J. Furch. 8 fs laser pulses from a compact gas-filled multi-pass cell. *Optics Express*, 29(17):27004–27013, Aug 2021.

[151] L. Daniault, Z. Cheng, J. Kaur, J.-F. Hergott, F. Réau, O. Tcherbakoff, N. Daher, X. Délen, M. Hanna, and R. Lopez-Martens. Single-stage few-cycle nonlinear compression of millijoule energy ti:sa femtosecond pulses in a multipass cell. *Optics Letters*, 46(20):5264–5267, Oct 2021.

[152] M. Ueffing, S. Reiger, M. Kaumanns, V. Pervak, M. Trubetskov, T. Nubbemeyer, and F. Krausz. Nonlinear pulse compression in a gas-filled multipass cell. *Optics Letters*, 43(9):2070–2073, May 2018.

[153] M. Seidel, P. Balla, C. Li, G. Arisholm, L. Winkelmann, I. Hartl, and C. M. Heyl. Factor 30 pulse compression by hybrid multipass multiplate spectral broadening. *Ultrafast Science*, 2022, 2022.

[154] K. Fritsch, M. Poetzlberger, V. Pervak, J. Brons, and O. Pronin. All-solid-state multipass spectral broadening to sub-20 fs. *Optics Letters*, 43(19):4643–4646, Oct 2018.

[155] L. Lavenu, M. Natile, F. Guichard, X. Délen, M. Hanna, Y. Zaouter, and P. Georges. High-power two-cycle ultrafast source based on hybrid nonlinear compression. *Optics Express*, 27(3):1958–1967, Feb 2019.

[156] P. Russbueldt, J. Weitenberg, J. Schulte, R. Meyer, C. Meinhardt, H. D. Hoffmann, and R. Poprawe. Scalable 30 fs laser source with 530 w avergae power. *Optics Letters*, 44(21):5222–5225, Nov 2019.

[157] E. Vicentini, Y. Wang, D. Gatti, A. Gambetta, P. Laporta, G. Galzerano, K. Curtis, K. McEwan, C. R. Howle, and N. Coluccelli. Nonlinear pulse compression to 22 fs at 15.6 µj by an all-solid-state multipass approach. *Optics Express*, 28(4):4541–4549, Feb 2020.

[158] P. L. Kramer, M. K. R. Windeler, K. Mecseki, E. G. Champenois, M. C. Hoffmann, and F. Tavella. Enabling high repetition rate nonlinear thz science with a kilowatt-class sub-100 fs laser source. *Optics Express*, 28(11):16951–16967, May 2020.

[159] A.-L. Viotti, S. Alisauskas, A. Bin Wahid, P. Balla, N. Schirmel, B. Manschwetus, I. Hartl, and C. M. Heyl. 60 fs, 1030nm FEL pump–probe laser based on a multi-pass post-compressed Yb:YAG source. *Journal of Synchrotron Radiation*, 28(1):36–43, Jan 2021.

[160] A. Omar, T. Vogel, M. Hoffmann, and C. J. Saraceno. Spectral broadening of 2-mj femtosecond pulses in a compact air-filled convex–concave multi-pass cell. *Optics Letters*, 48(6):1458–1461, Mar 2023.

[161] P. Russbueldt, T. Mans, J. Weitenberg, H. D. Hoffmann, and R. Poprawe. Compact diode-pumped 1.1 kw yb:yag innoslab femtosecond amplifier. *Optics Letters*, 35(24):4169–4171, Dec 2010.

[162] T. Nubbemeyer, M. Kaumanns, M. Ueffing, M. Gorjan, A. Alismail, H. Fattahi, J. Brons, O. Pronin, H. G. Barros, Z. Major, T. Metzger, D. Sutter, and F. Krausz. 1 kw, 200 mj picosecond thin-disk laser system. *Optics Letters*, 42(7):1381–1384, Apr 2017.

[163] M. Müller, C. Aleshire, A. Klenke, E. Haddad, F. Légaré, A. Tünnermann, and J. Limpert. 10.4 kw coherently combined ultrafast fiber laser. *Optics Letters*, 45(11):3083–3086, Jun 2020.

[164] Y. Pfaff, C. Forster, G. Barbiero, M. Rampp, S. Klingebiel, J. Brons, C. Y. Teisset, H. Wang, R. Jung, J. Jaksic, A. H. Woldegeorgis, C. J. Saraceno, and T. Metzger. Nonlinear pulse compression of a thin-disk amplifier and contrast enhancement via nonlinear ellipse rotation. *Optics Express*, 30(7):10981–10990, Mar 2022.

[165] S. Gröbmeyer, K. Fritsch, B. Schneider, M. Poetzlberger, V. Pervak, J. Brons, and O. Pronin. Self-compression at 1 µm wavelength in all-bulk multi-pass geometry. *Applied Physics B*, 126(10):159, Sep 2020.

[166] M. Karst, M. Benner, P. Gierschke, H. Stark, and J. Limpert. Dispersion engineering in nonlinear multipass cells for high-quality pulse compression. *Optics Letters*, 48(22):5899–5902, Nov 2023.

[167] C. Mei and G. Steinmeyer. Space-time focusing and coherence properties of supercontinua in multipass cells. *Physical Review Research*, 3:013259, Mar 2021.

[168] N. Daher, F. Guichard, X. Délen, Y. Zaouter, M. Hanna, and P. Georges. Spectral compression in a multipass cell. *Optics Express*, 28(15):21571–21577, Jul 2020.

[169] N. Daher, X. Délen, F. Guichard, M. Hanna, and P. Georges. Raman wavelength conversion in a multipass cell. *Optics Letters*, 46(14):3380–3383, Jul 2021.

[170] N. Daher, F. Guichard, S. W. Jolly, X. Délen, F. Quéré, M. Hanna, and P. Georges. Multipass cells: 1d numerical model and investigation of spatio-spectral couplings at high nonlinearity. *Journal of the Optical Society of America B*, 37(4):993–999, Apr 2020.

[171] N. Kovalenko, V. Hariton, K. Fritsch, and O. Pronin. Free-space quasi-phase matching. *Optics Letters*, 48(23):6220–6223, Dec 2023.

[172] V. Pajer and M. Kalashnikov. High temporal contrast ultrashort pulses generated by nonlinear ellipse rotation in multipass cells. *Laser Physics Letters*, 18(6):065401, May 2021.

[173] J. Kaur, L. Daniault, Z. Cheng, O. Tourneur, O. Tcherbakoff, F. Réau, J.-F. Hergott, and R. Lopez-Martens. Simultaneous nonlinear spectral broadening and temporal contrast enhancement of ultrashort pulses in a multi-pass cell. *Journal of Physics: Photonics*, 6(1):015001, Nov 2023.

[174] J. Itatani, J. Faure, M. Nantel, G. Mourou, and S. Watanabe. Suppression of the amplified spontaneous emission in chirped-pulse-amplification lasers by clean high-energy seed-pulse injection. *Optics Communications*, 148(1):70–74, 1998.

[175] S. Fourmaux, S. Payeur, S. Buffechoux, P. Lassonde, C. St-Pierre, F. Martin, and J. C. Kieffer. Pedestal cleaning for high laser pulse contrast ratio with a 100 tw class laser system. *Optics Express*, 19(9):8486–8497, Apr 2011.

[176] A. Dubietis, G. Jonušauskas, and A. Piskarskas. Powerful femtosecond pulse generation by chirped and stretched pulse parametric amplification in bbo crystal. *Optics Communications*, 88(4):437–440, 1992.

[177] H. Yoshida, E. Ishii, R. Kodama, H. Fujita, Y. Kitagawa, Y. Izawa, and T. Yamanaka. High-power and high-contrast optical parametric chirped pulse amplification in β-bab2o4 crystal. *Optics Letters*, 28(4):257–259, Feb 2003.

[178] C. Dorrer, I. A. Begishev, A. V. Okishev, and J. D. Zuegel. High-contrast optical-parametric amplifier as a front end of high-power laser systems. *Optics Letters*, 32(15):2143–2145, Aug 2007.

[179] M. Aoyama, T. Harimoto, J. Ma, Y. Akahane, and K. Yamakawa. Second - harmonic generation of ultra-high intensity femtosecond pulses with a kdp crystal. *Optics Express*, 9(11):579–585, Nov 2001.

[180] A. Lévy, T. Ceccotti, P. D'Oliveira, F. Réau, M. Perdrix, F. Quéré, P. Monot, M. Bougeard, H. Lagadec, P. Martin, J.-P. Geindre, and P. Audebert. Double plasma mirror for ultrahigh temporal contrast ultraintense laser pulses. *Optics Letters*, 32(3):310–312, Feb 2007.

[181] J. Buldt, M. Müller, R. Klas, T. Eidam, J. Limpert, and A. Tünnermann. Temporal contrast enhancement of energetic laser pulses by filtered self-phase-modulation-broadened spectra. *Optics Letters*, 42(19):3761–3764, Oct 2017.

[182] J.-L. Tapié and G. Mourou. Shaping of clean, femtosecond pulses at 1.053 μm for chirped-pulse amplification. *Optics Letters*, 17(2):136–138, Jan 1992.

[183] Zhang C.-M., Wang J.-L., Li C., Chen X.-W., Leng Y.-X., Lin L.-H., Li R.-X., and Xu Z.-Zh. Pulse temporal cleaner based on nonlinear ellipse rotation by using BK7 glass plate. *Chinese Physics Letters*, 25(7):2504–2507, Jul 2008.

[184] N G Khodakovskiy, M P Kalashnikov, V Pajer, A Blumenstein, P Simon, M M Toktamis, M Lozano, B Mercier, Z Cheng, T Nagy, and R Lopez-Martens. Generation of few-cycle laser pulses with high temporal contrast via nonlinear elliptical polarisation rotation in a hollow fibre compressor. *Laser Physics Letters*, 16(9):095001, Aug 2019.

[185] N. Smijesh, X. Zhang, P. Fischer, A. A. Muschet, R. Salh, A. Tajalli, U. Morgner, and L. Veisz. Contrast improvement of sub-4 fs laser pulses using nonlinear elliptical polarization rotation. *Optics Letters*, 44(16):4028–4031, Aug 2019.

[186] A. Jullien, L. Canova, O. Albert, D. Boschetto, L. Antonucci, Y.-H. Cha, J.P. Rousseau, P. Chaudet, G. Chériaux, J. Etchepare, S. Kourtev, N. Minkovski, and S.M. Saltiel. Influence of spectral phase on cross-polarized wave generation with short femtosecond pulses. *Applied Physics B*, 87:595–601, Jun 2007.

[187] L. Canova, O. Albert, N. Forget, B. Mercier, S. Kourtev, N. Minkovski, S. M. Saltiel, and R. Lopez Martens. Influence of spectral phase on cross-polarized wave generation with short femtosecond pulses. *Applied Physics B*, 93(2):443–453, Sept 2008.

[188] A. Jullien, S. Kourtev, O. Albert, G. Chériaux, J. Etchepare, N. Minkovski, and S.M. Saltiel. Highly efficient temporal cleaner for femtosecond pulses based on cross-polarized wave generation in a dual crystal scheme. *Applied Physics B*, 84:409–414, 2006.

[189] A. Jullien, J.-P. Rousseau, B. Mercier, L. Antonucci, O. Albert, G. Chériaux, S. Kourtev, N. Minkovski, and S. M. Saltiel. Highly efficient nonlinear filter for femtosecond pulse contrast enhancement and pulse shortening. *Optics Letters*, 33(20):2353–2355, Oct 2008.

[190] L.P. Ramirez, D.N. Papadopoulos, A. Pellegrina, P. Georges, F. Druon, P. Monot, A. Ricci, A. Jullien, X. Chen, J.P. Rousseau, and R. Lopez-Martens. Efficient cross polarized wave generation for compact, energy-scalable, ultrashort laser sources. *Optics Express*, 19(1):93–98, Jan 2011.

[191] L. Canova, X. Chen, A. Trisorio, A. Jullien, A. Assion, G. Tempea, N. Forget, T. Oksenhendler, and R. Lopez-Martens. Carrier-envelope phase stabilization and control using a transmission grating compressor and an aopdf. *Optics Letters*, 34(9):1333–1335, May 2009.

[192] D. E. Adams, T. A. Planchon, J. A. Squier, and C. G. Durfee. Spatiotemporal dynamics of cross-polarized wave generation. *Optics Letters*, 35(7):1115–1117, Apr 2010.

[193] A. Jullien, C. G. Durfee, A. Trisorio, L. Canova, J.-P. Rousseau, B. Mercier, L. Antonucci, G. Chériaux, O. Albert, and R. Lopez-Martens. Nonlinear spectral cleaning of few-cycle pulses via cross-polarized wave (xpw) generation. *Applied Physics B*, 96:293–299, Aug 2009.

[194] P. Balla, H. Tünnermann, S. H. Salman, M. Fan, S. Alisauskas, I. Hartl, and C. M. Heyl. Ultrafast serrodyne optical frequency translator. *Nature Photonics*, 17(2):187–192, Feb 2023.

[195] M. Hanna, F. Guichard, N. Daher, Q. Bournet, X. Délen, and P. Georges. Nonlinear optics in multipass cells. *Laser & Photonics Reviews*, 15(12):2100220, 2021.

[196] P. Gibbon. *Short Pulse Laser Interactions with Matter*. World Scientific Publishing Company, Singapore, 2004.

[197] M. Göppert-Mayer. Über elementarakte mit zwei quantensprüngen. *Annalen der Physik*, 401(3):273–294, 1931.

[198] P. Agostini, G. Barjot, J. Bonnal, G. Mainfray, C. Manus, and J. Morellec. Multiphoton ionization of hydrogen and rare gases. *IEEE Journal of Quantum Electronics*, 4(10):667–669, 1968.

[199] L. V. Keldysh. *Ionization in the field of a strong electromagnetic wave*. Selected Papers of Leonid V Keldysh, 2023.

[200] A. M. Perelomov, V. S. Popov, and M. V. Terentev. Ionization of atoms in an alternating electric field. *Zhurnal Eksperimental'noi i Teoreticheskoi Fiziki (U.S.S.R.) For English translation see Sov. Phys. - JETP (Engl. Transl.)*, 50, 5 1966.

[201] L. V. Keldysh. Ionization in the Field of a Strong Electromagnetic Wave. *J. Exp. Theor. Phys.*, 20(5):1307–1314, 1965.

[202] L. Chopineau. *Physique attoseconde relativiste sur miroirs plasmas*. Theses, Université Paris Saclay (COmUE), September 2019.

[203] W. Kruer. *The Physics Of Laser Plasma Interactions*. CRC Press, 2019.

[204] P. Mulser and D. Bauer. *High Power Laser-Matter Interaction*. Springer Tracts in Modern Physics. Springer, 2010.

[205] A. Macchi. *A Superintense Laser-Plasma Interaction Theory Primer*. SpringerBriefs in Physics. Springer, 2013.

[206] G. A. Mourou, T. Tajima, and S. V. Bulanov. Optics in the relativistic regime. *Reviews of Modern Physics*, 78:309–371, Apr 2006.

[207] P. Gibbon. Physics of high-intensity laser-plasma interactions. *La Rivista del Nuovo Cimento*, 35(12):607–644, Dec 2012.

[208] P. Mora. Plasma expansion into a vacuum. *Physical Review Letters*, 90:185002, May 2003.

[209] N. Zaïm. *Modélisation de l'accélération d'électrons par des impulsions lasers relativistes de quelques cycles optiques sur des plasmas surdenses*. PhD thesis, Université Paris Saclay (COmUE), Dec. 2019.

[210] J.-M. Rax. *Physique des plasmas: cours et applications*. Dunod, 2005.

[211] B. Quesnel and P. Mora. Theory and simulation of the interaction of ultraintense laser pulses with electrons in vacuum. *Physical Review E*, 58:3719–3732, Sep 1998.

[212] D. W. Forslund, J. M. Kindel, Kenneth Lee, E. L. Lindman, and R. L. Morse. Theory and simulation of resonant absorption in a hot plasma. *Physical Review A*, 11:679–683, Feb 1975.

[213] P. Gibbon and A. R. Bell. Collisionless absorption in sharp-edged plasmas. *Physical Review Letters*, 68:1535–1538, Mar 1992.

[214] F. Brunel. Not-so-resonant, resonant absorption. *Physical Review Letters*, 59:52–55, Jul 1987.

[215] J. P. Freidberg, R. W. Mitchell, R. L. Morse, and L. I. Rudsinski. Resonant absorption of laser light by plasma targets. *Physical Review Letters*, 28:795–799, Mar 1972.

[216] F. Quéré, C. Thaury, P. Monot, S. Dobosz, Ph. Martin, J.-P. Geindre, and P. Audebert. Coherent wake emission of high-order harmonics from overdense plasmas. *Physical Review Letters*, 96:125004, 2006.

[217] W. L. Kruer and K. Estabrook. J×B heating by very intense laser light. *The Physics of Fluids*, 28(1):430–432, 01 1985.

[218] S.C. Wilks and W.L. Kruer. Absorption of ultrashort, ultra-intense laser light by solids and overdense plasmas. *IEEE Journal of Quantum Electronics*, 33(11):1954–1968, 1997.

[219] S. D. Baton, J. J. Santos, F. Amiranoff, H. Popescu, L. Gremillet, M. Koenig, E. Martinolli, O. Guilbaud, C. Rousseaux, M. Rabec Le Gloahec, T. Hall, D. Batani, E. Perelli, F. Scianitti, and T. E. Cowan. Evidence of ultrashort electron bunches in laser-plasma interactions at relativistic intensities. *Physical Review Letters*, 91:105001, Sep 2003.

[220] B. Dromey, S. Kar, M. Zepf, and P. Foster. The plasma mirror—A subpicosecond optical switch for ultrahigh power lasers. *Review of Scientific Instruments*, 75(3):645–649, 03 2004.

[221] R. W. Means, L. Muschietti, M. Q. Tran, and J. Vaclavik. Electromagnetic radiation from an inhomogeneous plasma: Theory and experiment. *The Physics of Fluids*, 24(12):2197–2207, 12 1981.

[222] A. Malvache. *Optique non-linéaire à haute intensité : Compression d'impulsions laser Interaction laser-plasma*. PhD thesis, Ecole polytechnique, 2011. Thèse de doctorat dirigée par Mourou, Gérard Lasers et matière Palaiseau, Ecole polytechnique 2011.

[223] A. Malvache, A. Borot, F. Quéré, and R. Lopez-Martens. Coherent wake emission spectroscopy as a probe of steep plasma density profiles. *Physical Review E*, 87:035101, Mar 2013.

[224] K. Varjú, Y. Mairesse, B. Carré, M. B. Gaarde, P. Johnsson, S. Kazamias, R. López-Martens, J. Mauritsson, K. J. Schafer, PH. Balcou, A. L'huillier, and P. Salières. Frequency chirp of harmonic and attosecond pulses. *Journal of Modern Optics*, 52(2-3):379–394, 2005.

[225] C. Thaury, F. Quéré, H. George, J. P. Geindre, P. Monot, and Ph. Martin. High-order harmonic generation from plasma mirrors. *The European Physical Journal Special Topics*, 175(1):43–48, Aug 2009.

[226] F. Quéré, C. Thaury, J-P. Geindre, G. Bonnaud, P. Monot, and Ph. Martin. Phase properties of laser high-order harmonics generated on plasma mirrors. *Physical Review Letters*, 100:095004, Mar 2008.

[227] A. V. Mitrofanov, D. A. Sidorov-Biryukov, P. B. Glek, M. V. Rozhko, E. A. Stepanov, A. D. Shutov, S. V. Ryabchuk, A. A. Voronin, A. B. Fedotov, and A. M. Zheltikov. Chirp-controlled high-harmonic and attosecond-pulse generation via coherent-wake plasma emission driven by mid-infrared laser pulses. *Optics Letters*, 45(3):750–753, Feb 2020.

[228] C. Thaury, H. George, F. Quéré, R. Loch, J.-P. Geindre, P. Monot, and Ph. Martin. Coherent dynamics of plasma mirrors. *Nature Physics*, 4(8):631–634, Aug 2008.

[229] E. Porat, H. Yehuda, I. Cohen, A. Levanon, and I. Pomerantz. Diffraction-limited coherent wake emission. *Physical Review Research*, 3:L032059, Sep 2021.

[230] S. V. Bulanov, N. M. Naumova, and F. Pegoraro. Interaction of an ultrashort, relativistically strong laser pulse with an overdense plasma. *Physics of Plasmas*, 1(3):745–757, 03 1994.

[231] R. Lichters, J. Meyer-ter-Vehn, and A. Pukhov. Short-pulse laser harmonics from oscillating plasma surfaces driven at relativistic intensity. *Physics of Plasmas*, 3(9):3425–3437, 09 1996.

[232] S. Gordienko, A. Pukhov, O. Shorokhov, and T. Baeva. Relativistic doppler effect: Universal spectra and zeptosecond pulses. *Physical Review Letters*, 93:115002, Sep 2004.

[233] T. Baeva, S. Gordienko, and A. Pukhov. Theory of high-order harmonic generation in relativistic laser interaction with overdense plasma. *Physical Review E*, 74:046404, Oct 2006.

[234] D. von der Linde and K. Rzàzewski. High-order optical harmonic generation from solid surfaces. *Applied Physics B*, 63(5):499–506, Nov 1996.

[235] P. Gibbon. Harmonic generation by femtosecond laser-solid interaction: A coherent “water-window” light source? *Physical Review Letters*, 76:50–53, Jan 1996.

[236] A. A. Gonoskov, A. V. Korzhimanov, A. V. Kim, M. Marklund, and A. M. Sergeev. Ultrarelativistic nanoplasmonics as a route towards extreme-intensity attosecond pulses. *Physical Review E*, 84:046403, Oct 2011.

[237] D. an der Brügge and A. Pukhov. Enhanced relativistic harmonics by electron nanobunching. *Physics of Plasmas*, 17(3):033110, 03 2010.

[238] J. M. Mikhailova, M. V. Fedorov, N. Karpowicz, P. Gibbon, V. T. Platonenko, A. M. Zheltikov, and F. Krausz. Isolated attosecond pulses from laser-driven synchrotron radiation. *Physical Review Letters*, 109:245005, Dec 2012.

[239] B. Dromey, S. Rykovanov, M. Yeung, R. Hörlein, D. Jung, D. C. Gautier, T. Dzelzainis, D. Kiefer, S. Palaniyppan, R. Shah, J. Schreiber, H. Ruhl, J. C. Fernandez, C. L. S. Lewis, M. Zepf, and B. M. Hegelich. Coherent synchrotron emission from electron nanobunches formed in relativistic laser–plasma interactions. *Nature Physics*, 8(11):804–808, Nov 2012.

[240] M. R. Edwards and J. M. Mikhailova. The x-ray emission effectiveness of plasma mirrors: Re-examining power-law scaling for relativistic high-order harmonic generation. *Scientific Reports*, 10(1), 3 2020.

[241] R. Capdessus, E. d’Humières, and V. T. Tikhonchuk. Modeling of radiation losses in ultrahigh power laser-matter interaction. *Physical Review E*, 86:036401, Sep 2012.

[242] S. Tang, N. Kumar, and C. H. Keitel. Plasma high-order-harmonic generation from ultraintense laser pulses. *Physical Review E*, 95:051201, May 2017.

[243] J. P. Geindre, P. Audebert, and R. S. Marjoribanks. Relativistic ac gyromagnetic effects in ultraintense laser-matter interaction. *Physical Review Letters*, 97:085001, Aug 2006.

[244] C. Rödel, D. an der Brügge, J. Bierbach, M. Yeung, T. Hahn, B. Dromey, S. Herzer, S. Fuchs, A. Galestian Pour, E. Eckner, M. Behmke, M. Cerchez, O. Jäckel, D. Hemmers, T. Toncian, M. C. Kaluza, A. Belyanin, G. Pretzler, O. Willi, A. Pukhov, M. Zepf, and G. G. Paulus. Harmonic generation from relativistic plasma surfaces in ultrasteep plasma density gradients. *Physical Review Letters*, 109:125002, Sep 2012.

[245] L. Chopineau, A. Denoeud, A. Leblanc, E. Porat, P. Martin, H. Vincenti, and F. Quéré. Spatio-temporal characterization of attosecond pulses from plasma mirrors. *Nature Physics*, 17(8):968–973, Aug 2021.

[246] G. D. Tsakiris, K. Eidmann, J. Meyer ter Vehn, and F. Krausz. Route to intense single attosecond pulses. *New Journal of Physics*, 8(1):19, Jan 2006.

[247] B. Dromey, D. Adams, R. Hörlein, Y. Nomura, S. G. Rykovanov, D. C. Carroll, P. S. Foster, S. Kar, K. Markey, P. McKenna, D. Neely, M. Geissler, G. D. Tsakiris, and M. Zepf. Diffraction-limited performance and focusing of high harmonics from relativistic plasmas. *Nature Physics*, 5(2):146–152, Feb 2009.

[248] M. Bocoum, M. Thévenet, F. Böhle, B. Beaurepaire, A. Vernier, A. Jullien, J. Faure, and R. Lopez-Martens. Anticorrelated emission of high harmonics and fast electron beams from plasma mirrors. *Physical Review Letters*, 116:185001, May 2016.

[249] Z.-M. Sheng, K. Mima, Y. Sentoku, M. S. Jovanović, T. Taguchi, J. Zhang, and J. Meyer-ter Vehn. Stochastic heating and acceleration of electrons in colliding laser fields in plasma. *Physical Review Letters*, 88:055004, Jan 2002.

[250] J. T. Mendonça and F. Doveil. Stochasticity in plasmas with electromagnetic waves. *Journal of Plasma Physics*, 28(3):485–493, 1982.

[251] C. Zhou, Y. Bai, L. Song, Y. Zeng, Y. Xu, D. Zhang, X. Lu, Y. Leng, J. Liu, Y. Tian, R. Li, and Z. Xu. Direct mapping of attosecond electron dynamics. *Nature Photonics*, 15(3):216–221, Mar 2021.

[252] E. Esarey, P. Sprangle, and J. Krall. Laser acceleration of electrons in vacuum. *Physical Review E*, 52:5443–5453, Nov 1995.

[253] F. V. Hartemann, S. N. Fochs, G. P. Le Sage, N. C. Luhmann, J. G. Woodworth, M. D. Perry, Y. J. Chen, and A. K. Kerman. Nonlinear ponderomotive scattering of relativistic electrons by an intense laser field at focus. *Physical Review E*, 51:4833–4843, May 1995.

[254] L. Chopineau, A. Leblanc, G. Blaclard, A. Denoeud, M. Thévenet, J-L. Vay, G. Bonnaud, Ph. Martin, H. Vincenti, and F. Quéré. Identification of coupling mechanisms between ultraintense laser light and dense plasmas. *Physical Review X*, 9:011050, Mar 2019.

[255] N. Zaïm, F. Böhle, M. Bocoum, A. Vernier, S. Haessler, X. Davoine, L. Videau, J. Faure, and R. Lopez-Martens. Few-cycle laser wakefield acceleration on solid targets with controlled plasma scale length. *Physics of Plasmas*, 26(3):033112, 03 2019.

[256] Wei Yu, M. Y. Yu, J. X. Ma, Z. M. Sheng, J. Zhang, H. Daido, S. B. Liu, Z. Z. Xu, and R. X. Li. Ponderomotive acceleration of electrons at the focus of high intensity lasers. *Physical Review E*, 61:R2220–R2223, Mar 2000.

[257] I. Y. Dodin and N. J. Fisch. Relativistic electron acceleration in focused laser fields after above-threshold ionization. *Physical Review E*, 68:056402, Nov 2003.

[258] G. V. Stupakov and M. S. Zolotorev. Ponderomotive laser acceleration and focusing in vacuum for generation of attosecond electron bunches. *Physical Review Letters*, 86:5274–5277, Jun 2001.

[259] Y. I. Salamin and C. H. Keitel. Electron acceleration by a tightly focused laser beam. *Physical Review Letters*, 88:095005, Feb 2002.

[260] J. Pang, Y. K. Ho, X. Q. Yuan, N. Cao, Q. Kong, P. X. Wang, L. Shao, E. H. Esarey, and A. M. Sessler. Subluminous phase velocity of a focused laser beam and vacuum laser acceleration. *Physical Review E*, 66:066501, Dec 2002.

[261] A. Maltsev and T. Ditmire. Above threshold ionization in tightly focused, strongly relativistic laser fields. *Physical Review Letters*, 90:053002, Feb 2003.

[262] G. Malka, E. Lefebvre, and J. L. Miquel. Experimental observation of electrons accelerated in vacuum to relativistic energies by a high-intensity laser. *Physical Review Letters*, 78:3314–3317, Apr 1997.

[263] S. J. McNaught, J. P. Knauer, and D. D. Meyerhofer. Photoelectron initial conditions for tunneling ionization in a linearly polarized laser. *Physical Review A*, 58:1399–1411, Aug 1998.

[264] C. I. Moore, A. Ting, S. J. McNaught, J. Qiu, H. R. Burris, and P. Sprangle. A laser-accelerator injector based on laser ionization and ponderomotive acceleration of electrons. *Physical Review Letters*, 82:1688–1691, Feb 1999.

[265] S. Payeur, S. Fourmaux, B. E. Schmidt, J. P. MacLean, C. Tchervenkov, F. Légaré, M. Piché, and J. C. Kieffer. Generation of a beam of fast electrons by tightly focusing a radially polarized ultrashort laser pulse. *Applied Physics Letters*, 101(4):041105, 07 2012.

[266] S. Carbajo, E/ A. Nanni, L. J. Wong, G. Moriena, P. D. Keathley, G. Laurent, R. J. D. Miller, and F. X. Kärtner. Direct longitudinal laser acceleration of electrons in free space. *Physical Review Accelerators and Beams*, 19:021303, Feb 2016.

[267] M. Thévenet, A. Leblanc, S. Kahaly, H. Vincenti, A. Vernier, F. Quéré, and J. Faure. Vacuum laser acceleration of relativistic electrons using plasma mirror injectors. *Nature Physics*, 12(4):355–360, Apr 2016.

[268] M. Thévenet, H. Vincenti, and J. Faure. On the physics of electron ejection from laser-irradiated overdense plasmas. *Physics of Plasmas*, 23(6):063119, 06 2016.

[269] M. Thévenet. *Modeling the interaction between a few-cycle relativistic laser pulse and a plasma mirror : from electron acceleration to harmonic generation*. Theses, Université Paris Saclay (COmUE), December 2016.

[270] N. Zaïm, M. Thévenet, A. Lifschitz, and J. Faure. Relativistic acceleration of electrons injected by a plasma mirror into a radially polarized laser beam. *Physical Review Letters*, 119:094801, Aug 2017.

[271] N. Zaïm, D. Guénot, L. Chopineau, A. Denoeud, O. Lundh, H. Vincenti, F. Quéré, and J. Faure. Interaction of ultraintense radially-polarized laser pulses with plasma mirrors. *Physical Review X*, 10:041064, Dec 2020.

[272] W. Lu, M. Tzoufras, C. Joshi, F. S. Tsung, W. B. Mori, J. Vieira, R. A. Fonseca, and L. O. Silva. Generating multi-gev electron bunches using single stage laser wakefield acceleration in a 3d nonlinear regime. *Physical Review Special Topics Accelerators and Beams*, 10:061301, Jun 2007.

[273] E. Esarey, C. B. Schroeder, and W. P. Leemans. Physics of laser-driven plasma-based electron accelerators. *Reviews of Modern Physics*, 81:1229–1285, Aug 2009.

[274] A. Macchi, M. Borghesi, and M. Passoni. Ion acceleration by superintense laser-plasma interaction. *Reviews of Modern Physics*, 85:751–793, May 2013.

[275] M. Kaluza, J. Schreiber, M. I. K. Santala, G. D. Tsakiris, K. Eidmann, J. Meyer-ter Vehn, and K. J. Witte. Influence of the laser prepulse on proton acceleration in thin-foil experiments. *Physical Review Letters*, 93:045003, Jul 2004.

[276] S. C. Wilks, A. B. Langdon, T. E. Cowan, M. Roth, M. Singh, S. Hatchett, M. H. Key, D. Pennington, A. MacKinnon, and R. A. Snavely. Energetic proton generation in ultra-intense laser–solid interactions. *Physics of Plasmas*, 8(2):542–549, 02 2001.

[277] A. Macchi, F. Cattani, T. V. Liseykina, and F. Cornolti. Laser acceleration of ion bunches at the front surface of overdense plasmas. *Physical Review Letters*, 94:165003, Apr 2005.

[278] T. Schlegel, N. Naumova, V. T. Tikhonchuk, C. Labaune, I. V. Sokolov, and G. Mourou. Relativistic laser piston model: Ponderomotive ion acceleration in dense plasmas using ultraintense laser pulses. *Physics of Plasmas*, 16(8):083103, 08 2009.

[279] J. Denavit. Absorption of high-intensity subpicosecond lasers on solid density targets. *Physical Review Letters*, 69:3052–3055, Nov 1992.

[280] L. O. Silva, M. Marti, J. R. Davies, R. A. Fonseca, C. Ren, F. S. Tsung, and W. B. Mori. Proton shock acceleration in laser-plasma interactions. *Physical Review Letters*, 92:015002, Jan 2004.

[281] F. Fiuza, R. A. Fonseca, J. Tonge, W. B. Mori, and L. O. Silva. Weibel-instability-mediated collisionless shocks in the laboratory with ultraintense lasers. *Physical Review Letters*, 108:235004, Jun 2012.

[282] D. Haberberger, S. Tochitsky, F. Fiuza, C. Gong, R. A. Fonseca, L. O. Silva, W. B. Mori, and C. Joshi. Collisionless shocks in laser-produced plasma generate monoenergetic high-energy proton beams. *Nature Physics*, 8(1):95–99, Jan 2012.

[283] T. Esirkepov, M. Borghesi, S. V. Bulanov, G. Mourou, and T. Tajima. Highly efficient relativistic-ion generation in the laser-piston regime. *Physical Review Letters*, 92:175003, Apr 2004.

[284] A. P. L. Robinson, M. Zepf, S. Kar, R. G. Evans, and C. Bellei. Radiation pressure acceleration of thin foils with circularly polarized laser pulses. *New Journal of Physics*, 10(1):013021, Jan 2008.

[285] O. Klimo, J. Psikal, J. Limpouch, and V. T. Tikhonchuk. Monoenergetic ion beams from ultrathin foils irradiated by ultrahigh-contrast circularly polarized laser pulses. *Physical Review Accelerators and Beams*, 11:031301, Mar 2008.

[286] S. Macchi, A.and Veghini and F. Pegoraro. “light sail” acceleration reexamined. *Physical Review Letters*, 103:085003, Aug 2009.

[287] E. d’Humières, E. Lefebvre, L. Gremillet, and V. Malka. Proton acceleration mechanisms in high-intensity laser interaction with thin foils. *Physics of Plasmas*, 12(6):062704, 06 2005.

[288] T. Esirkepov, M. Yamagiwa, and T. Tajima. Laser ion-acceleration scaling laws seen in multiparametric particle-in-cell simulations. *Physical Review Letters*, 96:105001, Mar 2006.

[289] L. Yin, B. J. Albright, B. M. Hegelich, K. J. Bowers, K. A. Flippo, T. J. T. Kwan, and J. C. Fernández. Monoenergetic and GeV ion acceleration from the laser breakout afterburner using ultrathin targetsa). *Physics of Plasmas*, 14(5):056706, 04 2007.

[290] L. Yin, B. J. Albright, K. J. Bowers, D. Jung, J. C. Fernández, and B. M. Hegelich. Three-dimensional dynamics of breakout afterburner ion acceleration using high-contrast short-pulse laser and nanoscale targets. *Physical Review Letters*, 107:045003, Jul 2011.

[291] Y. Fukuda, A. Ya. Faenov, M. Tampo, T. A. Pikuz, T. Nakamura, M. Kando, Y. Hayashi, A. Yogo, H. Sakaki, T. Kameshima, A. S. Pirozhkov, K. Ogura, M. Mori, T. Zh. Esirkepov, J. Koga, A. S. Boldarev, V. A. Gasilov, A. I. Magunov, T. Yamauchi, R. Kodama, P. R. Bolton, Y. Kato, T. Tajima, H. Daido, and S. V. Bulanov. Energy increase in multi-mev ion acceleration in the interaction of a short pulse laser with a cluster-gas target. *Physical Review Letters*, 103:165002, Oct 2009.

[292] T. Nakamura, S. V. Bulanov, T. Zh. Esirkepov, and M. Kando. High-energy ions from near-critical density plasmas via magnetic vortex acceleration. *Physical Review Letters*, 105:135002, Sep 2010.

[293] A. Macchi. A Review of Laser-Plasma Ion Acceleration. 12 2017.

[294] S. P. Hatchett, C. G. Brown, T. E. Cowan, E. A. Henry, J. S. Johnson, M. H. Key, J. A. Koch, A. B. Langdon, B. F. Lasinski, R. W. Lee, A. J. Mackinnon, D. M. Pennington, M. D. Perry, T. W. Phillips, M. Roth, T. C. Sangster, M. S. Singh, R. A. Snavely, M. A. Stoyer, S. C. Wilks, and K. Yasuike. Electron, photon, and ion beams from the relativistic interaction of Petawatt laser pulses with solid targets. *Physics of Plasmas*, 7(5):2076–2082, 05 2000.

[295] D. Bauer and P. Mulser. Exact field ionization rates in the barrier-suppression regime from numerical time-dependent schrödinger-equation calculations. *Physical Review A*, 59:569–577, Jan 1999.

[296] M. Passoni, V. T. Tikhonchuk, M. Lontano, and V. Yu. Bychenkov. Charge separation effects in solid targets and ion acceleration with a two-temperature electron distribution. *Physical Review E*, 69:026411, Feb 2004.

[297] R. A. Snavely, M. H. Key, S. P. Hatchett, T. E. Cowan, M. Roth, T. W. Phillips, M. A. Stoyer, E. A. Henry, T. C. Sangster, M. S. Singh, S. C. Wilks, A. MacKinnon, A. Offenberger, D. M. Pennington, K. Yasuike, A. B. Langdon, B. F. Lasinski, J. Johnson, M. D. Perry, and E. M. Campbell. Intense high-energy proton beams from petawatt-laser irradiation of solids. *Physical Review Letters*, 85:2945–2948, Oct 2000.

[298] T. E. Cowan, J. Fuchs, H. Ruhl, A. Kemp, P. Audebert, M. Roth, R. Stephens, I. Barton, A. Blazevic, E. Brambrink, J. Cobble, J. Fernández, J.-C. Gauthier, M. Geissel, M. Hegelich, J. Kaae, S. Karsch, G. P. Le Sage, S. Letzring, M. Manclossi, S. Meyroneinc, A. Newkirk, H. Pépin, and N. Renard-LeGalloudec. Ultralow emittance, multi-mev proton beams from a laser virtual-cathode plasma accelerator. *Physical Review Letters*, 92:204801, May 2004.

[299] E. Brambrink, J. Schreiber, T. Schlegel, P. Audebert, J. Cobble, J. Fuchs, M. Hegelich, and M. Roth. Transverse characteristics of short-pulse laser-produced ion beams: A study of the acceleration dynamics. *Physical Review Letters*, 96:154801, Apr 2006.

[300] F. Wagner, O. Deppert, C. Brabetz, P. Fiala, A. Kleinschmidt, P. Poth, V. A. Schanz, A. Tebartz, B. Zielbauer, M. Roth, T. Stöhlker, and V. Bagnoud. Maximum proton energy above 85 mev from the relativistic interaction of laser pulses with micrometer thick ch_2 targets. *Physical Review Letters*, 116:205002, May 2016.

[301] T. Ceccotti, A. Lévy, H. Popescu, F. Réau, P. D'Oliveira, P. Monot, J. P. Geindre, E. Lefebvre, and Ph. Martin. Proton acceleration with high-intensity ultrahigh-contrast laser pulses. *Physical Review Letters*, 99:185002, Oct 2007.

[302] A. Borot, D. Douillet, G. Iaquaniello, T. Lefrou, P. Audebert, J.-P. Geindre, and R. Lopez-Martens. High repetition rate plasma mirror device for attosecond science. *Review of Scientific Instruments*, 85(1):013104, 2014.

[303] A. Borot, D. Douillet, G. Iaquaniello, T. Lefrou, P. Audebert, J.-P. Geindre, and R. Lopez-Martens. High repetition rate plasma mirror device for attosecond science. *Review of Scientific Instruments*, 85(1):013104, 01 2014.

[304] L. Li, J. C. P. Koliyadu, H. Donnelly, D. Alj, Delmas O, M. Ruiz-Lopez, O. de La Rochefoucauld, G. Dovillaire, M. Fajardo, C. Zhou, S. Ruan, B. Dromey, M. Zepf, and P. Zeitoun. High numerical aperture hartmann wave front sensor for extreme ultraviolet spectral range. *Optics Letters*, 45(15):4248–4251, Aug 2020.

[305] Lu Li. *Metrology of High Harmonics Seeded Soft X-ray Laser Based on Solid-Plasma Amplifier*. Theses, Ecole Polytechnique, November 2014.

[306] Y. Glinec, J. Faure, A. Guemnie-Tafo, V. Malka, H. Monard, J. P. Larbre, V. De Waele, J. L. Marignier, and M. Mostafavi. Absolute calibration for a broad range single shot electron spectrometer. *Review of Scientific Instruments*, 77(10):103301, 2006.

[307] R. Morlotti, M. Nikl, M. Piazza, and C. Boragno. Intrinsic conversion efficiency of X-rays to light in Gd2O2S : Tb3+ powder phosphors. *Journal of Luminescence*, 72-74:772–774, 1997.

[308] Sir J.J. Thomson. Xxvi. rays of positive electricity. *The London, Edinburgh, and Dublin Philosophical Magazine and Journal of Science*, 21(122):225–249, 1911.

[309] P.R. Bolton, M. Borghesi, C. Brenner, D.C. Carroll, C. De Martinis, F. Fiorini, A. Flacco, V. Floquet, J. Fuchs, P. Gallegos, D. Giove, J.S. Green, S. Green, B. Jones, D. Kirby, P. McKenna, D. Neely, F. Nuesslin, R. Prasad, S. Reinhardt, M. Roth, U. Schramm, G.G. Scott, S. Ter-Avetisyan, M. Tolley, G. Turchetti, and J.J. Wilkens. Instrumentation for diagnostics and control of laser-accelerated proton (ion) beams. *Physica Medica*, 30(3):255–270, 2014.

[310] J. P. Geindre, P. Audebert, A. Rousse, F. Falliès, J. C. Gauthier, A. Mysyrowicz, A. Dos Santos, G. Hamoniaux, and A. Antonetti. Frequency-domain interferometer for measuring the phase and amplitude of a femtosecond pulse probing a laser-produced plasma. *Optics Letters*, 19(23):1997–1999, Dec 1994.

[311] R. Evans, A. D. Badger, F. Falliès, M. Mahdieh, T. A. Hall, P. Audebert, J.-P. Geindre, J.-C. Gauthier, A. Mysyrowicz, G. Grillon, and A. Antonetti. Time- and space-resolved optical probing of femtosecond-laser-driven shock waves in aluminum. *Physical Review Letters*, 77:3359–3362, Oct 1996.

[312] C. Quoix, G. Hamoniaux, A. Antonetti, J.-C. Gauthier, J.-P. Geindre, and P. Audebert. Ultrafast plasma studies by phase and amplitude measurements with femtosecond spectral interferometry. *Journal of Quantitative Spectroscopy and Radiative Transfer*, 65(1):455–462, 2000.

[313] P. Audebert, J.-P. Geindre, S. Rebibo, and J.-C. Gauthier. Direct observation of the ponderomotive force effects in short-scale-length laser plasmas by frequency-domain interferometry. *Physical Review E*, 64:056412, Oct 2001.

[314] J.-P. Geindre, P. Audebert, S. Rebibo, and J.-C. Gauthier. Single-shot spectral interferometry with chirped pulses. *Optics Letters*, 26(20):1612–1614, Oct 2001.

[315] K. Adumi, K. A. Tanaka, T. Matsuoka, T. Kurahashi, T. Yabuuchi, Y. Kitagawa, R. Kodama, K. Sawai, K. Suzuki, K. Okabe, T. Sera, T. Norimatsu, and Y. Izawa. Characterization of preplasma produced by an ultrahigh intensity laser system. *Physics of Plasmas*, 11(8):3721–3725, 08 2004.

[316] M. Bocoum, F. Böhle, A. Vernier, A. Jullien, J. Faure, and R. Lopez-Martens. Spatial-domain interferometer for measuring plasma mirror expansion. *Optics Letters*, 40(13):3009–3012, 2015.

[317] M. Bocoum. *Harmonic and electron generation from laser-driven plasma mirrors.* PhD thesis, Université Paris-Saclay (ComUE), 2016. Thèse de doctorat dirigée par Lopez-Martens, Rodrigo Physique des plasmas Université Paris-Saclay (ComUE) 2016.

[318] J. Gao, B. Li, F. Liu, H. Cai, M. Chen, X. Yuan, X. Ge, L. Chen, Z. Sheng, and J. Zhang. Double optimal density gradients for harmonic generation from relativistically oscillating plasma surfaces. *Physics of Plasmas*, 26(10):103102, 10 2019.

[319] J.-L. Vay, A. Huebl, A. Almgren, L. D. Amorim, J. Bell, L. Fedeli, L. Ge, K. Gott, D. P. Grote, M. Hogan, R. Jambunathan, R. Lehe, A. Myers, C. Ng, M. Rowan, O. Shapoval, M. Thévenet, H. Vincenti, E. Yang, N. Zaïm, W. Zhang, Y. Zhao, and E. Zoni. Modeling of a chain of three plasma accelerator stages with the WarpX electromagnetic PIC code on GPUs. *Physics of Plasmas*, 28(2):023105, February 2021.

[320] E. d'Humières, A. Brantov, V. Yu. Bychenkov, and V. T. Tikhonchuk. Optimization of laser-target interaction for proton acceleration. *Physics of Plasmas*, 20(2):023103, 02 2013.

[321] P. M. Paul, E. S. Toma, P. Breger, G. Mullot, F. Augé, Ph. Balcou, H. G. Muller, and P. Agostini. Observation of a train of attosecond pulses from high harmonic generation. *Science*, 292(5522):1689–1692, 2001.

[322] M. Drescher, M. Hentschel, R. Kienberger, M. Uiberacker, V. Yakovlev, A. Scrinzi, Th. Westerwalbesloh, U. Kleineberg, U. Heinzmann, and F. Krausz. Time-resolved atomic inner-shell spectroscopy. *Nature*, 419(6909):803–807, Oct 2002.

[323] M. Uiberacker, Th. Uphues, M. Schultze, A. J. Verhoef, V. Yakovlev, M. F. Kling, J. Rauschenberger, N. M. Kabachnik, H. Schröder, M. Lezius, K. L. Kompa, H.-G. Muller, M. J. J. Vrakking, S. Hendel, U. Kleineberg, U. Heinzmann, M. Drescher, and F. Krausz. Attosecond real-time observation of electron tunnelling in atoms. *Nature*, 446(7136):627–632, Apr 2007.

[324] M. Schultze, M. Fieß, N. Karpowicz, J. Gagnon, M. Korbman, M. Hofstetter, S. Neppl, A. L. Cavalieri, Y. Komninos, Th. Mercouris, C. A. Nicolaides, R. Pazourek, S. Nagele, J. Feist, J. Burgdörfer, A. M. Azzeer, R. Ernstorfer, R. Kienberger, U. Kleineberg, E. Goulielmakis, F. Krausz, and V. S. Yakovlev. Delay in photoemission. *Science*, 328(5986):1658–1662, 2010.

[325] F. Calegari, D. Ayuso, A. Trabattoni, L. Belshaw, S. De Camillis, S. Anumula, F. Frassetto, L. Poletto, A. Palacios, P. Decleva, J. B. Greenwood, F. Martín, and M. Nisoli. Ultrafast electron dynamics in phenylalanine initiated by attosecond pulses. *Science*, 346(6207):336–339, 2014.

[326] E. Goulielmakis, M. Schultze, M. Hofstetter, V. S. Yakovlev, J. Gagnon, M. Uiberacker, A. L. Aquila, E. M. Gullikson, D. T. Attwood, R. Kienberger, F. Krausz, and U. Kleineberg. Single-cycle nonlinear optics. *Science*, 320(5883):1614–1617, 2008.

[327] E. J. Takahashi, P. Lan, O. D. Mücke, Y. Nabekawa, and K. Midorikawa. Attosecond nonlinear optics using gigawatt-scale isolated attosecond pulses. *Nature Communications*, 4(1):2691, Oct 2013.

[328] A. Nayak, I. Orfanos, I. Makos, M. Dumergue, S. Kühn, E. Skantzakis, B. Bodi, K. Varju, C. Kalpouzos, H. I. B. Banks, A. Emmanouilidou, D. Charalambidis, and P. Tzallas. Multiple ionization of argon via multi-xuv-photon absorption induced by 20-gw high-order harmonic laser pulses. *Physical Review A*, 98:023426, Aug 2018.

[329] B. Bergues, D. E. Rivas, M. Weidman, A. A. Muschet, W. Helml, A. Guggenmos, V. Pervak, U. Kleineberg, G. Marcus, R. Kienberger, D. Charalambidis, P. Tzallas, H. Schröder, F. Krausz, and L. Veisz. Tabletop nonlinear optics in the 100-ev spectral region. *Optica*, 5(3):237–242, Mar 2018.

[330] D. Popmintchev, B. R. Galloway, M.-C. Chen, F. Dollar, C. A. Mancuso, A. Hankla, L. Miaja-Avila, G. O'Neil, J. M. Shaw, G. Fan, S. Ališauskas, G. Andriukaitis, T. Balčiunas, O. D. Mücke, A. Pugzlys, A. Baltuška, H. C. Kapteyn, T. Popmintchev, and M. M. Murnane. Near- and extended-edge x-ray-absorption fine-structure spectroscopy using ultrafast coherent high-order harmonic supercontinua. *Physical Review Letters*, 120:093002, Mar 2018.

[331] P. Heissler, R. Hörlein, J. M. Mikhailova, L. Waldecker, P. Tzallas, A. Buck, K. Schmid, C. M. S. Sears, F. Krausz, L. Veisz, M. Zepf, and G. D. Tsakiris. Few-cycle driven relativistically oscillating plasma mirrors: A source of intense isolated attosecond pulses. *Physical Review Letters*, 108:235003, Jun 2012.

[332] A. Leblanc, S. Monchocé, H. Vincenti, S. Kahaly, J.-L. Vay, and F. Quéré. Spatial properties of high-order harmonic beams from plasma mirrors: A ptychographic study. *Physical Review Letters*, 119:155001, Oct 2017.

[333] A. L. Cavalieri, N. Müller, Th. Uphues, V. S. Yakovlev, A. Baltuška, B. Horvath, B. Schmidt, L. Blümel, R. Holzwarth, S. Hendel, M. Drescher, U. Kleineberg, P. M. Echenique, R. Kienberger, F. Krausz, and U. Heinzmann. Attosecond spectroscopy in condensed matter. *Nature*, 449(7165):1029–1032, Oct 2007.

[334] E. Goulielmakis, Z.-H. Loh, A. Wirth, R. Santra, N. Rohringer, V. S. Yakovlev, S. Zherebtsov, T. Pfeifer, A. M. Azzeer, M. F. Kling, S. R. Leone, and F. Krausz. Real-time observation of valence electron motion. *Nature*, 466(7307):739–743, Aug 2010.

[335] H. Vincenti and F. Quéré. Attosecond lighthouses: How to use spatiotemporally coupled light fields to generate isolated attosecond pulses. *Physical Review Letters*, 108:113904, Mar 2012.

[336] J. A. Wheeler, A. Borot, S. Monchocé, H. Vincenti, A. Ricci, A. Malvache, R. Lopez-Martens, and F. Quéré. Attosecond lighthouses from plasma mirrors. *Nature Photonics*, 6(12):829–833, Dec 2012.

[337] T. Baeva, S. Gordienko, and A. Pukhov. Relativistic plasma control for single attosecond x-ray burst generation. *Physical Review E*, 74:065401, Dec 2006.

[338] S. G. Rykovanov, M. Geissler, J. Meyer ter Vehn, and G. D. Tsakiris. Intense single attosecond pulses from surface harmonics using the polarization gating technique. *New Journal of Physics*, 10(2):025025, Feb 2008.

[339] M. Yeung, J. Bierbach, E. Eckner, S. Rykovanov, S. Kuschel, A. Sävert, M. Förster, C. Rödel, G. G. Paulus, S. Cousens, M. Coughlan, B. Dromey, and M. Zepf. Noncollinear polarization gating of attosecond pulse trains in the relativistic regime. *Physical Review Letters*, 115:193903, Nov 2015.

[340] C. M. Heyl, S. N. Bengtsson, S. Carlström, J. Mauritsson, C. L. Arnold, and A. L'Huillier. Noncollinear optical gating. *New Journal of Physics*, 16(5):052001, May 2014.

[341] R. Hörlein, S. G. Rykovanov, B. Dromey, Y. Nomura, D. Adams, M. Geissler, M. Zepf, F. Krausz, and G. D. Tsakiris. Controlling the divergence of high harmonics from solid targets: a route toward coherent harmonic focusing. *The European Physical Journal D*, 55(2):475–481, Nov 2009.

[342] J. P. Kennedy, B. Dromey, and M. Yeung. Isolated ultra-bright attosecond pulses via noncollinear gating. *New Journal of Physics*, 24(11):113004, Nov 2022.

[343] D. E. Rivas, A. Borot, D. E. Cardenas, G. Marcus, X. Gu, D. Herrmann, J. Xu, J. Tan, D. Kormin, G. Ma, W. Dallari, G. D. Tsakiris, I. B. Földes, S.-w. Chou, M. Weidman, B. Bergues, T. Wittmann, H. Schröder, P. Tzallas, D. Charalambidis, O. Razskazovskaya, V. Pervak, F. Krausz, and L. Veisz. Next generation driver for attosecond and laser-plasma physics. *Scientific Reports*, 7(1):5224, Jul 2017.

[344] A. Kessel, V. E. L., O. Jahn, M. Krüger, A. Münzer, A. Schwarz, V. Pervak, M. Trubetskov, S. A. Trushin, F. Krausz, Z. Major, and S. Karsch. Relativistic few-cycle pulses with high contrast from picosecond-pumped opcpa. *Optica*, 5(4):434–442, Apr 2018.

[345] A. Borot, A. Malvache, X. Chen, A. Jullien, J.-P. Geindre, P. Audebert, G. Mourou, F. Quéré, and R. Lopez-Martens. Attosecond control of collective electron motion in plasmas. *Nature Physics*, 8(5):416–421, May 2012.

[346] A. Gonoskov. Theory of relativistic radiation reflection from plasmas. *Physics of Plasmas*, 25(1):013108, 01 2018.

[347] M. Thévenet, H. Vincenti, and J. Faure. On the physics of electron ejection from laser-irradiated overdense plasmas. *Physics of Plasmas*, 23(6):063119, 06 2016.

[348] M. Hanna, X. Délen, L. Lavenu, F. Guichard, Y. Zaouter, F. Druon, and P. Georges. Nonlinear temporal compression in multipass cells: theory. *Journal of the Optical Society of America B*, 34(7):1340–1347, Jul 2017.

[349] J. Kaur, M. Ouillé, D. Levy, L. Daniault, A. Robbes, N. Zaïm, A. Flacco, E. Kroupp, V. Malka, S. Haessler, and R. Lopez-Martens. High repetition rate relativistic laser–solid–plasma interaction platform featuring simultaneous particle and radiation detection. *Review of Scientific Instruments*, 94(11):113002, 11 2023.

[350] S. Haessler, M. Ouillé, J. Kaur, M. Bocoum, F. Böhle, D. Levy, L. Daniault, A. Vernier, J. Faure, and R. Lopez-Martens. High-harmonic generation and correlated electron emission from relativistic plasma mirrors at 1 khz repetition rate. *Ultrafast Science*, 2022(9893418), 2022.

[351] A. Lorusso, F. Belloni, D. Doria, V. Nassisi, J. Wolowski, J. Badziak, P. Parys, J. Krása, L. Láska, F.P. Boody, L. Torrisi, A. Mezzasalma, A. Picciotto, S. Gammino, L. Calcagnile, G. Quarta, and D. Bleiner. Modification of materials by high energy plasma ions. *Nuclear Instruments and Methods in Physics Research Section B: Beam Interactions with Materials and Atoms*, 240(1):229–233, 2005. Accelerators in Applied Research and Technology.

[352] L. Torrisi, M. Cutroneo, A. Mackova, V. Lavrentiev, M. Pfeifer, and E. Krousky. An unconventional ion implantation method for producing au and si nanostructures using intense laser-generated plasmas. *Plasma Physics and Controlled Fusion*, 58(2):025011, jan 2016.

[353] S. Fritzler, V. Malka, G. Grillon, J. P. Rousseau, F. Burgy, E. Lefebvre, E. d'Humières, P. McKenna, and K. W. D. Ledingham. Proton beams generated with high-intensity lasers: Applications to medical isotope production. *Applied Physics Letters*, 83(15):3039–3041, 10 2003.

[354] D. Levy, I. A. Andriyash, S. Haessler, J. Kaur, M. Ouillé, A. Flacco, E. Kroupp, V. Malka, and R. Lopez-Martens. Low divergence proton beams from a laser-plasma accelerator at khz repetition rate. *Physical Review Accelerators and Beams*, 25:093402, Sep 2022.

[355] S. Kühn, M. Dumergue, S. Kahaly, S. Mondal, M. Füle, T. Csizmadia, B. Farkas, B. Major, Z. Várallyay, E. Cormier, M. Kalashnikov, F. Calegari, M. Devetta, F. Frassetto, E. Månsson, L. Poletto, S. Stagira, C. Vozzi, M. Nisoli, P. Rudawski, S. Maclot, F. Campi, H. Wikmark, C. L. Arnold, C. M. Heyl, P. Johnsson, A. L'Huillier, R. Lopez-Martens, S. Haessler, M. Bocoum, F. Boehle, A. Vernier, G. Iaquaniello, E. Skantzakis, N. Papadakis, C. Kalpouzos, P. Tzallas, F. Lépine, D. Charalambidis, K. Varjú, K. Osvay, and G. Sansone. The eli-alps facility: the next generation of attosecond sources. *Journal of Physics B: Atomic, Molecular and Optical Physics*, 50(13):132002, jun 2017.

[356] V. Ginzburg, I. Yakovlev, A. Kochetkov, A. Kuzmin, S. Mironov, I. Shaikin, A. Shaykin, and E. Khazanov. 11 fs, 1.5 pw laser with nonlinear pulse compression. *Opt. Express*, 29(18):28297–28306, Aug 2021.

[357] K. M. George, J. T. Morrison, S. Feister, G. K. Ngirmang, J. R. Smith, A. J. Klim, J. Snyder, D. Austin, W. Erbsen, K. D. Frische, and et al. High-repetition-rate ($\geqslant$ khz) targets and optics from liquid microjets for high-intensity laser–plasma interactions. *High Power Laser Science and Engineering*, 7:e50, 2019.

[358] J. T. Morrison, S. Feister, K. D. Frische, D. R. Austin, G. K. Ngirmang, N. R. Murphy, C. Orban, E. A. Chowdhury, and W. M. Roquemore. Mev proton acceleration at khz repetition rate from ultra-intense laser liquid interaction. *New Journal of Physics*, 20(2):022001, Feb 2018.

[359] P. Puyuelo-Valdes, D. de Luis, J. Hernandez, J. I. Apiñaniz, A. Curcio, J. L. Henares, M. Huault, J. A. Pérez-Hernández, L. Roso, G. Gatti, and L. Volpe. Implementation of a thin, flat water target capable of high-repetition-rate mev-range proton acceleration in a high-power laser at the clpu. *Plasma Physics and Controlled Fusion*, 64(5):054003, Mar 2022.

[360] S. Feister, D. R. Austin, J. T. Morrison, K. D. Frische, C. Orban, G. Ngirmang, A. Handler, J. R. H. Smith, M. Schillaci, J. A. LaVerne, E. A. Chowdhury, R. R. Freeman, and W. M. Roquemore. Relativistic electron acceleration by mj-class khz lasers normally incident on liquid targets. *Optics Express*, 25(16):18736–18750, Aug 2017.

[361] S. Backus, H. C. Kapteyn, M. M. Murnane, D. M. Gold, H. Nathel, and W. White. Prepulse suppression for high-energy ultrashort pulses using self-induced plasma shuttering from a fluid target. *Optics Letters*, 18(2):134–136, Jan 1993.

[362] Y. H. Kim, H. Kim, S. C. Park, Y. Kwon, K. Yeom, W. Cho, T. Kwon, H. Yun, J. H. Sung, S. K. Lee, T. T. Luu, C. H. Nam, and K. T. Kim. High-harmonic generation from a flat liquid-sheet plasma mirror. *Nature Communications*, 14(1):2328, Apr 2023.

[363] J. Schwinger. On gauge invariance and vacuum polarization. *Physical Review*, 82:664–679, Jun 1951.

[364] D. A. Uzdensky and S. Rightley. Plasma physics of extreme astrophysical environments. *Reports on Progress in Physics*, 77(3):036902, mar 2014.

[365] J. Esberg, U. I. Uggerhøj, B. Dalena, and D. Schulte. Strong field processes in beam-beam interactions at the compact linear collider. *Physical Review Special Topics Accelerators and Beams*, 17:051003, May 2014.

[366] J. W. Yoon, Y. G. Kim, I. W. Choi, J. H. Sung, H. W. Lee, S. K. Lee, and C. H. Nam. Realization of laser intensity over 10^{23} $\mathrm{W/cm^2}$. *Optica*, 8(5):630–635, May 2021.

[367] C. Bamber, S. J. Boege, T. Koffas, T. Kotseroglou, A. C. Melissinos, D. D. Meyerhofer, D. A. Reis, W. Ragg, C. Bula, K. T. McDonald, E. J. Prebys, D. L. Burke, R. C. Field, G. Horton-Smith, J. E. Spencer, D. Walz, S. C. Berridge, W. M. Bugg, K. Shmakov, and A. W. Weidemann. Studies of nonlinear qed in collisions of 46.6 gev electrons with intense laser pulses. *Physical Review D*, 60:092004, Oct 1999.

[368] J. Nees, N. Naumova, E. Power, V. Yanovsky, I. Sokolov, A. Maksimchuk, S.-W. Bahk, V. Chvykov, G. Kalintchenko, B. Hou, and G. Mourou. Relativistic generation of isolated attosecond pulses: a different route to extreme intensity. *Journal of Modern Optics*, 52(2-3):305–319, 2005.

[369] S. V. Bulanov, T. Esirkepov, and T. Tajima. Light intensification towards the schwinger limit. *Physical Review Letters*, 91:085001, Aug 2003.

[370] H. Vincenti. Achieving extreme light intensities using optically curved relativistic plasma mirrors. *Physical Review Letters*, 123:105001, Sep 2019.

[371] L. Fedeli, A. Sainte-Marie, N. Zaim, M. Thévenet, J. L. Vay, A. Myers, F. Quéré, and H. Vincenti. Probing strong-field qed with doppler-boosted petawatt-class lasers. *Physical Review Letters*, 127:114801, Sep 2021.

[372] N. Zaïm, A. Sainte-Marie, L. Fedeli, P. Bartoli, A. Huebl, A. Leblanc, J.-L. Vay, and H. Vincenti. Light-matter interaction near the schwinger limit using tightly focused doppler-boosted lasers. *Physical Review Letters*, 132:175002, Apr 2024.

[373] J. Clark and G. MacKerron. Great expectations: A review of nuclear fusion research. *Energy Policy*, 17(1):49–56, 1989.

[374] S. Meschini, F. Laviano, F. Ledda, D. Pettinari, R. Testoni, D. Torsello, and B. Panella. Review of commercial nuclear fusion projects. *Frontiers in Energy Research*, 11, 2023.

[375] C. Williams. Application of recommended design practices for conceptual nuclear fusion space propulsion systems. *40th AIAA/ASME/SAE/ASEE Joint Propulsion Conference and Exhibit*, 2004-3534, 2012.

[376] S. O. Dean. Applications of plasma and fusion research. *Journal of Fusion Energy*, 14(2):251–279, Jun 1995.

[377] H. Abu-Shawareb, R. Acree, P. Adams, and *et al.* Achievement of target gain larger than unity in an inertial fusion experiment. *Physical Review Letters*, 132:065102, Feb 2024.

[378] H. Kiriyama, M. Mori, Y. Nakai, T. Shimomura, M. Tanoue, A. Akutsu, H. Okada, T. Motomura, S. Kondo, S. Kanazawa, A. Sagisaka, J. Ma, I. Daito, H. Kotaki, H. Daido, S. Bulanov, T. Kimura, and T. Tajima. Generation of high-contrast and high-intensity laser pulses using an opcpa preamplifier in a double cpa, ti:sapphire laser system. *Optics Communications*, 282(4):625–628, 2009.

[379] S. Toth, T. Stanislauskas, I. Balciunas, R. Budriunas, J. Adamonis, R. Danilevicius, K. Viskontas, D. Lengvinas, G. Veitas, D. Gadonas, A. Varanavičius, J. Csontos, T. Somoskoi, L. Toth, A. Borzsonyi, and K. Osvay. Sylos lasers – the frontier of few-cycle, multi-tw, khz lasers for ultrafast applications at extreme light infrastructure attosecond light pulse source. *Journal of Physics: Photonics*, 2(4):045003, Jul 2020.

[380] C. I. D. Underwood, G. Gan, Z.-H. He, C. D. Murphy, A. G. R. Thomas, K. Krushelnick, and J. Nees. Characterization of flowing liquid films as a regenerating plasma mirror for high repetition-rate laser contrast enhancement. *Laser and Particle Beams*, 38(2):128–134, 2020.

[381] Y. Nomura, L. Veisz, K. Schmid, T. Wittmann, J. Wild, and F. Krausz. Time-resolved reflectivity measurements on a plasma mirror with few-cycle laser pulses. *New Journal of Physics*, 9(1):9, Jan 2007.

“There is always something !”
(If you know what I mean...)

ECOLE
DOCTORALE

Titre: Développement d'une source attoseconde intense basée sur des miroirs plasma relativistes à haute cadence

Mots clés: Impulsions ultrabreves, Interactions laser-plasma, Génération d'harmoniques, Miroirs plasma, Optique relativiste, Impulsions attosecondes

Résumé: Le travail expérimental présenté dans ce manuscrit a été réalisé au Laboratoire d'Optique Appliquée (LOA, Palaiseau, France) sur un système laser compact multi-mJ kHz, capable de délivrer des impulsions quasi-mono-cycle à phase enveloppe-porteuse (CEP) stabilisée. Le premier volet expérimental a consisté à améliorer les performances de la source laser grâce à l'intégration d'un étage d'amplification multi-passage cryogéné dans la chaîne destiné à augmenter l'énergie d'impulsion disponible, à améliorer la stabilité de la CEP, ainsi qu'à fiabiliser les performances quotidiennes du laser. En parallèle, une nouvelle technique a été testée, basée sur la propagation nonlinéaire dans une cellule multi-passage (MPC), afin de post-comprimer temporellement et d'améliorer le contraste temporel des impulsions laser. Dans l'avenir, une fois mis à l'échelle et intégré dans la chaîne laser, ce dispositif innovant de mise en forme temporelle d'impulsions laser, augmenter encore plus l'éclairement atteignable pour les expériences.
Le deuxième volet expérimental est axé sur l'utilisation de la chaîne laser afin de piloter des miroirs plasma relativistes et de générer du rayonnement attoseconde (1 as = 10-18 s) dans le domaine spectral de l'ultraviolet extrême, ainsi que des faisceaux d'électrons et d'ions fortement énergétiques. Nous avons pu produire des faisceaux d'électrons relativistes par injection localisée d'électrons du plasma dans le champ laser réfléchi de manière nonlinéaire par le miroir plasma. En outre, nous avons pu générer des faisceaux quasi-collimatés de protons avec des énergies proches du MeV dans le cadre d'une expérience pompe-sonde contrôlée. En stabilisant la forme d'onde des impulsions laser, nous avons pu restreindre temporellement le processus de génération d'harmoniques en-dessous du cycle laser et ainsi produire des impulsions attoseconde uniques. Nous avons réalisé une étude paramétrique complète afin d'optimiser les propriétés spatio-temporelles des impulsions attosecondes XUV ainsi émises, jetant ainsi les bases de leur refocalisation pour les applications.

Title: Development of an intense attosecond source based on relativistic plasma mirrors at high repetition rate

Keywords: Ultrashort pulses, Laser-plasma interactions, High-harmonic generation, Plasma Mirrors, Relativistic Optics, Attosecond pulses

Abstract: The experimental work presented in this manuscript was carried out at Laboratoire d'Optique Appliquée (LOA, Palaiseau, France) on a compact kHz multi-mJ energy laser system capable of delivering waveform-controlled near-single-cycle pulses. The first part of this work is focused on improving the performance of this laser source by integrating a cryogenically-cooled multi-pass amplifier in the laser chain in order to increase the output energy, enhance the laser waveform stability, making the laser source more stable and reliable, and with more overall reproducible day-to-day performance. Furthermore, we explore laser post-compression and temporal contrast enhancement in a multipass cells. In the future, this post-compression scheme when power-scaled and integrated into the laser chain will further enhance the focused pulse intensity for experiments.
The second part of this work focuses on using the laser system to drive relativistic plasma mirrors on the surface of initially-solid targets to generate highly energetic particle beams (ions and electrons) and harmonic radiation in the extreme ultraviolet region, corresponding to attosecond pulses ($1\,\mathrm{as} = 10^{-18}\,\mathrm{s}$) in the time domain. We could produce relativistic electron beams by localized injection of electrons into the nonlinearly reflected laser field by the plasma mirror. Additionally, we could generate nearly-collimated MeV-class proton beams in a controlled pump-probe experiment. By stabilizing the waveform of the driving laser pulses, we could temporally gate the interaction process on the target surface and produce isolated attosecond pulses. We performed a comprehensive parameter study to fully characterize and optimize the spatio-spectral properties of the emitted XUV attosecond pulses, laying the groundwork for their refocusing for applications.

Institut Polytechnique de Paris
91120 Palaiseau, France